The University Of Sheffield.

Magnetic Frustration Effects in the Double Perovskite Structure

Heather Mutch

A thesis submitted in partial fulfilment of the requirements for the degree of Doctor of Philosophy

The University of Sheffield

Faculty of Engineering

Department of Material Science and Engineering

31/07/2020

Abstract

The research contained within this thesis will focus on magnetically frustrated double perovskites containing various magnetic cations, outlining their structural and magnetic properties. The differences in the structures dependent on the spin state will then be compared.

This will initially outline findings from double perovskites containing the S = 5/2 magnetic cation, Mn^{2+}, Ba_2MnWO_6 and Sr_2MnWO_6. Discussing findings from neutron powder diffraction, muon spin relaxation, DC-susceptibility and inelastic neutron scattering, highlighting the similarities and differences between the two systems as well as a short-range magnetically correlated state in Ba_2MnWO_6 which has previously not been reported.

Following on from this the effect of magnetic percolation on the S = 3/2 solid solution of $Ba_2Co_{1-x}Zn_xMoO_6$ will be outlined in detail. Within this study, neutron powder diffraction and DC-susceptibility measurements were used to track how substitution of the magnetic Co^{2+} cation with the Zn^{2+} diamagnetic analogue affected the structural and magnetic properties of the series. Throughout the series, the undistorted $Fm\bar{3}m$ structure is adopted at room temperature and the thermal dependent nature of the Co^{2+} cation is shown to affect the magnetic behaviour of each material.

Finally, the structural and magnetic properties of the S = 1/2 solid solution of $Ba_{2-x}Sr_xLuMoO_6$ will be outlined. These have been measured using a variety of methods including neutron powder diffraction, DC-susceptibility, EXAFS, inelastic neutron scattering, muon spin relaxation and heat capacity measurements. These materials have each been suggested to be valence bond glasses, which will be covered in detail within this chapter.

The results collected within these studies indicate that creating only slight differences between related materials can lead to significant changes in their physical properties. These also show that materials which have previously been studied should be revisited.

Acknowledgements

Firstly, I extend many thanks to my supervisor, Dr Eddie Cussen, for his support, providing many explanations of key techniques and patience regarding my lack of understanding over 3D objects. A massive thanks to everyone in the Corr-Cussen group for their help and support and also providing light relief through social gatherings at the pub. They have each made the move to Sheffield much easier. I would also like to thank my friends at the University of Strathclyde for consistently checking in also.

I would also like to thank my family for their continued love and support. Many thanks to Colin for believing in me, listening to me ramble about science he does not understand and giving me tutorials on creating nice figures. And finally, to Grace, Jan and the rest of my friends for always being there for me and helping me to get through this.

Finally, I would like to extend thanks to the ISIS neutron source for beam time. Huge thanks to Peter Baker, Helen Walker and Ivan da Silva for their help with data analysis off the beam line and to Gavin Stenning for allowing us to use his wonderful facilities at the Materials Characterisation Laboratory. Thanks to Sian Dutton and her research group at the University of Cambridge for use of their PPMS and thanks to Dan Allwood, Nicola Morley, Zhao and Aris at University of Sheffield for their help with SQUID measurements. Finally, I would also like to thank the University of Sheffield and the University of Strathclyde for allowing me to carry out my PhD and providing funding for this research.

Abbreviations

JT	Jahn Teller
FM	Ferromagnetism
AFM	Antiferromagnetism
FCC	Face Centred Cubic
μ_{eff}	Effective Magnetic Moment
XRD	X-ray Diffraction
NPD	Neutron Powder Diffraction
DC-SQUID	Direct Current – Superconducting QUantum Interference Device
μSR	Muon Spin Relaxation
INS	Inelastic Neutron Scattering
NN	Nearest Neighbour
NNN	Next Nearest Neighbour
GSAS	General Structure Analysis System
MPMS	Magnetic Property Measurement System
PPMS	Physical Property Measurement System

Contents

1. Theory

Crystals and Symmetry

Solid state chemistry and material science requires an understanding of crystal structures and their internal symmetry. Crystals are arrays of atoms, molecules or ions which are described by a periodic repeating section, the unit cell. Bonding within crystals may be covalent or electrostatic. The unit cell is defined by lattice parameters; bond lengths, bond angles and internal symmetry [1].

Unit Cell

The unit cell describes the smallest possible repeating structure of any crystal and contains all necessary information for extension into a lattice. The unit cell removes the need to model the entire structure, which can be useful computationally by saving calculation time and expense. Unit cells are composed of lattice points, areas where atoms can reside. Figure 1.1 shows a permitted and non-permitted unit cell.

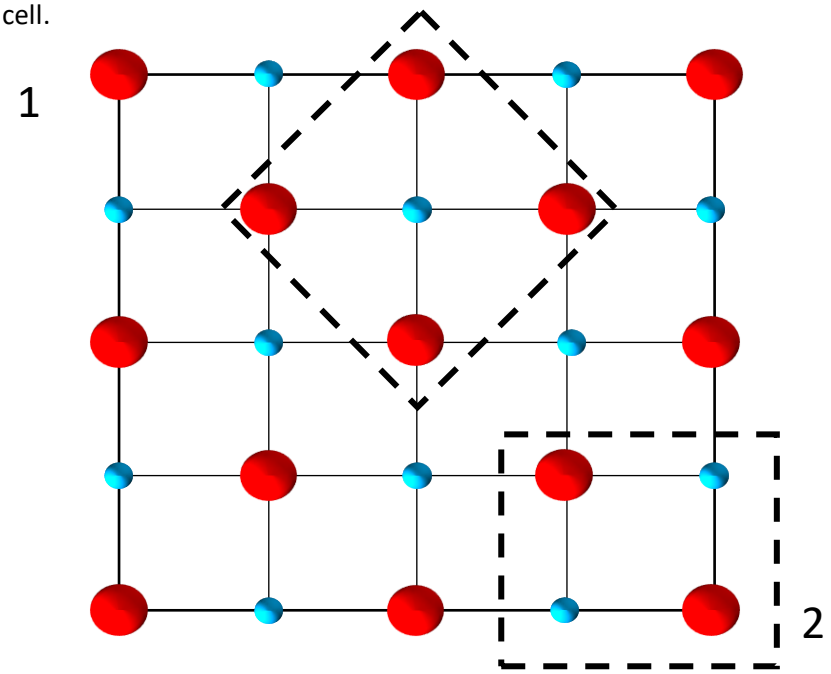

Figure 1.1: A 2D lattice with a correctly identified unit cell (1) which has a lattice point at each corner of the unit cell and (2) an incorrectly identified unit cell. The unit cells are outlined by the dashed lines and the red and blue spheres represent two distinct lattice points.

The unit cell is described by lattice parameters; a, b and c which are lengths and the angles between the ab, ac and bc planes which are denoted by γ, β and α respectively. The combination of the lattice

parameters defines the shape of the unit cell. Within extended crystals the unit cell must be either 3, 4 or 6 sided. Shapes which are unable to tesselate are not eligible as unit cells. Figure 1.2 depicts viable and prohibited unit cell shapes.

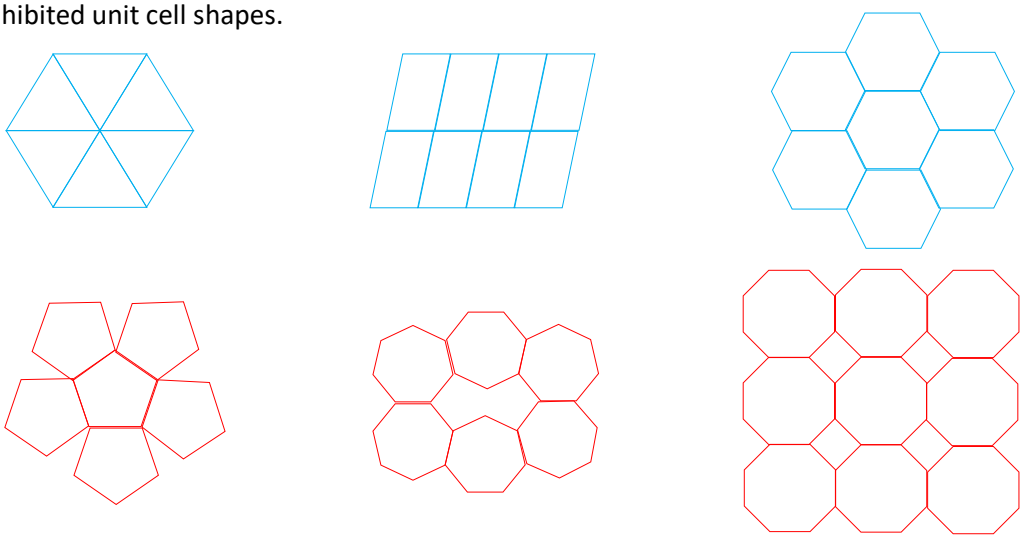

Figure 1.2: Acceptable 2D 3-, 4- and 5-sided unit cell shapes which are drawn in blue and those which are unacceptable as they cannot tesselate shown in red, pentagons, heptagons and octagons.

Cubic crystals are the highest symmetry as they have one variable lattice parameter, as the degrees of freedom increases, the symmetry is lowered. The crystal classes are outlined in Table 1:1 [2].

Table 1:1: Crystal classes with the distinct unit cell specification for the crystal class.

Crystal Class	**Unit Cell Vectors**	**Unit Cell Interaxial Angles**
Cubic	$a = b = c$	$\alpha = \beta = \gamma = 90°$
Tetragonal	$a = b \neq c$	$\alpha = \beta = \gamma = 90°$
Orthorhombic	$a \neq b \neq c$	$\alpha = \beta = \gamma = 90°$
Rhombohedral	$a = b = c$	$\alpha = \beta = \gamma \neq 90°$
Hexagonal	$a = b \neq c$	$\alpha = \beta = 90° \, \gamma = 120°$
Monoclinic	$a \neq b \neq c$	$\alpha = \gamma = 90° \, \beta \neq 90°$
Triclinic	$a \neq b \neq c$	$\alpha \neq \beta \neq \gamma$

Symmetry Within Crystals

Internal symmetry dictates the arrangement of the unit cell contents. Symmetry operations are divided into point or space operations. Point symmetry includes mirror planes and inversion axes, whilst spatial operations include glide planes. Different notations are used to describe the symmetry operations; Hermann-Maguin notation in crystallography and Schönflies for spectroscopic purposes. There are multiple symmetry operations which apply to crystals and these will be described [3].

Translational symmetry drives the periodic nature of crystals. This defines the unit cell and repeats it in all possible directions generating the final crystal, as shown in Figure 1.3 .

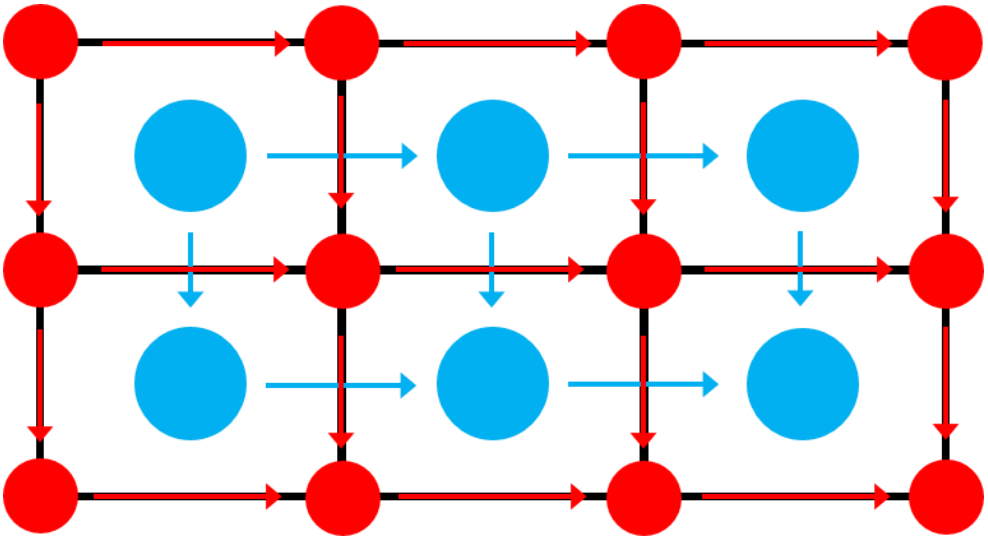

Figure 1.3: A depiction of translational symmetry within a unit cell. The top right-hand side cell is the origin and is translated in both the x and y directions. The arrows indicate the copying of the contents of the unit cell in all directions.

Rotational axes are imaginary lines which define points of rotation. These can be 1-, 2-, 3-, 4- or 6-fold.

Some shapes and their rotational axes are shown below in Figure 1.4.

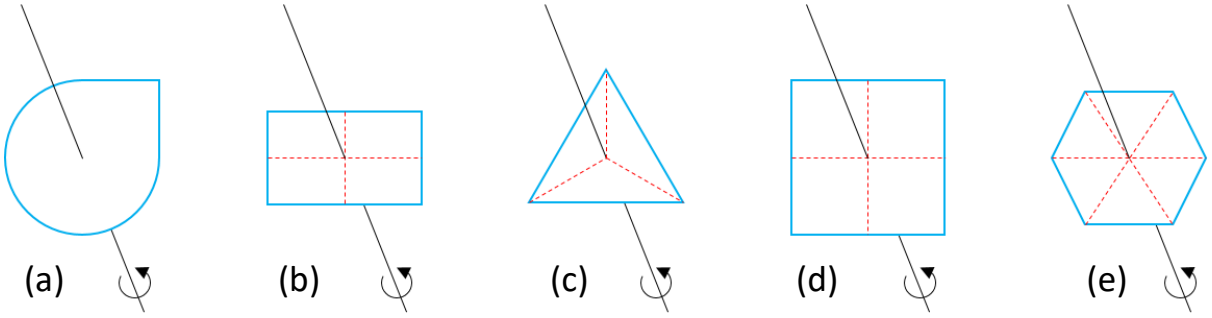

Figure 1.4: 2D shapes with a rotational axis drawn through them. (a) 1-fold a full 360° is necessary to get back to its original starting point, (b) 2-fold with a 180° rotation, (c) 3-fold, a triangle can return to normal through a 60° rotation, (d) a square showing 4-fold rotation and (e) 6-fold rotation which is observed in perfect hexagons.

Inversion centres are present when contents are translated through the origin, e.g. a translation from (x, y, z) to (-x, -y, -z) in a 3D plot. This is illustrated in Figure 1.5(a). Mirror planes are present when contents are reflected, these are similar to inversion centres however; the reflection of the contents only takes place across one axis, see Figure 1.5(b).

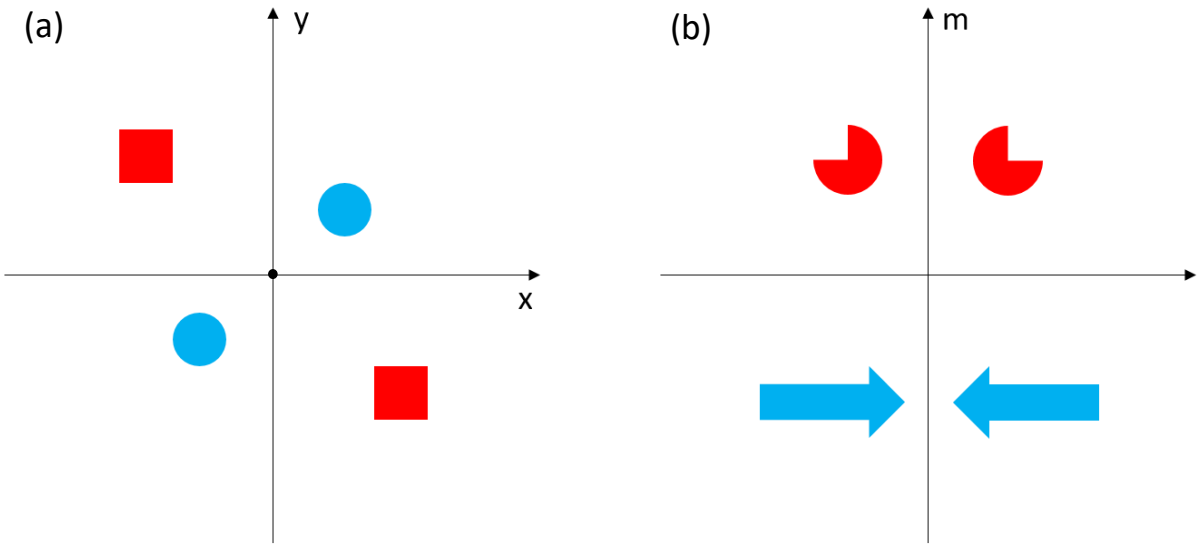

Figure 1.5: (a) A 2-dimensional plot which indicates how an inversion centre (the black sphere at the intersection of the x and y axes) affects the plot. Both the blue sphere and the red square are translated so they are observed in the opposite region of the plot in both the x and y directions. (b) A 2D plot showing how a mirror plane affects the graph. Mirror axes are denoted by m and the symbols are reflected across this plane.

Other symmetry operations include; inversion axes, glide planes and screw axes. Inversion axes are rotations followed by inversion through a centre of symmetry and these are only observed in large extended crystal structures. Alternating axes of symmetry are rotations followed by a reflection, these are not readily observed in crystals but appear in discrete structures. Glide planes result in an atom being reflected through a plane and then translated by some distance. Screw symmetry is a rotation which is then followed by a translation. The notation in both the Hermann-Maguin and Schönflies notation are outlined in Table 1:2 [4].

Table 1:2: Symmetry operations and the symbols from the Hermann-Maguin and Schönflies notation

Symmetry Element	Hermann-Maguin Symbols	Schönflies Symbols
Mirror Plane	m	σ_v, σ_h
Rotation Axis	n (2, 3, 4, 6)	C_n
Centre of Symmetry	$\bar{1}$	i
Inversion Axis	$\bar{n}\ (\overline{\bar{1}, \bar{2}..})$	N/A
Alternating Axis	N/A	S_n
Glide Plane	n, d, a, b, c	N/A
Screw Axis	2,3…	N/A

Bravais Lattice

The Bravais lattice defines the centering of the unit cell. Centering can decrease the size of a primitive cell, with options of face- (F), base- (A, B or C) or body centering (I). Face centred cells possesses lattice points on each corner plus the centre of each face. Body centred cells possess have lattice points on each corner plus an additional one in the centre of the cell. Base centred cells have extraneous lattice points on two parallel faces, which correspond to either the A, B or C faces. An illustration of these is shown in Figure 1.6 [2]. Centering is dependent on crystal class and internal symmetry therefore, there are only 14 potential Bravais lattices. Orthorhombic crystals may be primitive, face-, base- or body-centred. Table 1:3 shows the potential Bravais lattices for each crystal class [5].

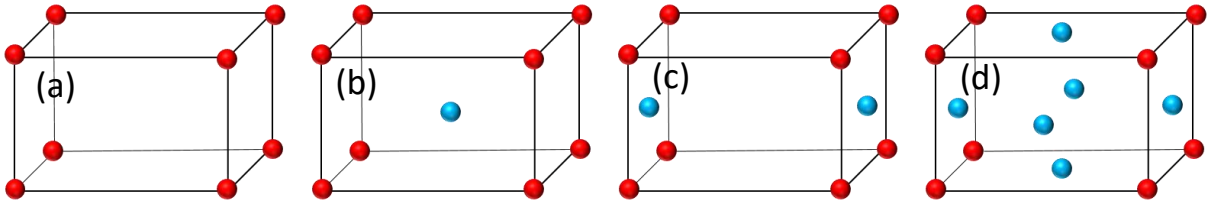

Figure 1.6: Orthorhombic Bravais lattices (a) primitive, (b) body centred, (c) base centred and (d) face centred. The additional centering lattice points are shown in a different colour to highlight them.

Table 1:3: The crystal classes and Bravais lattices which can be achieved in that unit cell [5].

Crystal Class	Bravais Lattice
Cubic	P, I, F
Tetragonal	P, I
Orthorhombic	P, I, C, F
Rhombohedral	P (R)
Hexagonal	P
Monoclinic	P, C
Triclinic	P

Space Groups

Combining the crystal class, centering and symmetry operations allows the space group to be established. There are 230 distinct space groups [5]. Throughout this research, the $Fm\bar{3}m$, *I4/m* and $P2_1/n$ space groups will be explored in detail. The face centred cubic space group $Fm\bar{3}m$ is the undistorted space group of the double perovskite; it contains two mirror planes and a 3-fold rotation through an inversion centre. The tetragonal, *I4/m*, is body centred with a 4-fold rotation and a mirror plane and the monoclinic, $P2_1/n$, is a primitive cell with a screw axis and a glide plane.

Miller Indices

Crystals are described using lattice planes, imaginary planes which intersect the lattice parameters. The planes are aligned parallel to each other, separated by a defined d-space. Miller indices are assigned by determining the intersection of the lattice parameters and taking the reciprocal. These are integer values denoted using (hkl), where; h, k and l correspond to the intersection of the *a*, *b* and *c* axes respectively. Lattice planes may be equivalent in higher symmetry systems which is shown as

{hkl}, e.g. {100}, which describes the (100), (010) and (001) Miller indices. The d-space may be calculated for each crystal class from the lattice parameter and Miller indices. These are outlined below. In these equations; *a*, *b*, *c*, *α*, *β* and *γ* are the lattice parameters, *h*, *k* and *l* are Miller indices and *d* is the interplanar spacing [2].

Equation 1.1: Relationship between d-space and lattice parameter for a cubic system

$$\frac{1}{d_{hkl}^2} = \frac{h^2 + k^2 + l^2}{a^2}$$

Equation 1.2: Relationship between d-space and lattice parameter for a tetragonal system

$$\frac{1}{d_{hkl}^2} = \frac{h^2 + k^2}{a^2} + \frac{l^2}{c^2}$$

Equation 1.3: Relationship between d-space and lattice parameter for an orthorhombic system

$$\frac{1}{d_{hkl}^2} = \frac{h^2}{a^2} + \frac{k^2}{b^2} + \frac{l^2}{c^2}$$

Equation 1.4: Relationship between d-space and lattice parameter for a hexagonal system

$$\frac{1}{d_{hkl}^2} = \frac{4}{3}\left(\frac{h^2 + hk + k^2}{a^2}\right) + \frac{l^2}{c^2}$$

Equation 1.5: Relationship between d-space and lattice parameter for a monoclinic system

$$\frac{1}{d_{hkl}^2} = \frac{1}{\sin^2\beta}\left(\frac{h^2}{a^2} + \frac{k^2\sin^2\beta}{b^2} + \frac{l^2}{c^2} - \frac{2hlcos\beta}{ac}\right)$$

Equation 1.6: Relationship between d-space and lattice parameter for a triclinic system

$$\frac{1}{d_{hkl}^2} = \frac{1}{V^2}[h^2b^2c^2\sin^2\alpha + k^2a^2c^2\sin^2\beta + l^2a^2b^2\sin^2\gamma + 2hkabc^2(cos\alpha cos\beta - cos\gamma)$$

$$+ 2kla^2bc(cos\beta cos\gamma - cos\alpha) + 2hlab^2c(cos\alpha cos\gamma - cos\beta)]$$

$$V = abc(1 - \cos^2\alpha - \cos^2\beta - \cos^2\gamma + 2cos\alpha cos\beta cos\gamma)$$

Ideal Crystals

Perfect crystals contain assigned positions for all contents within the unit cell, these are translated throughout the crystal without discrepancy. This is impractical due to atomic vibrations and a series of faults or irregularities. These imperfections include atomic vacancies or extraneous atoms being placed on interstitial sites. This section will describe why perfect crystals are not observed and different faults which take place.

The second law of thermodynamics states that entropy wants to increase whenever possible, therefore, highly regular perfect crystals are not entropically favoured. To satisfy entropy, small defects can be found within all crystals which can affect the system to different extents. Increases in entropy are governed by the Boltzmann law [6].

Equation 1.7: Boltzmann law of entropy

$$S = klnW$$

In Equation 1.7, *S* corresponds to the entropy of the system, *k* is the Boltzmann's constant and *W* is the probability of randomness, which in a large crystal could be monumental as there are many possible positions the defect could occur.

This increase in entropy can have a large effect on the Gibb's free energy. A large entropy (*S*) can result in the free energy (*G*) to fall, ensuring a more thermodynamically stable structure. The relationship between free energy and entropy is outlined in Equation 1.8, where *H* is the enthalpy of the system and *T* is the temperature.

Equation 1.8: Calculating Gibb's free energy

$$\Delta G = \Delta H - T\Delta S$$

A more thermodynamically stable structure can be obtained through non-stoichiometric or stoichiometric defects which occur in localised areas or spread throughout the crystal. Point defects, such as lattice vacancies or interstitial additions, result in the removal or addition of atoms throughout

the crystal. This can result in charge difference which can lead to an unpreferable large electrostatic potential. These can be observed in Figure 1.7. Other localised imperfections include Schottky and Frenkel defects. The Schottky defect results in both an anion and cation being simultaneously removed from the structure, preserving electroneutrality. The Frenkel defect arises when an atom is removed but an identically charged species is placed on an interstice. Both of these may cause small cluster of ions to aggregate due to electrostatic attractions [7].

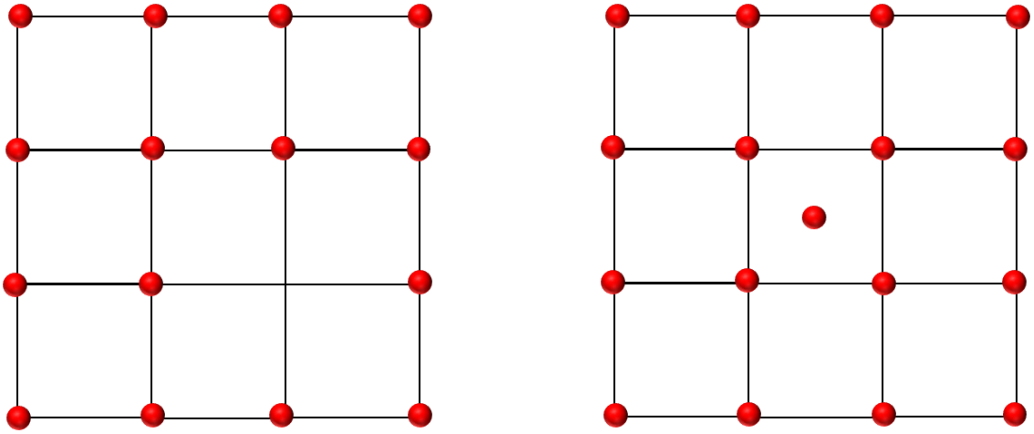

Figure 1.7: Representations of point defects which take place in crystals. The left-hand side shows how a lattice vacancy would arise within the system and the right-hand side shows the situation where a supplementary atom is added to the lattice but lies in an interstice. These can result in electroneutrality being compromised.

Linear defects like dislocations occur along one dimension of the crystal. Planar defects include shear planes and grain boundaries. Any of these extended defects can arise in random locations or persist regularly throughout the system. These can have a large effect on the crystal properties and can cause detriment to the mechanical properties [6,7].

Defects are often seen as problematic but can improve the performance of some materials. They are utilised in doped semi-conductors, where extraneous protons or electrons are inserted to promote conductivity. In solid state ionic conductors vacancies improve the mobility of charge carriers [8].

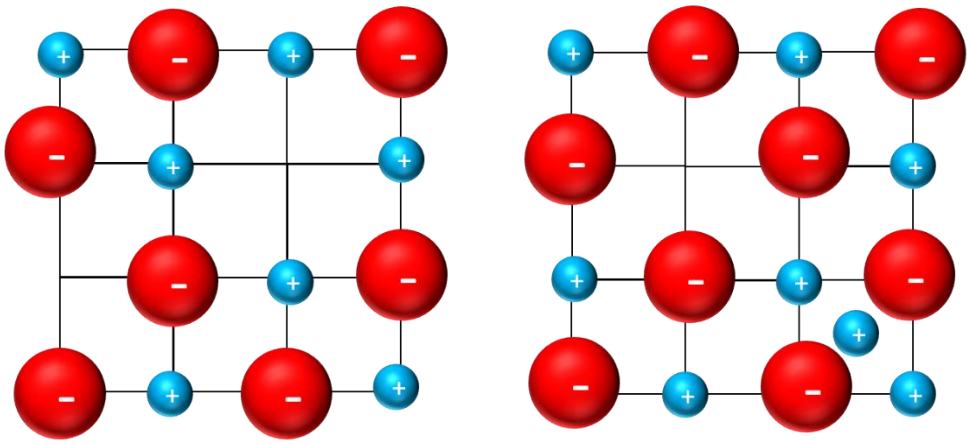

Figure 1.8: The left-hand side indicates a Schottky defect where both a cation and anion are removed from the crystal structure. The right-hand side indicates the Frenkel defect indicates where a cation is removed from its defined position and moves to an interstitial site. Both of these preserve electroneutrality as the same number of opposing ions are removed or all are retained by the system.

Bonding in Solids

Bonding within solid systems may be described as ionic, covalent, metallic or molecular bonding. This section will delve into most of these intramolecular bonding types.

Ionic Bonding

Ionic bonding occurs through an electrostatic attraction between two oppositely charged ions, quantified by a large difference in electronegativity. Identical ions repulse each other and are typically separated by an ion of opposite charge. This generates a regimental crystal and helps to ensure that electroneutrality is achieved. Coulomb's law describes the electrostatic force between the two ions, this is related to ionic charge (q), the force constant (k) and distance between the ions (r).

Equation 1.9: Coulomb's Law

$$F = k\frac{q_1 q_2}{r^2}$$

The repulsive force is described using the Born-Lande interaction. The energy of the repulsion is described by V, the scaling constant B, r is the ionic separation and n is the Born exponent which lies between 5 and 12. The value of the exponent is dependent on the repulsive force between the two

ions. A modified version, the Born-Mayer repulsion equation can be used if the ions are exceptionally close to each other. In this equation, ρ is a constant.

Equation 1.10: Born-Lande repulsive interaction

$$V = \frac{B}{r^n}$$

Equation 1.11: Born-Mayer repulsion equation

$$V = Bexp\left(-\frac{r}{\rho}\right)$$

The attractive and repulsive forces compete, allowing an energy diagram to be drawn. These forces are highly dependent on ionic separation and the energy diagram can predict the distance corresponding to the energy minimum [9].

Covalent Bonding

Covalent bonding occurs between atoms through the sharing of electrons when significantly smaller differences in electronegativity are involved. Covalent bonding in solids results in the formation of large networks of atoms or molecules, such as the metastable form of diamond.

Partial Covalent Bonding

Partial covalent bonding takes place in systems when an intermediate between covalent and ionic bonding takes place. Here, the electron density is more strongly polarised towards the ion with higher electronegativity. Partial covalent bonding can be described by either Sanderson's "Co-ordinated Polymeric Structures" model or Mooser's and Pearson's "Plots and Ionicities". The Sanderson's model approaches this from a more covalent basis, using effective nuclear charge to determine the partial charge of the contents of the material. Whilst, the Mooser model comes from an ionic perspective, utilising the average principal quantum number and the difference in electronegativity to produce plots of these [9].

Bond Valence

Crystals cannot be described by Valence Bond Theory as they are often electron deficient and therefore, their intramolecular bonds are regarded as partial bonds. This was established by Pauling who developed the bond valence method, which can determine the oxidation state of each ion within the crystal using the following equations.

Equation 1.12: Bond valence sum calculation

$$BVS = \sum v_i$$

Equation 1.13: Individual bond valence calculation

$$v_i = \exp\left(\frac{R_0 - R_i}{b}\right)$$

In these equations, *BVS* is the bond valence sum, v_i is the individual bond valences, R_0 is the bond length when the valence of the atom is equal to 1. R_i is the bond length obtained from the diffraction pattern of the material being examined. Whilst the *b* parameter is an empirically obtained constant which is related to the R_0 value, both of which were determined through experimentation. The *b* parameter is often equal to 0.37Å but due to the dependence on R_0 this can change [10]. Bond valence sums can be used calculate the oxidation state of multivalent cations. This is important in magnetically frustrated species as it can determine the spin state of the magnetic cation.

Crystal Field Splitting

Field splitting is observed when atoms are moved from a spherical field to a non-spherical field e.g. octahedral or tetrahedral. In a spherical field the d orbitals are degenerate and when removed from this the degeneracy is lost causing an energy split [9].

When placed in an octahedral field the e_g ($d_{x^2-y^2}$ and d_{z^2}) orbitals are increased in energy whilst the t_{2g} (d_{xy}, d_{xz} and d_{yz}) orbitals are lowered in energy. The ligands lie closer to the e_g orbitals resulting in a repulsion, raising the energy. Simultaneously, the ligands move further from the orbitals which lie in the plane, and therefore these are lowered in energy. This generates a crystal field splitting energy,

Δ_O, which is dependent on both the metal cation and surrounding ligands. When placed in a tetrahedral field, the energy of the t_{2g} orbitals rises whilst the e_g orbitals decreases. Tetrahedral field splitting is a weaker effect than octahedral splitting by approximately 60%.

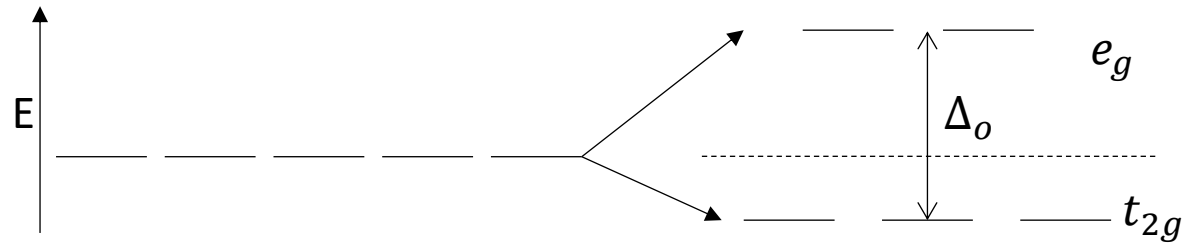

Figure 1.9: Octahedral field splitting diagram. Originally in the spherical field all the d-orbitals are degenerate. When placed in the octahedral field, the d orbitals are split with the e_g orbitals being raised in energy and subsequently the t_{2g} orbitals are lowered in energy. This is a result of the ligands either coming closer or further away from these orbitals. Δ_O represents the crystal field splitting energy for the octahedral field.

Jahn-Teller distortions also reduce the degeneracy of the d orbitals. The Jahn-Teller effect causes an octahedral distortion yielding distinct equatorial and axial bond lengths. When the axial bonds are significantly longer than the equatorial bonds the octahedra experiences a tetragonal elongation. When the axial bonds are significantly shorter than the equatorial bonds the octahedra is described as tetragonally compressed. Jahn-Teller distortions are only observed in specific electronic configurations of Jahn-Teller distortions as either the e_g or t_{2g} orbitals must have an unequal occupancy of electrons. Therefore, this will not be observed in d^{10} ions, d^3 ions, the high spin equivalent of d^5, the low spin equivalent of d^6 or d^8 electron configurations.

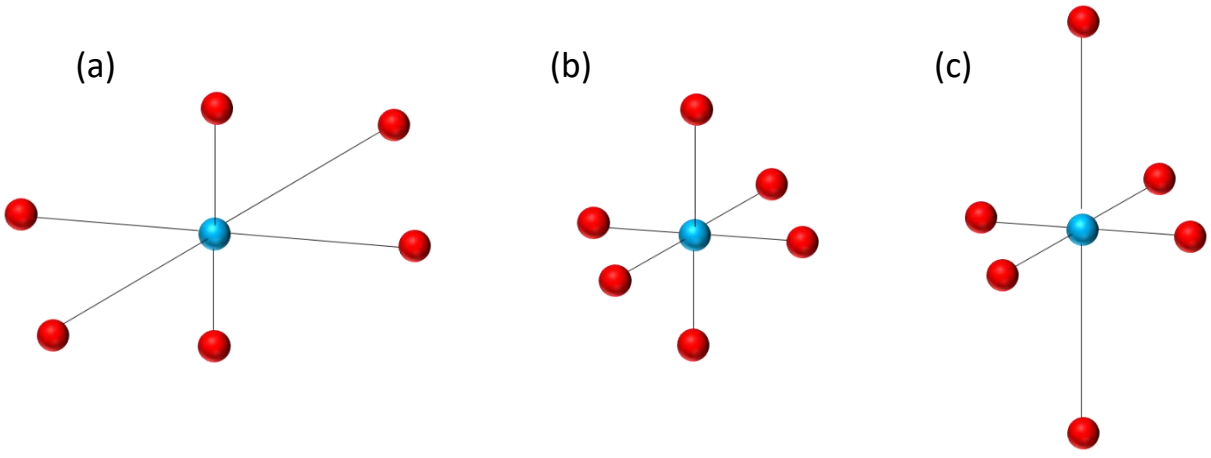

Figure 1.10: (b) the perfect octahedra which experiences no Jahn-Teller distortion. (a) The tetragonally compressed octahedra and (c) The tetragonally elongated octahedra.

Jahn-Teller distortions tend to be more pronounced when the unequal occupancy takes place in the e_g orbitals compared to the t_{2g} orbitals. Notable Jahn-Teller active cations include Cu^{2+} and Ag^{2+} cations which have the electronic configuration d^9, experiencing a tetragonal elongation [11]. High spin d^4 cations such as Cr^{2+} and low spin d^7 cations such as Co^{2+} or Ni^{3+} are also able to exhibit these stronger Jahn-Teller distortions [11].

Magnetism

Magnetism arises due to interactions between magnetic moments or poles, with the attractive force quantified by Coulomb's law. Where; *F* is the attraction between the magnetic moments, *k* is the force constant, *m* represents the magnetic strength of each moment, *r* is the separation of the moments and r_O is a vector running along the length of *r*.

Equation 1.14: Coulomb's law - magnetic attraction

$$F = \frac{km_1m_2r_O}{r^2}$$

The magnetisation of a system is a vector quantity defined as the magnetic moment per unit volume, measured in $cm^3\ mol^{-1}$ G. This can be calculated by multiplying an individual magnetic moment (μ) by the total number of magnetic moments (*N*) and dividing this by the volume of the system (*V*) [12]. The magnetic moment originates when electrons orbit a nucleus and rotate around their own axis [13].

Equation 1.15: Magnetisation relationship

$$\boldsymbol{M} = \frac{\mu N}{V}$$

In a vacuum the magnetic flux density, *B*, is related to the applied field strength, *H,* and the permittivity of free space, μ_0, using the following equation.

Equation 1.16: Magnetic flux density in a vacuum

$$\boldsymbol{B} = \mu_0 \boldsymbol{H}$$

When the magnetic flux density and applied magnetic field are unequal, the magnetisation is included.

Equation 1.17: Magnetic flux density containing magnetisation

$$\boldsymbol{B} = \mu_0(\boldsymbol{H} + \boldsymbol{M})$$

Magnetic susceptibility, units $cm^3\ mol^{-1}$, indicates the field dependence of magnetisation, yielding the following equation;

Equation 1.18: Magnetic susceptibility calculation

$$\chi = \frac{\boldsymbol{M}}{\boldsymbol{H}}$$

The magnetic susceptibility can be based on mass or moles, which can be useful for comparison purposes. The mass susceptibility is calculated by dividing by the density of the material. Multiplying by the molecular weight gives the molar susceptibility.

Susceptibility characterises magnetic type: diamagnetic, paramagnetic, ferromagnetic, ferrimagnetic and antiferromagnetic. The latter three are cooperative forms of magnetism and can achieve long range magnetic order without the presence of an external magnetic field [13].

Diamagnetism

Diamagnetism occurs when no unpaired electrons are present. Here, magnetisation occurs in the opposite direction to the applied magnetic field, resulting in a temperature independent and negative susceptibility [14]. In strong magnetic fields, diamagnetic materials may be levitated [15].

Paramagnetism

Paramagnets experience a random distribution in the orientation of magnetic moments. Below the Curie temperature the majority of these align with the applied magnetic field. Ideal paramagnets exhibit a temperature dependent magnetic susceptibility, which is independent of the applied field. This is described by Curie's Law where the relationship is found by the Curie constant parameter (*C*) [16]. This is depicted in Figure 1.11.

Equation 1.19: Curie's Law

$$\chi = \frac{C}{T}$$

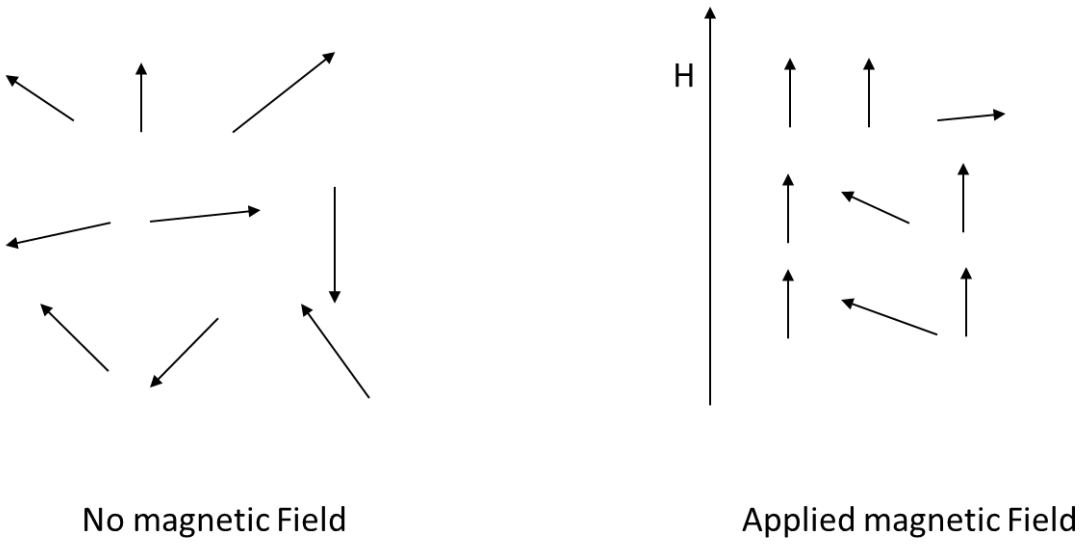

Figure 1.11: When no magnetic field is applied to a paramagnet the moments are orientated randomly. When an external field is applied most of the moments align with the field.

Curie's law assumes the systems have a permanent magnetic dipole, which prevents it from being applied to all materials. Due to this, materials which slightly deviate from this ideal are described by Curie-Weiss law [17].

Equation 1.20: Curie-Weiss Law

$$\chi = \frac{C_{CW}}{T - \theta_{CW}}$$

Curie-Weiss law also shows a temperature dependent susceptibility but allows both the Curie constant (C_{CW}) and Weiss constant (ϑ_{CW}) to be extracted. The Weiss constant, ϑ_{CW}, describes the interaction between magnetic moments. When this is positive, ferromagnetic interactions take place and when this is negative antiferromagnetic interactions are involved. The magnitude of ϑ_{CW} refers to the strength of the interaction, therefore, stronger interactions are attributed to larger ϑ_{CW}.

The Curie constant is used to calculate the effective magnetic moment using the following equation, which requires the Boltzmann constant and Avogadro's number.

Equation 1.21: Effective magnetic moment from the Curie constant

$$\mu_{eff} = \left(\frac{3k_B}{N_A}C\right)^{\frac{1}{2}}$$

$$\mu_{eff} = \left(\frac{3k_B}{N_A}\right)^{\frac{1}{2}} C^{\frac{1}{2}}$$

$$\mu_{eff} \approx 2.84\left(\sqrt{C}\right)$$

Magnetic susceptibility is comprised of diamagnetic and paramagnetic susceptibilities. Diamagnetic susceptibility is significantly weaker than paramagnetic, however, it is not negligible [16].

Paramagnetism is described by the spin (*S*) and angular momentum (*L*) of a system as shown in the following equation, where *g* is the gyromagnetic factor;

Equation 1.22: Calculation of magnetic moment based on spin and orbital momentum contribution

$$\mu_{eff} = \left(g^2 S(S+1) + L(L+1)\right)^{\frac{1}{2}}$$

This equation is used when both the spin-spin interactions plus the orbital angular moment must be taken into account and typically is used for atoms with small atomic numbers, i.e. Z < 30. This equation tends to only be applicable in systems with very high symmetry and when orbitals containing unpaired electrons are degenerate.

When the splitting of the orbital energy levels is large relative to kT, the product of the Boltzmann constant and the temperature then the following equation may be applied, where *J = L+S*. This is important when considering systems which are susceptible to spin-orbit coupling.

Equation 1.23

$$\mu_{eff} = g(J(J+1))^{\frac{1}{2}}$$

Typically, the contribution from the spin-spin interactions are stronger than those from orbital angular momentum and therefore, the spin only magnetic moment can be derived.

Equation 1.24: Spin only magnetic moment

$$\mu_{SO} = \left(4S(S+1)\right)^{\frac{1}{2}}$$

This can be rewritten so it is based on the number of unpaired electrons (*n*) within the system.

Equation 1.25: Spin only magnetic moment based on number of electrons

$$\mu_{SO} = \left(n(n+2)\right)^{\frac{1}{2}}$$

In situations where the orbital contribution must be considered, Russell-Saunders theory may be applied. In these instances, the electrons possess orbital angular momentum which is not equal to 0 and therefore may be transformed through rotation to an equivalent configuration. Considering d-orbitals within an octahedral field; the t_{2g} orbitals may be transformed purely by rotation whilst the e_g orbitals cannot. The d^1, d^2, d^6 (high spin) and d^7 (high spin) all experience an orbital contribution. Whenever the three t_{2g} orbitals are filled a sole arrangement of the t_{2g} orbitals is achieved and therefore no orbital angular momentum is observed.

Russell-Saunders coupling uses the quantum numbers (outlined in Table 1:4) to describe the effect of spin orbit coupling in a crystal field. There are three ways that magnetic coupling can arise; spin-spin coupling, orbit-orbit coupling and spin-orbit coupling. Using this theory, spin-spin coupling is found to be stronger than orbit-orbit and these are both greater than spin-orbit coupling.

Table 1:4: The quantum numbers and their description

Quantum number	**Description**	**Values**
n	The principal quantum number which mainly governs size and energy	1,2,3….
l	The orbital quantum number which determines the orbital shape	$0 \leq l \leq n - 1$
m_l	The magnetic quantum number which describes the orientation of the subshell (e.g. p_x, p_y or p_z)	$l \leq m_l \leq - l$
m_s	The spin quantum number	Can range through a variety of number for an electron $m_s = \pm 1/2$

Spin-spin coupling (*S*) is calculated by adding the individual m_s values together. Orbit-orbit coupling is calculated from the total orbital angular momentum of the system, e.g. s orbitals have L = 0, p, L = 1 and d orbitals possess L = 2. Spin-orbit coupling occurs between resultant spin and orbital momenta of an electron and this gives rise to *J*. The Russell-Saunders coupling ground term is given as $^{(2S+1)}L$, which describes the behaviour of an isolated, free ion. When placed in a crystal field the orbital angular momentum is quenched, this occurs fully in s orbital states and to an extent in p, d and f orbitals, where some residual orbital momentum remains. Spin-orbit coupling is temperature dependent as the energy levels are now able to be populated with increasing temperature and explains why ions such as Co^{2+} do not adhere to Curie-Weiss behaviour [18,19].

Antiferromagnetism

Antiferromagnetism arises when interactions between magnetic moments result in an antiparallel arrangement of spins [14]. Developed by Néel, this was initially described as two magnetic sublattices with a parallel alignment of moments, orientated antiparallel to each other achieving a net magnetisation of zero [20,21]. Antiferromagnets exhibit a distinctive kinked susceptibility, which increases as temperature decreases before reaching a maximum at the Néel temperature, before tending towards zero as the temperature further decreases as shown in Figure 1.12. In an idealised antiferromagnet the susceptibility should fall to zero, however, finite crystal sizes, surfaces and crystal imperfections prevent this from being precisely observed experimentally [20].

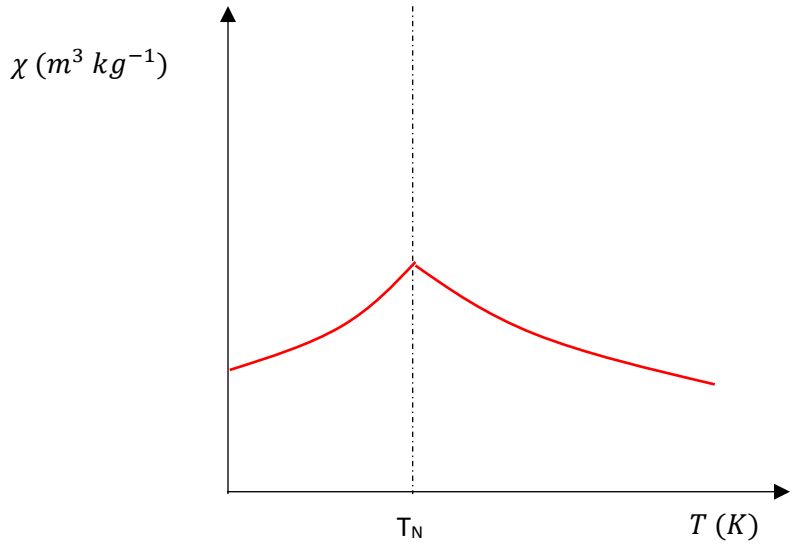

Figure 1.12: An example of the DC-susceptibility response of a 3-D antiferromagnetic material. The red line indicates that the magnetisation is low at high temperature with a maximum at the Néel temperature. Below the transition temperature the susceptibility falls towards zero, without reaching this value.

Antiferromagnetic coupling can take place in G-, A- or C-type ordering, see Figure 1.13. In G-type ordering, moments are arranged antiparallel to all adjacent moments. In A-type antiferromagnetism, magnetic moments are aligned parallel within layers, but adjacent layers are arranged antiparallel to each other. In C-type antiferromagnetic structures, magnetic moments within columns are parallel but adjacent columns are antiparallel to each other. Both A- and C-type antiferromagnets experience ferromagnetic interactions but overall exhibit antiferromagnetic behaviour.

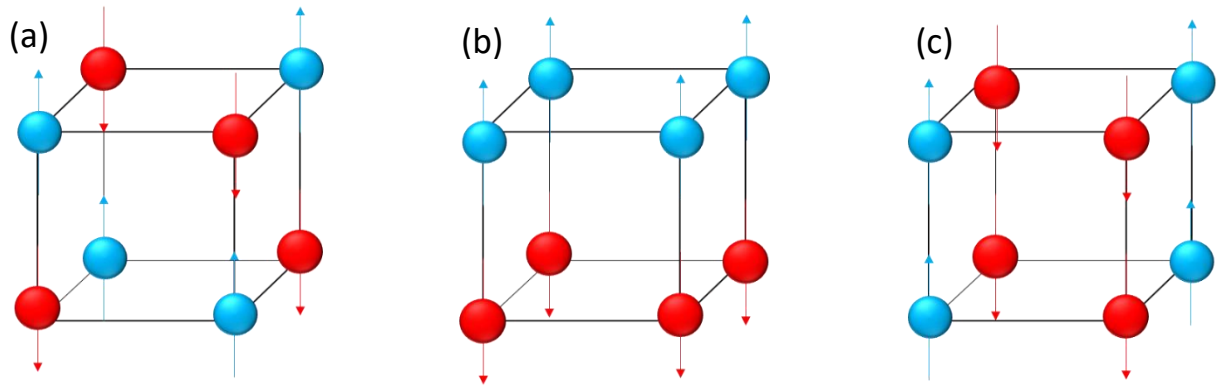

Figure 1.13: Simple examples of the different types of antiferromagnetism (a) G-type, (b) A-type, (c) C-type. G-type antiferromagnetism shows all nearest neighbour interactions are antiferromagnetic.

Exchange Interactions

Exchange interactions drive magnetic behaviour, their strength is denoted by the magnetic exchange parameter, *J*. This minimises the energy via Equation 1.26.

Equation 1.26: Equation showing the energy which is dependent on the dot product of two vectors which represents the spins on two magnetic centres.

$$E = -J\ (S_i . S_j)$$

As indicated by Equation 1.26 when the magnetic exchange parameter is positive it defines ferromagnetic interactions and conversely a negative *J* suggests antiferromagnetic alignment leading to a lower energy configuration. The magnitude of *J* defines the strength of the magnetic interaction and therefore, a larger exchange parameter corresponds to stronger interactions. The strength is dependent on orbital overlap and the distance between magnetic cations. J_1 is the magnetic exchange interaction arising between nearest neighbour magnetic cations, whilst J_2 is the magnetic exchange interaction which occurs between two next nearest neighbour interactions. The nearest neighbour cations are those which are separated by the shortest distance and the next nearest neighbour cations are separated by a slightly larger distance. Exchange interactions are brought about by two primary routes; direct exchange and superexchange [22,23].

Direct exchange arises when two metal centres interact without a ligand separating them. These interactions are not observed frequently as the overlap between the metal centres is generally poor, due to repulsion [24].

Superexchange interactions require at least one supplementary ligand between the two metal centres. The outcome of the superexchange interaction is determined from the Goodenough-Kanamori rules which were developed to derive both the type and strength of the magnetic interaction. Superexchange interactions are highly dependent on orbital overlap and the angle connecting the metal cations.

Linear alignment of the metal cations allows ideal antiferromagnetic superexchange interaction to occur. The overlap between the identical half-filled metal d-orbitals, and the p-orbital of the ligand drives the electron spin to be opposite in the neighbouring magnetic metal cations. This is shown in Figure 1.14 where the electron of the first metal aligns spin up, the ligand then completed this bond with a spin down electron. The remaining ligand electron then aligns antiparallel to this as expected from the Pauli exclusion principle, which forces the remaining electron on the metal to align spin down. This results in the antiferromagnetic interaction from the superexchange interaction.

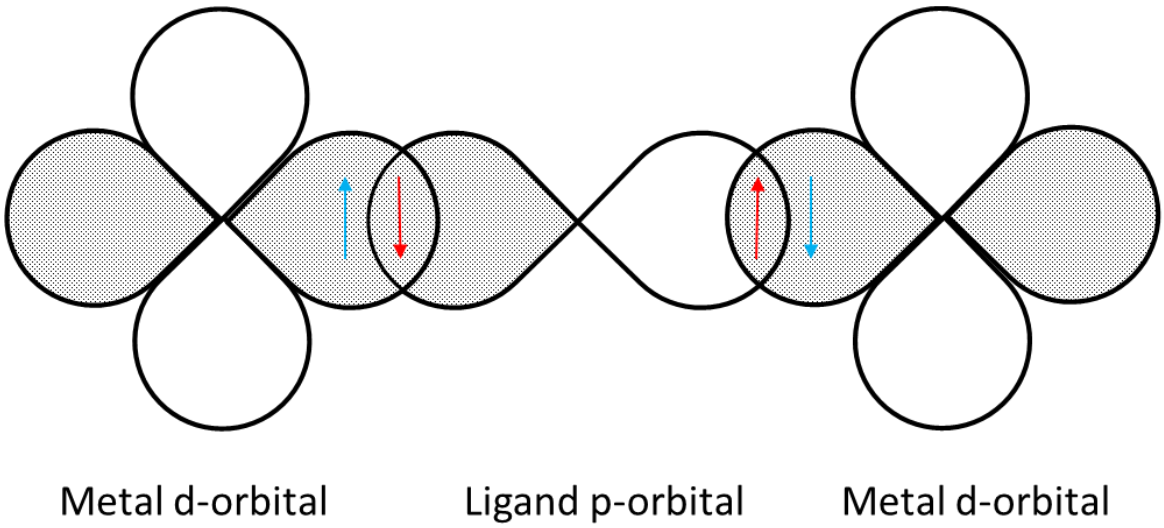

Figure 1.14: The superexchange interaction which takes place when the two metal d orbitals are aligned 180° from each other. This simply shows why the spins are driven antiferromagnetic, the blue arrows correspond to the metal electrons and the red arrows are attributed to the ligand, the direction of the arrows then implies the spin directions.

When two magnetic cations are separated by an angle of 90° then a weak ferromagnetic interaction is observed, the reasoning behind this is shown in Figure 1.15. This is rationalised as this requires two ligand orbitals which lie perpendicular to each other. If the first metal cation has a spin up electron, then the adjacent ligand electron must be spin down. The orthogonal ligands then experience exchange stabilisation, so the closest electrons have the same spin orientation. The second metal electron then aligns the same way as the first metal electron resulting in a ferromagnetic interaction.

The ferromagnetic superexchange interaction is highly dependent on the 90° angle, only taking place if deviations are small. The antiferromagnetic superexchange angle is more flexible and greater deviations from 180° can still result in an antiferromagnetic superexchange interaction taking place [25]. A strong antiferromagnetic interaction can also take place at an angle of 90° when the two metal cation d-orbitals are different e.g. $d_{x^2-y^2}$ and d_{xy} [26].

One final interaction which had to be considered was the Dzyaloshinsky-Moriya interaction which considers the interaction between two magnetic moments. This tends to cause canting of antiferromagnetic moments within predominately antiferromagnetic materials resulting in weak ferromagnetic behaviour within the system [27,28].

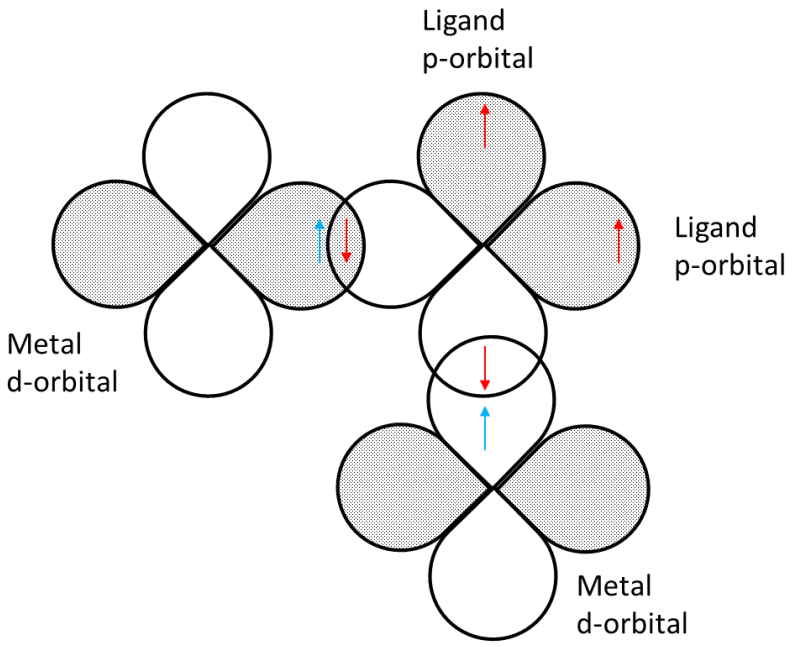

Figure 1.15: The reasoning behind ferromagnetic superexchange interaction. This requires two separate ligands which drive this process through exchange stabilisation which allows the metal cation spins to be the same when separated at a 90° angle. The blue arrows correspond to metal electrons and red arrows ligand, the direction implies spin directions.

Magnetic Percolation

Percolation theory is a tool which may be utilised to observe the effects of site dilution within a material. This utilises geometrical models and the arrangement of the contents, introducing a random nature into the system which affects the connectivity of the model. This randomness is often generated through site dilution, allowing the connectivity of the lattice to be disrupted. The point at which this disruption occurs resulting in breakdown of the lattice is known as the percolation threshold. Within the *fcc* lattice the percolation threshold, $p_c = 0.1965$ [29–31].

Although the concept of percolation is geometrical in nature, it can be readily applied to magnetic systems. Magnetic percolation can be used to extract insight into complex magnetic behaviour. The practice of this replaces magnetic cations with diamagnetic cations of similar ionic radii to ensure isostructural systems. As the magnetic cations are replaced by the non-magnetic analogues in a random distribution, the magnetic pathways are disrupted. At the critical percolation point, long range magnetic order can no longer take place as the proportion and distribution of diamagnetic cations is too large [29,30]. Studies have shown that the magnetic percolation threshold is reliant on the reciprocal coordination number of the magnetic cation [32].

The transfer of ideas from the purely geometrical model to the magnetic can cause slight complications as the number of magnetic interactions which are involved must be considered. The percolation threshold decreases as the number of magnetic interactions involved in the long-range magnetic order increases [33].

Perovskite

Perovskites are crystal systems which have the general formula AMX_3. In these materials, the *A*-site cation can be an alkali metal, alkaline earth metal or lanthanide, the *M*-site cations are typically transition metals or lanthanides and the anionic *X*-site is typically a halide or chalcogenide. The variety of elements which can occupy the perovskite lattice result in a highly versatile structure which has been investigated widely [34].

Undistorted perovskites crystallise in the cubic space group $Pm\bar{3}m$, a primitive cubic lattice composed of corner sharing MX_6 octahedra with a central *A*-site cation. The *A*-site cation is surrounded by up to 12 anions and the *M*-site cations are octahedrally coordinated by six *X* anions [35]. A representation of the undistorted structure is shown in Figure 1.16.

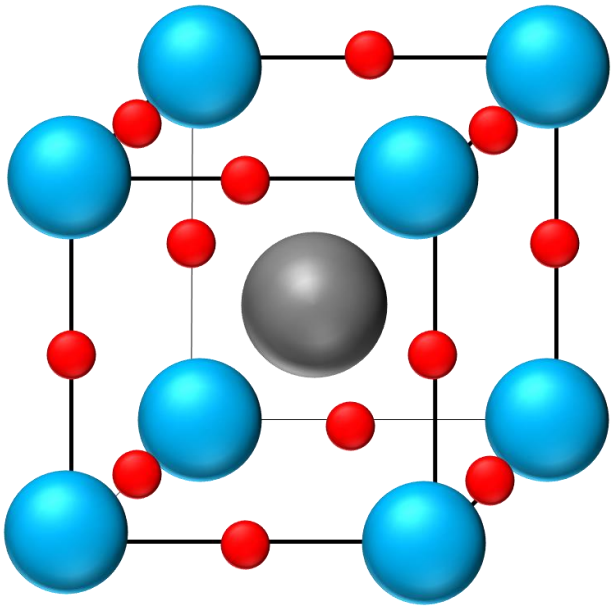

Figure 1.16: A depiction of an undistorted cubic perovskite. The *A*-site cation is depicted by the large grey sphere and lies in the centre of the cubic structure, the blue spheres are the *M*-site cations, which are not shown in their octahedra so the structure is not hindered and the *X*-site anions are represented by the small red spheres.

Cation Ordering in Perovskites

Despite the versatility of the simple perovskite a limited number of materials can form within this structure. Double perovskites have the general formula $A_2MM'O_6$ and can be readily substituted at both the *A*- and *M*-site allowing a range of new materials to be accessed that cannot form in the simple perovskite structure. The introduction of an additional *M* cation can result in some interesting

properties due to the cation ordering. The ease of substitution also provides an opportunity for some tuning of the properties within these materials.

In double perovskites, ordering of the *A*- and *M*-site cations can occur when there is a large difference in the cationic radii and charge. *M*-site ordering can lead to interesting properties [36].

Cation ordering may result in rock salt, layered or columnar structures. Rock salt ordering results in all adjacent cations alternating, this is frequently observed in *M*-site ordered systems [36] but rock salt *A*-site ordering is rare as anions struggle to compensate for large charge differences [37]. In columnar species, columns of identical cations are present but adjacent columns alternate. Columnar *M*-site ordering is uncommon and requires additional effects such as Jahn-Teller distortions [38]. *A*-site layered ordering occurs frequently, requiring a tetragonal distortion to the double perovskite. Finally, both the *A*- and *M*-site are able to order simultaneously as exhibited in $NaLaMgWO_6$, where the *A*-site ordering is layered and rock salt *M*-site ordering is observed [39].

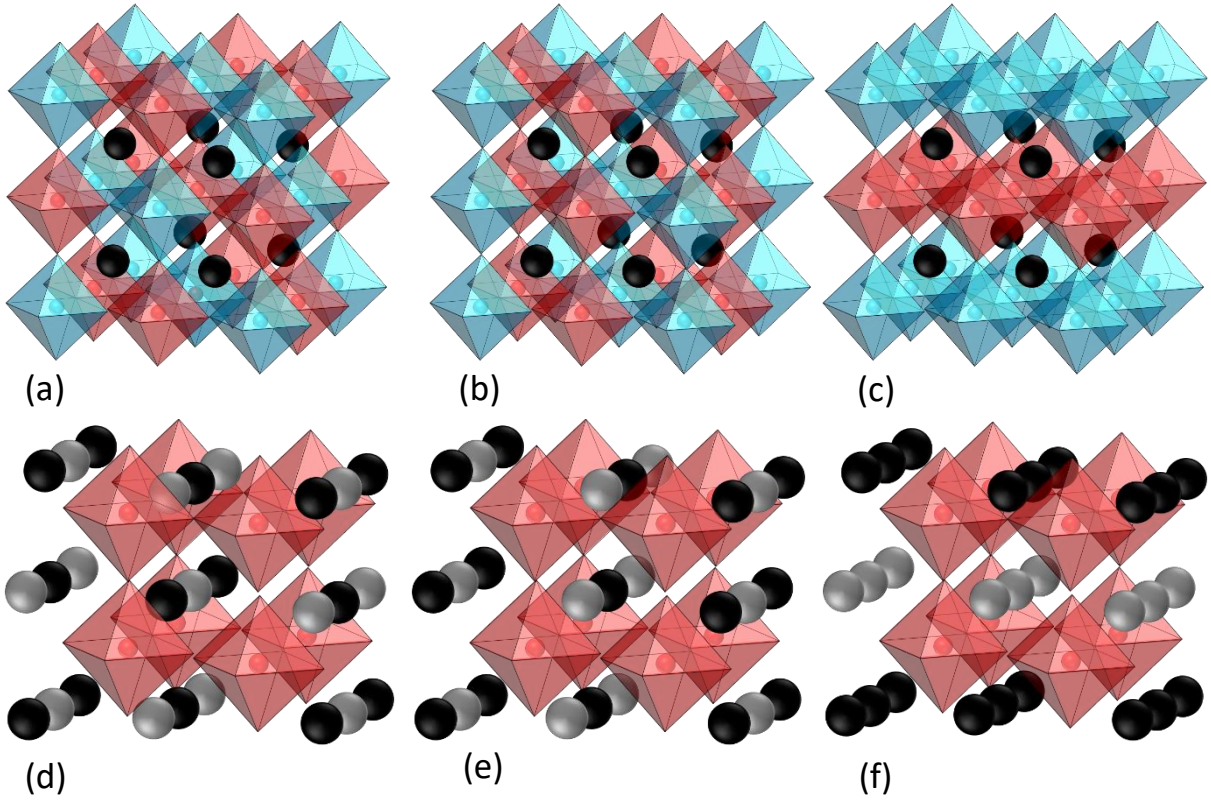

Figure 1.17: Simplistic depictions of *A*- and *M*-site cation ordering. (a) The rock-salt *M*-site ordered double perovskite (b) The columnar *M*-site ordered double perovskite (c) The layered *M*-site ordered double perovskite (d) The rock-salt *A*-site ordered double perovskite (e) The columnar *A*-site ordered double perovskite (f) The layered *A*-site ordered double perovskite.

Perovskite Distortions

The double perovskite structure is susceptible to external or internal distortions which can result in the emergence of some novel physical properties. External effects such as changing the temperature or pressure can cause structural phase transitions or induce magnetic properties. Internal distortions of the phase include octahedral distortion, ionic displacement and octahedral tilting.

Octahedral distortions often take place in double perovskites due to effects such as the Jahn-Teller distortion. Jahn-Teller active *M*-site cations cause an intrinsic distortion of the octahedra due to the unequal occupancy of the d orbital [40].

Cationic displacement takes place in ferroelectric double perovskites. Ferroelectrics display spontaneous field dependent electric polarisation. Ferroelectrics exhibit hysteresis and remanence effects within an electric field. These distortions cause cations to move with the electric field as a dipole is induced, resulting in changing bond lengths [41,42]. Figure 1.18 shows an exaggerated depiction of distortion brought about by polarisation.

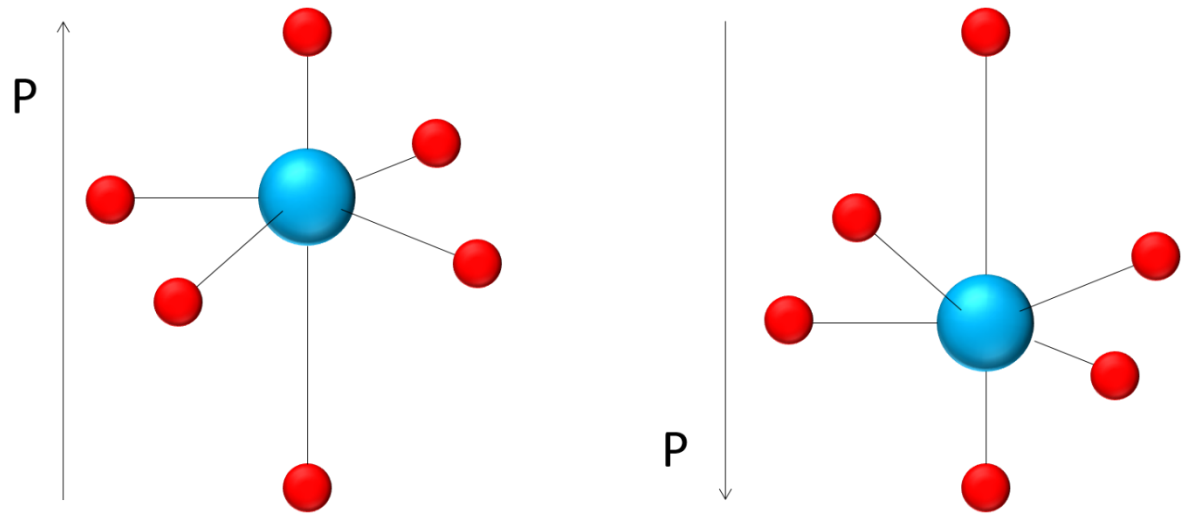

Figure 1.18: This indicates how the application of an electric field can affect the geometry of the double perovskite octahedra when this contains a ferroelectric cation. The perovskite distorts as the axial bond length changes.

Octahedral tilting is dependent on the ionic radii of the species within the perovskite [43]. This deviation changes the *A*-*X* bond distances with minimal changes to the *M*-*X* bond lengths and can

significantly affect the structure and properties [37]. Octahedral tilting is described using bond valence theory and the Goldschmidt tolerance factor [41].

Octahedral tilts are classified by Glazer notation, 23 distinct tilt systems are defined with zero, 1-, 2- or 3-tilt as options. Glazer notation describes tilting using the axes of the unit cell, *a*, *b* and *c* whilst the direction of rotation is annotated by a subscript +, for in phase rotation, -, for out of phase rotation or 0 for no rotation [44,45]. Group theory analysis completed more recently has indicated that only 15 of the tilt systems are observed in practice [46]. The undistorted cubic structure has the Glazer tilt system $a^0\ a^0\ a^0$, this requires large *A*-site cations to ensure that this material is stabilised [47].

Octahedral tilting predominantly affects the *A*-site cation therefore, its nature and coordination is integral in this structural rearrangement. The Goldschmidt tolerance factor (*t*) allows the extent of octahedral tilting to be determined by evaluating the relationship between the ionic radii of each ion in the structure.

Equation 1.27: Goldschmidt tolerance factor

$$t = \frac{R_A + R_O}{\left[2^{\frac{1}{2}}(R_M + R_O)\right]}$$

If *t* lies close to 1 then the material will most likely adopt the cubic crystal structure. When it is significantly lower than 1, octahedral tilting is likely to take place. If the tolerance factor is significantly greater than 1, then the structure distorts to a hexagonal structure [48].

Double perovskites commonly distort from $Fm\bar{3}m$ to the tetragonal space group, *I4/m*, or the monoclinic $P2_1/n$ through octahedral tilting, these are known as subgroups. A representation of the tilting in each of these undistorted and distorted models is shown in Figure 1.19. $Fm\bar{3}m$ is defined by $a^0a^0a^0$, with no observed tilting. I4/m is defined by the Glazer tilt system $a^0a^0c^-$. This contains two distinct dimensions, no rotations take place around the *a*-axes, however there is an antiphase rotation around the c axis. Monoclinic systems which adopt the space group $P2_1/n$ possess the Glazer tilt

system; $a^-a^-c^+$. This is a three-tilt system and those around the *a*- axis rotate in an opposite direction to those along the *c*-axis [49].

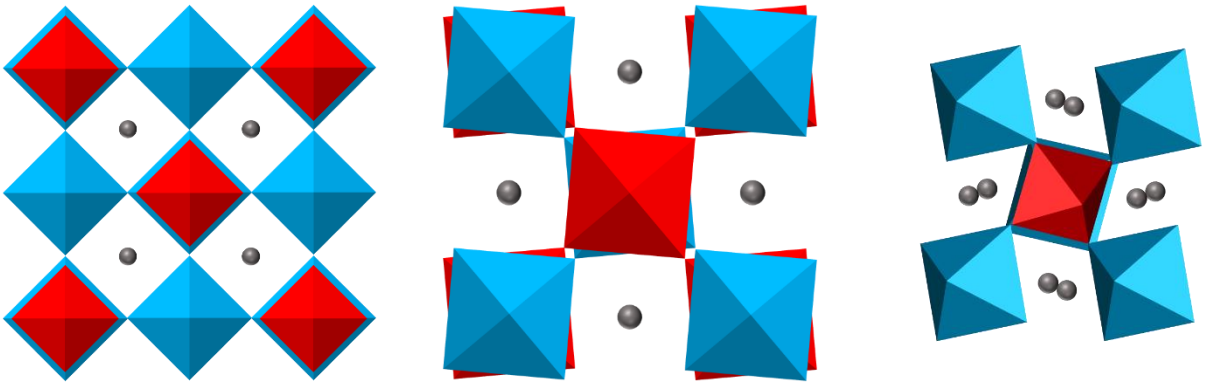

Figure 1.19: Octahedral tilting is shown within double perovskites ideal and distorted structures. From left to right the cubic system, the tetragonal *I4/m* and finally the monoclinic *P2₁/n* system.

In *I4/m* the *a* and *b* axes are equal, whilst the *c* axis is contracted or elongated. In this instance the *A*- and *M*-site cations remain in special positions whilst there are two distinct oxide positions which sit on (*x*, *y*, 0) or (0, 0, *z*). In the monoclinically distorted *P2₁/n*, the *a* and *b* axes are compressed and lie close to each other but are not equal, and the *c* axis remains close to what would be expected in the cubic material. The relationship is as follows [50];

Equation 1.28: Cubic ($Fm\bar{3}m$) to monoclinic (*P2₁/n*) lattice parameter relationships

$$a_{mon} \approx 1/\sqrt{2}\, a_{nuc},\ b_{mon} \approx 1/\sqrt{2}\, a_{nuc},\ c_{mon} \approx a_{nuc}$$

Within the *P2₁/n* structure the *β* angle deviates from 90°. The *A*-site cations no longer reside on a special position and sit on any x, y or z coordinate. Three distinct oxide anion position are also observed, these each can lie anywhere on the *a*, *b* or *c* axes.

Geometrical Frustration

Geometrical magnetic frustration is a phenomenon which prevents the formation of a unique ground state due to competing magnetic interactions. This is caused by the relative arrangement of the spins and tends to be observed in antiferromagnets. Equilateral triangles are used to explain the phenomenon. If arrows lie on each corner of the triangle, they cannot simultaneously be orientated antiparallel to each other. This effect is also observed in tetrahedra and extended structures consisting of equilateral triangles. This is not observed in isosceles or scalene triangles due to differing dimensions [51].

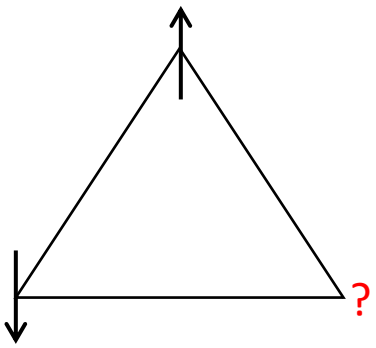

Figure 1.20: A demonstration of geometrical magnetic frustration. The directions of each of the arrows cannot be antiparallel to all adjacent arrows simultaneously. Competing interactions prevent a unique ground state.

Materials affected by geometrical frustration include triangular, kagome, pyrochlore and face centred cubic (*fcc*) lattices [51,52]. Each of these materials are related due to their composition of equilateral triangles or tetrahedra. The planar triangular lattices and 3D *fcc* lattices are connected by edge sharing triangles or tetrahedra whilst the 2D kagome lattice and 3D pyrochlore systems are connected through corners. When these materials are unable to reach collinear antiferromagnetic states, unconventional behaviour can occur such as the novel spin states; spin glass, spin liquid and spin ice [51].

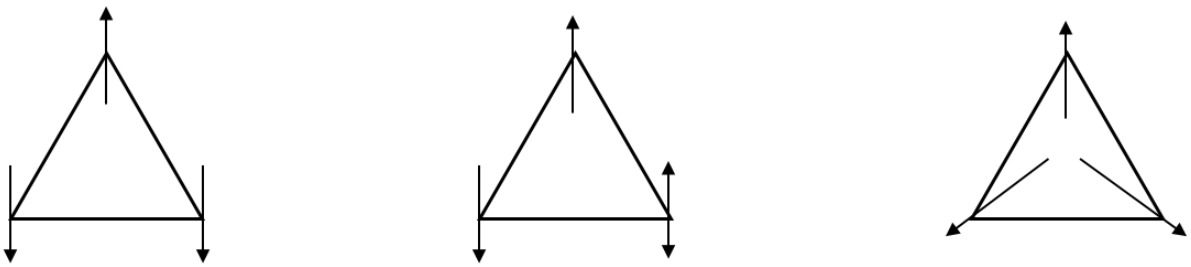

Figure 1.21: Simplified arrangement of potential outcomes of geometrical magnetic frustration. The left-hand structure indicates compensated structure, not all components are aligned in an antiparallel fashion to each other. The middle structure indicates dynamic behaviour with rapidly changing spin. The right-hand side indicates when a non-collinear ground state is achieved with the spins compensating by pointing out of the triangle in a move to relieve frustration effects.

Spin glasses are an amorphous distribution of spins which become stationary below a distinct freezing or glass transition temperature. No long range magnetic order is observed although structural ordering can be achieved [53]. Spin glasses are identified using AC-susceptibility, as the susceptibility observed at the spin glass transition temperature is frequency dependent and therefore the magnitude of the susceptibility decreases with increasing frequency [53,54]. They can also be determined using muon spin relaxation experiments, where the relaxation curve obtained can be fitted using variations of the Kubo-Toyabe fitting function [55]. $G_z(t)$ is the relaxation function, $\alpha_d = \sqrt{1-Q}\alpha$, the dynamic decay rate, $\alpha_s = \sqrt{Q}\alpha$, the static muon decay rate, v, the muon hopping rate.

Equation 1.29: Static and dynamic Kubo-Toyabe function

$$G_z(t) = \frac{1}{3}\exp\left[-\left(\frac{4\alpha_d^2 t}{v}\right)^{\frac{1}{2}}\right] + \frac{2}{3}\left[1 - \frac{\alpha_s^2 t^2}{\left(\frac{4\alpha_d^2 t}{v} + \alpha_s^2 t^2\right)^{\frac{1}{2}}}\right]\exp\left[-\left(\frac{4\alpha_d^2 t}{v + \alpha_s^2 t^2}\right)^{\frac{1}{2}}\right.$$

Spin ice compounds exhibit various degenerate ground states at low temperature preventing a unique ground state. In the spin ice state, magnetic moments behave like cooperative paramagnets, however, long range magnetic interactions are unable to take place [56]. For spin ice behaviour to arise, Ising-like weak magnetic moments must be present in a two-in, two-out arrangement plus strong dipolar forces [57]. These stringent rules, allow the four magnetic moments to be arranged in 16 different ways, leading to a complex ground state with $(3/2)^{N/2}$ possibilities where N is the number of magnetic cations [58]. This means that spin ice compounds are rare and tend to be pyrochlore compounds.

Spin liquids are also the result of numerous degenerate ground states. These disordered ground states experience dynamic behaviour, where magnetic moments fluctuate down to very low temperature, in contravention to the third law of thermodynamics [59]. This dynamic behaviour prevents long range magnetic order [60]. Spin liquids contain a random distribution of magnetic moments which can interact. These may also be described classically or using quantum mechanics. In quantum spin liquids, the magnetic moments are strongly correlated and therefore cannot be estimated separately [61].

Geometrical Frustration Within Face Centred Cubic Lattices

This body of work will focus on geometrical frustration in the *fcc* lattice of double perovskites. Geometrical magnetic frustration prevents the *fcc* lattice from gaining a fully antiferromagnetic ground state and instead, three distinct possibilities which exhibit long range antiferromagnetic order can be achieved. The type of magnetism observed within the *fcc* lattice is dependent on the nearest neighbour (NN) and the next nearest neighbour (NNN) magnetic interactions. The NN and NNN interactions are also described by the J_1 and J_2, magnetic exchange coupling constants. Within the *fcc* system, J_1 interactions are unable to fully align antiferromagnetically which results in frustrated behaviour whilst the J_2 interactions can. The long range antiferromagnetically ordered states adopt either the Type I, Type II or Type III structures.

The Type I structure occurs when J_1 interactions are dominant, resulting in ferromagnetic layers of magnetic moments with antiferromagnetic alignment of adjacent layers (Figure 1.22). Type II is observed when the J_2 interaction is dominant or when both the J_1 and J_2 interactions are close in magnitude. The Type II structure, shown in Figure 1.23, results in ferromagnetic interactions along the (111) plane, simultaneously, adjacent (111) planes couple antiparallel to each other. The Type III structure is more complex and is split into four separate sublattices as depicted in Figure 1.24. A complex combination of the Type I and Type III antiferromagnetic species has also been proposed. This is split into 6 different sublattices, see Figure 1.25 [62].

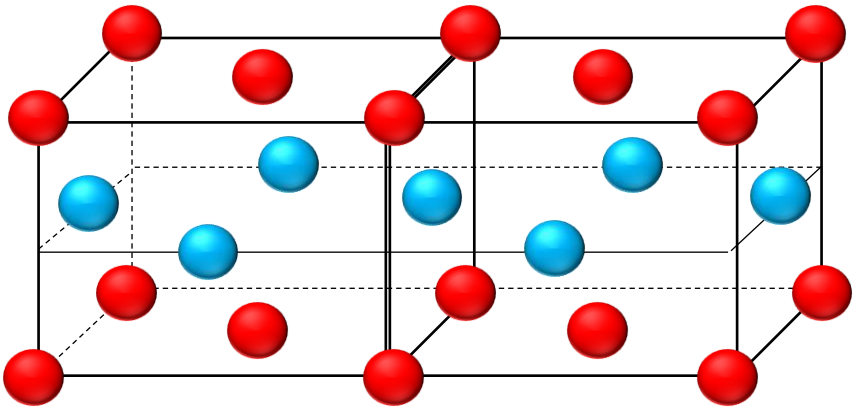

Figure 1.22: *FCC* Type I long range antiferromagnetic structure. This is divided into two separate sublattices with ferromagnetic layers where adjacent layers are aligned antiferromagnetically to each other. The red and blue spheres correspond to the spin up and spin down configurations respectively.

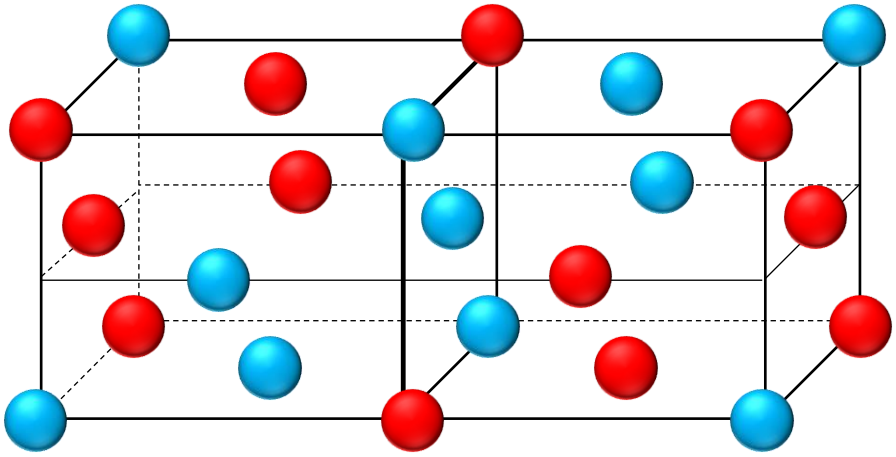

Figure 1.23: *FCC* Type II long range antiferromagnetic structure. Like Type I, this is split into two different sublattices, where ferromagnetic planes occur along the (111), adjacent (111) planes have an antiparallel alignment to each other. The red and blue spheres correspond to the spin up and spin down configurations respectively.

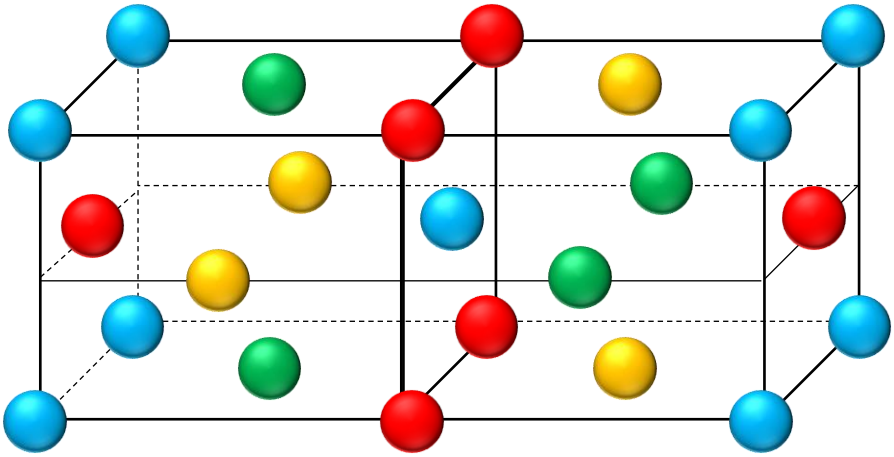

Figure 1.24: *FCC* Type III long range antiferromagnetic structure. The structure is split into four individual sublattices. The red and green spheres correspond to the spin up magnetic configuration whilst the blue and yellow spheres correspond to the spin down configurations.

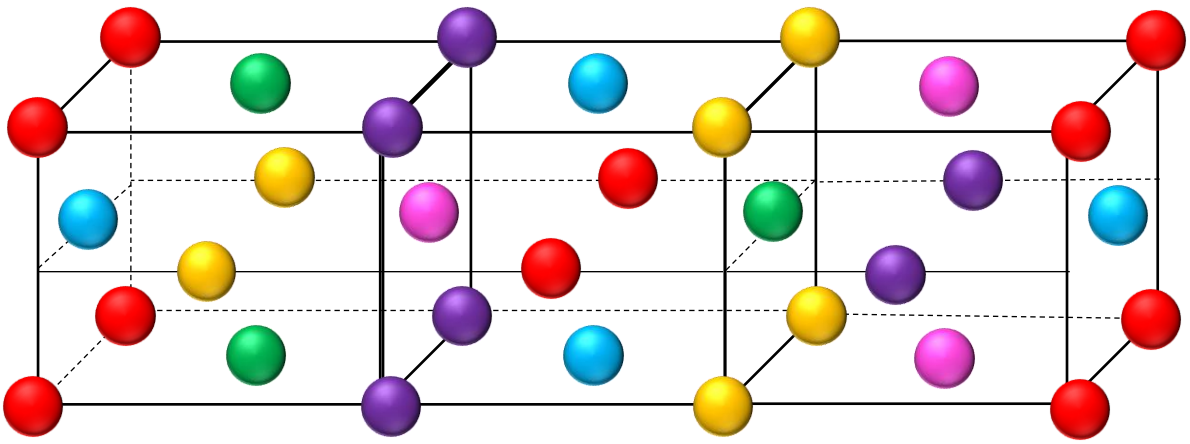

Figure 1.25: This is a combination of the Type I and Type III long range antiferromagnetic structures, this is divided into the six separate sublattices. The red, green and pink spheres correspond to the spin up magnetic configuration whilst the blue, yellow and purple spheres correspond to the spin down configurations.

2. Experimental theory

Solid-State Synthesis

Solid-state synthesis involves thoroughly grinding stoichiometric quantities of powdered materials in a mortar and pestle until a homogeneous powder is achieved. Throughout these studies the uniform powder was then pressed into a pellet and placed into a furnace. After pelletising, each material was transferred into a crucible prior to being heated inside of a furnace. This heating step was preliminary and was utilised to remove any carbonates from the system. Subsequent heating steps were completed at significantly higher temperature, in enclosed atmosphere if necessary to facilitate the formation of the desired product.

These steps help to facilitate bond breakage within the parent powders and allows new bonds to form in the desired product. This rearrangement of the components within the pellet is completed via solid state diffusion, adhering to Fick's Law. In Fick's law, the flux (*J*) is described as the quantity of substance which is able to flow through a given area in a given time. Flux is defined by the diffusivity (*D*) of the different ions and is driven by a concentration (*c*) gradient along a defined length of material (*x*) [63].

Equation 2.1: Fick's Law

$$J = -D\left(\frac{dc}{dx}\right)$$

Grinding generates small particles with large surface areas. This promotes the interaction of the particles with each other allowing the reaction to take place over shorter lengths and/or time scales. When the particles are pressed into pellets the distance separating them decreases, reducing the path length and increasing flux and reaction rate. The pellets are subjected to high temperature, where heat is transferred to the particles and can be converted to kinetic energy to drive the formation of the desired phase. This can be a slow process taking days or weeks to reach completion. To facilitate this manufacture of materials, intermediate grinding processes are completed throughout the heating process. This is not an exact science and often trial and error must be used to synthesise materials [64].

Powder X-ray Diffraction

Powder X-ray diffraction is a valuable tool which identifies crystal structure. This can be completed due to the periodic nature of crystalline materials which allows sharp peaks at defined d-spaces. Disordered materials appear as broad bumps, due to their lack of symmetry. This is possible as the structural d-spacing is comparable to X-ray wavelength. Powder X-ray diffraction is used extensively in laboratories and does not require a specialist institution or training. In some instances, a higher energy X-ray source may be necessary which can be achieved at synchrotrons.

X-ray Generation

X-rays are a form of electromagnetic radiation, as such it's energy and wavelength are represented by the following equation, where *E* is the energy, *h* is Planck's constant, *c* is the speed of light and λ is the wavelength.

Equation 2.2: Relationship between the energy of electromagnetic radiation and the wavelength

$$E = \frac{hc}{\lambda}$$

X-rays are naturally occurring but can also be generated within laboratories. Laboratory generation of X-rays is completed within sealed vacuum tubes, where a beam of high energy electrons is generated by a cathode, often composed of tungsten. These high energy electrons are then accelerated into a metal target (anode). If the accelerating voltage is large enough then core electrons can be ejected from the metal target upon this collision. When core electrons are ejected, electrons from higher energy levels fill the vacancies, emitting X-rays as they fall. The target anode material is selected by the desired d-space range and range from Cu, Mo, Fe or Ag.

When a copper source is utilised, the generated characteristic X-rays are known as $K\alpha_1$, $K\alpha_2$ and $K\beta$ which correspond to electrons falling from the $2p_{3/2}$, $2p_{1/2}$, and 3p orbitals. $K\alpha_1$ has an intensity which is double $K\alpha_2$ as the population of $2p_{3/2}$ is two times greater than $2p_{1/2}$. Electrons which fall from the 3p orbital correspond to $K\beta$ energy with significantly less intensity. To ensure that only $K\alpha_1$ is observed,

a monochromator is required to remove the $K\alpha_2$ peaks and a nickel filter can strip away the Kβ response [65]. In addition to these characteristic X-rays, continuous radiation or Bremsstrahlung X-rays are observed which arise due to deceleration of electrons upon collision with each other. This continuous radiation forms as the electron loses kinetic energy which is then converted into radiation.

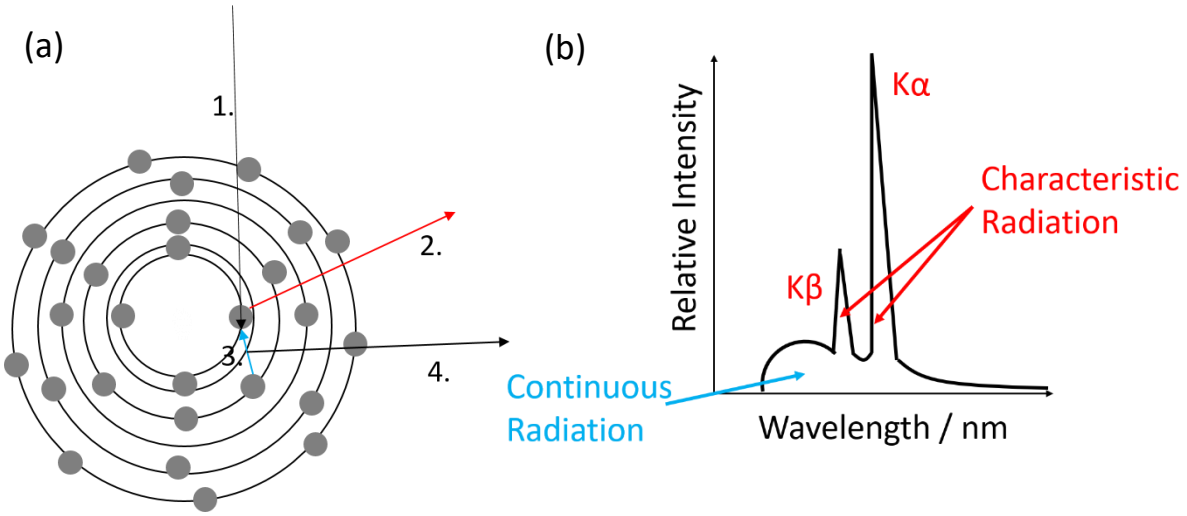

Figure 2.1: (a) Depiction of how X-rays are formed within a target source. 1. Indicates the incident of high energy electrons. 2. Shows the core electrons which are ejected. 3. The descent of an electron from the 2p energy level to the core 1s orbital. 4. The emission of an X-ray with specific energy and wavelength. (b) Diffraction pattern showing both continuous and characteristic X-ray radiation.

Upon generation, X-rays are able to interact with matter through absorption or scattering processes and can transfer energy via ionisation or excitation. Ionisation removes electrons leaving a resultant net positive charge, whilst excitation sends the target into a more energetic state. As absorption is a key mode of interaction for X-rays, the X-rays must leave the tube via a material which has a low absorption of X-rays. Beryllium is transparent to X-rays and therefore energy transmission is kept low when this is used. Despite the usefulness of beryllium in this application, it is toxic and therefore must be handled with care [66]. Both processes can cause damage to humans, such as hair loss, radiation burns or scarring and therefore safety is of the highest concern.

X-rays can safely be generated within a laboratory setting; however, occasionally higher energy X-rays are desirable which could not be easily contained within a laboratory diffractometer. In this instance, a synchrotron may be a viable option. X-rays are generated in the synchrotron by accelerating high

energy electrons around a circular path. This allows significantly higher energy X-rays to be generated which result in exceptionally high resolution data [67]. As even higher energy X-rays are produced, the safety concerns are even greater and therefore access to specialist facilities is necessary such as the Diamond Light Source, Didcot, Oxfordshire [68].

Detectors collect the generated X-rays allowing diffraction patterns to be captured. For high quality diffraction patterns, the detectors should collect a high number of X-rays and give accurate readings of intensity. The intensity is dependent on the number of photons detected in a given time frame, therefore response time must be quick and dead time minimised. Intensity determination is completed relatively rather than using absolute values as these are inconsistent across detectors. High resolution detectors allow greater differentiation between similar energy X-rays [65].

X-ray detectors are described as point or area. Point detectors include gas proportional, scintillation or solid-state detectors, which are useful but offer no spatial resolution [69–71]. Area detectors such as position sensitive, charge coupled devices and image plate devices provide spatial resolution in either one or two directions [72–76].

Overwhelmingly, the most important aspect of X-ray generation and usage is safety. The ionising and excitation properties of X-rays can cause significant damage, such as hair loss, radiation burns, scarring and in chronic cases cancers and therefore safety should always be the highest concern whether in the laboratory or at an external facility. In order to minimise any risk, X-Ray diffractometers are equipped with multiple safety interlocks: appropriate shielding which encases X-ray source, shutters which contain the primary beam, fail-safe interlocks which close the shutter if the doors are opened, and constant maintenance to ensure that there is no leakage of any radiation.

Diffraction

As stated previously X-rays interact with matter through, elastic and inelastic scattering and absorption [77]. Elastic scattering takes place when energy is conserved throughout the scattering process and inelastic scattering occurs when energy is not conserved. This is described by either

kinematical or dynamical theory. Kinematical diffraction states that an X-Ray may only be scattered once before leaving the crystal. This assumes; the interaction between the X-Ray and material is negligible and the crystal is composed of miniscule blocks which experience significant misalignment preventing numerous interactions. Conversely, dynamical theory permits multiple scattering processes for each X-Ray, accounting for crystallite interaction. However, the effects of secondary interactions are typically negligible and therefore kinematical theory is often used. Absorption causes X-Rays to be captured, this energy transfer causes a core electron to either be excited to a higher energy level, and a secondary electron is falls to fill the gap left behind [78].

X-Ray interaction generates waves, this can occur constructively or destructively. Constructive interference occurs when waves interact in phase with each other. Destructive interference arises when waves are out of phase with each other causing cancellation, see Figure 2.2 [79].

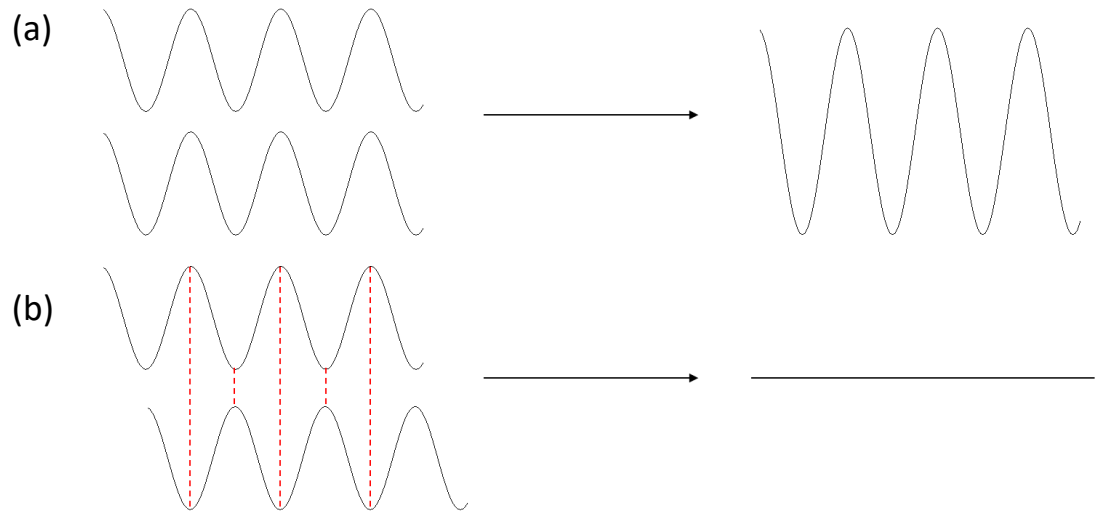

Figure 2.2: A depiction of purely constructive and destructive interference. (a) Coherent interference occurs when two waves which are in phase with each other, generate a wave of larger amplitude. (b) Destructive interference results in the wave being minimised or cancelled out.

X-rays are waves of electromagnetic radiation and therefore when scattering takes place it occurs between photons and the electron cloud of the scattering atom. As the atomic number increases, the number of electrons and electron density increases as does the likelihood that the X-ray will be scattered by the atom. This atomic dependence means that X-ray diffraction is more effective at

identifying heavier atomic species and is not as sensitive to lighter elements. This atomic dependence is known as the intrinsic form factor which is shown below. dependence on both the scattering and phase angles, the intrinsic form factor.

Equation 2.3: X-Ray form factor function

$$f\left(\frac{sin\theta}{\lambda}\right) = \sum_{i=1}^{4} a_i \exp\left(-b_i \sin^2\theta/\lambda^2\right) + c$$

In Equation 2.3; ϑ is the scattering angle, λ is the wavelength of the X-Ray and a_i, b_i and c_i are the coefficients of the form function which are dependent on the atom [80].

The form factor is dependent on scattering angle, $sin\vartheta/\lambda$, and tends to decrease as the scattering angle increases. This is a result of interference between scattered X-rays which is more prevalent at higher scattering angle and causes X-ray diffraction patterns to have their most intense peaks at large scattering angles.

Laue Diffraction

Diffraction was initially described by Max von Laue who developed the Laue classification system, where 11 single crystal classes and six distinct powder crystal classes were established. Laue derived three equations and stated that diffraction would take place if all three were satisfied simultaneously. These equations are dependent on the unit cell of the crystal, the diffraction plane at which the atoms sit and the incident and scattering angles of the X-Ray [79].

Equation 2.4: Laue diffraction equations

$$a(cos\psi - \cos\varphi_1) = h\lambda$$

$$b(cos\psi - \cos\varphi_2) = k\lambda$$

$$c(cos\psi - \cos\varphi_1) = l\lambda$$

Bragg Diffraction

Bragg's law suggests that crystals are split into layers and when incident X-Rays encounter these layers they are reflected. Since the initial theory, it has been established that reflection is not the correct description of the process, however, this hypothesis underpins diffraction behaviour.

Equation 2.5: Bragg' s Law

$$n\lambda = 2d_{hkl}sin\theta$$

In Bragg's law *n* describes the order of "reflection", typically equal to one, λ is the characteristic wavelength of incident light, *d* is the d-spacing of crystal planes and θ is the incidence angle [77].

Diffraction occurs in 3-dimensions in a polycrystalline powdered sample, allowing an Ewald sphere to be drawn. This construct is used to form a cone of diffraction by making the centre of the sphere a starting point and finishing at the outer sphere of the surface. The outer edge of the cone then becomes the Debye ring, a region where the intensity of the peaks should be equal providing the crystallites are randomly distributed. Taking a slice from the centre to the outer edge of the ring gives a 1D powder diffraction pattern [81].

Powder Diffraction Patterns

Powder diffraction generates a one-dimensional pattern where intensity is plotted against scattering angle (2θ), d-space or Q-space ($Q = 4\pi\sin(\theta)/\lambda$). These are composed of peaks which lie amongst a low background. The peaks sit at specific positions, determined by permitted Bragg reflections, and are described by the peak profile. The area under the peak is the intensity. In continuous wavelength diffraction patterns the peak profile can be characterised by the Voigt or pseudo-Voigt functions or occasionally the Pearson-VII function. The Voigt function is the convolution of the Gaussian and Lorentzian curves whilst the pseudo-Voigt function is a linear combination of the two. The Pearson-VII function is a Lorentzian function raised to a power. These functions are typically used to describe the peak profile as they are superior to the Gaussian and Lorentzian functions individually [82].

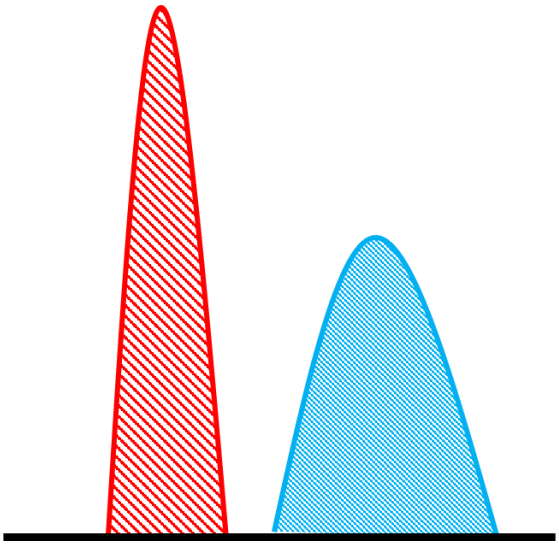

Figure 2.3: Two peaks with different peak profile. The red peak has a higher height but is significantly narrower than the blue peak. By eye it could be difficult to identify which possess the highest intensity and therefore the most intense peak must be established by integrating the area under each peak.

Powder diffraction data can be complicated to resolve due to overlapping peaks. These are a result of data compression caused by the polycrystalline nature and unfortunately cannot be avoided. Peak overlap is exacerbated at low d-space and in low symmetry samples [83]. Peak broadening is common within diffraction and this can arise from a range of internal and external effects. External effects cause characteristic broadening across the diffraction pattern include polychromatic radiation and instrumental issues [84]. Internal strain or particle size effects can cause peak shapes to be broadened although this affects the peaks differently [85].

Peak position is dependent on the permitted Bragg reflections, determined using Bragg's law and the symmetry of the unit cell. Systematic absences occur when a symmetry element of the cell prevents the detection of diffracted peaks at equivalent positions, this can be caused by unit cell centering. Peak position can be affected by instrumental parameters, including; axial and in-plane divergence of the incoming X-ray beam, and sample displacement. Axial divergence, which can result in peak asymmetry, may be abated by incorporating Soller slits into the experimental set-up or during refinement [86]. In-plane divergence requires optimisation of the detector slit. Sample displacement can be minimised by ensuring the sample lies flat on the holder. One final instrumental parameter which affects the peak position is the zero-point error. This arises due to small errors when setting up

the instrumental axes. It is vital that the zero-point error is resolved otherwise the lattice parameters will not be accurately calculated [83]. This can be fixed during refinement stages.

Calculating Bragg peak intensity requires the structure factor calculation. This is dependent on atomic position and equivalents and scattering potential [79].

Equation 2.6: Relationship of Bragg peak intensity and structure factor

$$I_{hkl} \propto |F_{hkl}|^2$$

Equation 2.7: Structure factor calculation

$$F_{hkl} = \sum_{j=1}^{m} N_j f_j \exp\left[2\pi i\left(hx_j + ky_j + lz_j\right)\right]$$

Where; I_{hkl} is the intensity of the Bragg peak, F_{hkl} is the structure factor, *N* corresponds to the number of atoms in the cell, *f* is the atomic scattering factor, *h*, *k* and *l* are miller indices and *x*, *y* and *z* are the atomic coordinates. This must be calculated across the entire structure.

The intensity itself is also dependent on numerous factors;

$$I_{hkl} = K \times p_{hkl} \times L_\theta \times P_\theta \times A_\theta \times T_{hkl} \times E_{hkl} \times |F_{hkl}|^2$$

Where; I_{hkl}, is the integrated intensity, *K* is the scale factor, p_{hkl}, is the multiplicity factor, L_θ is the Lorentz multiplier, P_θ is the polarization factor, A_θ is the absorption factor, T_{hkl} is the preferred orientation factor, E_{hkl} is the extinction multiplier and F_{hkl} is the structure factor.

The scale factor is a constant value which minimises the difference between the experimental data and an ideal system, determined by the starting model. Deviations from ideal occur due to competing processes such as inelastic scattering or absorption taking place.

The multiplication factor considers equivalent positions of atoms, allowing shorter calculation time. This is useful in high symmetry materials.

The Lorentzian multiplier accounts for small changes in diffraction angle and the effect of this on peak intensity. This considers the intrinsic form factor, making the largest changes to the higher intensity peaks at low angle. The dependence of the Lorentzian factor on the scattering angle is shown below, the constant 1/4 is often removed and added to the scale factor;

Equation 2.8: Lorentzian multiplier dependence on scattering angle

$$L \propto \frac{1}{4cos\theta \sin^2 \theta}$$

The polarisation multiplier accounts for the electrical and magnetic properties of X-rays. The polarisation of the radiation propagates in one direction and is scattered in different directions with a variety of magnitudes. Therefore, this is characterised using the following relationship;

Equation 2.9: Polarisation factor

$$P \propto \frac{1 + \cos^2 \theta}{2}$$

When a monochromator is used all but one of the energies are removed, which affects the polarisation of the radiation beam. This causes the polarisation parameter to become more complicated.

Equation 2.10: Polarisation factor for monochromated radiation.

$$P \propto \frac{1 - K + Kcos^2(2\theta) \cos^2(2\theta_M)}{2}$$

Where; *K* is the polarisation of the radiation. *K* is dependent on the radiation type, when a monochromatic source is used the value of this should be experimentally calculated and $2\vartheta_M$ is the Bragg angle which corresponds to the monochromator.

Absorption of the radiation can result in decreased peak intensity. The extent of absorption is dependent on the atom, the sample geometry, the focussing technique and the wavelength utilised.

Preferred orientation can result in changes from expected diffraction patterns, it can cause certain reflections to have a different (higher, lower or zero) intensity than expected if the polycrystallites

within the sample were randomly distributed. This is apparent when crystallites become needle- or disk-like. Needles lie perpendicularly to the sample holder whilst disks lie flat against the sample holder. Preferred orientation may be ameliorated through thorough grinding, however, cannot always be avoided. This can be accounted for using functions such as the spherical harmonic correction or the March-Dollase function [87,88]. The extinction factor is only really observed in crystals which are close to perfect and therefore this will not be covered in any detail [89].

Neutron Powder Diffraction

Neutron diffraction is a non-destructive technique which utilises neutrons, electrically neutral subatomic particles with a mass of 1.67×10^{-27} kg and an intrinsic spin of S = 1/2. They are described by the de Broglie equation due to their wave-particle duality. Neutron diffraction complements X-ray diffraction due to different interaction methods. Unlike X-rays, neutrons are scattered by the nucleus which behaves like a point source, experiencing no form factor. Neutron scattering can occur coherently or incoherently. Coherent scattering results in desired Bragg peaks whilst incoherent scattering results in a higher background with poorer signal to noise ratio. Neutron scattering processes occur via elastic, inelastic or absorption processes.

Equation 2.11: De Broglie equation

$$\lambda = \frac{h}{mv}$$

Neutrons may be used for diffraction due to their variable wavelength which is comparable to interatomic spacing in materials. Their neutral charge allows deep penetration ensuring the bulk of the sample is investigated. Neutron diffraction is governed by the coherent scattering cross section (σ) which is atom dependent. Neutron diffraction is also beneficial for biological structure determination where the hydrogen positions may be evaluated upon deuteration, due to the significant difference between the σ value of hydrogen and deuterium. The intrinsic spin of the neutron also allows magnetic structures to be observed.

Despite these advantages, the technique also exhibits several limitations. Neutron diffraction is notoriously weak due to the isolation of the nucleus which results in long experiments. To minimise the duration, large samples are necessary which is not always facile [90,91]. Costly travel to a specialist institution is required. Specialist institutions are reactor sources such as the Institut Laue-Langevin (ILL) in Grenoble, France or spallation sources such as the ISIS Neutron and Muon Source based at the Rutherford Appleton Laboratories in Didcot, UK [92].

Neutron generation is source dependent. Reactor sources generate neutrons using nuclear fission which requires highly enriched uranium fuel. Neutrons are accelerated into a heavy nucleus, which splits upon impact, releasing fast neutrons and energy. The supplementary fast neutrons initialise a chain reaction allowing propagation throughout the reactor. These reactors must be moderated to prevent thermal runaway. Suitable moderators include light and heavy water. The reactor source allows fast, thermal and cold neutrons to be produced. Each neutron possesses different energy and monochromators allow the required energy to be chosen.

Time-of-flight spallation sources manufacture neutrons by accelerating heavy charged particles down a linear accelerator then driving them through a gold foil which strips away electrons, leaving protons. The protons are then accelerated around a ring before collision with a heavy metal source, causing high energy neutrons to be generated. The neutrons are moderated prior to distribution around the facility in small pulses which contain a range of neutrons with different energies [93].

Time-of-flight neutron diffraction is more complex than constant wavelength diffraction as it exploits a range of neutron energies. The energy and velocity are intrinsically linked and therefore the time between entering the system and detection must be known. The Time-of-flight is calculated by combining the De Broglie equation and Bragg's law and the relationships are shown below. In these equations, λ is the wavelength measured in m, d refers to the d-space, h is Planck's constant, t is the Time-of-flight, the time taken for the neutrons to travel down a given length, m is the neutron mass, L is the length of the flight path, and ϑ is the diffraction angle. Unlike the constant wavelength case the scattering angle remains fixed to resolve the d-space [94].

Equation 2.12: Time-of-flight and wavelength relationship

$$\lambda = \frac{ht}{mL}$$

Equation 2.13: Time-of-flight and d-space relationship

$$d = \frac{ht}{2mLsin\theta}$$

Rietveld Refinement

Single crystal diffraction yields three dimensional structures giving atomic positions and bond lengths. In powder diffraction the data is compressed due to the random distribution of polycrystallites. Therefore, the atomic positions cannot be facilely calculated, and refinement techniques such as Rietveld refinement are necessary to determine the structure [83]. Rietveld refinement uses least squares regression therefore, requires a calculated model to compare to data. The difference between the two are minimised until a satisfactory fit is achieved. The starting model tends to be poor initially. But further refinements to the lattice parameter, instrumental constants, peak profile coefficients and atomic parameters, allow improvements to the fit. The refinement adheres to the following equation;

Equation 2.14: Rietveld least squares minimisation calculation

$$S_y = \sum_i w_i \, (y_i - y_{ci})^2$$

Where, w_i is the reciprocal of y_i, y_i is the observed gross intensity at any point *i*, and y_{ci} is the intensity calculated from the model at point *i*.

The calculated intensity can then be calculated from the following equation;

Equation 2.15: Calculated intensity

$$y_{ci} = s \sum_K L_K |F_K|^2 \, \phi(2\theta_i - 2\theta_K) P_K A + y_{bi}$$

Where; y_{ci} is the calculated intensity at point *i*, *K* defines the miller indices *h*,*k* and *l*, L_K, contains Lorentz, polarisation and multiplicity factors, F_K is the structure factor, ϕ is the reflection profile function, which estimates the effect of instrumental set-up and any sample features, P_K is the preferred orientation factor, *A* is the absorption factor and y_{bi} is the background intensity at point *i* [95]. These calculations form a matrix, which increases in size with the number of refined parameters. As refinements are made the calculated line should closely resemble the observed data set.

Refinements should be completed until the calculated model converges at a chemically sensible stopping point.

The fit of the calculated model to the experimentally collected data is described by statistical parameters known as the R-values. The most useful of these is the weighted pattern R factor, R_{wp}.

Equation 2.16: Weighted R pattern calculation

$$R_{wp} = \left\{ \frac{\Sigma w_i \left(y_i(obs) - y_i(calc) \right)^2}{\Sigma w_i \left(y_i(obs) \right)^2} \right\}^{\frac{1}{2}}$$

In this equation, w_i is the weighting factor, the reciprocal of y_i, $y_i(obs)$, is the experimental intensity at point *i* and $y_i(calc)$ is the calculated intensity at point *i* [96].

This value can be used as an indicator of the progression of the refinement. As the R_{wp} value tends towards zero the fit improves. An ideal fit has $R_{wp} = 0$, however, this is never achieved practically [97]. χ^2 otherwise known as the "goodness of the fit" is also commonly used in refinement to determine the quality of the fit. A perfect fit would have χ^2 equal to 1. The χ^2 value is not always a great indication of fit is as it can be fudged and can also fall below zero if the experimental data is not high enough quality for the number of refined variables. Therefore, the R_{wp} should be used preferentially to this [97].

Equation 2.17: Goodness of Fit

$$\chi^2 = \frac{R_{wp}}{R_e}$$

Equation 2.18: Expected R-Factor

$$R_e = \left[\frac{N - P + C}{\Sigma w_i y_i^2} \right]^{1/2}$$

Where, R_e is the expected R-factor, *N* is the total number of observations, *P* is the number of parameters being refined and *C* is the number if constraints which have been applied. Often the numerator can be reduced to *N* as *P* and *C* are always far smaller than this value [95].

SQUID Magnetometry

DC-susceptibility allows the thermal dependent bulk magnetic behaviour to be observed. This is typically performed using a Superconducting Quantum Interference Device, SQUID, which measures subtle changes in magnetic flux [98]. The SQUID has high sensitivity as it is comprised of two superconductors separated by a thin layer of insulator generating two parallel Josephson junctions. The Josephson effect arises when current flows between two superconductors without the application of an external voltage. SQUID magnetometers measure the change in magnetic flux by moving the sample through a superconducting pick up coil. This changes the magnetic flux, causing a phase shift which is converted to a voltage for digital display [99–101].

In DC-magnetometry the magnetic response is initially measured without a magnetic field, zero field cooling (ZFC). The external magnetic field is then switched on and field cooled (FC) measurements are recorded. The ZFC and FC lines are then superimposed to compare the responses. ZFC/FC Divergence can indicate ferromagnetism, deviation from Curie-Weiss behaviour or impurities but most simply shows that the material responds differently in a magnetic field.

In AC-magnetometry a small oscillating AC-field is applied to the sample and the moment is detected. A small DC-magnetic field is required. The experiment requires two coils, one to apply the oscillating field and the other to detects the sample response. In AC-susceptibility measurements, the real AC moment (χ') and an imaginary AC moment (χ'') are measured. The real AC moment applies to responses in phase with the first coil and the imaginary AC moment responds to the secondary coil. The χ'' response indicates dynamic processes if frequency dependence is observed [100].

Susceptibility measurements require a small sample of approximately 100 mg. These are tightly packed into a gelatine capsule to ensure the sample stays firmly in place. This packing can be carried out with the end of a gel capsule, or small quantities of materials with a small diamagnetic response. The gel capsule is then regularly placed in a plastic drinking straw although alternative sample holders include quartz or brass depending on the measurement. The quartz holder is preferred for low spin

states and miniscule samples. The brass alternative is favoured due to its robustness; however, it decreases the sensitivity of the measurement. The sample must be placed at a defined position to ensure it lies within the detection coils. When the straw is used, the capsule can be secured using excess pieces of the straw, orientated perpendicular to the capsule. This also provides a symmetrical diamagnetic background for the sample. Kapton tape applied to the bottom of the straw ensures no spillages inside the chamber. Finally, the straw should be punctured to prevent bursting under vacuum.

The sample holder is then placed on to a stick before being transferred to the sample chamber, where it must be centred. The is to ensure that the magnetic sample lies in between the detection coils. Without this centering step, spurious measurements may be obtained [98].

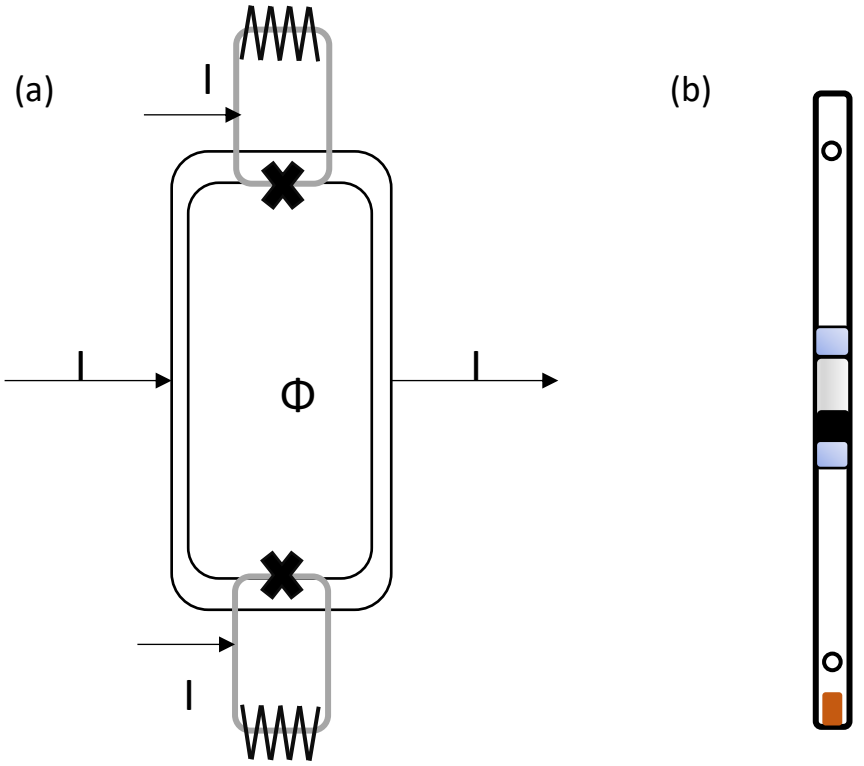

Figure 2.4: (a) A model of the DC-SQUID present in the magnetometer. The current is split along the two different directions, where they go through the two different Josephson junctions (represented by X) and summate to the total value of the current, $I = I_1 + I_2$. The current is related to voltage using $V = IR$ [101]. (b) The set up used for the magnetometry measurements. This depicts the sample straw; the gelatine capsule is shown in grey to ensure that it is distinguishable from the straw. The packed powder is indicated in black and lies in the capsule. The offcuts of the straw are shown in the light blue colour, again to ensure that they are easily distinguished from the straw. The holes which are placed into the straw to prevent bursting are depicted by open circles and the Kapton tape which prevents any losses from the straw is shown in

Muon Spin Relaxation (μSR)

Muon spin relaxation measures local magnetic behaviour, separating static and dynamic magnetism. Muons are leptons, fundamental particles which are indivisible as they are not composed of quarks. They can possess a positive or negative charge, permitting different behaviour dependant on chemical environment. They possess magnetic spin, S = ½ and a short life span of approximately 2.2 μs [102,103]. The positively charged muon, μ^+, is preferential for μSR measurements as it has greater sensitivity to magnetism [104], μ^- is disfavoured as it is attracted to nuclei and is rapidly captured upon implantation [102]. Conversely, μ^+ is repulsed by nuclei. Its attraction to electrons allows stable muonium to form which allows observation of magnetic behaviour [103].

Cosmic rays generate a low intensity of muons naturally. Higher intensities of muons are synthesised using particle accelerators, where protons are rapidly accelerated around a circular or elliptical track forming a beam of high energy protons which collide with a heavy target. Upon collision, pions are formed. Pions can be neutral, positively charged or negatively charged, described by π, π^+ and π^- respectively. In the particle accelerator, the positively charged pion, π^+, tends to be formed. These form when two protons interact, resulting in π^+, a proton and a neutron emerging. Pions have an incredibly short average lifespan of 26 ns, decaying into a muon plus a muon neutrino [105]. The production of the pions and their decay into positively is shown below.

Equation 2.19: Production of pions which forms in the particle accelerator

$$p + p \rightarrow \pi^+ + p + n$$

Equation 2.20: Decay of a positively charged pion

$$\pi^+ \rightarrow \mu^+ + \nu_\mu$$

Pions are stationary upon formation, therefore, decay products must conserve momentum with an equal and opposite momentum to each other. Spin must also be conserved; as pions have S = 0, the muon and muon neutrino must have equal but opposite spin. Intrinsically neutrinos possess spin

which is aligned antiparallel to the direction of its momentum, due to negative helicity [102]. This produces a spin polarised beam of muons.

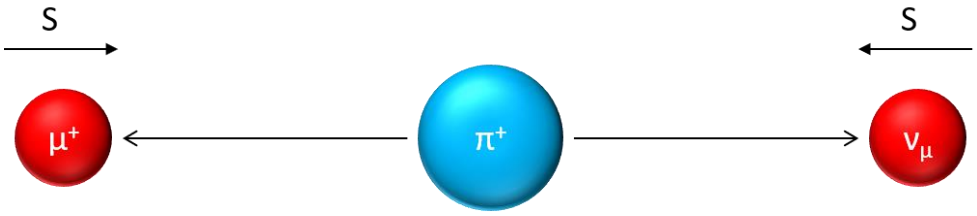

Figure 2.5: The decay of a positively charged pion. The pion decays at rest and therefore has zero momentum and no intrinsic spin. Upon its decay, the breakdown of the pion forms a μ^+ and a muon neutrino. To ensure that both momentum and spin are conserved, the two decay products emerge from the pion in separate directions with spin in the opposite direction.

The muons are implanted into the sample with high energies. This energy is lost rapidly as electrons are scattered and ionisation takes place. After 2.2 μs, the muons tend to decay forming a positron, an electron neutrino and a muon antineutrino.

Equation 2.21: The decay process of the positively charged muon

$$\mu^+ \rightarrow e^+ + \nu_e + \overline{\nu_\mu}$$

The charged positron is used for detection. Upon decay the momentum of the muon must be conserved. The negative helicity of the neutrinos allows the positrons to possess the same spin direction as the muon upon decay. This allows the magnetic behaviour to be inferred more directly [102,103]. The decay of μ^+ is depicted in Figure 2.6.

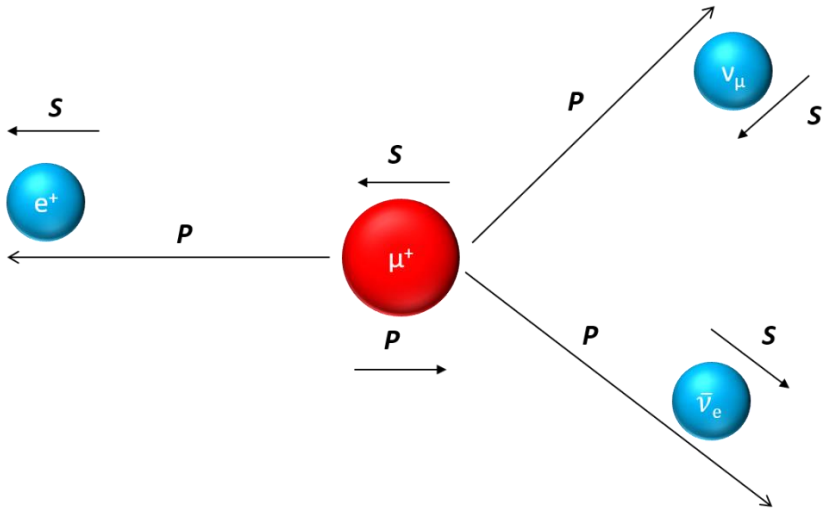

Figure 2.6: A depiction of the decay pattern of μ^+. The decay of the muon results in a positron, a muon neutrino and an electron antineutrino. The positively charged positron possesses the same direction of spin as the muon, allowing the behaviour of the system to be inferred.

Muon Spin Relaxation Experiment

Upon implantation, muons reside in an interstice and are affected by the chemical environment, with precession occurring near magnetic fields. This Larmor precession occurs with a definitive angular frequency, which is field dependent. The angular frequency (ω_μ) is related to the gyromagnetic ratio, γ_μ, and strength of the applied field, B [106].

Equation 2.22:The angular frequency of the muon precession

$$\omega_\mu = \gamma_\mu B$$

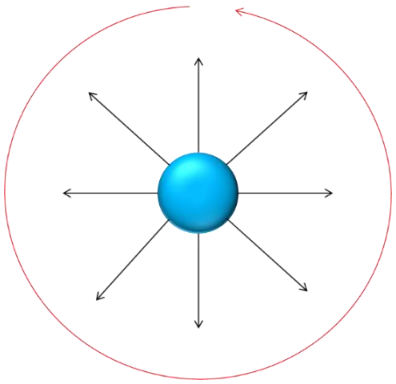

Figure 2.7: This shows the Larmor precession of the muon when it experiences the effects of an applied magnetic field. The blue sphere shows the muon, the red arrow indicates the direction of the precession or rotation of the muon and the black arrows indicate how the direction of the muon spin changes through the precession.

The measurement can be carried out in longitudinal field (LF) or transverse field (TF). Typically, TF-μSR is used for data calibration using small magnetic field strengths. When these are carried out the magnitude field is aligned perpendicularly to the sample. This is shown in Figure 2.8.

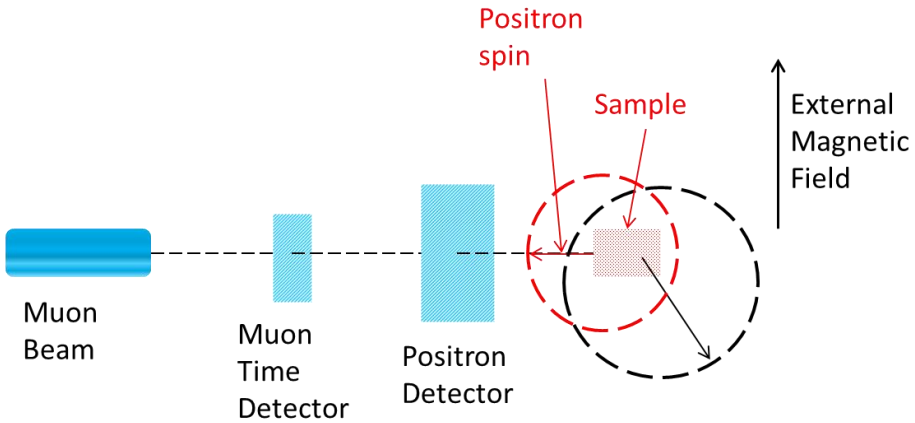

Figure 2.8: The set-up of the TF-μSR measurement. The spin polarised muon beam travels toward a muon time detector, which records the time. The muons are then implanted into the sample, precess and decay. The positrons are then emitted from the sample and can be detected. The external magnetic field is perpendicular to the sample. The red arrow and dashed circle indicates the muon spin direction at time, 0 whilst the black arrow and dashed circle represents the muon spin direction at time, t.

In LF-μSR measurements, the external magnetic field is applied in a parallel configuration to the sample. This is used for ZF- and LF-μSR measurements. This set-up is shown in Figure 2.9 [104,107].

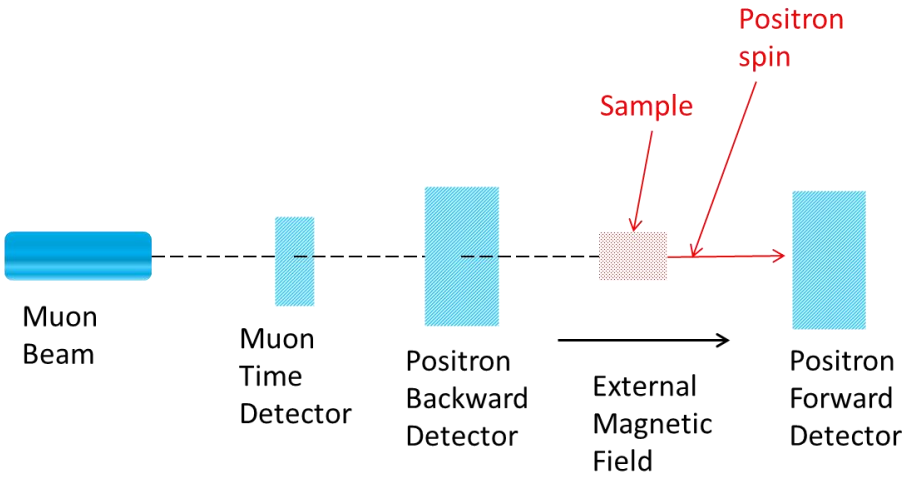

Figure 2.9:The LF-μSR measurement configuration. The spin polarised muons travel towards the sample through a time detector and then implant into the sample prior to decay. The positrons which emerge from the decay process are then detected by the forward or backwards detector. In this set up the external magnetic field is parallel to the sample.

In the LF arrangement, a forward and backward detector are utilised. If muons immediately decay upon implantation, then the positrons are witnessed by the backwards detector. If muons live longer and experience precession, then the positrons can be counted by the forward detector. A profile, the asymmetry function, can be established from the number of positrons collected by each detector.

Equation 2.23: Muon spin relaxation asymmetry function

$$A(t) = \frac{N_B(t) - N_F(t)}{N_B(t) + N_F(t)}$$

In the μSR asymmetry function, *A(t)* describes the asymmetry value of the function at time *t* and $N_B(t)$ and $N_F(t)$ correspond to the number of positrons collected by the backwards and forwards detectors respectively within a specific time frame.

The asymmetry value can then be normalised by the following equation;

Equation 2.24: Normalised asymmetry of the muon spin relaxation function

$$G(t) = \frac{A(t)}{A_{Max}}$$

Where; *G(t)* is the normalised asymmetry at time *t*, *A(t)* is the asymmetry function and A_{Max} is the maximum asymmetry value, which tends to occur at t = 0. The value of A_{Max} is dependent on the polarisation of the incident muon beam, the detector efficiency and intrinsic sample properties. These factors decrease the value of A_{Max} from 1 to an average of 0.25 [102].

The responses from μSR measurements tend to be carried out from time zero to 16 μs or longer. The signal to noise is highest at low time scales, decreasing significantly as time proceeds and the muon lifespan is exceeded. In TF-μSR measurements, the asymmetry oscillates periodically throughout the experiment, with the largest amplitude at low time scales as shown in Figure 2.10 (a). In LF-μSR measurements the asymmetry response decays with largest asymmetry at time zero. No oscillations are observed unless the sample is magnetically ordered, see Figure 2.10 (b).

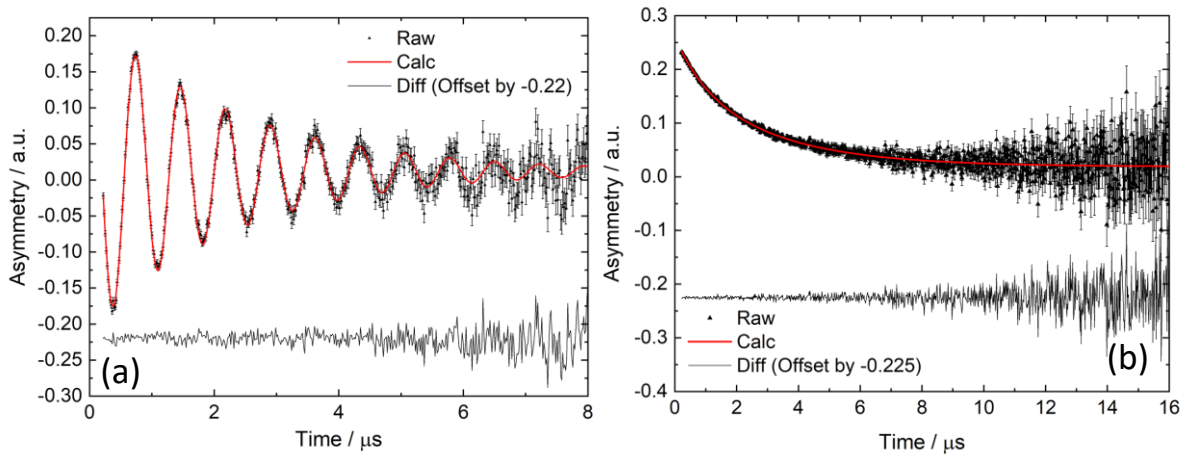

Figure 2.10: Examples of results from μSR measurements (a) a TF measurement, the asymmetry oscillates, decreasing as the experiment carries on. (b) a LF measurement, the asymmetry experiences a decay. In both configurations the data shows a decreased signal to noise ratio as the time increases.

Once μSR has been completed the data must be analysed by fitting functions to the relaxation curves, this can be completed using software such as Mantid [108]. The fitting function used is dependent on the behaviour of the system and therefore will not be covered in detail here.

Inelastic Neutron Scattering

Inelastic neutron scattering (INS) takes place when energy is not conserved during neutron scattering. The difference between incident and scattered energies is often accounted for by internal vibrational or magnetic excitations. Whether the neutron loses or gains energy is dependent on the scattering atom, chemical environment and the (de-)excitations experienced during the measurement [109].

INS is a complementary technique to Infrared and Raman spectroscopies but is unaffected by selection rules due to direct interaction of neutron and nucleus. Limitations associated with INS include, the need for large samples, long experiments and expense. When high energy is required low resolution data is achieved and low temperatures are necessary to minimise Debye-Waller effects [110].

Magnetic excitations indicate interaction between magnetic moments. In magnetically ordered systems periodic spin waves are observed in the inelastic neutron scattering pattern. From the form of the spin wave the magnetic nature of the structure can be examined by applying linear spin wave theory and calculating the Hamiltonian equation for that specific system. The Hamiltonian used is dependent on the magnetic nature of the sample. These interactions can range from J_1 interactions to much further distances. INS can also provide qualitative evidence of short-range magnetic excitations, these are present as higher intensity regions rather than spin waves [111].

INS can be carried out using direct or indirect geometries. When TOF INS is measured, the incident or scattered energies of the neutron must be defined to establish the time scale. This is vital as the pulses of neutrons contain different energies. In the direct geometry, the initial TOF pulse is chopped into a single incident energy and the time is recorded when the neutron and sample interact. The scattering process produces a range of energies which are detected, and the time is recorded again. In the indirect alignment, the incident energies remain pulsed, upon interaction the time is taken where a further range of energies pass through the system. Prior to detection and time stamping the range of energies pass through a crystal monochromator determining the final scattered energy. Direct

geometry Time-of-flight instruments based at the ISIS Neutron and Muon Source include Mari, LET and Merlin, whilst indirect geometry instruments include Tosca and Iris [112–115].

INS is plotted in energy transferred against momentum transferred (***Q***) with colour charts indicating the high intensity regions on the plot. Magnetic excitations tend to be present at low values of ***Q***. whilst vibrations tend to be observed at high values of ***Q***. Magnetic interactions also tend to take place at low temperature, the intensity of these decreases as the temperature increases. Vibrational excitations typically occur at higher temperatures when the kinetic energy is higher.

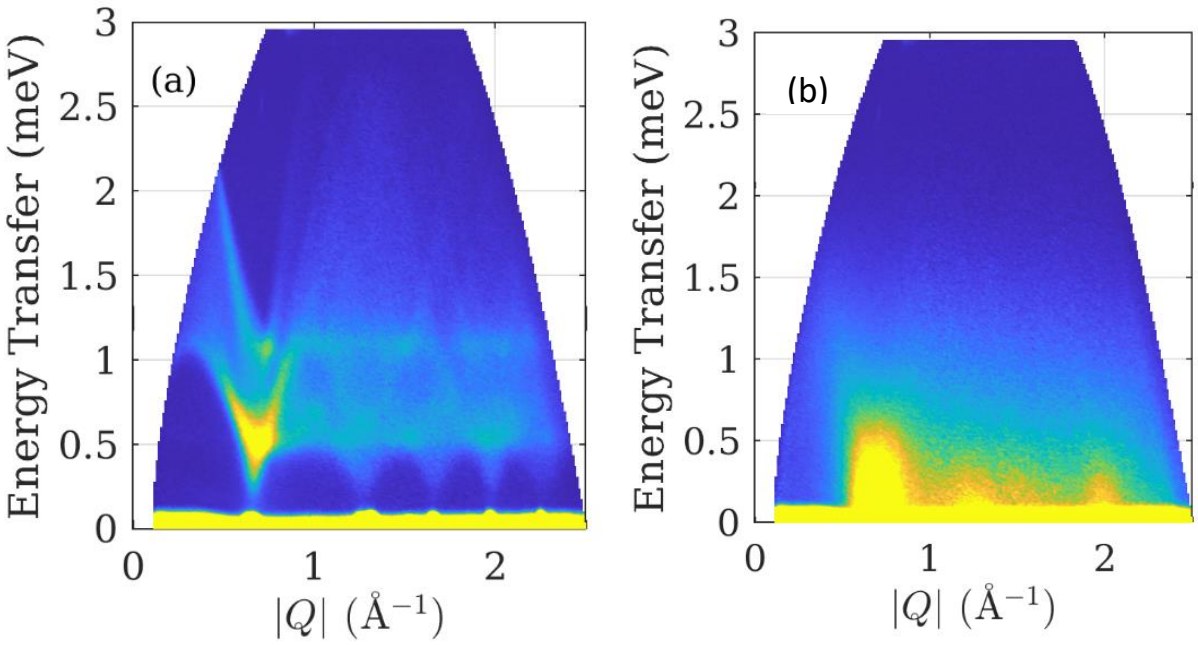

Figure 2.11: An example of the inelastic neutron scattering plot which shows magnetic behaviour. (a) indicates the situation where the material experiences long range magnetic order and therefore magnetic spin waves are observed. (b) indicates when magnetic excitations take place within the material, however, these do not propagate throughout the system and therefore spin waves cannot be observed.

Heat Capacity

Heat capacity can examine electronic or magnetic behaviour. Within the field of frustrated magnetism, heat capacity is an invaluable technique which has been used to identify valence bond glass states or quantum spin liquid like behaviour [116–119]. Heat capacity may be measured at constant pressure according to the following equation where C_P is heat capacity, this measures the energy change (dQ) with the change in temperature dT [120].

Equation 2.25: Heat capacity at constant pressure

$$C_P = \left(\frac{dQ}{dT}\right)_P$$

Measurements are completed by providing a specific quantity of heat to the sample over a fixed period using constant power to provide heat. The sample is cooled for the same duration to observe temperature changes, indicating how successfully the sample can retain the applied thermal energy. This is completed using the puck which contains the sample platform, a thermometer and a heater. Prior to sample application, the platform is treated with a layer of grease which secures the sample and acts as a thermal contact. The sample should have a small mass between 1 and 200 mg and contain a flat edge [121]. An addenda of the empty puck plus grease is taken for calibration purposes [121].

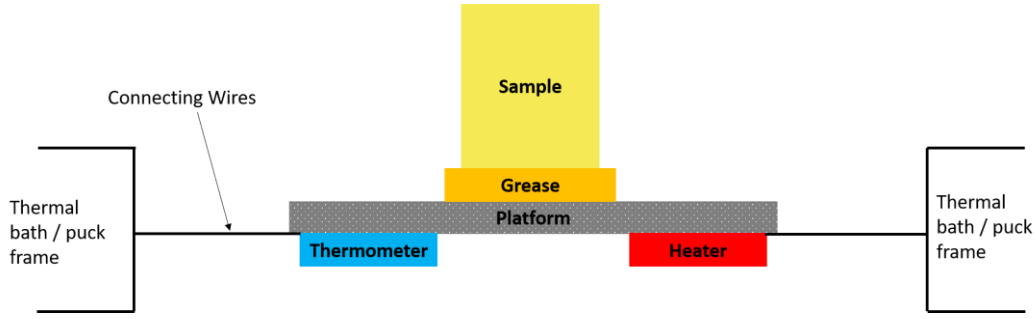

Figure 2.12: A schematic of the puck used in the Quantum Design PPMS for heat capacity measurements.

This can be represented using the thermal dependence of C_P/T. The response tends to be small at low temperature, increasing with thermal energy. Phase transitions are represented by sharp spikes and described as lambda anomalies. These are the result of a large loss or gain of energy. Otherwise, broad humps can be observed in the system which indicates the slow gain or release of energy [122].

3. Literature Review

Geometrical magnetic frustration is a phenomenon which has resulted in the emergence of several novel spin states and therefore it has been researched from both theoretical and experimental outlooks. Geometrical frustration affects a number of different lattices, with the main four of these; the Kagome lattice, equilateral triangular lattices, pyrochlores and face centred cubic (*fcc*) systems [51,123]. Figure 3.1 roughly depicts the number of manuscripts published about geometrical frustration with these systems over the last three decades. From this figure the effect within planar triangular lattices have been reported most widely, closely followed by Kagome lattices in recent years. The number of studies on geometrical frustration in pyrochlore systems experienced a significant increase after 2000 which could coincide with the discovery of the spin ice states in $Ho_2Ti_2O_7$ or the cooperative paramagnetism observed in $Tb_2Ti_2O_7$ [124,125]. Figure 3.1 indicates that since 1990 the number of publications in frustrated *fcc* lattices has experienced a gradual increase but now has the fewest publications out of the big four. The *fcc* lattices which are affected by magnetic frustration include simple metal oxides, dilute metal and Heusler alloys, spinels and double perovskites. The focus of this research is double perovskites and therefore, the number of studies of these has been included in Figure 3.1, where it has experienced a steady increase, however, remains comparatively small to the others. As a result of this a large scope for investigation into geometrical frustration in double perovskites remains.

MnO is an archetypical *fcc* lattice, it was the first material shown to exhibit antiferromagnetic long-range order by neutron powder diffraction in an investigation completed by Shull and Smart in 1949. This antiferromagnetic ordering was identified by extraneous Bragg peaks, observed at d-space values which violate the symmetry and space group of MnO with a propagation vector of $\boldsymbol{k}$ = (1/2, 1/2, 1/2) [126]. Later reports identified Type II antiferromagnetic behaviour using inelastic neutron scattering, this calculated proximate antiferromagnetic exchange parameters with a slightly dominant J_2, J_1 = -10 K and J_2 = -11 K [127]. Deriving the orientation of the magnetic moments within MnO was

not a facile task and led to several contradictory reports. The spins were reported to align either along the [100] planes [128] or perpendicular to the (111) direction [129,130]. It was determined that the latter orientation was correct when the dipolar interaction was calculated, provided that multiaxial spin arrangement was negligible [127,130]. This assumption is viable due to the structural distortion of the nuclear MnO lattice at Néel temperature. This phase transition was originally described as a rhombohedral distortion, rationalised by magnetostriction or exchange-striction [131]. However, this was more recently found to be monoclinic in nature, distorting to space group *C2,* by total neutron scattering and reverse Monte Carlo simulations [132]. In 2018, MnO was reported to experience short-range magnetic correlations above T_N [133]. This was suggested by diffuse scattering observed in earlier neutron diffraction experiments [126,128]. The short-range magnetic excitations were observed using single crystal neutron scattering in conjunction with reverse Monte Carlo calculations. From these techniques, comparisons could be drawn from the ordered antiferromagnet and the short-range correlated state [133]. MnO is an arguably simple material, however, it has continued to be the basis of novel research spanning almost a century. This bolsters the reasoning behind revisiting previous simple systems and studying them in different ways than they were previously.

The research outlined within this thesis, is based on double perovskites of the form $(Ba,Sr)_2MM'O_6$. These systems are ideal for studying the effects of magnetic frustration due to their versatility, which permits extensive substitution of magnetic and non-magnetic cations. The exploitation of this can allow a range of interesting properties to be accessed and analysed [134]. The structure supports high spin states such as S = 5/2, observed in MnO, as well as significantly lower spin states, where the likelihood of quantum behaviour is increased dramatically. Throughout this section, a number of interesting magnetically frustrated double perovskites ranging from S = 5/2 to S = 1/2 and their properties will be outlined.

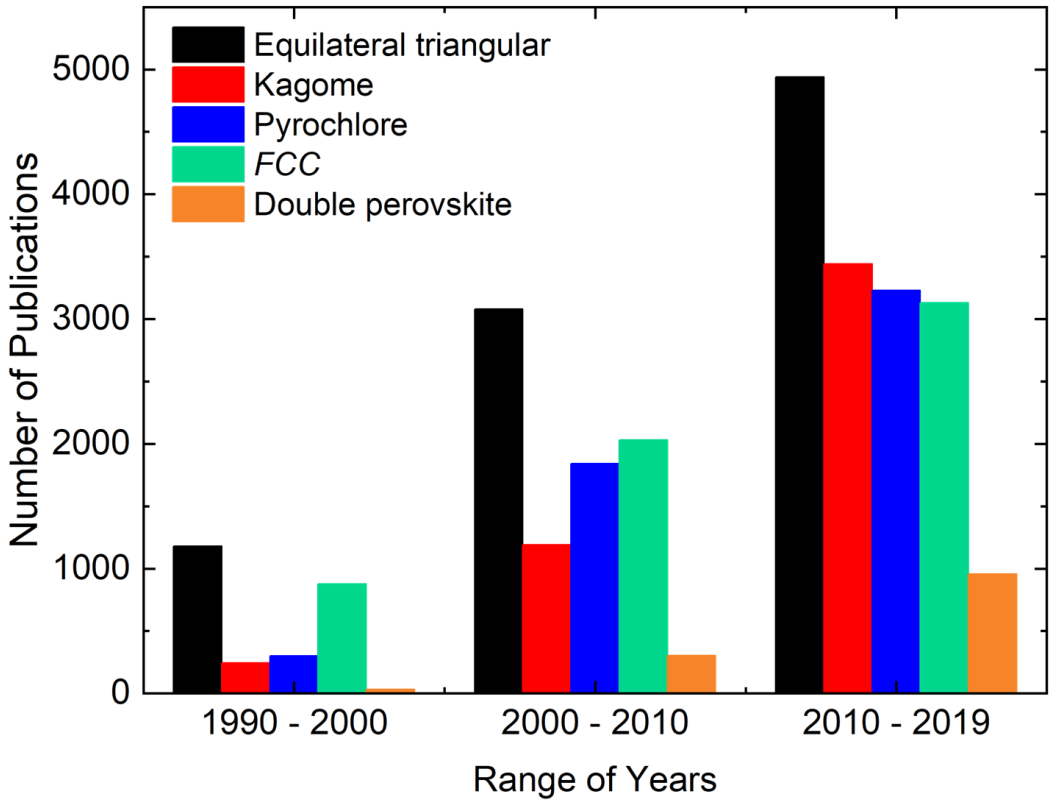

Figure 3.1: This bar chart indicates the number of publications published about each of the lattices in relation to magnetic frustration over the last three decades. These were collected by a bibliographic search conducted on the Web of Science database using the key words “geometrical frustration” and “magnetic” and the lattice type.

S = 5/2

Magnetically frustrated species which possess the S = 5/2 spin state tend to exhibit classical magnetic behaviour, entering long-range antiferromagnetically ordered states below a given Néel temperature. This is a consequence of the strong magnetic interactions which occurs between these cations. The S = 5/2 spin state is the highest accessible by the d-electrons, requiring five unpaired electrons as stated by Hund’s rule of maximum multiplicity. The high spin state is quite rare as few elements can achieve this electronic configuration and remain stable. The transition metals Mn^{2+} or Fe^{3+} are frequently used to achieve this spin state. Mn^{2+} requires a counterbalance *M’* cation present in the +6-oxidation state in (Ba,Sr)Mn*M’*O_6 double perovskites, i.e. diamagnetic Mo^{6+} or W^{6+}. Conversely, those containing Fe^{3+} can be balanced by a +5 *M’*-site cation which can be either diamagnetic or paramagnetic. In these S = 5/2 spin systems, the d-orbitals are degenerate when in a spherical field and experience no angular

momentum (L = 0) as the orbitals are unable to rearrange themselves. This allows only the spin-spin coupling contribution to be considered.

One example of an S = 5/2 system is Ba_2MnWO_6, a frustrated double perovskite initially reported by Khattak, Cox and Wang. Ba_2MnWO_6 was reported to adopt $Fm\bar{3}m$ symmetry from ambient temperature to 4.5 K with an antiferromagnetic transition below 7.5(10) K [135]. Further investigations into Ba_2MnWO_6 suspected potential diffuse magnetic scattering above the transition temperature and observed a ferromagnetic transition at approximately 45 K. This ferromagnetism was not observed in other studies and therefore, this is thought to be the result of a magnetic impurity, Mn_3O_4 [136–138]. Computational studies completed on Ba_2MnWO_6 indicate that the material is an antiferromagnetic insulator, with coupling constants close in magnitude [139,140]. Similarly, Sr_2MnWO_6 experiences long range antiferromagnetic order below approximately 13 K. Like Ba_2MnWO_6, Sr_2MnWO_6 has also experienced controversy as the structure has been disputed, having been reported as tetragonally ($P4_2/n$) or monoclinically ($P2_1/n$) distorted [141–143].

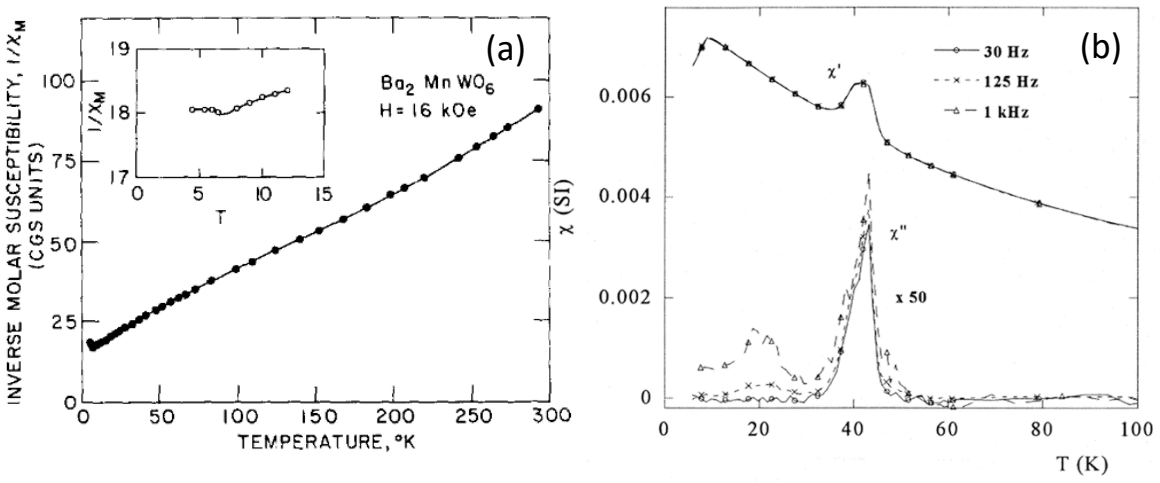

Figure 3.2: (a) The DC-magnetometry results collected on Ba_2MnWO_6 which indicate the inverse susceptibility plot which shows an antiferromagnetic transition at 7.5(10) K [135]. (b) A different data set of DC-magnetometry measurements completed on Ba_2MnWO_6. Like the previous report, the antiferromagnetic transition occurs at low temperature close to 8 K, however, a ferromagnetic transition is observed at approximately 45 K. This ferromagnetic transition is not reported in other research articles concerning Ba_2MnWO_6 which suggests that this originates from an antiferromagnetic impurity [136].

Replacement of W^{6+} allows Ba_2MnMoO_6 to be formed, this has been reported to behave similarly to Ba_2MnWO_6. Ba_2MnMoO_6 crystallises in $Fm\bar{3}m$ between 2 K and ambient temperature with an antiferromagnetic transition at 10.8 K [144]. Theoretical studies give varying reports with density functional theory suggests metallic behaviour [145] whilst first principle calculations using GGA (Generalised Gradient Approximation) state insulating behaviour with exchange coupling constants J_1 = -1.17 meV and J_2 = -0.87 meV [146]. The J_2/J_1 value is comparable to that reported for MnO, illustrating the strong effect of the spin state of magnetic cation on the magnetic behaviour. The related structure Sr_2MnMoO_6 has also experienced dispute, predominately over space group settings and has been suggested to behave similarly to Sr_2MnWO_6, experiencing antiferromagnetic order around 13 K [142,147,148].

These examples of S = 5/2 materials each experience long-range antiferromagnetic order below their respective Néel temperature. Despite this apparent simplicity, each material has experienced its own controversy with contradictory results being reported. This indicates that these systems require further investigation and that greater understanding about the high spin state could be gathered from doing so.

When the Fe^{3+} ion is considered, significantly more complex magnetic behaviour is achieved. An early study carried out on Sr_2FeNbO_6 reported that the material was a disordered cubic perovskite, with an random distribution of the Fe^{3+} and Nb^{5+} cations, unlike the rock salt ordering achieved in the previous Mn^{2+} cation containing double perovskites [149]. This lack of *M*-site ordering changes the magnetic properties and is potentially the result of the cations being too close in both valence state and ionic radii to drive any distinct order, however could also be the result of the synthesis conditions [36,150]. This disorder prevents magnetic order of the Fe^{3+} cations and instead a spin glass transition arises at 32.5 K. The susceptibility deviates from Curie-Weiss law due to the formation of a short-range correlated state [149]. Further investigations suggest a tetragonal space group *I4/m*, with partial ordering of the Fe^{3+} and Nb^{5+} cations [150] and also antiferromagnetic transitions persisting despite

the antisite disorder [151]. This indicates that the synthesis conditions and interpretation of results can cause contrasting reports of the properties. Therefore, greater effort must go into understanding the effects of these changes and that reproducibility of measurements is of the utmost importance.

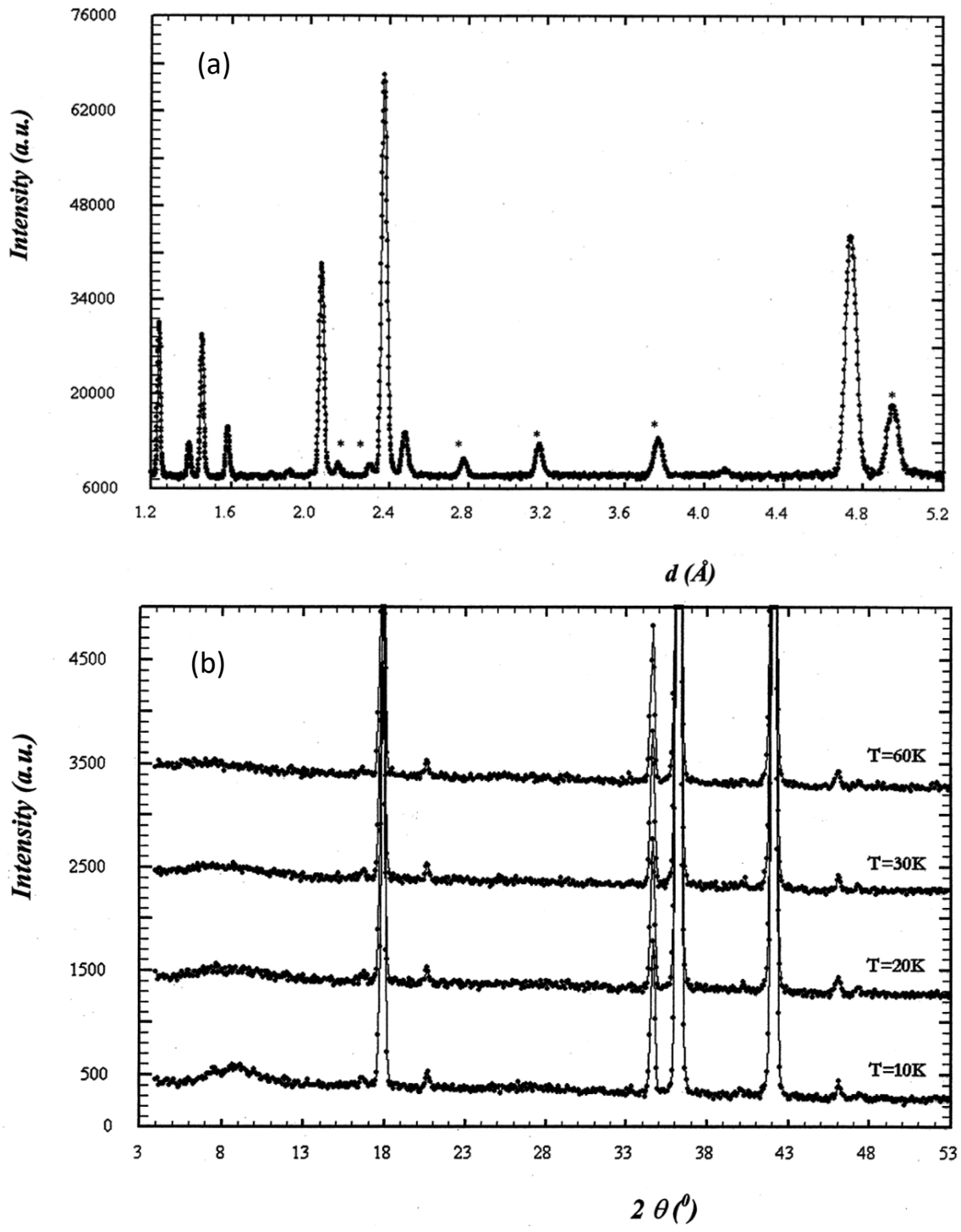

Figure 3.3: Neutron powder diffraction measured on Ba_2MnWO_6. (a) magnetic Bragg peaks outlined by asterisks. (b) shows the neutron powder diffraction collected at certain temperatures, at 10 K a broad bump is observed around 9° 2θ. This diffuse magnetic scattering could suggest some short range correlations taking place within the material [136].

Double perovskites with a sole magnetic S = 5/2 cation can experience complicated structural distortions and magnetic behaviour, but typically show long-range magnetic order [62,152]. The addition of a supplementary magnetic ion allows interactions between like or opposite cations which can result in the stabilisation of ferrimagnetic or ferromagnetic states [153]. This is evident in the magnetoresistance observed in Sr_2FeMoO_6. The signature of magnetoresistance is a decrease in the resistance when placed in a magnetic field. This was originally observed in lanthanide manganate perovskites, prior to reports it could be observed at ambient conditions in Sr_2FeMoO_6 [154]. The Fe^{3+} and Mo^{5+} cations were suggested to order in an alternate fashion resulting in long-range antiferromagnetic behaviour which could induce a magnetic tunnelling effect. This study initiated many reports to substantiate these calculations. As a result, a number of disparate claims about the cationic valences, proportion of disorder, transition temperatures and the effective magnetic moment were established [155–158].

The contrast within these reports could be the result of changes made during the synthesis conditions. Altering the sintering temperature by a few hundred degrees has been shown to have a profound effect on the magnetic properties of ferrite materials, due to changing particle sizes and grain boundaries [159]. Changes to the solid-state synthesis method used, i.e. using different reagents, reaction times and utilising different atmospheres have also been found to cause significant changes to the properties of different materials. [160,161] Since the initial report of $Sr_2FeMoO6$, it has continued to be extensively investigated, garnering approximately 100 new publications every year on the magnetic behaviour. The number of reports which concern Sr_2FeMoO_6 or makes mention of the material shows the significance of this discovery and has promoted the emergence of many new double perovskites.

Despite the apparent simplicity of the classical behaviour of the S = 5/2 double perovskites, further study is crucial to gain a fuller understanding of these materials. To ensure that this is achieved, a wider range of techniques should be implemented to comprehend the nature of the ordered magnetic

state. In addition to this, further studies should be completed on the effect of changing synthesis conditions on the properties of these systems.

S = 3/2

Reducing the spin state from S = 5/2 to S = 3/2 can result in an increase in the complexity of the observed magnetic behaviour. The S = 3/2 spin state is observed in d^3 or high spin d^7 electronic octahedral configurations. The d^3 configuration is comprised of half-filled t_{2g} and empty e_g orbitals. As the t_{2g} orbitals are half-filled no spin orbital contribution should be observed. In the high spin d^7 electronic configuration, the occupancy of the d subshell is $t_{2g}^5e_g^2$. The ion will experience significant orbital angular momentum as the t_{2g} can be rearranged and therefore spin-orbit coupling contributions must be considered. Spin-orbit coupling can cause deviations from Curie-Weiss behaviour and affect the magnitude of the effective magnetic moment. Long-range antiferromagnetic order is often observed in S = 3/2 systems due to the high spin state, however, more unique behaviour can also be observed.

Ba_2CoWO_6 and Ba_2CoMoO_6 both contain the $3d^7$ cation Co^{2+} and exhibit similar antiferromagnetic ordering below 19 and 27 K respectively [162]. Each material retains *fcc* symmetry down to 2 K, adopting a Type II antiferromagnetic structure with $\boldsymbol{k}$ = (1/2, 1/2, 1/2). Ba_2CoWO_6 has been suggested to have magnetic moments which are slightly offset from the (111) plane by approximately 20°, giving an effective magnetic moment of 2.0(3) μ_B [163]. Neither material shows Curie-Weiss paramagnetism at temperatures $T \leq 10xT_N$ [162]. Substitution was carried out on Ba_2CoMoO_6 to synthesise the solid solution $Ba_{2-x}La_xCoMoO_6$ ($0 \leq x \leq 0.5$). This study showed that greater quantities of La^{3+} suppress the antiferromagnetic behaviour, showing properties of a semi-conductor rather than an insulator [164].

The related compounds Sr_2CoWO_6 and Sr_2CoMoO_6 are both tetragonally distorted at ambient temperature and Sr_2CoWO_6 has been reported to experience a further monoclinic distortion at T_N. The transition temperature is 24 K for Sr_2CoWO_6 and 36 K for Sr_2CoMoO_6 [165–167]. This shows that despite the change from Ba^{2+} to Sr^{2+}, the magnetic behaviour is only slightly affected. Sr_2CoMoO_6 has

been reported to show an improper ferroelectric transition, making it more complex than the other related systems, with potential for multiferroicity [168].

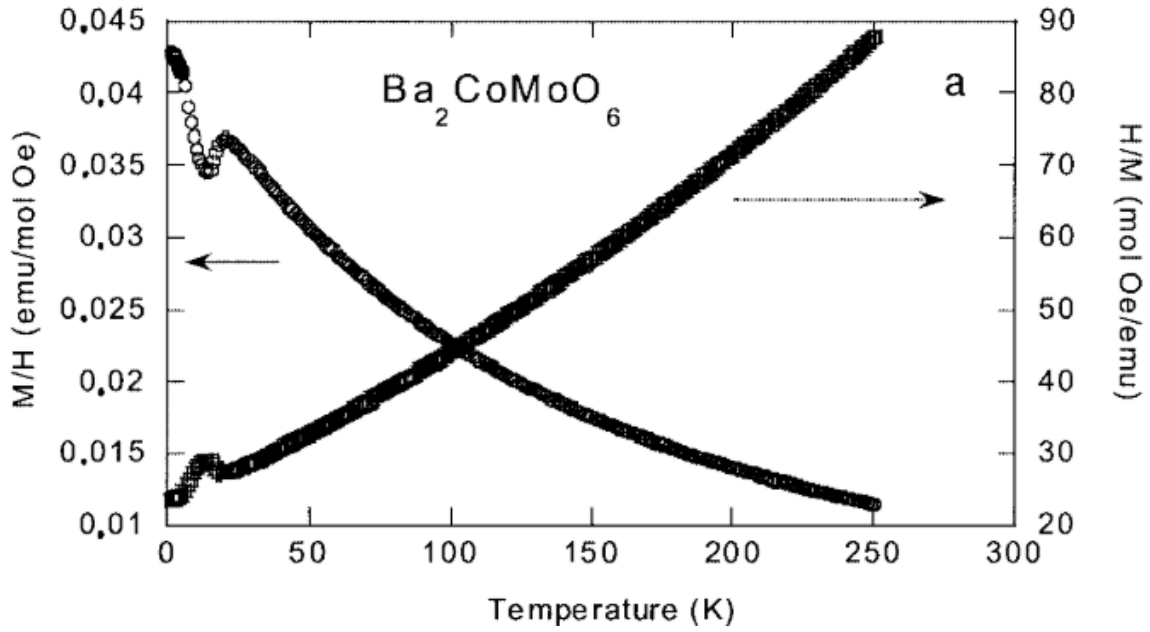

Figure 3.4: DC-magnetic susceptibility data collected from Ba_2CoMoO_6 between 2 and 250 K. The left-hand axis shows the thermal dependence of the molar susceptibility and the right-hand axis shows the reciprocal susceptibility over the temperature range. This measurement shows that Curie-Weiss behaviour is not observed at high temperature as the reciprocal susceptibility response is curved rather than linear.

Ba_2YRuO_6 contains Ru^{5+} ($4d^3$, S = 3/2) as the sole magnetic cation. Despite Ru^{5+} being a d^3 cation, it is susceptible to spin orbit coupling as it is a 4d transition metal. Ba_2YRuO_6 experiences no structural phase transition between 4.2 K and ambient temperature and undergoes an antiferromagnetic transition into a Type 1 antiferromagnet [169]. Ba_2YRuO_6 is strongly frustrated with a frustration index equal to 16 [170]. Inelastic neutron scattering shows that the spin waves experience a large gap, the result of strong spin orbit coupling effects of the Ru^{5+} cation [171]. Short-range magnetic correlations were observed above the transition temperature [172].

Sr_2YRuO_6 behaves similarly to Ba_2YRuO_6 adopting a Type I AFM structure below 26 K, however it experiences a lower than anticipated effective magnetic moment and a significantly smaller frustration index of 5.5 [173]. More recent reports on Sr_2YRuO_6 have shown that the DC-susceptibility contains two separate features at 32 and 27 K with resolved peaks in the heat capacity corresponding to two distinct transitions [174]. These features have been attributed to a transition to a 2D

antiferromagnetically ordered state, then a subsequent 3D transition to the Type 1 antiferromagnetically ordered state [175,176]. Further measurements have indicated that Sr_2YRuO_6 experiences magnetisation reversal, a result of Dzyaloshinsky-Moriya interactions between the Ru^{5+} cations [177]. Similarly Sr_2LuRuO_6 and Ba_2LuRuO_6, both show Type I antiferromagnetic ordering [169,178].

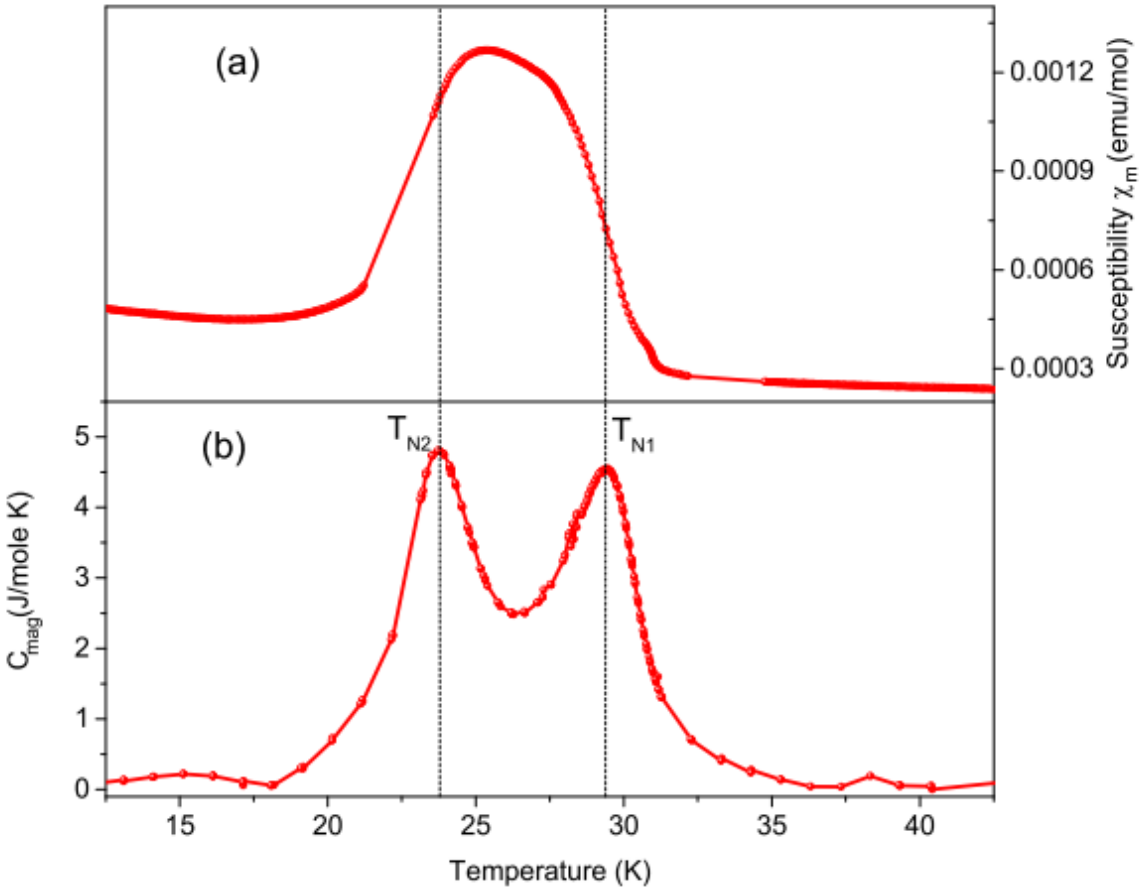

Figure 3.5: Measurements completed on Sr_2YRuO_6. (a) DC-susceptibility the broad hump is attributed to a transition from a paramagnetic to a magnetically ordered state. (b) The specific heat capacity measurements allow the broad hump to be extracted into two distinct peaks which are assigned as Néel temperatures 1 and 2 [174].

La_2NaRuO_6 crystallises in the $P2_1/n$ space group with T_N equal to 16 K [179]. Neutron powder diffraction measurements indicate no structural phase transition but an incommensurate magnetic structure with $\boldsymbol{k}$ = (0 0 0.091). This magnetic structure is unique, composed of two distinct, independent helices which simultaneously intersect each other which arises from alternating planes of magnetic moments. This behaviour is suggested to be a result of the large deviation of the β angle

to a value of 90.387(2)°, combined with frustration effects [180]. This structural deviation is greater than is typically observed in monoclinic double perovskites, with the exception of Ln_2LiRuO_6 [181]. Muon spin relaxation and inelastic neutron scattering measurements suggest short range magnetic order above the transition temperature with gapped excitations observed up at 100 K, significantly higher than T_N. The energy gap is rationalised to be the result of strong spin orbit coupling in the system brought about by the Ru^{5+} cation [182].

La_2NaOsO_6 was closely compared to La_2NaRuO_6 however, significant differences occur between the two. Both experience a significant monoclinic distortion, although this deviation occurs to a greater extent in La_2NaOsO_6. Long-range antiferromagnetic order could not be confirmed in La_2NaOsO_6 through heat capacity or neutron powder diffraction, potentially caused by the weak effective magnetic moment brought about by spin orbit coupling effects [180]. La_2NaOsO_6 shows evidence of a short-range correlated magnetic state, however, does not show gapped magnetic excitations below the suspected transition temperature [182]. The vast differences between La_2NaRuO_6 and La_2NaOsO_6 shows the complexity of the S = 3/2 spin state, as minimal changes resulted in vastly different magnetic properties. The comparison of the two materials show the importance of spin orbit coupling, especially in the 4d and 5d transition metals, and that this can cause the emergence of new interesting behaviour and that it must be considered in the S = 3/2 systems.

Comparison of the S = 5/2 and S = 3/2 double perovskites indicates that typically antiferromagnetic long-range order can be achieved readily. This is likely a result of the large effective magnetic moments within these systems. Interestingly, the Type II antiferromagnetic structure is more commonly observed in the S = 5/2 materials, whilst Type I antiferromagnetic behaviour arises more frequently in the S = 3/2 systems. In Type I antiferromagnetic structures the dominant interactions take place between adjacent magnetic cations whilst in Type II antiferromagnets, the next nearest neighbours experience the strongest interactions.

S = 1

Decreasing the spin state to S = 1, allows magnetic cations with two unpaired electrons such as Ni^{2+}, Os^{6+} and Re^{5+}, to be incorporated into the double perovskite. The $3d^8$ Ni^{2+} cation should experience fairly simple behaviour within the double perovskite structure, experiencing no Jahn-Teller distortion, whilst the 5d Os^{6+} and Re^{5+} experience strong spin orbit coupling which affects these transition metals. Double perovskites containing these magnetic cations will be explained throughout this section.

Ba_2NiWO_6 crystallises in $Fm\bar{3}m$ from room temperature down to 4.2 K, experiencing no Jahn-Teller distortion [163]. Ba_2NiWO_6 exhibits a Type II antiferromagnetic structure below 48 K with magnetic moments aligned orthogonally to the (111) direction resulting in an effective magnetic moment of 1.9(3) μ_B [163,183]. Sr_2NiWO_6 is tetragonally distorted adopting the *I4/m* space group, ordering in a Type II antiferromagnetic structure below 54 K [184–186]. Ba_2NiMoO_6 and Sr_2NiMoO_6 show similar characteristics to their tungsten analogues, but notably they exhibit higher T_N. These similarities indicate minimal changes in the magnetic behaviour and show that replacing the $4d^0$ and $5d^0$ *M'*-site cation has only slight effect [187].

The $(Ba,Sr)_2Ni(W,Mo)O_6$ double perovskites show significantly higher transition temperatures than their Mn^{2+} or Co^{2+} equivalents. This suggests that the Ni^{2+} materials are less frustrated; this must be a result of the difference in the electronic configurations. The $t_{2g}^6e_g^2$ configuration is non-degenerate and the filled t_{2g} orbitals lead to quenching of the orbital angular momentum.

Ba_2CaOsO_6 also crystallises within an *fcc* lattice and overcomes frustration to exhibit long range order at approximately 50 K. The effective magnetic moment is significantly smaller than the spin only value for the Os^{6+} cation, the result of significant spin orbit coupling [188,189].

Conversely, Ba_2YReO_6 exhibits a large frustration index of 23 indicative of very strong antiferromagnetic interactions, however, an antiferromagnetic transition could not be definitively confirmed by neutron powder diffraction, muon spin relaxation or heat capacity measurements [190,191]. Muon spin relaxation measurements indicate that that the magnetic

moments may experience spin freezing [191]. Recent theoretical studies suggest that the material could adopt a complex quadrupolar spin nematic phase [189,192].

Like Ba_2YReO_6, Ba_2LuReO_6 experiences antiferromagnetic interactions, without achieving long-range order. Below the proposed transition it experiences ZFC/FC divergence which is attributed to weak ferromagnetism due to Dzyaloshinskii-Moriya interactions. Similar ZFC/FC divergence is observed in Ba_2SmReO_6 which appears to order at approximately 82 K. However, Ba_2SmReO_6 and Ba_2EuReO_6 deviate from Curie-Weiss paramagnetism due to the temperature dependent moment of the lanthanide cations. Ba_2ErReO_6, Ba_2TmReO_6 and Ba_2YbReO_6 remain paramagnetic between 2 and 300 K with effective magnetic moments which correlate closely with the expected values of the paramagnetic Ln^{3+} cations and Re^{5+} cations. Ba_2NdReO_6, Ba_2GdReO_6, Ba_2DyReO_6 and Ba_2HoReO_6 experience antiferromagnetic transitions at 100, 65, 70 and 27 K respectively, with no ZFC/FC divergence below T_N. All the samples show effective magnetic moments which are slightly lower than calculated which could insinuate some crystal field splitting occurs in the partially filled orbitals of the Ln^{3+} cations. Ba_2TbReO_6 is the most anomalous of all of the Ba_2LnReO_6 series with evidence of two separate transitions at 2.4 and 29 K, caused by respective ordering of the Re^{5+} and Tb^{3+} magnetic cations [190]. The strontium analogues show similar behaviours to these outlined [193].

The S = 1 spin state is seemingly more complex than the high spin states previously mentioned. When long-range antiferromagnetic order is achieved in the 3d transition metal systems it occurs at higher temperatures than in the S = 3/2 and S = 5/2 spin states. When the magnetic cation is a $4d^2$ or $5d^2$ cation the magnetic moments are suppressed, the result of significant spin orbit coupling. The materials also appear to be more complex; this is especially clear for Ba_2YReO_6 which has been suggested to enter a quadrupolar state which is not typically observed.

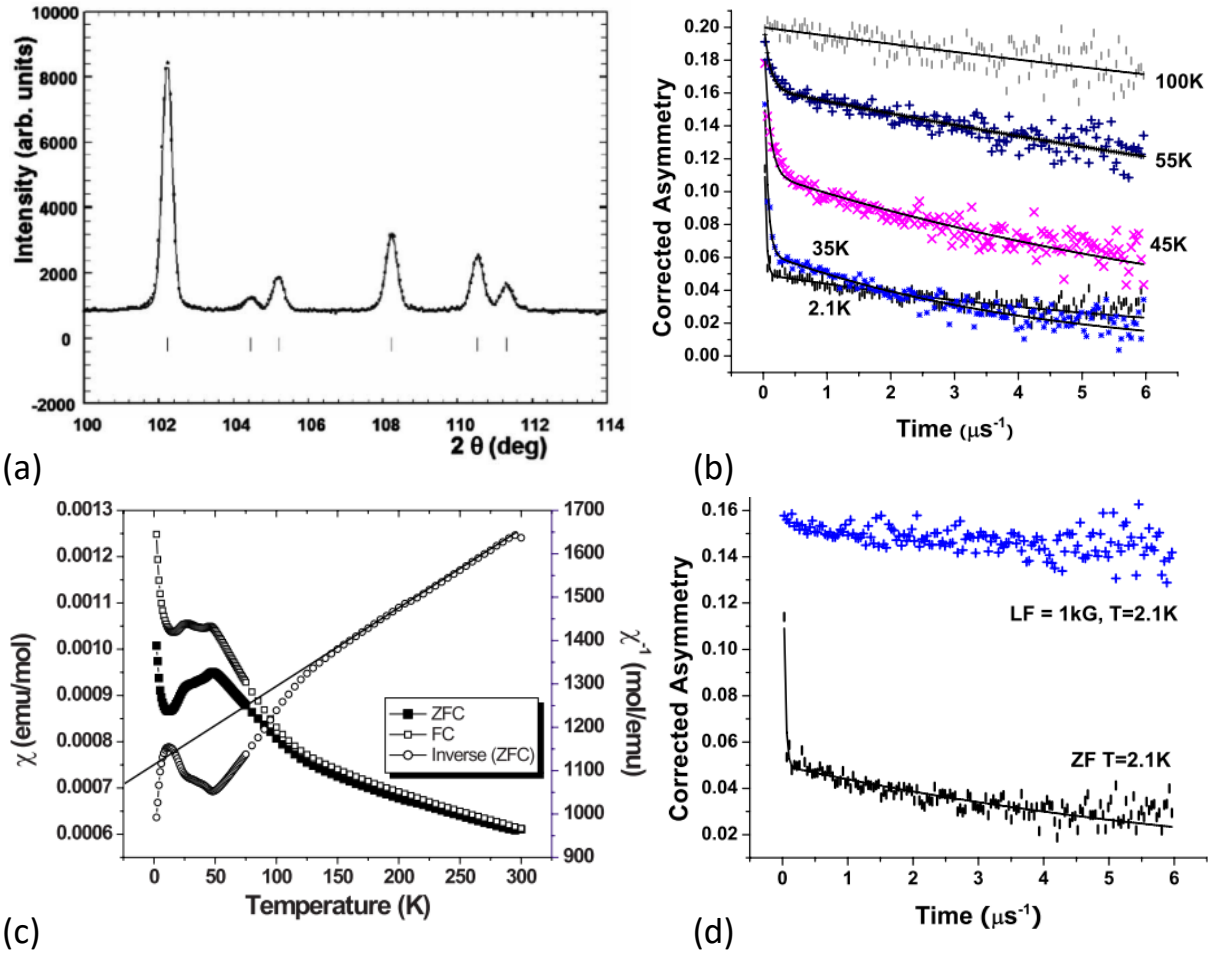

Figure 3.6: Structural and magnetic measurements carried out on Ba_2YReO_6. (a) Neutron powder diffraction data set, indicating that no additional magnetic Bragg peaks are observed in the structure. (b) Zero field muon spin relaxation measurements which are fitted to two exponentials. (c) DC-magnetometry which shows two transitions are observed. (d) Longitudinal field muon spin relaxation measurements which suggest that that material experiences spin freezing, as the full decoupling of the relaxation curve indicates that the spins are static [189].

S = 1/2

Cations which contain a sole unpaired electron allow the S = 1/2 spin state to be accessed. This spin state has a higher probability of novel quantum behaviour than the higher spin states. This is brought about by the quantum effects of the single cation, which through isolation can behave differently than a large group of cations. Although novel phases are more likely to be observed these are still incredibly rare and long-range magnetic order can still prevail within S = 1/2 materials.

Utilising Cu^{2+} ($3d^9$) can allow a hotbed of novel behaviour to take place. Cu^{2+} has a $t_{2g}^6e_g^3$ configuration which leads to strong Jahn-Teller distortions. Frustrated double perovskites which have been reported to contain Cu^{2+} take the form $(Ba, Sr)_2Cu(Mo, W, Te)O_6$, where the magnetic cations are connected by a square lattice. The strong Jahn-Teller distortion results in deviation from the *fcc* structure, typically to the tetragonal *I4/m* space group. Ba_2CuWO_6, Ba_2CuTeO_6, Sr_2CuMoO_6, Sr_2CuWO_6 and Sr_2CuTeO_6 experience long range order below 28, 16, 28, 24 and 29 K respectively [194–197]. The long-range magnetic order has been described to be Type II in molybdate and tungstate examples and Type I AFM ordering in the tellurates [198]. Inelastic neutron scattering and computational techniques indicate that four distinct magnetic exchange interactions are necessary to describe the magnetic behaviour of these systems. J_1 the NN interaction, J_2 the NNN, J_3 the interplanar NN and J_4 the NNN interplanar interaction. In those which adopt Type II antiferromagnetic ordering J_2 is significantly greater than J_1 with J_3 and J_4 tending to be significantly smaller. Both J_2 and J_4 indicate strong antiferromagnetic interactions within the systems [195,199,200]. Conversely, in Ba_2CuTeO_6 and Sr_2CuTeO_6, J_1 is the dominant interaction, with J_2, J_3 and J_4 all significantly smaller than the nearest neighbour Cu^{2+}-Cu^{2+} interaction [195,201].

Each of the $(Ba, Sr)_2Cu(Mo, W, Te)O_6$ double perovskites also displays two dimensional magnetic order [196,197,199,202]. This is observed through broad local maxima in the magnetic susceptibility and has been suggested to occur through spin ladders which span the structure. These short-range correlations have been investigated in Ba_2CuTeO_6 and are thought to take place due to competing thermal and quantum fluctuations [195,202–205]. This two dimensional magnetic behaviour has led to magnetic excitations being observed above the transition temperature in Sr_2CuWO_6 [200,206].

Solid solutions of $Sr_2Cu(W_{1-x}Mo_x)O_6$ were synthesised at ambient pressure when $0 \leq x \leq 0.6$ but higher pressures were required for $x \geq 0.7$. Each composition shows 2-dimensional magnetism but no 3D long-range antiferromagnetic order [207]. The $Sr_2Cu(W_{1-x}Te_x)O_6$ series has been suggested to behave like either a valence bond glass states or quantum spin liquid based on changes observed in the DC-

susceptibility from the parent phases [80–82]. $Sr_2CuW_{0.5}Te_{0.5}O_6$ has also been measured using muon spin relaxation measurements showing that spins remain dynamic down to 19 mK, a characteristic observed in quantum spin liquids [117]. It has also been reported that $Ba_2CuW_{0.5}Te_{0.5}O_6$ may experience potential spin liquid behaviour [195].

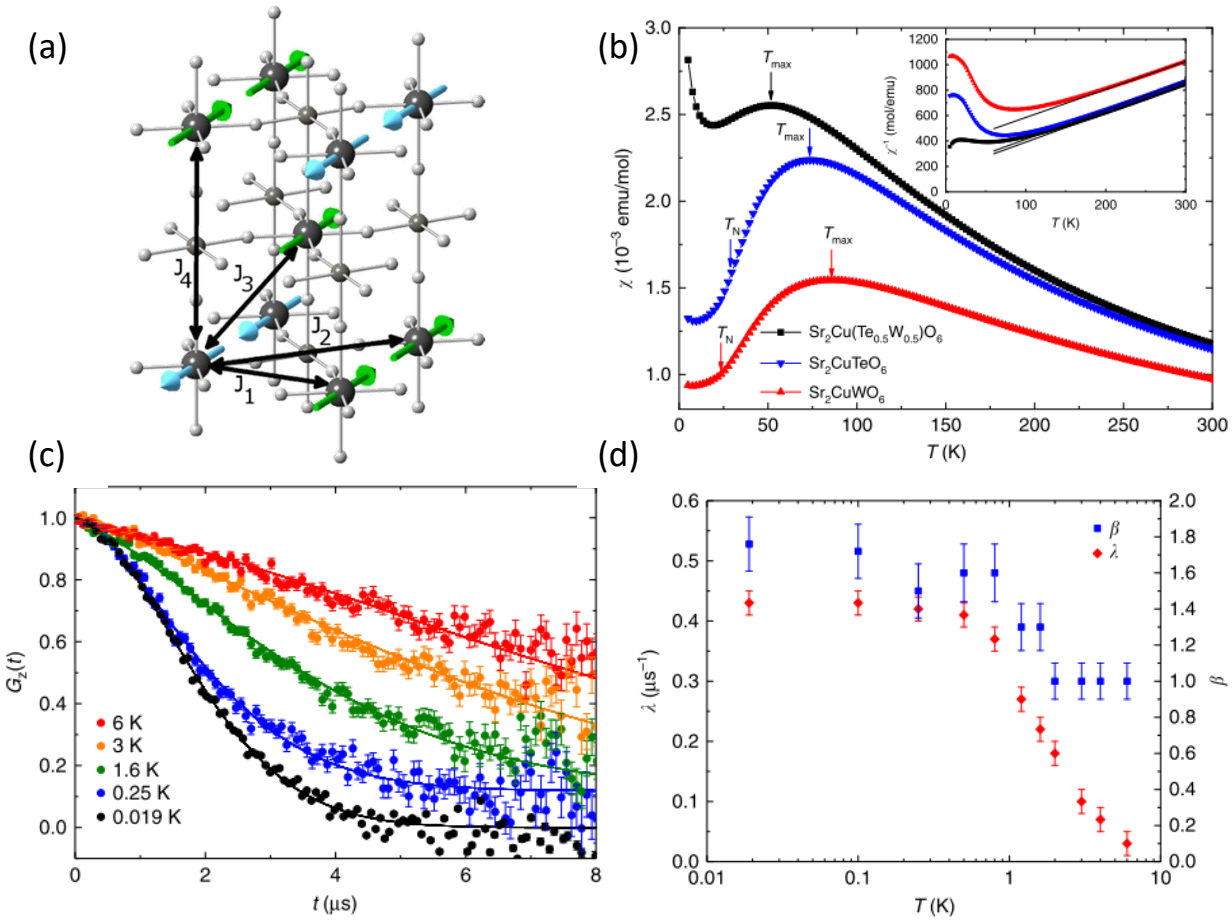

Figure 3.7: (a) Crystal structure of Ba_2CuTeO_6 with the exchange coupling constants outlined [202]. (b)Magnetic susceptibility of Sr_2CuWO_6, Sr_2CuTeO_6 and $Sr_2CuTe_{0.5}W_{0.5}O_6$ showing a change in the magnetic properties. (c) Zero field muon spin relaxation measurements completed on $Sr_2CuTe_{0.5}W_{0.5}O_6$ showing a distinct relaxation at 19 mK (d) The results of the zero field muon spin relaxation measurements collected on $Sr_2CuTe_{0.5}W_{0.5}O_6$, showing that the relaxation rate is plateaued from around 1 K, suggesting that this would not freeze at lower temperatures [117].

Table 3:1: Magnetic coupling constants of (Ba, Sr)$_2$Cu(Mo, W, Te)O$_6$

	AFM Type	**J_1**	**J_2**	**J_3**	**J_4**
Ba_2CuWO_6 [195]	II	-1.25	-14.71	0.05	0.03
Ba_2CuTeO_6 [195]	I	-23.65	0.13	1.28	-0.30
Sr_2CuMoO_6 [199]	II	-2.9	-8.68	-0.03	-5.05
Sr_2CuWO_6 [200]	II	-1.2	-9.5	0	-0.01
Sr_2CuTeO_6 [201]	I	-4.83	-0.18	0.75	-0.32

Mo^{5+} has also been keenly investigated due it its appearance in Sr_2FeMoO_6 and the fact it is a $4d^1$ cation and therefore, possesses strong electronic correlations [208]. Often the Mo^{5+} cation is paired with a lanthanide or rare earth cation as these are consistently in the +3-oxidation state stabilising the Mo^{5+} cation. The most widely researched of these is the proposed valence bond glass Ba_2YMoO_6.

Ba_2YMoO_6 is frustrated, crystallises as an *fcc* lattice and retains cubic symmetry to 2 K with no observed Jahn-Teller distortion [209]. The DC-susceptibility indicates no antiferromagnetic transition but contains two distinct Curie-Weiss regimes. The results of the analysis at high temperature yield effective magnetic moments which are close to the spin only value [210] or significantly suppressed [116] whilst experiencing very strong antiferromagnetic interactions. These differences could be the result of differences in the synthetic conditions, similarly to Sr_2FeMoO_6. The low temperature regime shows a large decrease in the effective magnetic moment and the Weiss constant falls to within error of zero [116]. A frequency dependent peak is observed in the imaginary response of the AC-susceptibility measurements. This peak spans the temperature range of 26 to 70 K but is not thought to be caused by a spin glass transition as the peak becomes sharper with increasing frequency and the opposite effect would be observed in a spin glass [116]. Both heat capacity and muon spin

relaxation measurements show no evidence of long range magnetic order [116,210]. Further investigation suggested that Ba_2YMoO_6 consisted of an amorphous array of non-magnetic singlets alongside residual isolated unpaired magnetic moments [211]. Inelastic neutron scattering identified a singlet to triplet transition which persisted up to 125 K, confirming the presence of these singlets [212]. This allowed the material to be described as a potential valence bond glass [213].

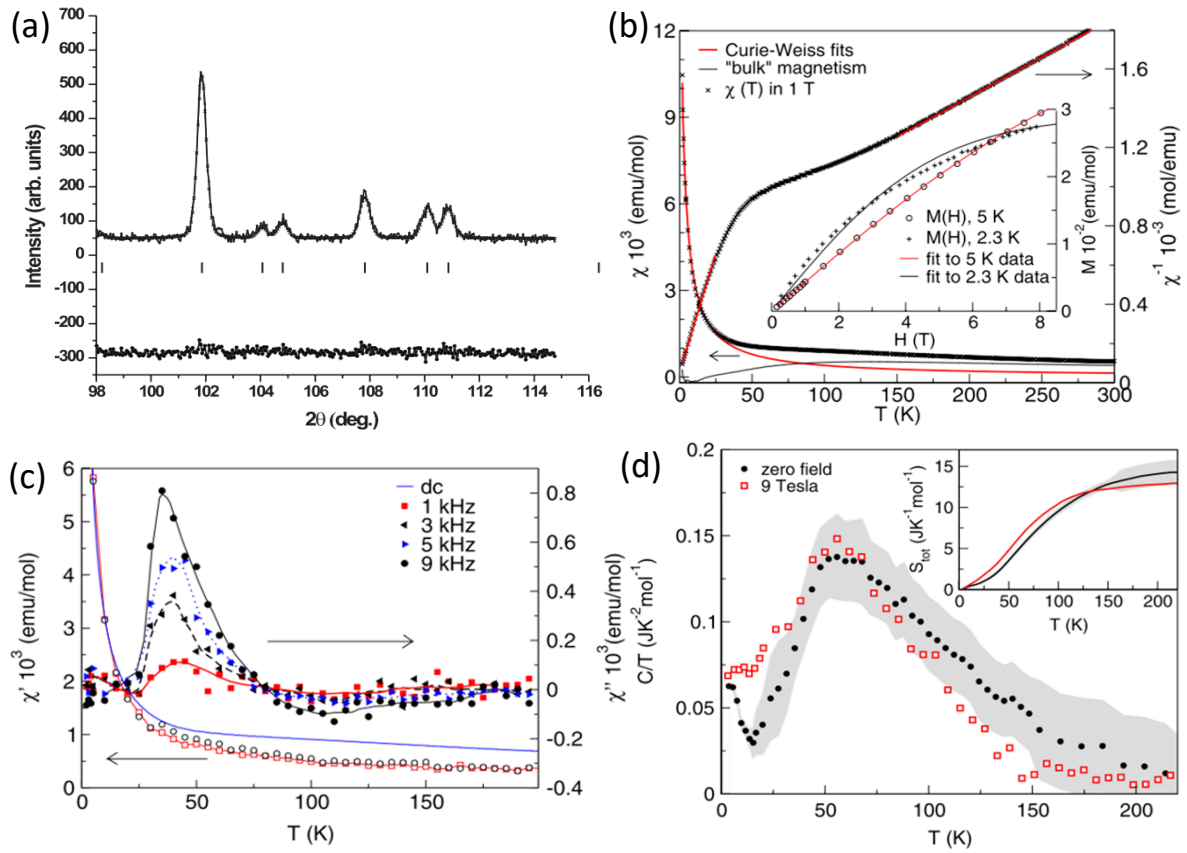

Figure 3.8: Measurements collected on Ba_2YMoO_6. (a) Neutron powder diffraction indicating the *fcc* nature of the structure. (b) DC-susceptibility measurements which show the two distinct regions of Curie-Weiss behaviour. (c) AC-susceptibility measurements which show the real and imaginary responses of the measurement. (d) Heat capacity which shows the slow release of entropy over a wide temperature range [116,210].

The solid solution $Ba_{2-x}Sr_xYMoO_6$ exhibited similar behaviour to Ba_2YMoO_6 when DC-magnetometry was measured bar Sr_2YMoO_6 which experiences a weak ferromagnetic transition around 8 K [214]. These experiments indicated that the valence bond glass state is fairly robust and persists despite a decrease in the symmetry of the magnetic lattice.

Ba_2LuMoO_6 has also been reported to potentially exhibit valence bond glass behaviour due to similarities with Ba_2YMoO_6 [215]. However, further research must be carried out to ascertain whether it enters a collective spin-singlet state with residual magnetic moments or valence bond glass phase.

The Ba_2LnMoO_6 (Nd, Sm, Eu, Gd, Dy, Er and Yb) series has also been investigated, these materials vary from the previous two examples as these contain two magnetic cations. Like Ba_2YMoO_6 and Ba_2LuMoO_6; Ba_2YbMoO_6 and Ba_2ErMoO_6 crystallise in the *fcc* lattice at ambient temperature and exhibit no structural or magnetic phase transition down to 2 K [209]. Further study on the $Ba_{2-x}Sr_xErMoO_6$ solid solution shows that progressive reduction in symmetry with reducing *A*-site cation size leads to antiferromagnetic ordering at $T \leq 4.0$ K for monoclinically distorted members of the $Ba_{2-x}Sr_xErMoO_6$ series [216]. Ba_2NdMoO_6 becomes antiferromagnetically ordered below 15(1) K, where both the Nd^{3+} and Mo^{5+} cations can arrange themselves. This antiferromagnetic transition is accompanied by a structural transition to the triclinic $I\bar{1}$ phase [209]. Both Ba_2SmMoO_6 and Ba_2EuMoO_6 have been reported to show antiferromagnetic transition temperatures of 130 K and 112 K respectively. These temperatures are significantly higher than other reported temperatures, which may be due to the fact these exhibit very strong superexchange interactions along the linear Mo-O-Sm/Eu-O-Mo path length [217]. Ba_2GdMoO_6 has been reported as a ferroelastic, experiencing strain caused by an external stressor. This is evidenced by a change in crystal structure from cubic to tetragonal at 220 K to the triclinic $I\bar{1}$ space group at 80 K [218].

As these examples show the spin state S = ½ produces more complex behaviour than the higher spin states. Long-range antiferromagnetic order can still be achieved in the materials however this often arises in conjunction with other interesting behaviour. Novel states and behaviour such as valence bond glasses, spin glasses such as Sr_2CaReO_6 and Sr_2MgReO_6 [219,220] and ferroelasticity can be achieved which are not exhibited in any of the higher spin states. Often it is found that these behaviours cannot be easily described using basic physics or chemistry and require a greater understanding of the quantum behaviour of the systems involved. Also, a wider variety and more

techniques are necessary to define the observed properties. The S = 1/2 double perovskites provide a rich environment to test these behaviours and therefore should continue to be examined.

This study has shown that double perovskites are ideal to analyse geometrical frustration. This structure supports a wide variety of magnetic and non-magnetic cations, allowing for a huge number of materials to be formed. *A*- and *M*-site substitution can readily be completed, which lets the magnetic properties be thoroughly tested. This has demonstrated that the higher spin states of S = 5/2 and S = 3/2 generally undergo antiferromagnetic transitions and that replacement of the *A*- and *M*-cations tends to have little effect on this. Conversely, lower spin states can exhibit novel properties and emerge into rare phases which are not observed in these higher spin states. In order to explore this further the research within this thesis will cover material which contain magnetic cations with the S = 5/2, 3/2 and 1/2 spin states.

The S = 5/2 system Ba_2MnWO_6, was revisited as previous reports included magnetic impurities and further investigation of the potential diffuse scattering has not been completed. By carrying out a thorough study of this material information about the exchange coupling constants, the magnetic structure and behaviour above the transition temperature can be gained. The S = 3/2 system Ba_2CoMoO_6 was also re-investigated. The purpose of this research is to further understand the magnetism of the structure, establish why the material does not behave like a Curie-Weiss paramagnet and discover the effects of the spin orbit coupling of the Co^{2+} ($4d^7$) cation. To gather this information the magnetic Co^{2+} cation will be substituted by diamagnetic Zn^{2+} to create the $Ba_2Co_{1-x}Zn_xMoO_6$ solid solution. Finally, the potential valence bond glass state of Ba_2LuMoO_6, (S = 1/2) will be investigated. Carrying out further measurements on this material will allow the role of quantum fluctuations to be more thoroughly investigated.

4. Long- and Short-Range Magnetism in Ba_2MnWO_6

Ba_2MnWO_6 is a *fcc* double perovskite which adopts a rock salt ordered arrangement of the Mn^{2+} and W^{6+} *M*-site cations [36,134]. The magnetic lattice is composed of Mn^{2+} cations which are present in the $3d^5$ electronic configuration which can achieve either high or low spin states. When in a high spin configuration, the d-orbitals are split into 3d $t_{2g}^3e_g^2$, S = 5/2 and when in a low spin state S = 1/2 is achieved with only one unpaired electron in the 3d t_{2g}^5. The high spin Mn^{2+} cation is octahedral experiencing no Jahn-Teller distortions, spin-orbit coupling nor anisotropy. The simplicity of the high spin Mn^{2+} cation, which is more favourable due to the half filled d-orbital, is ideal for studying frustrated magnetic behaviour.

Ba_2MnWO_6 was initially reported to remain cubic down to 4.5 K, with an antiferromagnetic transition at 7.5(10) K. The magnetic structure is a Type II antiferromagnet with propagation vector $\boldsymbol{k}$ = (1/2, 1/2, 1/2) and Mn^{2+} moments aligned perpendicular to the (111) direction. Calculation of the effective magnetic moment (μ_{eff}) indicated that this was slightly lower than anticipated for the high spin Mn^{2+} ion, but conclusively determined that Ba_2MnWO_6 was present in the high spin state as this is much higher than would be anticipated for S=1/2 system [135].

A further study agreed fairly closely with the initial report, however, a G-type antiferromagnetic structure with canted antiferromagnetism was hypothesised. This study also suggests that diffuse magnetic scattering is observed above the transition temperature. The two bodies of work deviate when the latter reported a ferromagnetic transition between 43 and 45 K [221]. As this is not observed in both studies there is potential that this is the result of a small ferromagnetic impurity such as Mn_3O_4 which is present in such a small quantity that this cannot be observed in either the X-ray or neutron diffraction studies [137,138,221].

Diffuse scattering above the transition temperature could suggest short range magnetic behaviour within Ba_2MnWO_6. This allows comparisons to be drawn to MnO, which has recently been shown to enter a short-range magnetically correlated state above T_N. MnO is a frustrated *fcc* lattice which also

achieves Type II antiferromagnetic order with propagation vector $\boldsymbol{k}$ = (1/2, 1/2, 1/2). In MnO, Mn^{2+} cations are ferromagnetic within (111) planes but adjacent (111) planes are aligned antiparallel to each other [127,131,132]. The short-range magnetic correlations within MnO are suggested to be the result of small domains of magnetic moments which remain strongly interacted even above the transition temperature [133].

The purpose of this study is to further investigate the magnetic properties of Ba_2MnWO_6. Previous investigations into this material have suggested a short-range correlated state which has not been further explored. Recently, a number of materials have been observed to experience these interactions and further investigation into this shall allow greater insight into the frustrated behaviour of *fcc* lattices [222,223].

Experimental

Stoichiometric quantities of $BaCO_3$, MnO_2 and WO_3 were used to synthesise approximately 8 g of Ba_2MnWO_6 using solid-state synthesis. Calcination was completed at 800 °C for 24 hours and further heating was carried out at 1250 °C in a reducing atmosphere of 5% H_2/N_2. Ba_2MnWO_6 was synthesised when an olive-green powder had formed. X-ray powder diffraction was completed utilising a Cu Kα source over the 2θ range 10-75 °, using a step size of 0.01 °.

Time-of-flight neutron powder diffraction was completed on GEM, the GEneral Materials diffractometer at the ISIS Neutron and Muon Source, Rutherford Appleton Laboratories based in Didcot, Oxfordshire, UK [224]. This was carried out to gain an accurate picture of both the low temperature nuclear and magnetic structures of Ba_2MnWO_6. The sample was densely packed into an 8 mm vanadium can. Absorption corrections were carried out on the data. Rietveld refinement was completed using GSAS, the General Structure Analysis System [225]. The Time-of-flight peak shapes have an intrinsic asymmetry brought about by the neutron pulse, which was described using a convolution of the Ikeda-Carpenter and Pseudo-Voigt functions. Background features were

characterised using a shifted Chebyshev function. The magnetic form factor was taken from the neutron data booklet [226]. All refinements were completed on detector banks 2 – 6.

Thermal dependent magnetic susceptibility measurements were carried out using the Quantum Design MPMS3 based at the Materials Characterisation Laboratory, Rutherford Appleton Laboratories. These measurements were carried out between 2 and 300 K using techniques previously outlined.

Muon spin relaxation (μSR) measurements assessed the local magnetic behaviour of Ba_2MnWO_6. These were carried out using EMU, based at the ISIS Neutron and Muon Source where measurements were carried out in zero, transverse and longitudinal fields (ZF, TF and LF respectively) [227]. ZF-μSR measurements were carried out between 2 and 30 K . TF-μSR was utilised to accurately pinpoint the Néel temperature between 1.6 and 70 K using a field strength of 100 G. LF-μSR was carried out at various temperatures using field strengths ranging from 5 to 4000 G. To prepare for the experiment, Ba_2MnWO_6 was firmly packed into silver foil and then placed into a silver sample holder. All μSR measurements were analysed and functions were fitted using the Mantid software [108].

Inelastic neutron scattering measurements (INS) were completed to calculate the magnetic exchange coupling constants, J_1 and J_2. This was measured using the Time-of-flight direct geometry spectrometer LET at the ISIS Neutron and Muon Source [112]. Ba_2MnWO_6 was decanted into an aluminium can of 10 mm diameter and 30 mm height with helium exchange gas. A helium cryostat was used to cool the sample environment. An incident neutron energy of 3.7 meV was used and each measurement was collected for 3 hours at temperatures between 2 and 100 K. The data was corrected for detector efficiency plus the time independent background and was then reduced using Mantid [108,109]. Linear spin wave theory was used to simulate the data set collected at 2 K [228].

Results

X-ray Powder Diffraction

X-ray powder diffraction indicated that the sample of Ba_2MnWO_6 was phase pure, with no impurity peaks present. At ambient temperature Ba_2MnWO_6 crystallises in the high symmetry space group $Fm\bar{3}m$ which agrees with previous reports.

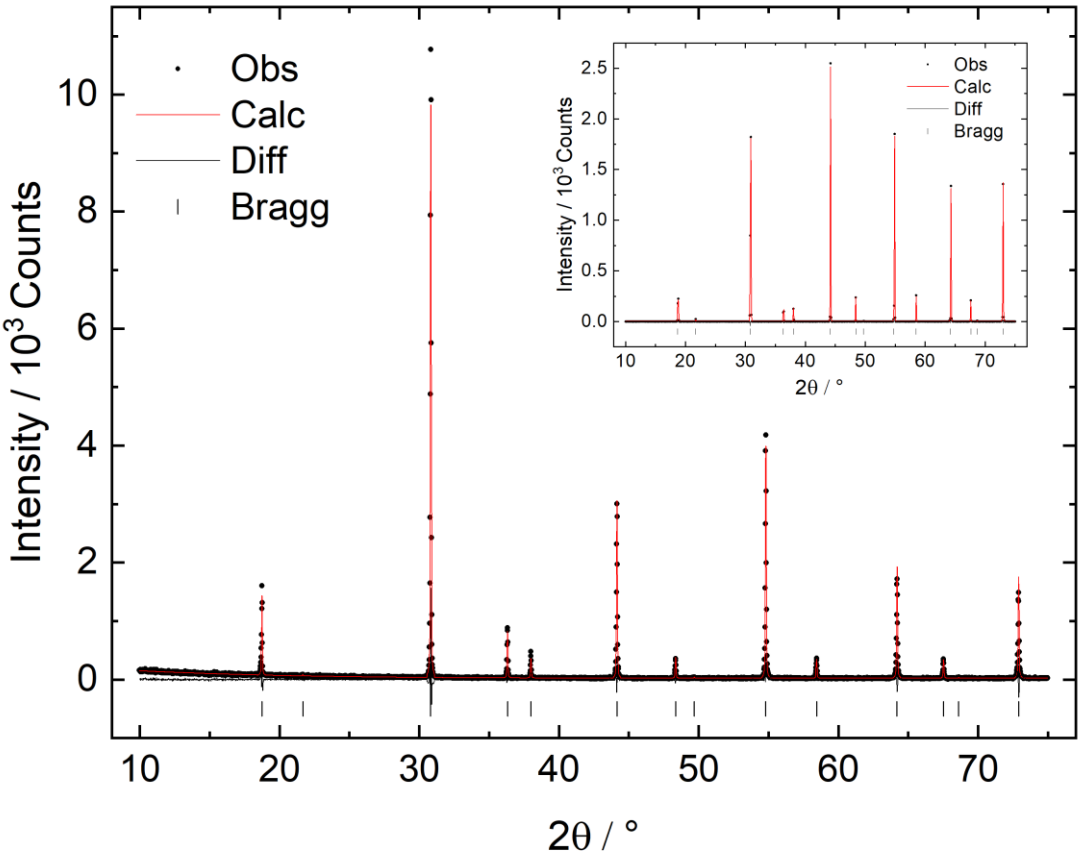

Figure 4.1: Rietveld refinement of X-ray powder diffraction measurements carried out on $BaMnWO_6$. The inset shown is a dummy histogram collected from a reference from the ICSD which indicates the phase purity of the synthesised sample. All peaks are accounted for and no extraneous peaks are observed.

Neutron Powder Diffraction

At 69(2) K Ba_2MnWO_6 retains $Fm\bar{3}m$ symmetry, as shown in Figure 4.2. Throughout this chapter, neutron powder diffraction from detector bank 4 will be displayed in figures. This detector bank was chosen as it has a wide d-space range as well as a relatively high peak resolution. At 2.1(2) K, there was no evidence of peak broadening or splitting confirming the retention of the cubic structure as previously stated. The structure generally abides by conventional thermal expansion as the lattice

parameters and volume increase with temperature. However, around 9.1(2) K a change is observed in the gradient of the lattice parameter. Around 5 K, the lattice parameter is minimised followed by a slight increase as the temperature decreases to 2 K. The thermal evolution of the lattice parameter is shown in Figure 4.3.

At 8.2(2) K, additional Bragg peaks which do not comply with the $Fm\bar{3}m$ space group emerge in the diffraction pattern. These occur in highest intensity at larger d-space with a definite form factor and therefore were characterised as magnetic Bragg peaks. These peaks were indexed using the magnetic propagation vector, $\boldsymbol{k}$ = (1/2, 1/2, 1/2), which corresponds to a magnetic unit cell which is eight times bigger than the nuclear unit cell. The magnetic lattice parameter (a_{mag}) can be calculated by doubling the nuclear lattice parameter (a_{nuc}) in all three directions. The thermal evolution of the magnetic Bragg peaks can be observed in Figure 4.4.

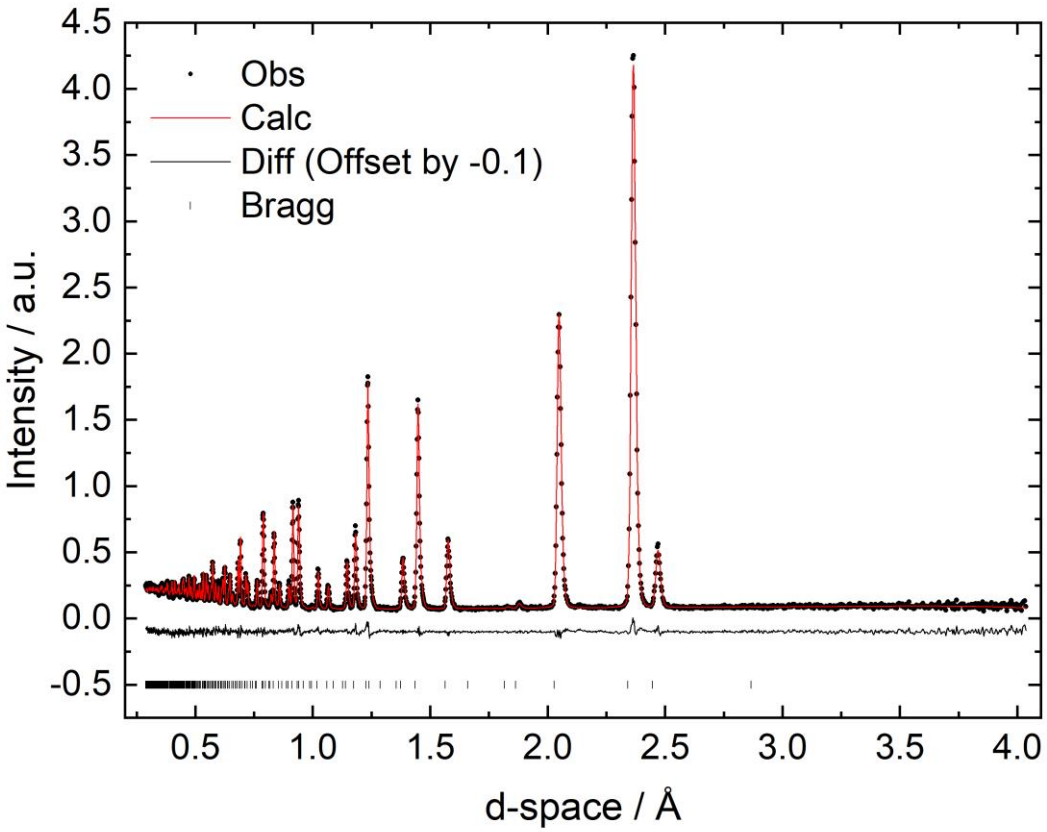

Figure 4.2: Rietveld refinement of neutron powder diffraction measurements collected on Ba_2MnWO_6 at 69(2) K. This is taken from detector bank 4. The Bragg reflections correspond to the space group $Fm\bar{3}m$. The difference curve is offset by -0.1 so it can be clearly observed. The peaks are well fitted by the cubic space group with only minor differences observed between the experimental data sets and the calculated model.

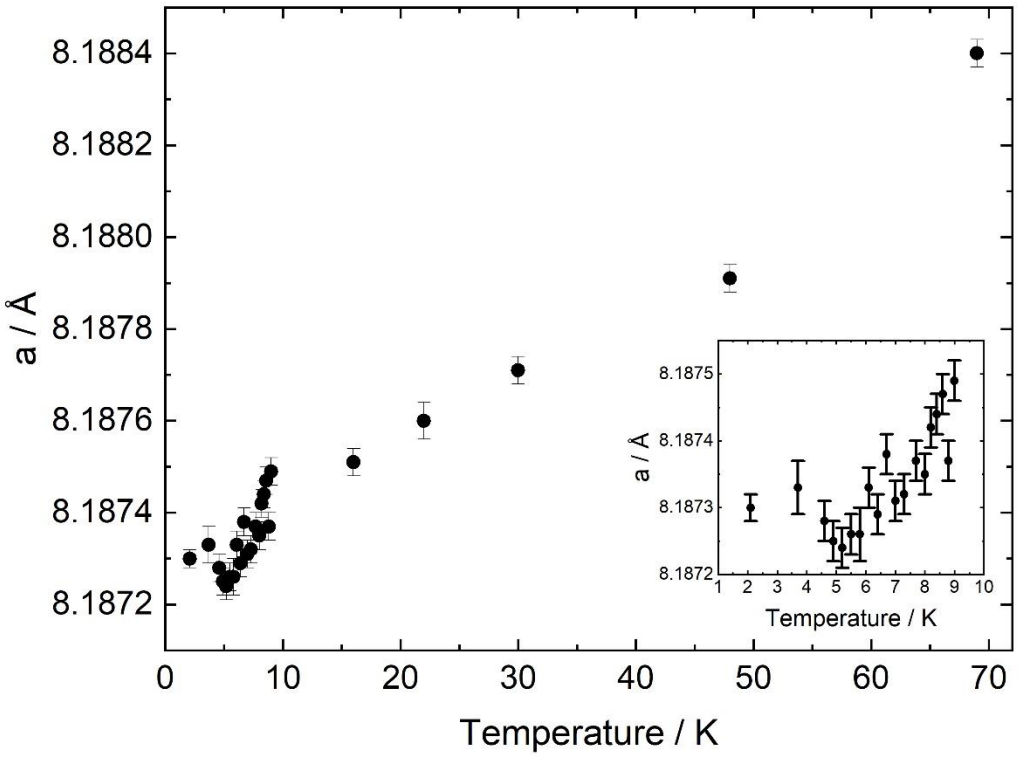

Figure 4.3: Thermal evolution of the lattice parameter of Ba_2MnWO_6 between 2 and 69 K. Generally, conventional thermal expansion properties are observed. A distinct change in slope occurs at 9.1(2) K and below. The inset image shows the thermal evolution of the lattice parameter between 2 and 10 K.

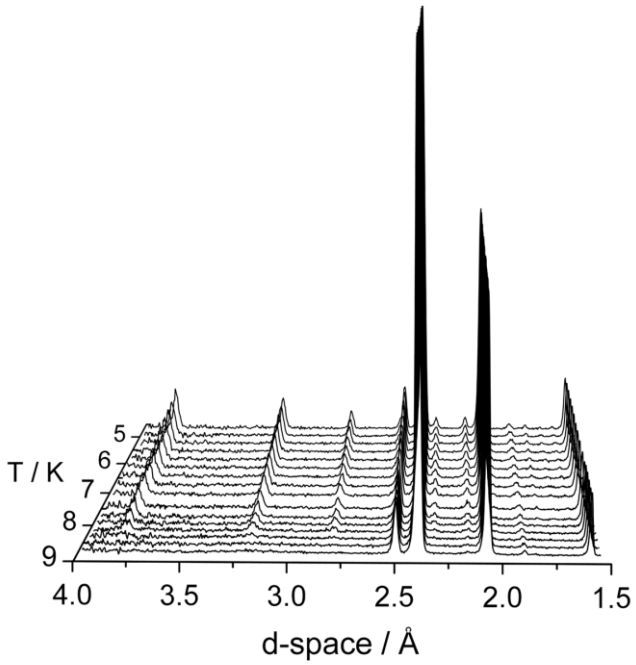

Figure 4.4: The thermal evolution of the neutron diffraction pattern collected on Ba_2MnWO_6 between 4.7(2) K and 8.8(2) K and 1.5 Å and 4.0 Å. The neutron diffraction pattern is taken from detector bank 4. This figure shows the intensity of both the nuclear and magnetic Bragg peaks against both temperature and d-space. The large peaks which remain roughly constant throughout the temperature range are attributed to nuclear Bragg peaks, whilst those which begin to emerge at 8.2(2) K arise due to the onset of long-range antiferromagnetic order.

The magnetic structure of Ba_2MnWO_6 was characterised using both GSAS and FULLPROF software, to assess the potential of three different magnetic structure possibilities; the Ising spin model, a non-collinear model previously outlined for $Ba_2Nd_{0.05}Mn_{0.95}MoO_6$ and the magnetic model reported for the archetypical *fcc* lattice MnO [127,131,144,229]. The Ising spin model had previously been outlined for the similar material Ba_2MnMoO_6 and this was thought to be a good initial start due to the slight differences between the two systems. Also, as the Ba_2MnWO_6 sample is a powder, the direction cannot be accurately determined from Rietveld refinement [144]. Similarly, the non-collinear G-type model reported for $Ba_2Nd_{0.05}Mn_{0.95}MoO_6$ was used as this was thought to be very close to Ba_2MnWO_6 as only 5% of the Mn^{2+} cations were substituted by the Nd^{3+} cation and hence it was believed that this may be a reasonable starting model for Ba_2MnWO_6 [229]. The final proposed model of MnO was used as this is frustrated and contains an *fcc* lattice of interconnecting high spin (S = 5/2) Mn^{2+} cations, which is remarkably similar to what is observed in Ba_2MnWO_6 [127,131,132]. A fourth model where the magnetic moments were aligned with the [111] direction was used, however, this calculated zero intensity for the first observed magnetic Bragg peak and therefore was discounted.

FULLPROF was used for preliminary refinements to test the potential of each model as the magnetic structure of Ba_2MnWO_6, whilst the full refinement was completed using the GSAS software [225,230]. The k-search function of FULLPROF confirmed the propagation vector of $\boldsymbol{k}$ = (1/2, 1/2, 1/2). The BasIReps function then reported the potential irreducible representations which describe the relation of the magnetic moments and symmetry of the magnetic unit cell. Using this it was found that only one equivalent Mn^{2+} cation was represented within the magnetic unit cell. A preliminary refinement then gave some indication into the best option.

GSAS was then used to fit each of the models using a modified technique of that reported by Cui and Toby [231]. This first required the nuclear phase to be modelled. This was completed using the 69(2) K data set and was transferred down each temperature until 2.1(2) K. Each magnetic model was then added as a secondary phase. The models were fitted using the triclinic space group *P1*, utilising this

low symmetry space group allows all the potential magnetic reflections to be observed. Each of the 32 magnetic Mn^{2+} cations were then added to the refinement, the coordinates of which can be observed in Table 4:1. Due to the low symmetry of the P1 space group, all 32 had to be inputted separately as any equivalence from the cubic system was lost. The vectors of the magnetic moments were also given to the model. Once this is carried out the thermal displacement potentials of Mn^{2+} and the profile coefficients were constrained within the nuclear and magnetic phases so they both refined to identical values. The magnetic phase fraction was set to 0.125 in each detector bank as the magnetic structure is eight times larger than the nuclear structure. The lowest resolution Histogram was then removed from the Rietveld refinement, due to poor signal to noise ratio. After the initial set-up of the model, the refinements could be completed. The Mn^{2+} thermal displacement factors and profile coefficients, σ_1 and γ_1, were then refined. Finally, the magnetic phase fraction was refined. The results of the MnO refinement at 2.1(2) K is shown in Figure 4.5, this gave the best fit to the data sets, characterising both the nuclear and magnetic Bragg peaks better than either of the other two models. The statistics for the refinement of each model can be found in Table 4:2.

Table 4:1: The position of the Mn^{2+} cations and the direction of the magnetic moment vectors for each model applied to the neutron powder diffraction data set completed on Ba_2MnWO_6.

Mn^{2+} Position	**Ising Model Magnetic Vector**	**Non-Collinear Model Magnetic Vector**	**MnO Model Magnetic Vector**
(0, 0, 0)	(2, 0, 0)	(2, 2, 2)	(1, 1, -2)
(0, 0, 0.5)	(-2, 0, 0)	(-2, -2, -2)	(-1, -1, 2)
(0, 0.25, 0.25)	(-2, 0, 0)	(2, -2, -2)	(-1, -1, 2)
(0, 0.25, 0.75)	(2, 0, 0)	(-2, 2, 2)	(1, 1, -2)
(0, 0.5, 0)	(-2, 0, 0)	(-2, -2, -2)	(-1, -1, 2)

(0, 0.5, 0.5)	(2, 0, 0)	(2, 2, 2)	(1, 1, -2)
(0, 0.75, 0.25)	(2, 0, 0)	(-2, 2, 2)	(1, 1, -2)
(0, 0.75, 0.75)	(-2, 0, 0)	(2, -2, -2)	(-1, -1, 2)
(0.25, 0, 0.25)	(-2, 0, 0)	(2, -2, 2)	(-1, -1, 2)
(0.25, 0, 0.75)	(2, 0, 0)	(-2, 2, -2)	(1, 1, -2)
(0.25, 0.25, 0)	(-2, 0, 0)	(2, 2, -2)	(-1, -1, 2)
(0.25, 0.25, 0.5)	(2, 0, 0)	(-2, -2, 2)	(1, 1, -2)
(0.25, 0.5, 0.25)	(2, 0, 0)	(-2, 2, -2)	(1, 1, -2)
(0.25, 0.5, 0.75)	(-2, 0, 0)	(2, -2, 2)	(-1, -1, 2)
(0.25, 0.75, 0)	(2, 0, 0)	(-2, -2, 2)	(1, 1, -2)
(0.25, 0.75, 0.5)	(-2, 0, 0)	(2, 2, -2)	(-1, -1, 2)
(0.5, 0, 0)	(-2, 0, 0)	(-2, -2, -2)	(-1, -1, 2)
(0.5, 0, 0.5)	(2, 0, 0)	(2, 2, 2)	(1, 1, -2)
(0.5, 0.25, 0.25)	(2, 0, 0)	(-2, 2, 2)	(1, 1, -2)
(0.5, 0.25, 0.75)	(-2, 0, 0)	(2, -2, -2)	(-1, -1, 2)
(0.5, 0.5, 0)	(2, 0, 0)	(2, 2, 2)	(1, 1, -2)
(0.5, 0.5, 0.5)	(-2, 0, 0)	(-2, -2, -2)	(-1, -1, 2)
(0.5, 0.75, 0.25)	(-2, 0, 0)	(2, -2, -2)	(-1, -1, 2)
(0.5, 0.75, 0.75)	(2, 0, 0)	(-2, 2, 2)	(1, 1, -2)

(0.75, 0, 0.25)	(2, 0, 0)	(-2, 2, -2)	(1, 1, -2)
(0.75, 0, 0.75)	(-2, 0, 0)	(2, -2, 2)	(-1, -1, 2)
(0.75, 0.25, 0)	(2, 0, 0)	(-2, -2, 2)	(1, 1, -2)
(0.75, 0.25, 0.5)	(-2, 0, 0)	(2, 2, -2)	(-1, -1, 2)
(0.75, 0.5, 0.25)	(-2, 0, 0)	(2, -2, 2)	(-1, -1, 2)
(0.75, 0.5, 0.75)	(2, 0, 0)	(-2, 2, -2)	(1, 1, -2)
(0.75, 0.75, 0)	(-2, 0, 0)	(2, 2, -2)	(-1, -1, 2)
(0.75, 0.75, 0.5)	(2, 0, 0)	(-2, -2, 2)	(1, 1, -2)

Table 4:2: Magnetic structure of Ba_2MnWO_6 - Comparison of statistical parameters obtained from the Rietveld refinement carried out on the 2 K data set.

Bank	**Ising Model R_{WP}**	**Non-Collinear Model R_{WP}**	**MnO Model R_{WP}**
Overall	5.23	4.57	4.52
2	9.36	5.72	5.52
3	5.94	5.00	4.40
4	4.86	4.41	4.35
5	4.86	4.69	4.67
6	3.56	3.54	3.55

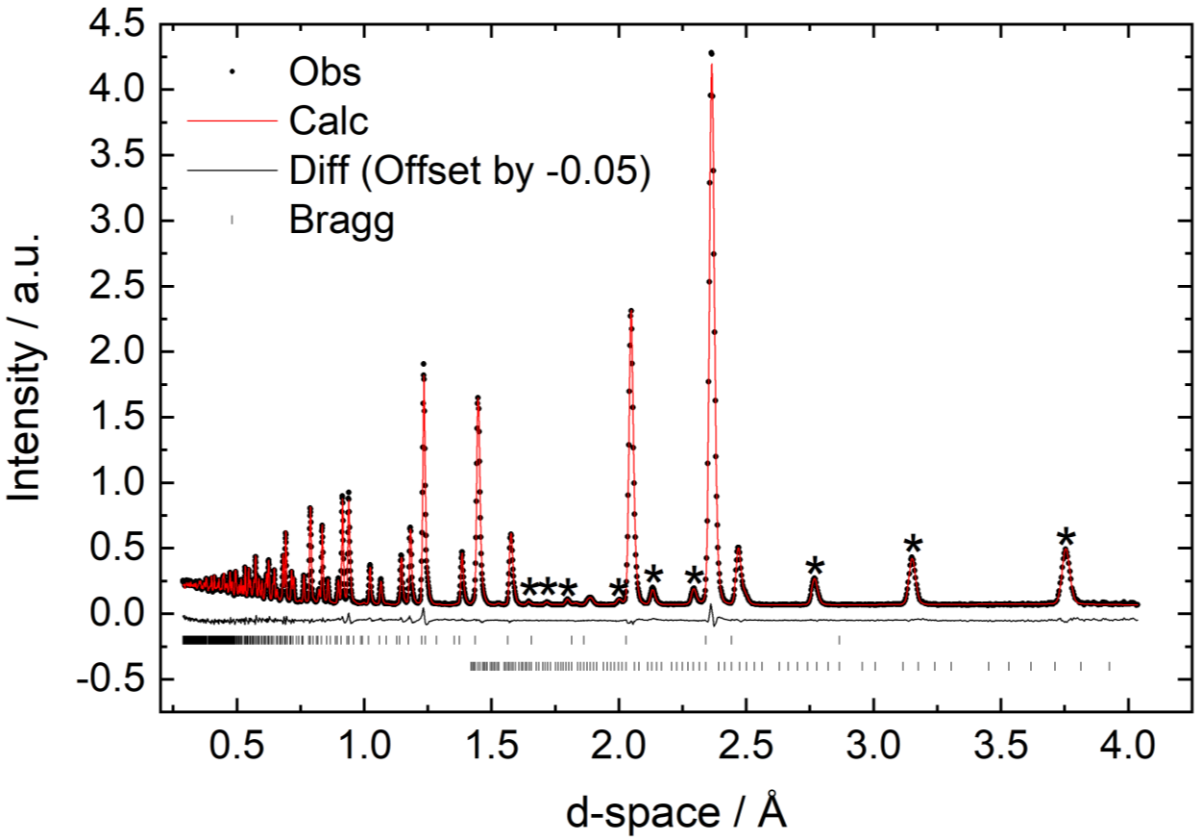

Figure 4.5: The results of Rietveld refinement carried out against the neutron powder diffraction data set collected on Ba_2MnWO_6 at 2.1(2) K. The upper row of Bragg reflections corresponds to the $Fm\bar{3}m$ nuclear structure whilst the lower row are attributed to the antiferromagnetic structure fitted using the triclinic P1 space group. The difference curve has been offset by -0.05.. The histogram shown is from detector bank 4 of the Time-of-flight data sets. The asterisks (*) outline the magnetic Bragg peaks.

The magnetic model of MnO is composed of Mn^{2+} magnetic moments ferromagnetically aligned within (111) planes. Within this structure, the adjacent (111) planes are aligned antiparallel to each other resulting in ferromagnetic sheets which arise from the frustrated nature of the *fcc* lattice. Despite the frustration, antiferromagnetic long-range order occurs within Ba_2MnWO_6 below 8.2(2) K. Both the nuclear and magnetic structures are depicted in Figure 4.6 (a) and (b) respectively. Figure 4.6 (b) indicates the magnetic exchange coupling constants J_1 and J_2, which are attributed to the nearest neighbour (NN) and next nearest neighbour (NNN) interactions respectively, this shows only the Mn^{2+} cations. The J_1 interactions are frustrated as not all are antiferromagnetic whilst the next nearest neighbour (J_2) interactions are all able to be antiferromagnetic.

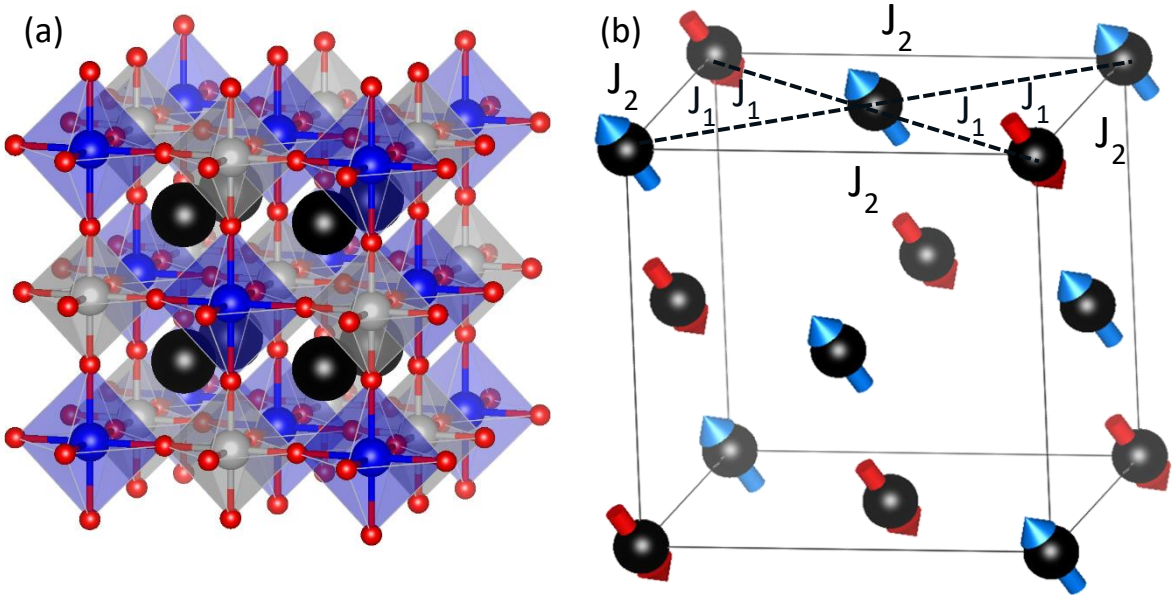

Figure 4.6: (a) A representation of the nuclear structure of Ba_2MnWO_6; the large black spheres correspond to Ba^{2+} cations, the grey and blue spheres to the Mn^{2+} and W^6 cations and the red spheres represent the O^{2-}anions. Ba_2MnWO_6 crystallises in the *fcc* space group $Fm\bar{3}m$. (b) This shows a small proportion of the proposed magnetic structure of Ba_2MnWO_6, the unit cell is not shown in entirety for the ease of the reader. Each sphere corresponds to a Mn^{2+} cation with a red or blue arrow which corresponds to antiparallel configuration within the magnetic unit cell. The magnetic exchange coupling constants are outlined as J_1 or J_2 on this, J_1 is attributed to the NN interactions and J_2 corresponds to the NNN interactions.

The atomic and magnetic parameters from the refinement of the nuclear and magnetic structure of Ba_2MnWO_6 at 2 K can be found in Table 4.3. This refinement yielded the lattice parameter 8.18730(2) Å, the Ba^{2+}, Mn^{2+} and W^{6+} cations all sit on special positions and the oxide anion sits on (0.26519(3), 0, 0) in agreement with earlier studies [221]. Bond valence sum calculations completed on each of the cations showed that the Ba^{2+} cation was slightly overbonded with a BVS equal to 2.32. Mn and W cations are present in the +2 and +6 oxidation states, and antisite disorder between the two ions was less than 1 %. This is unsurprising due to the large difference between both the charge and ionic radii of Mn^{2+} and W^{6+}. The fractional occupancy of the oxide anion refined to within error of 100%.

The effective magnetic moment of Ba_2MnWO_6 at 2 K was calculated using the following equation;

Equation 4.1: Calculating the ordered magnetic moment from neutron powder diffraction data

$$\mu_{ord} = \sqrt{(\mu_{ref})^2 \left(\frac{PF_{ref}}{PF_{act}}\right)}$$

In this equation μ_{ord} is the ordered magnetic moment of the Mn^{2+} cations, μ_{ref} is the magnetic moment inputted into the refinement, PF_{ref} is the refined phase fraction of the magnetic phase and PF_{act} is the phase fraction of the magnetic phase related to the nuclear phase. Using this method μ_{ord} = 4.5(1) $\mu_{B,}$ corresponding closely with previous reports of 4.2(1) μ_B [135]. The value is slightly lower than the theoretical magnetic moment of μ_{th} = gS = 5 μ_B, however, this is regularly observed in practice due to covalency between the metal and oxygen centres. The covalent nature of the bond causes the distance between the metal centres to be large, orbital overlap to be reduced and therefore the magnetic interaction to be weaker and therefore the ordered magnetic moment to be smaller than the theoretical value [232,233]. The thermal evolution of μ_{ord} is shown in Figure 4.7

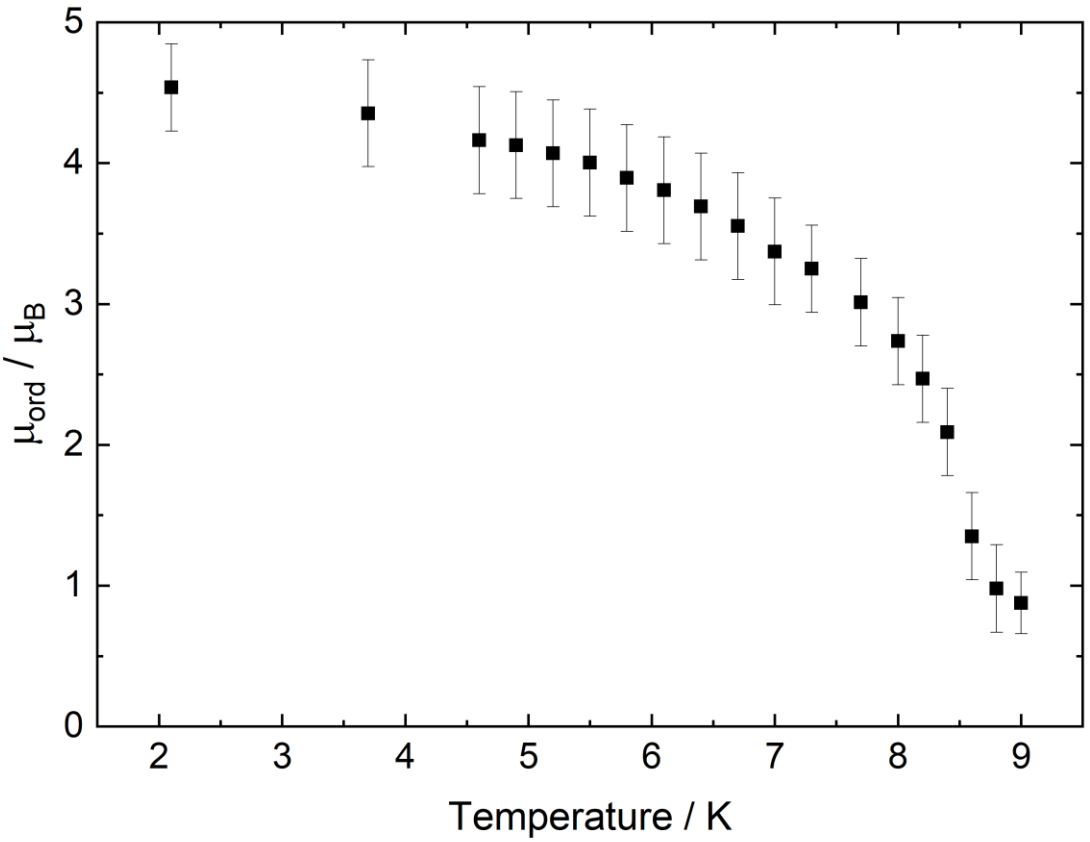

Figure 4.7: The thermal evolution of Mn^{2+} μ_{ord} in Ba_2MnWO_6., calculated from Rietveld refinement. The maximum μ_{ord} is established at 2 K as the AFM state accumulates. As the temperature increases μ_{ord} drops off. Diffuse scattering is observed in detector bank 2 above 8.4 K which affects the drop off of the magnetic moment, so it does not fall directly to zero.

The drop off was initially used to calculate the critical exponent of the Mn^{2+} magnetic cation. The critical exponent determines the magnetic transition temperature and the magnetic behaviour of the

cations, outlining whether they exhibit Ising spins or 3D Heisenberg magnetic moments. Ising spins are fixed in 1D, typically along one of the unit cell axes. Heisenberg magnetic moments have the freedom to lie anywhere in 3-dimensions which can result in non-collinear behaviour [234]. Unfortunately, this fit gave no conclusive results as the neutron powder diffraction was not carried out at enough temperatures close to the magnetic transition.

Table 4:3: Nuclear and magnetic parameters obtained from the Rietveld refinement of Ba_2MnWO_6 at 2 K, using the magnetic structure of MnO. Ba resides on (1/4, 1/4, 1/4), Mn on (0, 0, 0) and W on (1/2, 1/2, 1/2).

Parameter / Unit	**Value (e.s.d.)**
a / Å	8.18730(2)
Ba 100U_{iso} / Å^2	0.16(1)
Mn 100U_{iso} / Å^2	0.26(2)
W 100U_{iso} / Å^2	0.08(1)
O position	(0.26519(3), 0, 0)
O 100U_{iso} / Å^2	0.392(6)
Ba-O bond length / Å	2.897(1)
Ba BVS	2.32
Mn-O bond length / Å	2.171(3)
Mn BVS	2.14
W-O bond length / Å	1.923(1)
W BVS	5.98

DC-Susceptibility

Figure 4.8 shows the DC-susceptibility measurements were carried out in ZFC/FC modes between 2 and 300 K, as shown in. This measurement indicated an antiferromagnetic transition at 8.4(2) K. The susceptibility then falls towards zero as the magnetic moments begin to cancel each other out. No ZFC/FC divergence was observed. Curie-Weiss behaviour was observed between 100 and 300 K and the reciprocal susceptibility response remains clearly linear throughout this temperature regime. Curie-Weiss analysis yielded; C_{CW} = 4.91(1) cm^3 K mol^{-1}, θ_{CW} = -63(1) K and μ_{eff} = 6.3(3) μ_B. This value corresponds well with the spin-only magnetic moment of the S=5/2 Mn^{2+} cation of μ_{SO} = 5.9 μ_B, which indicates that Mn^{2+} is in its high spin state. Dividing θ_{CW} by the transition temperature allows the frustration index to be calculated, f = 8(1). Therefore, Ba_2MnWO_6 is moderately frustrated.

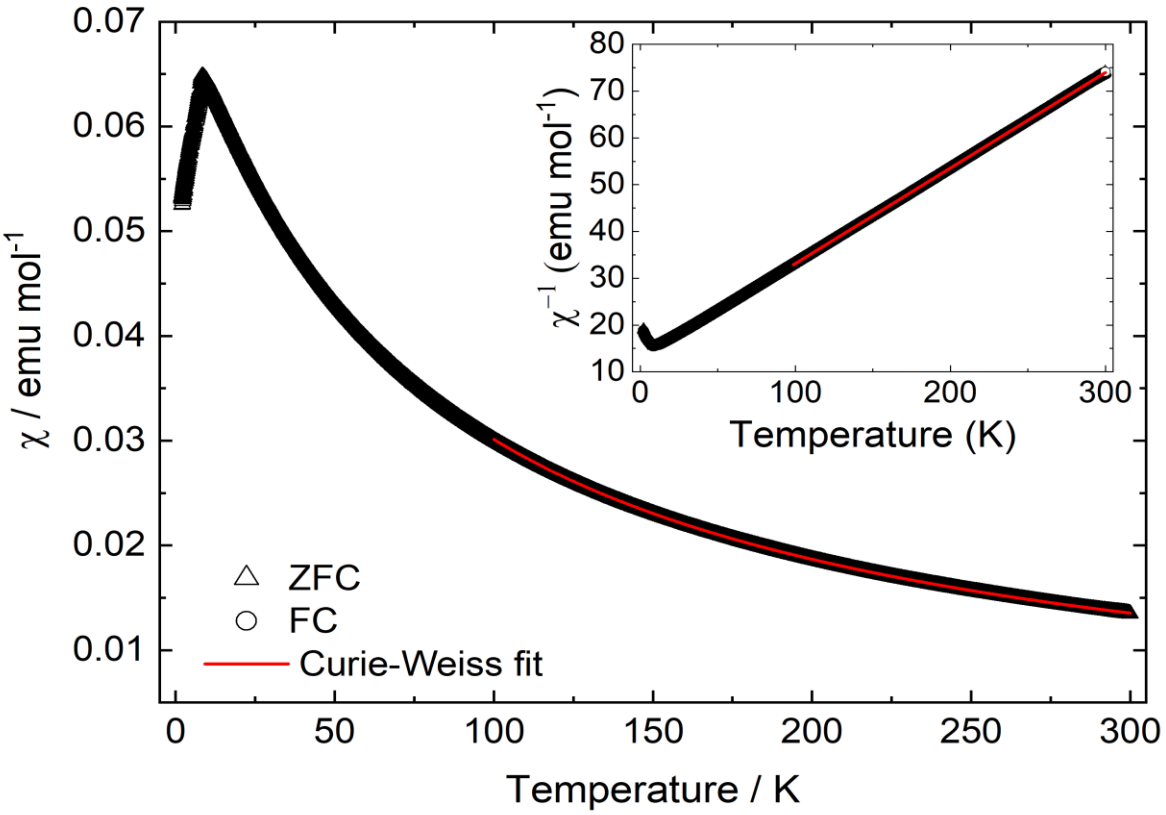

Figure 4.8: DC-susceptibility measurements collected on Ba_2MnWO_6 between 2 and 300 K. The main graph shows the susceptibility response against temperature whilst the inset indicates the reciprocal susceptibility against temperature. No ZFC/FC divergence is observed in these measurements. A clear kink is observed at 8.4(2) K which corresponds to the onset of long-range antiferromagnetic order within Ba_2MnWO_6.

Muon Spin Relaxation

Transverse field muon spin relaxation (TF-μSR) was measured to identify the Néel temperature of Ba_2MnWO_6, between 1.6(2) and 70.0(5) K, which was thought to be within the paramagnetic regime. When in a paramagnetic state in TF-μSR, the intrinsic muon spin can couple to the applied perpendicular field resulting in a large oscillating signal. At 20.0(5) K, this behaviour is observed, as shown in Figure 4.9.

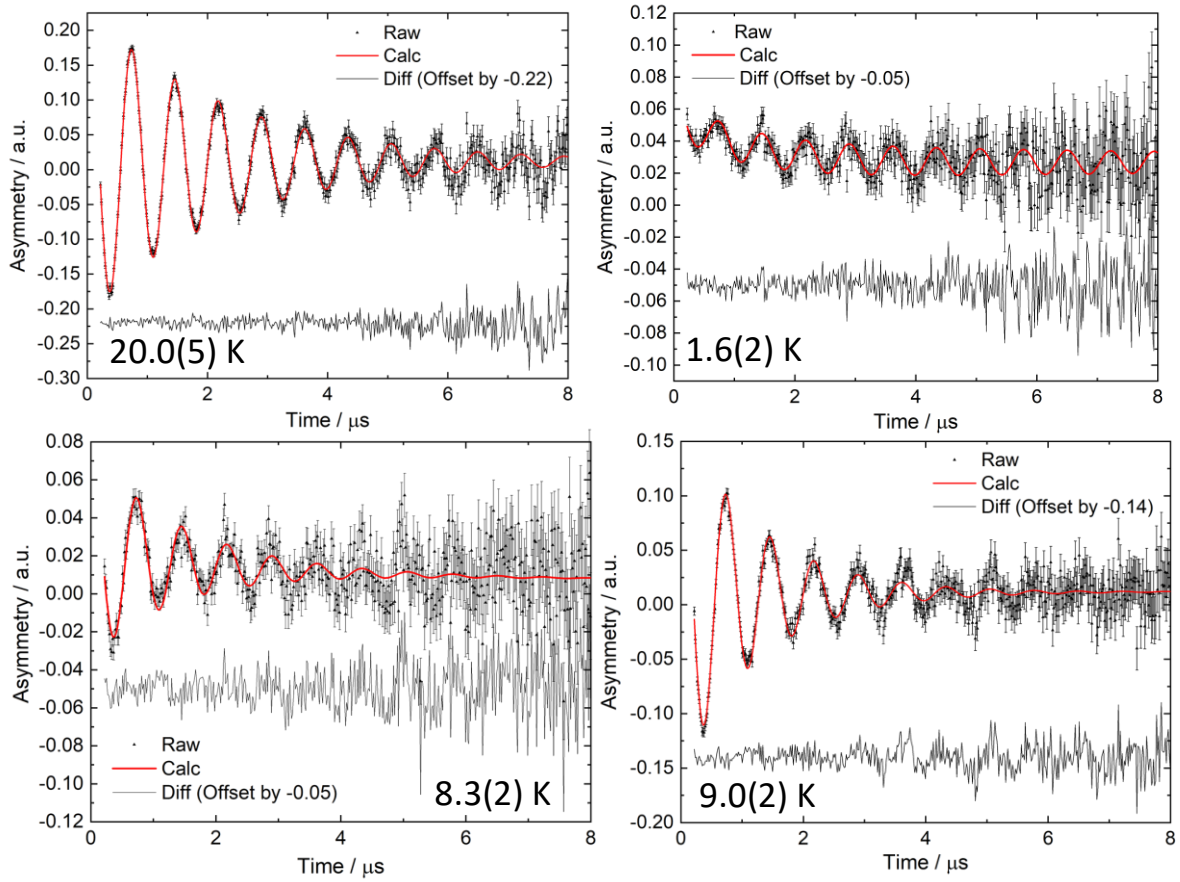

Figure 4.9: TF-μSR collected on Ba_2MnWO_6 at 20.0(5), 1.6(2), 8.3(2) and 9.0(2) K using a 100 G field. Each data set was fitted using; $A(t) = (A_{osc}\exp(-\lambda_{osc}t)\cos(2\pi fx+\varphi)) + (A_2\exp(-\lambda_2 t)) + A_3$. The difference curves are offset to aid the reader.

When long range magnetic order is present, magnetic moments interact and generate internal magnetic fields. These internal magnetic fields are significantly stronger than the applied transverse field and the muons no longer couple to the external field. This results in a flat background where oscillations are no longer observed. In Figure 4.9, the TF-μSR response at 1.6(2) K shows a small oscillation which is attributed to the silver foil and sample holder. Hence, the magnitude of the

oscillation changes depending on the experience of the muons, allowing T_N to be extracted. Figure 4.9 also depicts the fitted TF-μSR at 8.3(2) K and 9.0(2) K, indicating the large change in asymmetry over a small temperature interval.

The TF-μSR data sets between 1.6(2) and 8.3(2) K were fitted using the following function;

Equation 4.2: Asymmetry fitting function of TF-μSR measurements for Ba_2MnWO_6 between 1.6(2) K and 8.3(2) K

$$A(t) = (A_{osc}\exp(-\lambda_{osc}t)\cos(2\pi fx+\varphi)) + (A_2\exp(-\lambda_2 t)) + A_3$$

$A(t)$ is the overall asymmetry at any time (t), A_{osc}, A_2 and A_3 are the asymmetries of the oscillating and exponential decays and the flat signal, λ_{osc} is the oscillating relaxation, λ_2 is the exponential relaxation, f is the oscillation frequency and φ is the phase of oscillation. The constant signal is the result of ordered magnetism whilst the relaxation was the result of paramagnetism.

The thermal evolution of A_{osc}, A_2, A_3, λ_{osc} and λ_2 between 1.6(2) and 8.3(2) K are shown in Figure 4.10(a) – (e) respectively. A_{osc} remains fairly constant over the temperature range until a dramatic increase at 8.3(2) K. A_2 experiences a slight increase over the temperature range prior to a significant decrease at 8.3(2) K. The constant signal steadily decreases as the temperature increases. The oscillating relaxation rate remains approximately constant, but a large increase is observed at 8.3(2) K and λ_2 varies slightly between 1.6(2) and 8.0(2) K showing no significant trend, but a substantial decrease is observed at 8.3(2) K.

At 8.5(2) and 8.8(2) K the function is reduced to Equation 4.3, but no real trends can be discerned as these are only composed of two data points.

Equation 4.3: Asymmetry fitting function of TF-μSR data collected on Ba_2MnWO_6 between 8.5(2) and 8.8(2) K

$$A(t) = (A_{osc}\exp(-\lambda_{osc}t)\cos(2\pi fx+\varphi)) + (A_2\exp(-\lambda_2 t))$$

Between 9.0(2) and 30.0(5) K, λ_2 becomes too slow for the muons to detect changing the function to;

Equation 4.4: Asymmetry fitting function of TF-μSR measurements for Ba_2MnWO_6 between 9.0(2) and 30.0(5) K

$$A(t) = (A_{osc}\exp(-\lambda_{osc}t)\cos(2\pi fx+\varphi)) + A_2$$

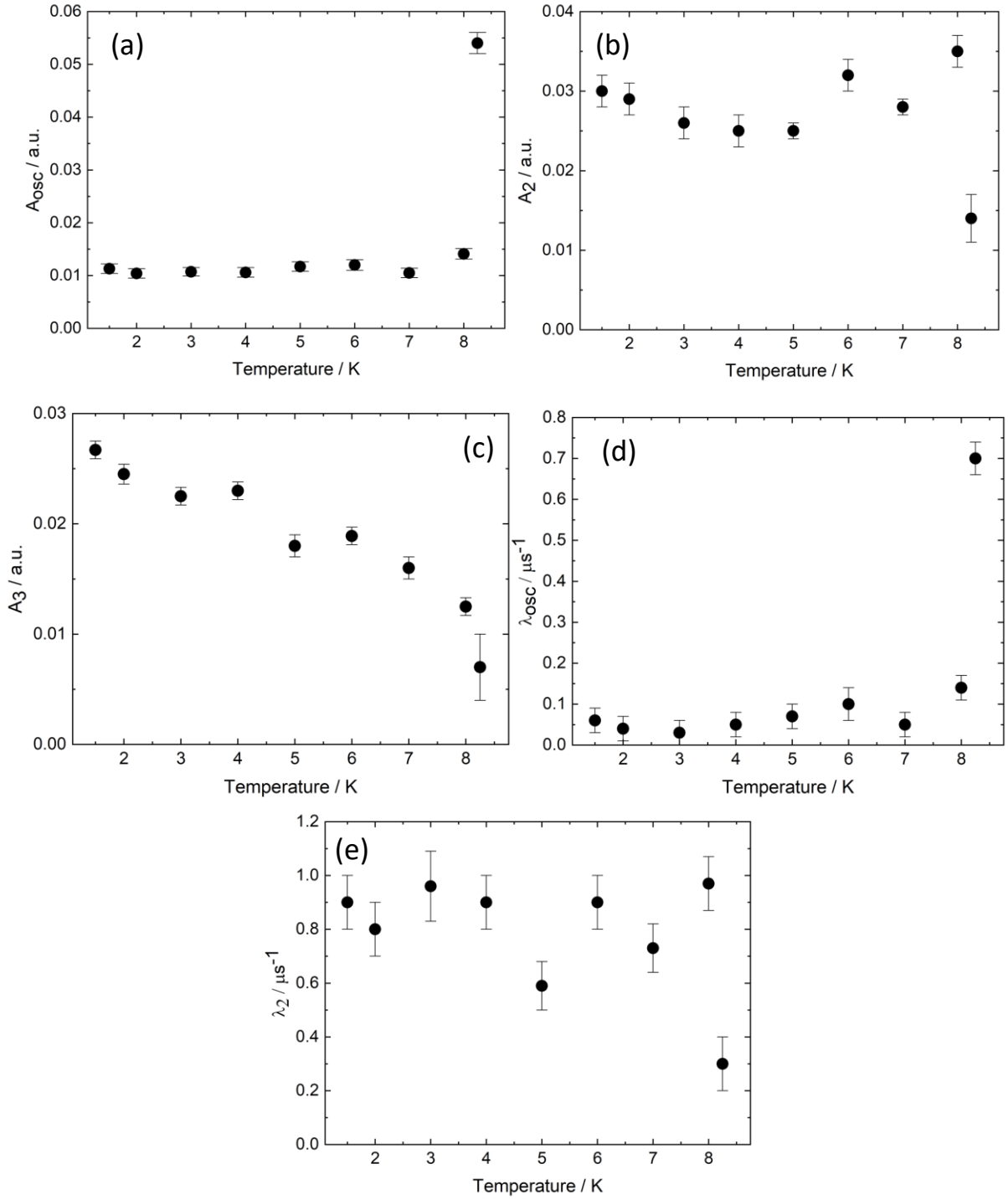

Figure 4.10: Results of fittings from TF-μSR measurements collected on Ba_2MnWO_6 between 1.6(2) and 8.3(2) K. The thermal dependence of (a)A_{osc}, (b) A_2, (c) A_3, (d) λ_{osc} and (e) λ_2.

Throughout this temperature range, the oscillating component dominates, as shown in Figure 4.11. A_{osc} is found to increase with temperature as Ba_2MnWO_6 heads further away from transition temperature, at the same time the relaxation rate of this component decreases as there is less of a drive for the magnetic moments to couple with each other.

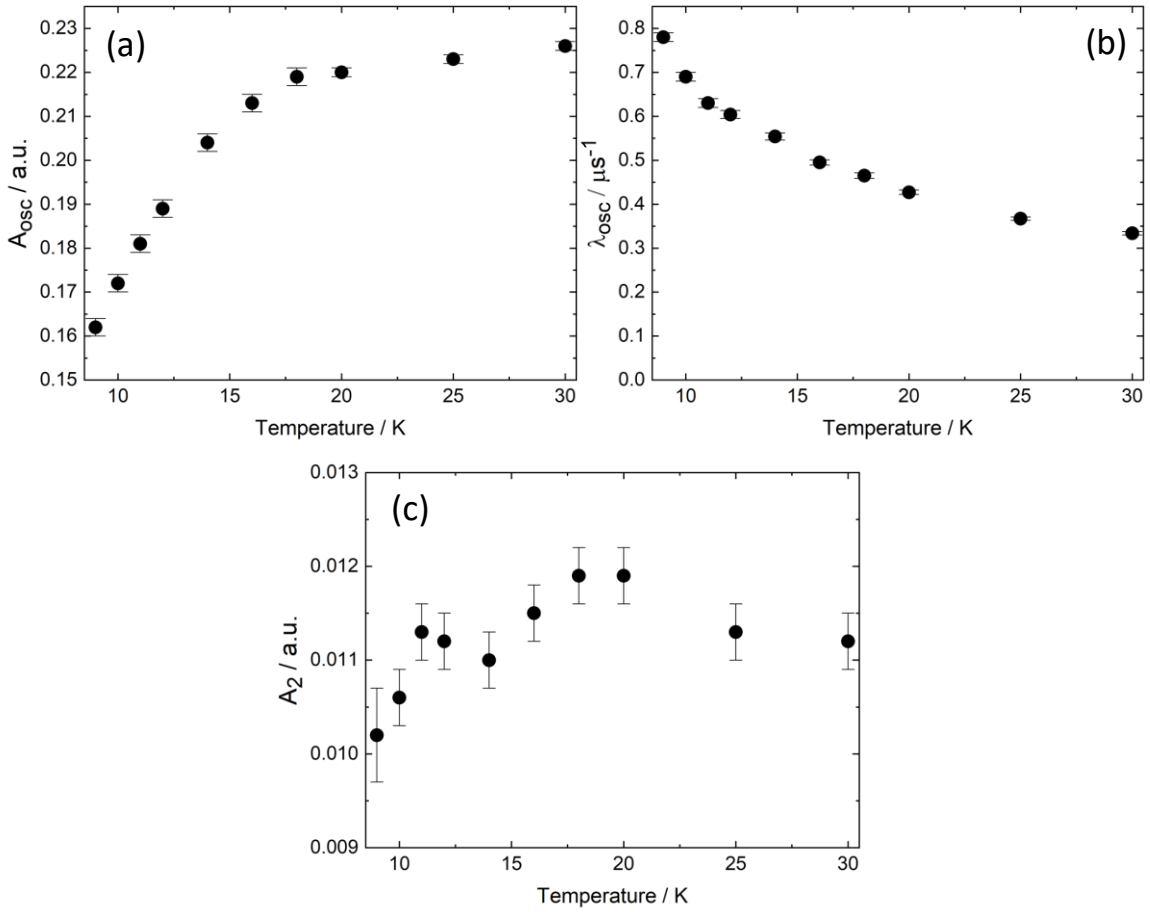

Figure 4.11: Results of fittings from TF-μSR data sets collected on Ba_2MnWO_6. The thermal evolution of (a) A_{osc}, (b) λ_{osc} and (c) A_2. A_{osc} increases with temperature and simultaneously the relaxation rate decreases. A_2 shows a small increase over the temperature range but remains minute compared to the relaxing asymmetry.

Further information can be extracted from TF-μSR measurements when the asymmetry of the oscillating component is normalised. This was completed by dividing the oscillating asymmetry at any time by the oscillation at 70.0(8) K, $A_{osc}(t)/A_{osc}$(70.0(8) K). Between 1.6(2) and 8.0(2) K, the normalised asymmetry is close to zero. A sharp increase is observed at 8.3(2) K, which corresponds to the onset of long-range antiferromagnetic order and therefore this is taken as T_N. At 8.5(2) K a further sharp increase is observed which is followed by a gradual increase until 30.0(5) K. This steady incline from approximately 0.6 was unexpected and potentially caused by short-range magnetic correlations within Ba_2MnWO_6. The thermal dependence of the normalised asymmetry is illustrated in Figure 4.12.

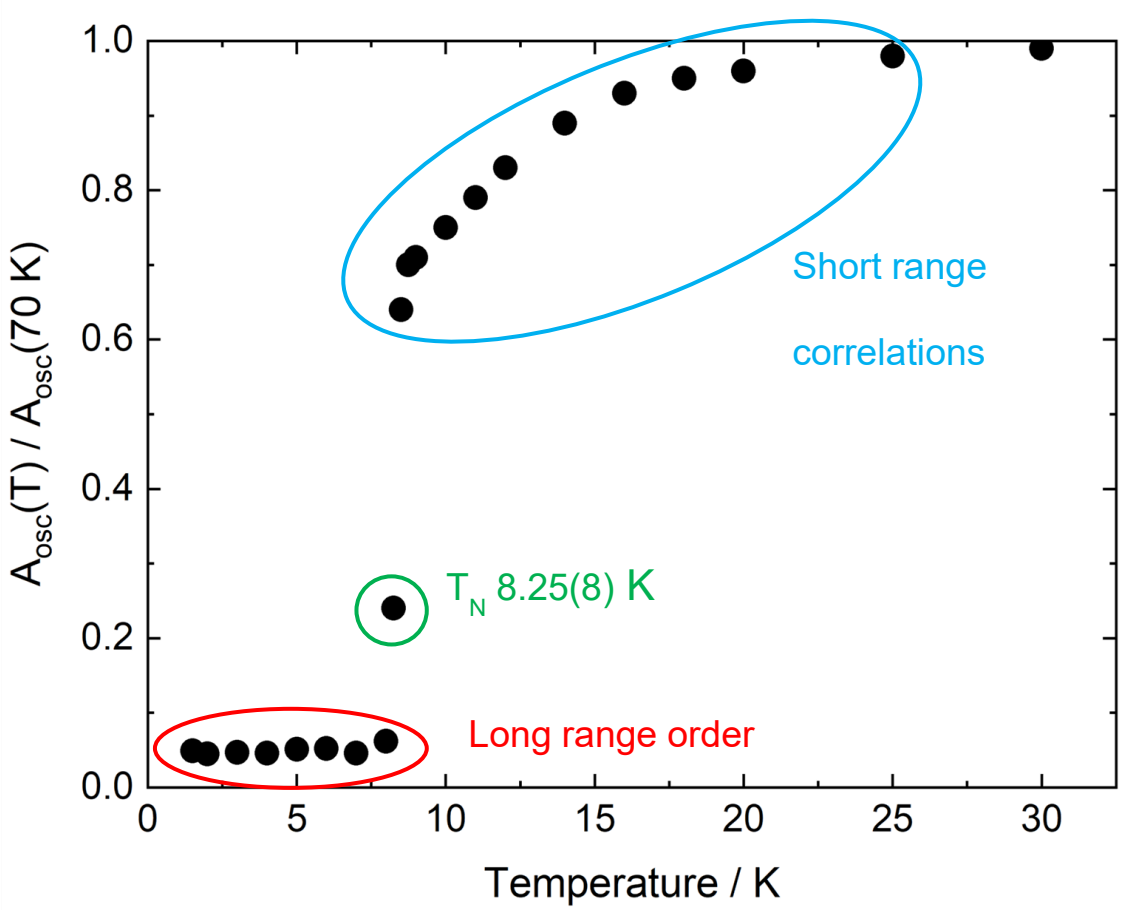

Figure 4.12: The thermal evolution of the normalised oscillating asymmetry obtained from TF-μSR measurements carried out on Ba_2MnWO_6. The normalised asymmetry is close to zero at low temperature. A sharp increase is observed at 8.3(2) K, attributed to the Néel temperature. Another sharp increase is observed at 8.5(2) K and then a gradual increase is observed until 25 K, surmised to be caused by short-range magnetic correlations. Error bars are applied but are smaller than the icons.

Zero-field muon spin relaxation (ZF-μSR) measurements were completed between 1.6(2) and 30.0(5) K to observe the behaviour of Ba_2MnWO_6 without the presence of an applied magnetic field. Below 8.3(2) K, the overall maximum asymmetry was significantly lower than expected. A low initial asymmetry is characteristic of long-range magnetic ordering, although this is typically combined with an oscillating relaxation. Below this temperature no oscillations were observed as the pulse width distribution at the muon source used did not allow these to be observed. Between 1.6 and 20 K the ZF-μSR can be fitted using the following function;

Equation 4.5: Asymmetry fitting function of ZF-μSR for Ba_2MnWO_6 between 1.6(2) and 20.0(5) K

$$A(t) = (A_1\exp(-\lambda_1 t)) + (A_2\exp(-\lambda_2 t)) + A_3$$

A fit of the data collected at 20.0(5) K, can be observed in Figure 4.13(a). This function is composed of two distinct exponential relaxations which are attributed to paramagnetic behaviour plus a constant signal term which describes static magnetism. A_1 corresponds to muons experiencing a relatively slow relaxation, whilst A_2 corresponds to a faster relaxation.

A_1 and A_2, are small until 8.3(2) K where they both significantly increase. This increase is larger in A_1 than in A_2 suggesting that the faster relaxation is present in a smaller proportion above 8.3(2) K. A_3 is present in approximately the same quantity as A_1 and A_2 below 8.3(2) K, but it remains small throughout the temperature range. The thermal evolution of the asymmetry values from ZF-μSR data sets is shown in Figure 4.13(b). The slower relaxation rate, λ_1, experiences an initial decrease between 1.6(2) and 5.0(K) prior to increasing to a maximum at 8.3(2) K before gradually decreasing as the temperature was raised. The faster relaxation rate, λ_2, also shows a maximum at 8.3(2) K and decreases as the temperature tends to 20.0(5) K, however, the trend is not as clear as λ_1. This is thought to be a result of the large error observed at lower temperature where the A_2 component is present in a low quantity. Despite these large errors, the inclusion of λ_2 is necessary to accurately described the relaxation curve. The temperature dependence of λ_1 and λ_2 are depicted in Figure 4.13(c) and (d) respectively. The persistence of the two separate relaxation rates above 8.3(2) K, could be driven by short-range magnetic correlations.

At 30 K, the fitting function changes where the fast fluctuations can no longer be detected by the muons and therefore A_2 must be removed from the fitting function. The results of this fit will not be shown on a figure as this is a single data point.

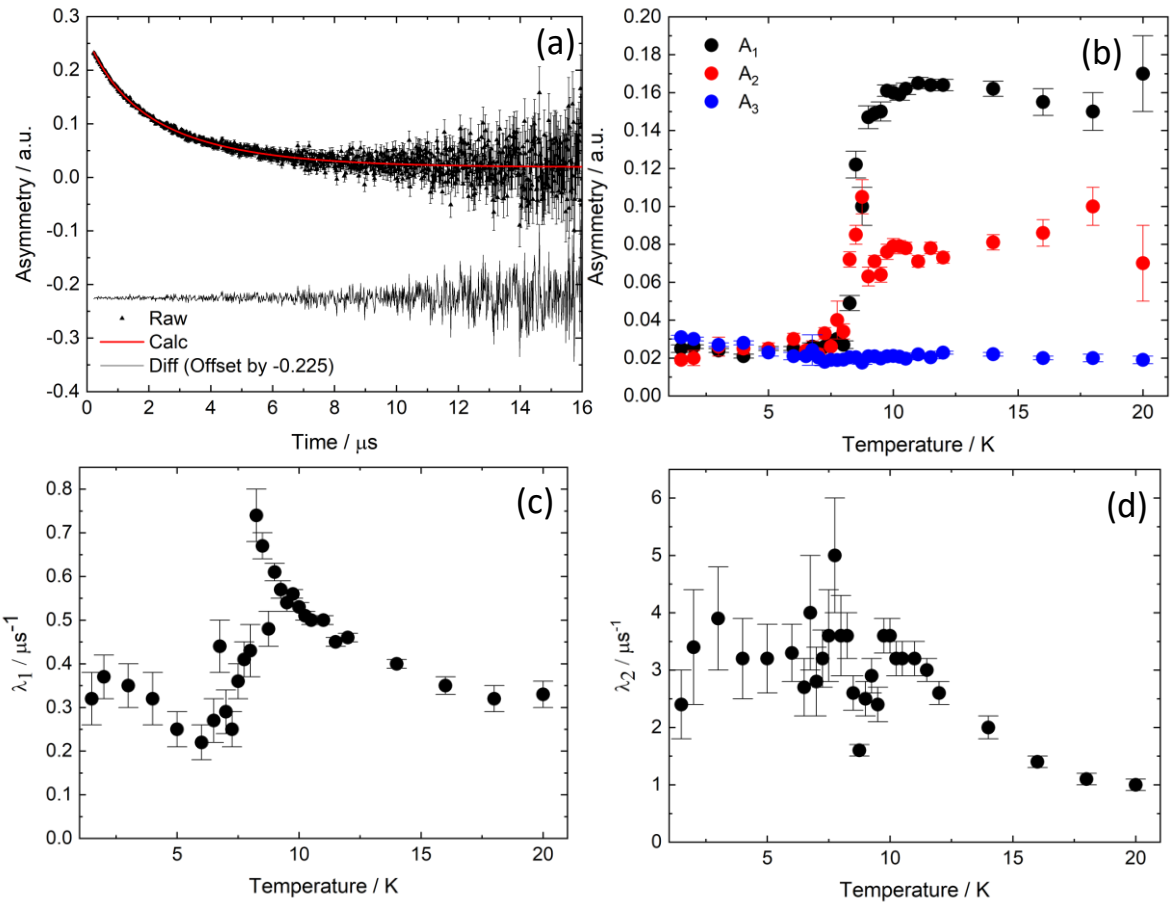

Figure 4.13: (a) ZF-μSR measurement collected on Ba_2MnWO_6 at 20 K, fitted using $A(t) = (A_1\exp(-\lambda_1 t)) + (A_2\exp(-\lambda_2 t)) + A_3$. The difference curve has been offset by -0.225. (b), (c) and (d) the thermal evolution of the asymmetries (A_1, A_2 and A_3), λ_1 and λ_2 respectively between 1.6(2) and 20.0(5) K.

Longitudinal field measurements were completed to observe the behaviour of the muons when placed in a magnetic field and ensure conventional long-range antiferromagnetic behaviour. Below T_N, the application of the longitudinal field is unlikely to decouple the relaxation curve due to the strong internal fields. Above T_N, the strong static fields are absent and therefore a complete decoupling of the relaxation should be observed, resulting in a completely flat line.

LF-μSR was measured significantly below, slightly above and significantly above T_N. The measured data is shown in Figure 4.14. In all instances, the relaxation curve is not fully decoupled even when a strong external field of 4000 G is applied to the system. This is indicative of strong internal magnetism above the transition temperature. A further suggestion of potential short-range magnetic correlations.

The fits of each of these data sets showed that no significant changes took place in asymmetry or relaxation above or below the transition temperature and therefore these data sets will not be included in this chapter.

The results of fitting the LF-μSR measurements both above and below the temperature gave no conclusive results regarding the state of a short-range correlated state and therefore, further measurements were required to observe these in greater detail.

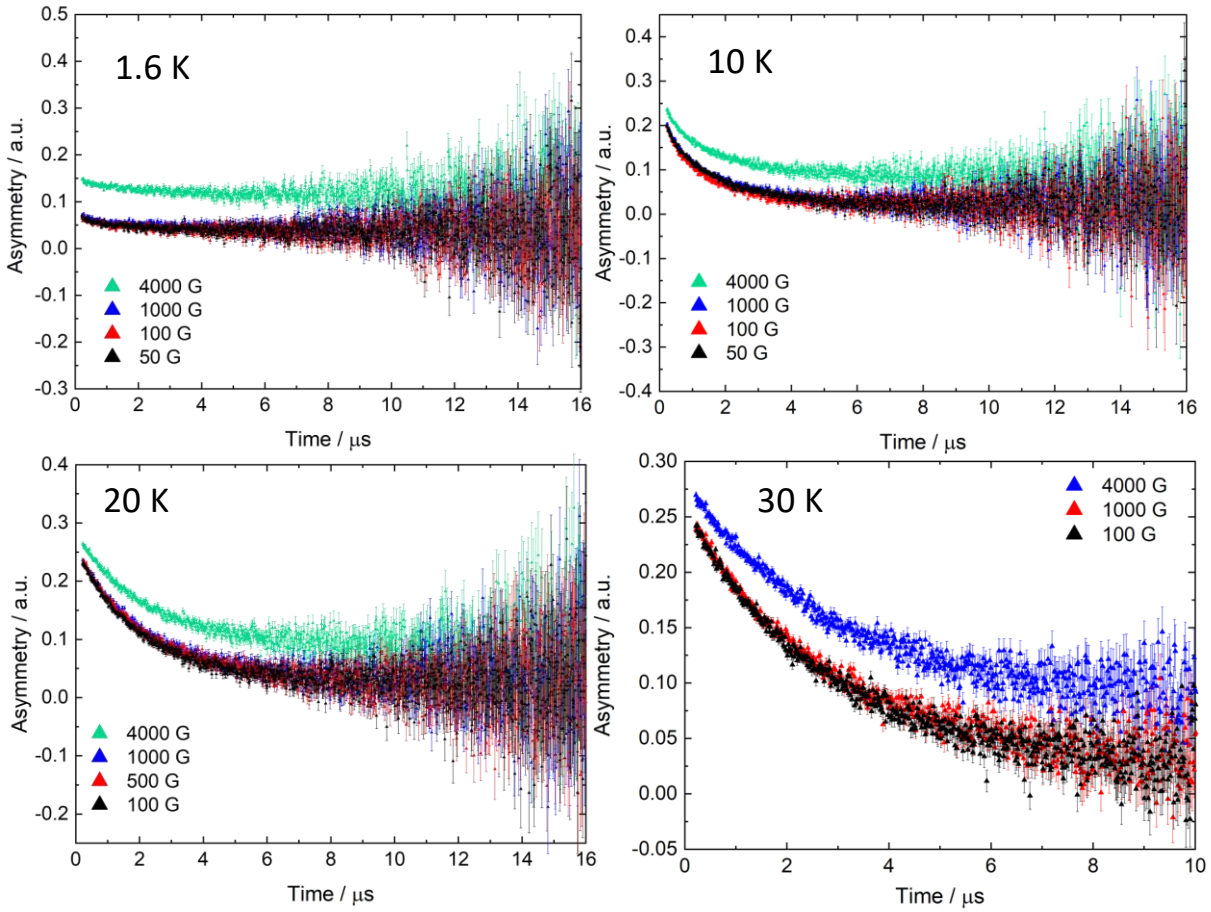

Figure 4.14: LF-μSR measurement collected on Ba_2MnWO_6 at (a) 1.6 (b) 10 K, (c) 20 K and (d) 30 K at a variety of different magnetic fields. These data sets show that both below and above the transition temperature the 4000 G magnetic field does not decouple the magnetic field.

Inelastic Neutron Scattering

Inelastic neutron scattering was measured on Ba_2MnWO_6 to assess the magnetic character both above and below the transition temperature. Below the transition temperature, information could be collected about the long-range antiferromagnetic nature of the system including the magnitude of the magnetic exchange constants, J_1 and J_2. Above the transition temperature, these could give firm evidence of short-range magnetic excitations taking place within Ba_2MnWO_6.

Initial experiments were completed at 2 K, well below the transition temperature. As Ba_2MnWO_6 experiences long range antiferromagnetic order at this temperature, distinct spin waves were observed in the spectrum. A simulation of this data set was generated using the SpinW program and linear spin wave theory [228]. The measured data and the simulation can be observed in Figure 4.15 (a) and (b) respectively. This was based on the following Hamiltonian;

Equation 4.6: Hamiltonian used to extract magnetic coupling constants from inelastic neutron scattering

$$\widehat{H} = -J_1 \sum_{\langle ij \rangle} \boldsymbol{S}_i \cdot \boldsymbol{S}_j - J_2 \sum_{(ij)} \boldsymbol{S}_i \cdot \boldsymbol{S}_j$$

J_1 and J_2 correspond to the nearest neighbour (NN) and the next nearest neighbour (NNN) interactions respectively. S_i corresponds to the spin at site *i*, with sums taken over all the J_1 and J_2 interactions respectively. In this instance, antiferromagnetic interactions are denoted using a negative sign.

The purpose of the simulation was to extract the magnitudes of the magnetic coupling constants, J_1 and J_2, by comparing to the experimental observations. The completed simulation was an excellent fit to the measured data set allowing the values of J_1 = -0.080 meV and J_2 = -0.076 meV to be extracted. These values have no errors as they are initially estimated by hand and therefore are not exact fits to the inelastic neutron scattering data. The J_2/J_1 ratio of 0.95 corresponds to a Type II antiferromagnet. The comparison of both the experimentally collected data and the simulation showed that only the J_1 and J_2 interactions had to be considered, insinuating that any interactions which occur over a farther distance do not affect the overall long range antiferromagnetic structure. No extra terms were

necessary such as an anisotropy term because the high spin Mn^{2+} cation has no spin orbital contribution due to the equal occupancy of the t_{2g} orbitals.

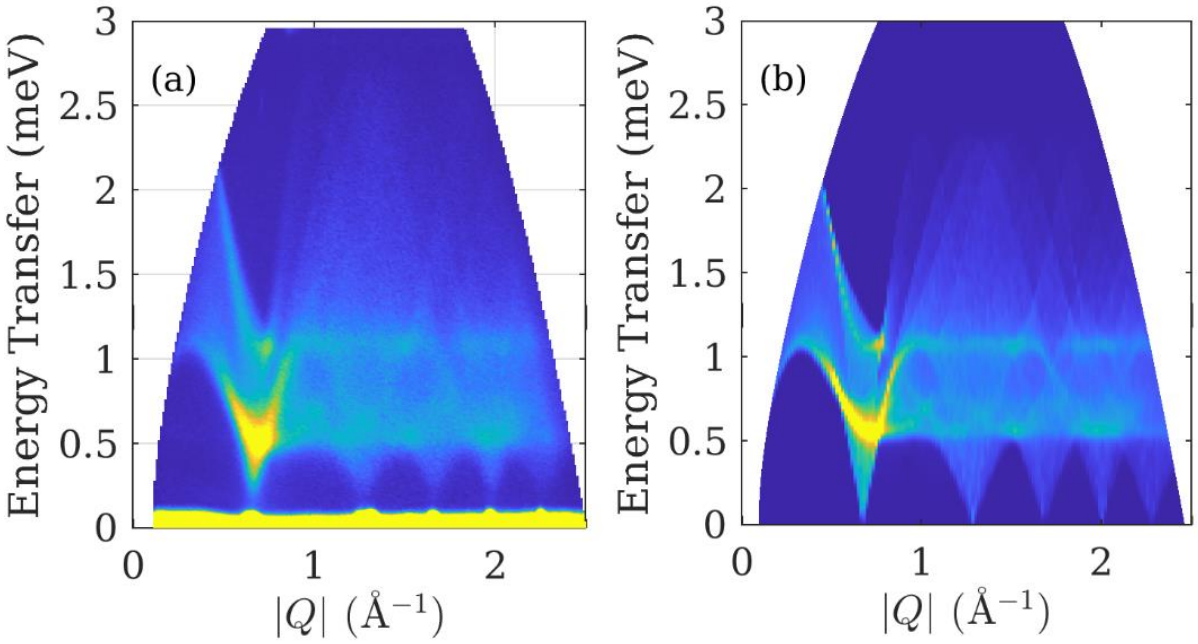

Figure 4.15: (a) Inelastic neutron scattering measurements completed on Ba_2MnWO_6 at 2 K. The bright yellow areas are regions of high intensity, the darker blue areas are regions of low intensity. The bright yellow zero-energy transfer line is the elastic energy line. Distinct spin waves propagate throughout the system. (b) A simulation of the inelastic neutron scattering data which closely correlates with the measured data set. This required J_1 = -0.080 meV and J_2 = -0.076 meV, therefore the interactions are antiferromagnetic and J_1 is the dominant interaction.

Further inelastic neutron scattering measurements were also completed above the transition temperature to investigate the potential short-range correlated state in Ba_2MnWO_6. These measurements were completed at 12, 40 and 100 K, as depicted in Figure 4.16. At 12 and 40 K, excitations are observed. These were determined to be magnetic as they had highest intensity at low $|Q|$ and decreases as $|Q|$ increased. If these excitations arose through vibrations within Ba_2MnWO_6 then the highest intensity excitations would be observed at higher $|Q|$ values and decrease as $|Q|$ decreases. Therefore, these measurements provide evidence of a short range magnetic correlated state present in Ba_2MnWO_6. It is important to note that these magnetic excitations originate from the same points in the elastic line as the spin waves emerge from in the 2 K data set. This suggests that short-range correlations are related to the long-range antiferromagnetically ordered state. The magnetic excitations persist up to 40 K, which is approximately five time the transition temperature,

and suggest that the material still experiences fairly strong magnetic behaviour which could be the result of the high spin state. At 100 K, the excitations are now firmly diminished with no evidence of short-range magnetic behaviour.

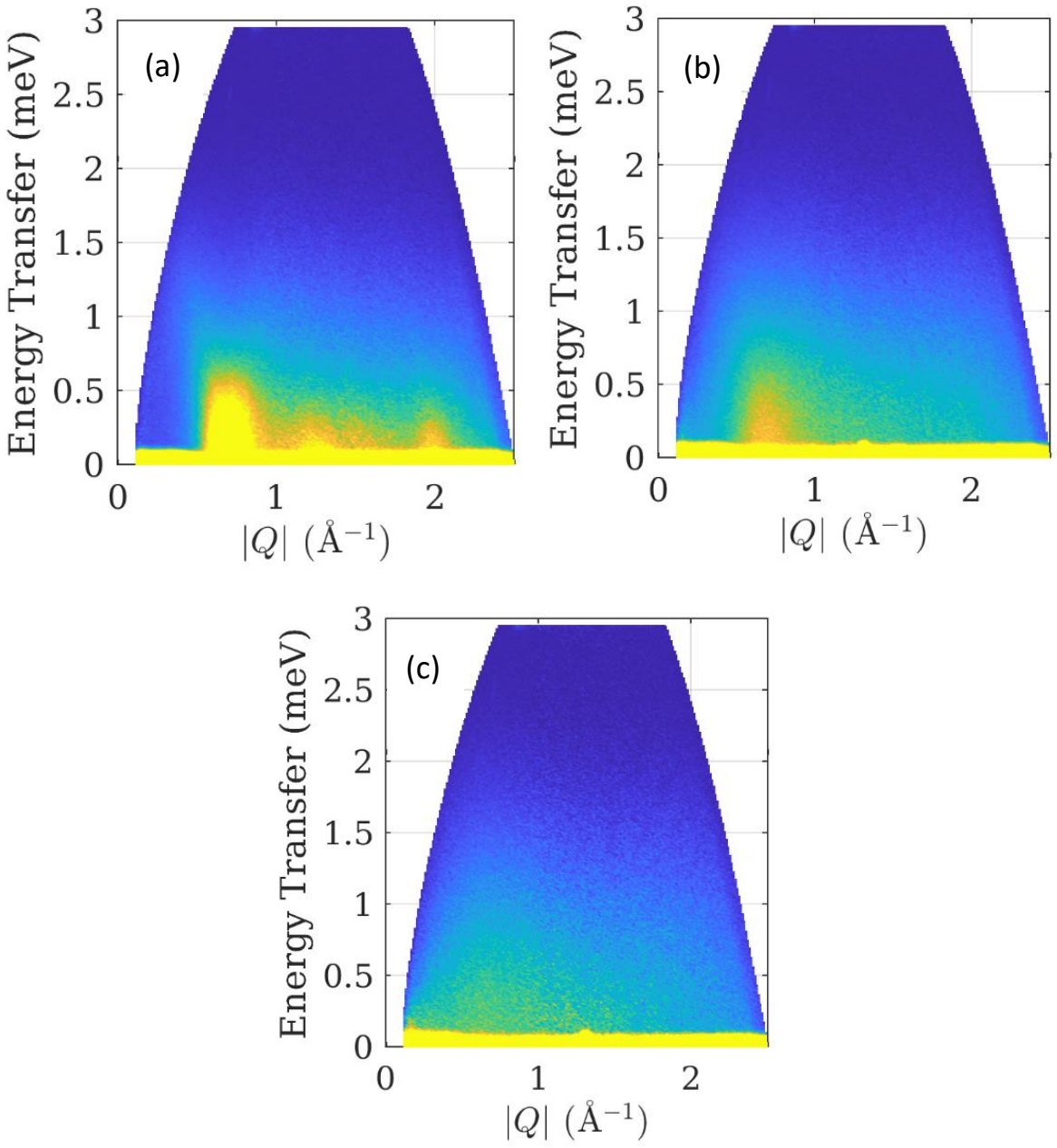

Figure 4.16: Inelastic neutron scattering measurements collected on Ba_2MnWO_6 above the transition temperature at (a) 12 K, (b) 40 K and (c) 100 K. Magnetic excitations can be observed at 12 K and 40 K which give evidence of a short-range correlated state. These short-range magnetic interactions can no longer be observed at 100 K, indicating that the correlated state is disrupted.

Discussion

Ba_2MnWO_6 is a moderately frustrated double perovskite, with f = 8(1). It crystallises in the *fcc* space group $Fm\bar{3}m$. Within this material, magnetic interactions are driven by Mn^{2+} cations connected via the frustrated *fcc* lattice. Each of the techniques outlined indicate that Ba_2MnWO_6 is able to overcome this frustration and become antiferromagnetically ordered below the transition temperature of 8(1) K. Muon spin relaxation was utilised to precisely identify the transition temperature from a paramagnetic state to 8.3(2) K. Neutron powder diffraction indicated that the Ba_2MnWO_6 retains its cubic structure without going through any structural phase transition and that the nuclear and magnetic structures are related by the propagation vector $\boldsymbol{k}$ = (1/2, 1/2, 1/2). The magnetic structure corresponds to a Type II antiferromagnet, where the moment alignment results in sheets of ferromagnetic interactions along the (111) plane with adjacent (111) planes interacting in an antiferromagnetic manner. Inelastic neutron scattering agreed with neutron powder diffraction and assigned the magnetic structure of Ba_2MnWO_6 as Type II antiferromagnetic, with the magnetic exchange coupling constants both antiferromagnetic; J_1 = -0.080 meV and J_2 = -0.076 meV. J_2/J_1 = 0.95 which agrees with Type II antiferromagnetism [62].

J_1 and J_2 correspond to the NN and the NNN interactions respectively, the shortest distances between Mn^{2+} cations. Only these interactions are necessary to characterise the antiferromagnetic order within Ba_2MnWO_6. These magnetic interactions take place along superexchange pathways; through Mn-O-O-Mn or Mn-O-W-O-Mn. The J_1 interaction occurs via a 90° superexchange angle, which typically result in ferromagnetic interactions taking place. Whilst J_2 interactions arise along a linear 180° path, the ideal situation for antiferromagnetic behaviour to take place. In Type II *fcc* antiferromagnetic structures, NN interactions are unable to all align antiferromagnetically simultaneously, but this is permitted in the NNN interactions. The frustrated nature of the J_1 interactions results in geometrical frustration within the system. In Ba_2MnWO_6, a rare situation arises where J_1 is very slightly dominant compared to J_2, -0.080 meV versus -0.076 meV. Due to this, Ba_2MnWO_6 has a fairly high frustration

index of 8(1), as J_1 is dominant, however, the magnetic Type II structure prevents antiferromagnetic order in all of these connections [62]. These values compare closely with what has been reported from the values calculated from a recent computational study. These calculations were completed using a generalised gradient approximation plus Hubbard U (GGA + U) approach. The exchange parameters J_1 and J_2 were found to both be antiferromagnetic with the nearest neighbour interaction dominant at any value of U. The closest value to the experimentally collected values occur when U = 0, where J_1 = -0.53 meV and J_2 = -0.42 meV [140].

Calculating J_1 and J_2 allowed a comparison to be drawn between similar double perovskites, of the form $(Ba,Sr)_2MWO_6$ – where *M* is a 3d transition metal, which adopt a Type-II antiferromagnetic structure. Recent studies on the cuprate systems, Ba_2CuWO_6 and Sr_2CuWO_6, indicate that J_2 interactions are significantly greater in magnitude than J_1. In these instances, the J_2/J_1 ratios, estimated from inelastic neutron scattering measurements are approximately 50 times larger for Ba_2CuWO_6 and 8 times larger for Sr_2CuWO_6 [195,200]. Sr_2NiWO_6 was previously studied experimentally and was calculated to have a J_2/J_1 ratio ≈ 90, although recent theoretical studies have established that J_2 should only be 20 times larger than this which shows that some disparity between experimental and theoretical simulations remains when considering magnetic exchange constants [183,186]. These systems are fair comparisons however, there are a number of differences which prevent these from being direct comparisons. Ba_2MnWO_6 is cubic whilst the others are all tetragonally distorted. The distortion in these materials could relieve some of the frustration they experience, allowing these to adopt a more conventional Type-II antiferromagnetic structure. The spin states are also drastically different compared to Ba_2MnWO_6 which has a spin state of S = 5/2, compared to Sr_2NiWO_6 where S = 1 and the cuprate systems where S = ½. Ba_2MnWO_6 experiences more classical behaviour whilst the other materials exhibit more quantum-like behaviour. These differences could be the cause of the large differences in the J_2/J_1 ratio.

Comparing the J_2/J_1 ratio of more similar double perovskites proved more difficult as many of these materials such as Ba_2CoWO_6 have not had their magnetic coupling constants calculated [163]. Ba_2NiWO_6 is a cubic double perovskite which has reported exchange constants. However, it does not resemble Ba_2MnWO_6 showing a strongly dominant NNN interaction compared with $J_2/J_1 \approx 80$ [163,183]. Once again, a direct comparison cannot be drawn between Ba_2MnWO_6 and Ba_2NiWO_6 due to the differences in the spin state. However, from this investigation it does suggest that the character of the magnetic interactions is brought about by the spin state of the magnetic cation, rather than from the structure. This comparison also indicates that Ba_2MnWO_6 is a somewhat unique example of a (Ba,Sr)MWO$_6$ double perovskite and further investigation is necessary into these materials to assess why this is the case. Table 4:4 contains several materials plus their spin state and nuclear space group.

It was pertinent that inelastic neutron scattering was checked to ensure that the situation where $J_2 >> J_1$ is conclusively not possible for Ba_2MnWO_6. To do this, the simulation was re-ran with J_1 = -0.010 meV and J_2 = -0.146 meV, this poorly described the experimentally obtained scattering pattern. Whilst $J_1 \approx J_2$ agreed strongly with the obtained data set. This can be observed due to the proximity of the two large peaks observed in Figure 4.17, as this is defined by the magnitude of J_1 and J_2 and the ratio of these. The closeness of the two peaks, indicates that J_1 and J_2 should be close in magnitude and if $J_2 >> J_1$, the two peaks would be further apart. Although Ba_2MnWO_6 experiences $J_1 \approx J_2$ it is still able to adopt the Type-II antiferromagnetic structure. This study has shown the robust nature of the Type-II antiferromagnetic structure, which can prevail in many different situations despite changes in geometry and large differences in spin state ranging from S = 1/2 to S = 5/2.

Table 4:4: Magnetic coupling constant ratio of different materials

Material	**Space Group**	**S**	J_1/J_2
Ba_2MnWO_6	$Fm\bar{3}m$	5/2	0.95
Ba_2NiWO_6	$Fm\bar{3}m$	1	80
Sr_2NiWO_6	$I4/m$	1	90
Ba_2CuWO_6	$I4/m$	1/2	50
Sr_2CuWO_6	$I4/m$	1/2	8
MnO	$P2_1/n$	5/2	1.1

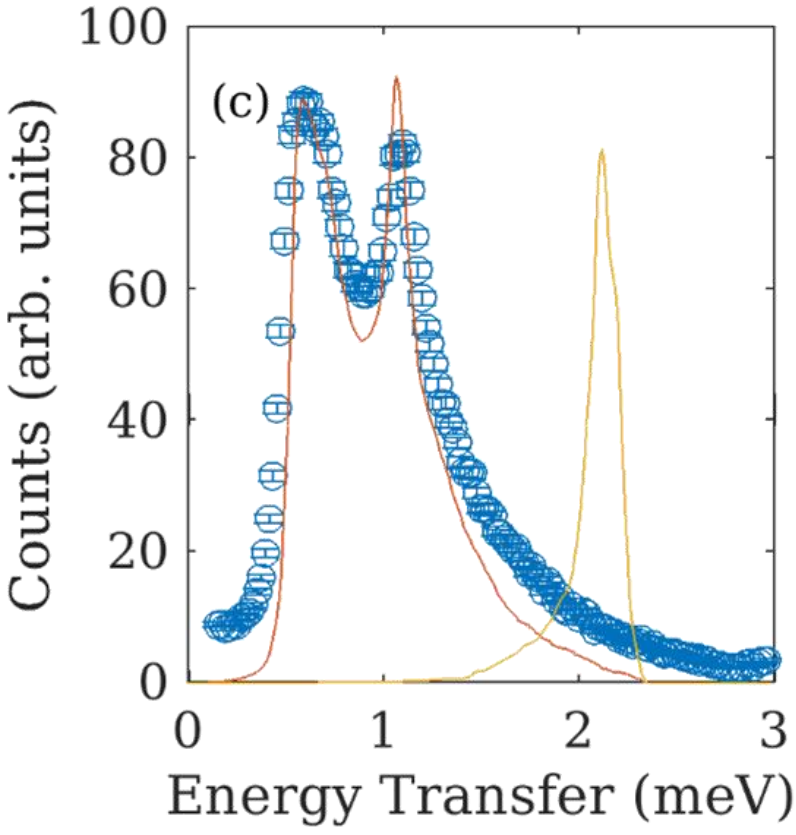

Figure 4.17: Inelastic neutron scattering simulation for Ba_2MnWO_6 at 2 K. This displays a vertical cut through the data set at this temperature for $0.9 \leq |Q| \leq 1.1$ Å^{-1}. In this data set the blue circles correspond to the experimentally collected data, the orange calculated line on the left hand side corresponds to the situations where J_1 = -0.080 meV and J_2 = -0.076 meV and the yellow calculated line on the right hand side corresponds to the situation where J_1 = -0.010 meV and J_2 = -0.146 meV. From this it is evident that J_1 and J_2 must have very similar magnitudes, and the ratio between the split peak determines the values of J_1 and J_2.

A short-range correlated magnetic state was suggested to persist above T_N in Ba_2MnWO_6 from μSR. This was evidenced due to exotic behaviour observed in the thermal dependence of the normalised oscillatory asymmetry, which showed a gradual increase between 9.0(2) and 25.0(5) K when a sharp jump to ~1 was anticipated. This was also indicated in ZF-μSR where, the same function was utilised either side of the transition temperature. Despite this being the case, the physical nature of Ba_2MnWO_6 is distinctly different in these instances. As previously stated, below T_N oscillations are expected. However, as these oscillations could not be resolved by the instrument they appear as the fast relaxation A_2 which experiences a dramatic increase at T_N, in line with the increase of the overall asymmetry. Above T_N, the oscillations are no longer anticipated and therefore, the persistence of the function adds to the case of short-range magnetism within Ba_2MnWO_6. A_1, the relatively slow relaxation, is attributed to conventional paramagnetism. This is rationalised as the relaxation rate is inversely proportional to the frequency of the dynamic fluctuations within the system. In paramagnets the fluctuations are fast and therefore, the relaxation rate is small. Conversely, A_2 instead corresponds to short-range correlations within the system as these are slower fluctuations within the system which result in a significantly faster relaxation rate. This was further suggested by the lack of decoupling of internal magnetic fields found within Ba_2MnWO_6 even in longitudinal fields of strength equal to 4000 G. Inelastic neutron scattering was then carried out to confirm the presence of magnetic excitations above the transition temperature and these were observed up to 40 K, approximately five times T_N. More information about the short-range correlated state is currently unavailable, however, inelastic neutron scattering measurements insinuate that these are related to the long-range antiferromagnetic order. There is some potential that this could resemble the established short- range correlated magnetic state observed in the archetypical *fcc* lattice MnO.

Ba_2MnWO_6 and MnO show Type-II antiferromagnetic character, composed of a frustrated lattice of S = 5/2 Mn^{2+}. Both form relatively frustrated lattices with frustration indexes equal to 8 and 5 for Ba_2MnWO_6 and MnO respectively. MnO has a J_2/J_1 ratio approximately equal to 1.1, which out of all the compared materials is the most like Ba_2MnWO_6 due to the close magnitudes [132]. However, J_2 is

still dominant in this structure, unlike in Ba_2MnWO_6, where J_1 is the dominant interaction. The lower J_2/J_1 ratio could explain the higher frustration index observed in Ba_2MnWO_6 as previously outlined the Type-II antiferromagnetic structure as the J_1 interactions cannot be fully satisfied within this structure. Short-range magnetic interactions above T_N have also been reported in MnO [133]. Structurally the two systems are fairly different, Ba_2MnWO_6 crystallises in the *fcc* lattice and remains cubic down to 2 K but MnO experiences a structural phase transition at the onset of long range antiferromagnetic order to a monoclinic species [132]. This has been of interest, as it could suggest that a very subtle monoclinic distortion of the Ba_2MnWO_6 lattice could take place. However, this was not observed in the neutron diffraction patterns collected on Ba_2MnWO_6.

Conclusion

Neutron powder diffraction, DC-susceptibility measurements, muon spin relaxation spectroscopy and inelastic neutron scattering were utilised to study the structural and magnetic behaviour of Ba_2MnWO_6. Neutron powder diffraction and inelastic neutron scattering proved that Ba_2MnWO_6 experiences a long-range antiferromagnetic transition which results in Type-II magnetic order at 8(1) K. The magnetic structure was identified to be similar to MnO with propagation vector $\boldsymbol{k}$ = (1/2 1/2 1/2). The nearest neighbour magnetic coupling constant J_1 = -0.80 meV and the next nearest neighbour interaction, J_2 = -0.076 meV. Short-range magnetic excitations above the transition temperature were evidenced by both muon spin relaxation and inelastic neutron scattering up to 40 K.

Future Work

Given further time, neutron powder diffraction would have been carried out between 9 and 15 K. At 9 K, the first observed magnetic peak around 9 Å, does appear to look less peak like and instead resembles a broad hump. This suggests diffuse magnetic scattering within Ba_2MnWO_6, which is evidenced in both the μSR and INS. However, measurements above 15 K, tend to not show any diffuse scattering which is unusual as the short-range magnetic excitations do arise up to 40 K. It is possible that these interactions are too weak to be observed in the neutron powder diffraction measurement.

As the *fcc* structure violates the potential for antiferromagnetic long-range order, neutron diffraction on a higher resolution instrument or synchrotron X-ray diffraction may be able to pick up on whether there is a subtle monoclinic distortion. A monoclinic distortion is observed in MnO, around the transition temperature therefore it is possible that this is taking place. If this monoclinic distortion is observed, then this is incredibly subtle.

Magnetic diffuse scattering and polarised neutrons may be useful to try and extract further information about the short-range magnetically correlated state. At this moment very little is known about the short-range magnetic state and it would be beneficial to gain a greater understanding.

5. Comparison of Frustrated S = 5/2 Sr_2MnWO_6 with Ba_2MnWO_6

The purpose of this study was to investigate the structural and magnetic behaviour of the previously reported frustrated double perovskite Sr_2MnWO_6 and to compare it to Ba_2MnWO_6. Like Ba_2MnWO_6, Sr_2MnWO_6 experiences rock salt alignment of the *M*-site cations Mn^{2+} and W^{6+} and Mn^{2+} is the only magnetic cation, allowing parallels to be drawn between the two systems.

Sr_2MnWO_6 has previously been reported in the literature, however, there has been conflicting evidence about the space group which it adopts; the unconventional $P4_2/n$ or $P2_1/n$ [141,142,235]. The reported transition temperature is slightly higher in Sr_2MnWO_6 than in Ba_2MnWO_6 at approximately 13 K. There has also been some controversy surrounding the magnetic spin state of Mn^{2+} within the structure, with one report suggesting that Mn^{2+} is not present in the high spin state in neutron diffraction [141].

A-site doping on Sr_2MnWO_6, to generate $Sr_{2-x}La_xMnWO_6$ ($0 \leq x \leq 1$) explored the potential of magnetoresistance within the system as the La^{3+} ion may force W^{6+} to become W^{5+}. Across the $Sr_{2-x}La_xMnWO_6$ solid solution the structures adopt the $P2_1/n$ space group for $x \leq 0.75$, when x = 1 this becomes a tetragonal *I4/m* phase and between x = 0.75 and x = 0.9 a phase boundary is present. Increasing the lanthanum concentration results in a larger number of ferromagnetic interactions taking place within the material resulting in canted antiferromagnetism [143].

The conflicting reports on both the Néel temperature, nuclear and magnetic structure and the magnetic behaviour of Sr_2MnWO_6 drove the reinvestigation of the material. This was particularly important after the observation of short-range antiferromagnetic correlations in Ba_2MnWO_6 [236]. The introduction of the smaller Sr^{2+} cation into the structure allows the effect of lifting the degeneracy of the exchange interactions via crystallographic distortion to be examined. Furthermore, the impact of this distortion on the magnetic frustration of the lattice may be tested.

Experimental

Approximately 8 g of Sr_2MnWO_6 was prepared by solid-state synthesis, combining $SrCO_3$, MnO_2 and WO_3 stoichiometrically within a mortar and pestle and grinding thoroughly. Primary heating was carried out at 800 °C. Secondary heating was completed at 1250 °C in a controlled atmosphere of 5% H_2/N_2 over a period of approximately 96 hours. The finished reaction yielded a bright orange product. X-ray diffraction patterns suitable for Rietveld analysis were collected using Cu Kα radiation.

Time-of-flight neutron powder diffraction experiments was conducted on the General Materials diffractometer, GEM, based at the ISIS Neutron and Muon Source, Rutherford Appleton Laboratories, Didcot, Oxfordshire, UK [224]. During these measurements Sr_2MnWO_6 was placed into a sealed 8 mm vanadium can. Data from all six detector banks were corrected for absorption. Rietveld analysis was carried out using GSAS and data collected from detector bank 2 – 6. Data collected on detector bank 1 was discarded due to poor signal to noise ratio. The peak shapes were described using a convolution of the Ikeda-Carpenter and Pseudo-Voigt functions and the background was fitted using a shifted Chebyshev polynomial. The magnetic form factor of the Mn^{2+} ion was characterised using values from the neutron data booklet [226]. All neutron diffraction images are from detector bank 4 unless otherwise stated.

Magnetometry was completed at the Material Characterisation Laboratory (based at Rutherford Appleton Laboratories) using the Quantum Design MPMS3 between 2 K and 300 K. Sample preparation and measurement analysis was performed as previously outlined.

Zero, transverse and longitudinal field muon spin relaxation measurements (ZF-, TF-, LF-μSR) were carried out on EMU, ISIS Neutron and Muon Source. ZF-μSR and TF-μSR were completed between 1.5 and 70 K, where the TF-μSR measurements used a field of 100 G. LF-μSR were completed at 1.5 K, 11 K, 15 K and 20 K using magnetic field strengths between 50 and 4000 G. These measurements were completed by creating a packet of Sr_2MnWO_6 which was contained in silver foil and then adhered onto a silver sample holder.

Results

X-ray Powder Diffraction

X-ray powder diffraction indicated that the Sr_2MnWO_6 sample was single phase with all peaks indexed by the monoclinic space group *P2₁/n* in agreement with a number of previous reports [142,143], R_{WP} = 16.9, χ^2 = 1.5. The *P4₂/n* space group was also used as a model and despite indexing each peak this resulted in a poorer fit to the experimental data set than the fit using *P2₁/n*, R_{WP} = 27.6, χ^2 = 3.8 [141]. This combined with the significantly smaller unit cell indicated that *P2₁/n* was the correct setting for Sr_2MnWO_6 with *a* = 5.6800(1) Å, *b* = 5.6713(1) Å, *c* = 8.0188(1) Å and *β* = 89.934(2) °.

Table 5:1: Structural information derived from the results of Rietveld refinement carried out on the X-ray powder diffraction measurement completed on Sr_2MnWO_6 at ambient temperature. This was carried out using the space group $P2_1/n$ with *a* = 5.6800(1) Å, *b* = 5.6713(1) Å, *c* = 8.0188(1) Å and *β* = 89.934(2) °. Mn resides (1/2, 0, 0) and W is located on (1/2, 0, 1/2). This yielded R_{WP} = 16.9 and χ^2 = 1.5. The isotropic displacement factors were fixed for each of the three oxides and the Mn and W cations.

Parameter / Unit	**Value (e.s.d.)**
Sr (x, y, z)	(0.992(2), 0.020(6), 0.250(1)
Sr 100U_{iso} / Å²	1.4(1)
Mn/W 100U_{iso} / Å²	0.70(7)
O(1) (x, y, z)	(0.547(7). 0.009(3), -0.258(4))
O(2) (x, y, z)	(0.735(6), 0.288(7), 0.0356(8))
O(3) (x, y, z)	(0.203(6), 0.226(6), -0.038(7))
O(1,2,3) 100U_{iso} / Å²	0.8(4)

Neutron Powder Diffraction

Neutron powder diffraction data were collected on Sr_2MnWO_6 between 2.1(2) and 90(2) K. Rietveld refinement completed against the 90(2) K indicates that Sr_2MnWO_6 remains monoclinic, adopting the space group $P2_1/n$, see Figure 5.1. The inset of Figure 5.1 shows a portion of the pattern collected on the highest resolution data bank to demonstrate that the peak splitting is well characterised. When the temperature is decreased to 2.1(2) K, there is no change in peak distribution or profile shape at shorted d-spacings indicating that the nuclear structure retains the monoclinic symmetry.

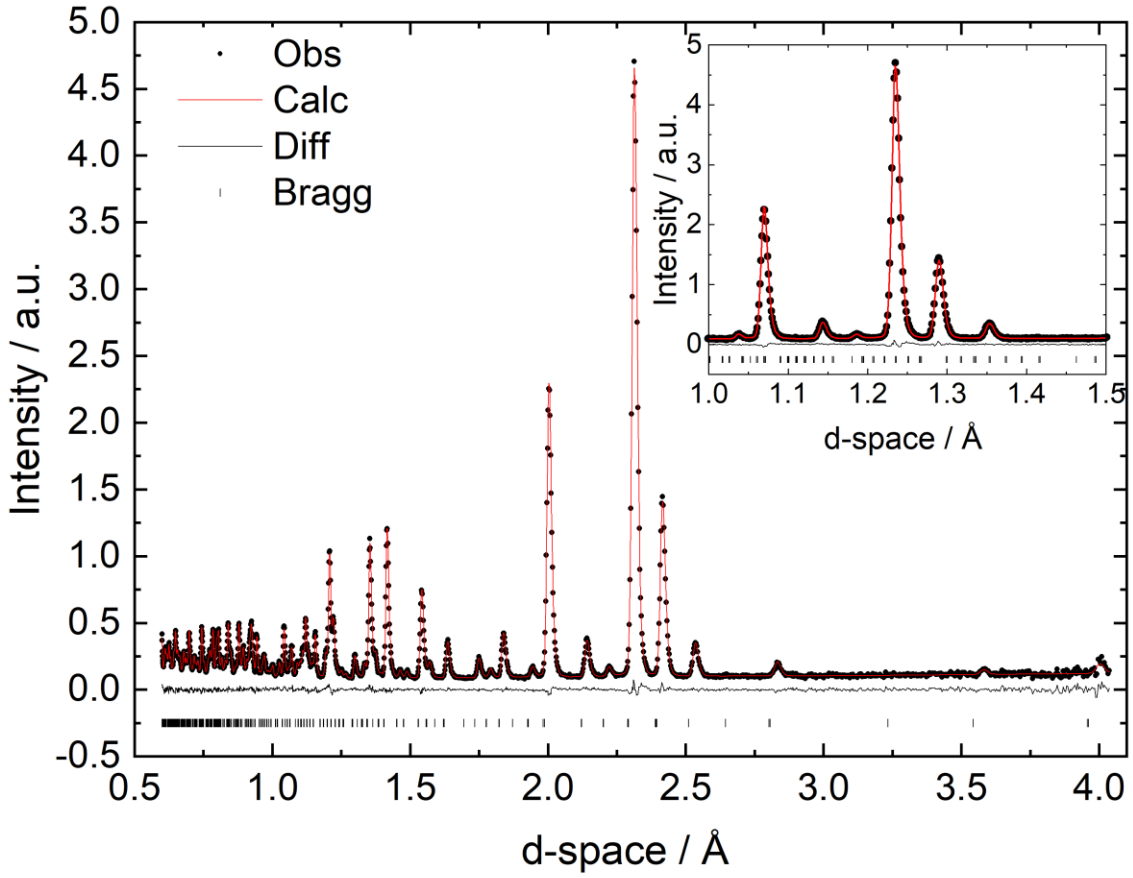

Figure 5.1: Rietveld refinement of neutron powder diffraction data collected on Sr_2MnWO_6 at 90 K. The Bragg reflections correspond to the monoclinic space group *$P2_1/n$*. This pattern is from detector bank 4. The inset image shows the results from the highest resolution detector bank, bank 6, between 1.0 and 1.5 Å d-space, this is to show peak splitting more clearly.

Figure 5.2 shows the thermal dependence of the lattice parameters *a*, *b* and *c* and the *β* angle in Sr_2MnWO_6 over the measured temperature range. The dimensions of the nuclear unit cell each generally expand as the temperature increases, confirming that Sr_2MnWO_6 exhibits conventional thermal expansion properties. The *β* angle deviates slightly from 90° throughout the temperature

range lying between 89.92(2) ° and 89.96(2) °. Small changes in the lattice parameters suggest a change in behaviour around 14.4(5) K, with negative thermal expansion along c and a change in gradient for β.

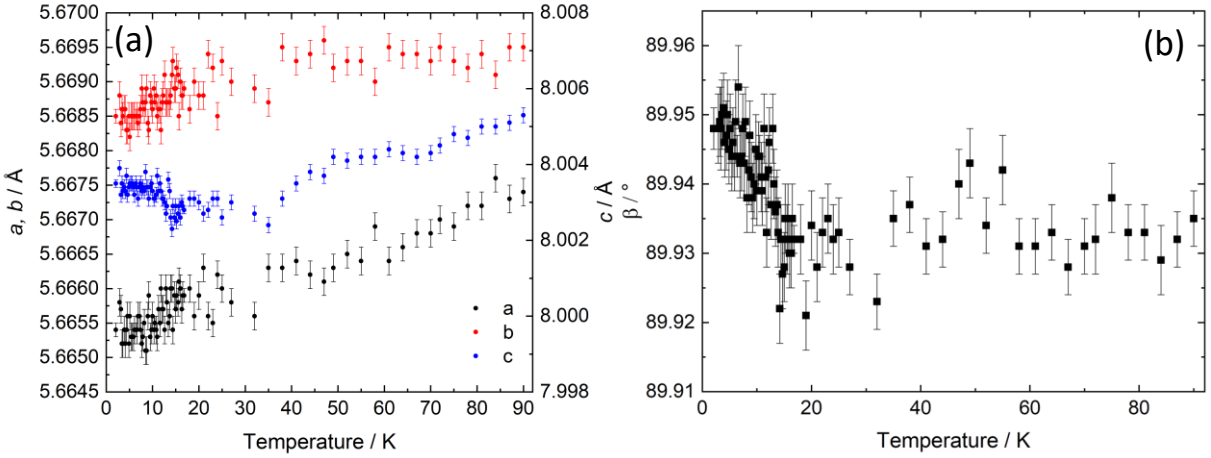

Figure 5.2: (a) The trends of the lattice parameters *a,b* and *c* of Sr_2MnWO_6 between 2 and 90 K obtained from the Rietveld refinement carried out against neutron powder diffraction data sets. Each lattice parameters increases with temperature as would be expected in conventional thermal expansion properties, apart from axes *c* below 14.4(5) K. (b) The trend of the *β* angle of Sr_2MnWO_6 between 2 and 90 K. The angle is found to remain fairly constant with only a 0.04° change over the temperature range.

The bond lengths of the Sr^{2+}, Mn^{2+} and W^{6+} cations to the oxide anions are shown in Figure 5.3. At all temperatures there are 12 distinct Sr-O bonds, four to each individual oxide and three pairs of Mn-O and W-O bond lengths. The 12 Sr -O bond lengths suggest that Sr has a coordination number equal to eight, implied by the presence of four bond lengths > 2.9 Å. Bond valence analysis give a sum of 2.091(2) [10]. Throughout the temperature range, the Sr-O bond lengths experience little change. The coordination environments for the transition metals show MO_6 octahedra that are regular, within accuracy of the bond lengths, and bond valence sums indicate that Mn^{2+} and W^{6+} are both present in Sr_2MnWO_6 [10]. Over the measured temperature range, minimal changes are observed in the *M*-O bond lengths.

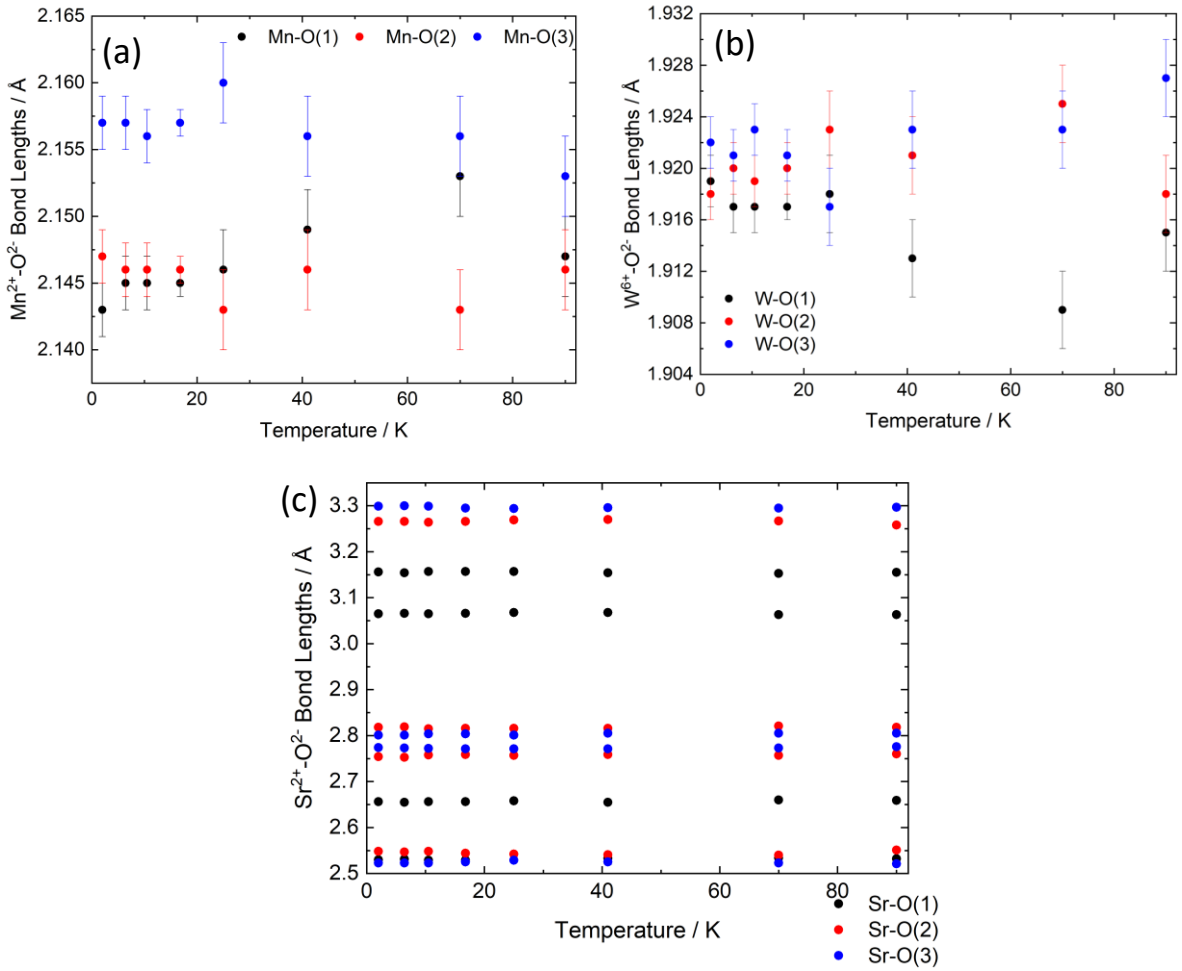

Figure 5.3: The bond lengths of (a) Mn-O, (b) W-O and (c) Sr-O. The Mn-O and W-O bond lengths appear to remain fairly constant throughout the temperature range with no distinct Jahn-Teller effects in either material which is to be expected. The Sr-O bond lengths also appear to remain fairly constant throughout the temperature range.

The 2.1(2) K data set contained additional Bragg peaks corresponding to antiferromagnetic long-range order. A previous study of Sr_2MnWO_6 gave four potential solutions for the magnetic structure outlined in Table 5:2 [142]. Each solution resulted in no significant variation in the fit quality or statistical parameters and do not indicate a unique model. Each contained two inequivalent magnetic Mn^{2+} cations and the symmetry relating them was outlined. Options 1 and 2 are collinear solutions whilst options 3 and 4 are non-collinear solutions derived from linear combinations of the previous options. The collinear options allow the material to show anisotropy as one direction is favoured compared to the others, whilst the non-collinear options remain isotropic. The spherical nature of Mn^{2+} gives no grounds for anisotropy therefore, options 3 and 4 were exclusively explored.

Table 5:2: Muñoz *et al* potential solutions for magnetic structure of Sr_2MnWO_6 [142].Mn(1) and Mn(2) are the two inequivalent ions, these columns show how the two cations are related within the magnetic structure, M_x, M_y and M_z are the coordinates of the magnetic moments and μ_{eff} is the magnitude of the magnetic moment.

Solution	**Mn(1)**	**Mn(2)**	**M_x**	**M_y**	**M_z**	**$\lvert\mu_{eff}\rvert$ (μ_B)**
1	[1 1 1]	[1 $\bar{1}$ 1]	2.5(2)	3.3(2)	-1.7(3)	4.54(6)
2	[1 1 1]	[$\bar{1}$ 1 $\bar{1}$]	2.3(2)	3.7(2)	1.3(3)	4.54(5)
3	[1 1 1]	[1 1 1]	2.3(2)	3.6(2)	-1.4(3)	4.54(5)
4	[1 1 1]	[$\bar{1}$ $\bar{1}$ $\bar{1}$]	2.4(2)	3.5(3)	1.5(3)	4.54(6)

These solutions were initially analysed using FULLPROF. The k-search function was used to determine the propagation vector of Sr_2MnWO_6. This yielded two potentials which had similar probabilities **k** = (1/2, 0, 1/2) or **k** = (0, 1/2, 1/2). The first propagation vector was utilised as this was calculated to be marginally more likely and was also suggested in the previous report [142]. Solution 4 failed to calculate any intensity for the first magnetic peak, at *ca.* 9 Å. Option 3 provided a good match to the observed intensity distribution and was refined using GSAS.

Table 5:3: Magnetic structure of Sr_2MnWO_6 used in Rietveld refinement at 2 K.

Magnetic Mn^{2+} position	**Mn^{2+} magnetic moment vector**
(0, 1/2, 1/4)	(2.3, 3.6, -1.4)
(0, 1/2, 3/4)	(-2.3, -3.6, 1.4)
(1/4, 0, 0)	(2.3, 3.6, -1.4)
(1/4, 0, 1/2)	(-2.3, -3.6, 1.4)
(1/2, 1/2, 1/4)	(-2.3, -3.6, 1.4)
(1/2, 1/2, 3/4)	(2.3, 3.6, -1.4)
(3/4, 0, 0)	(-2.3, -3.6, 1.4)
(3/4, 0, 1/2)	(2.3, 3.6, -1.4)

Fitting the magnetic structure was completed in a similar fashion to Ba_2MnWO_6 and therefore this chapter should be referred to for an in-depth description. Figure 5.6 indicates the proposed magnetic structure of Sr_2MnWO_6. This resulted in an excellent fit to the diffraction pattern with R_{wp} = 3.00, see Figure 5.4. The results of the 2 K refinement can be observed in Table 5:4 [225,230,231].

The effective magnetic moment was calculated from the neutron powder diffraction using the equation outlined in the Ba_2MnWO_6 chapter, it has been reiterated below for simplicity.

Equation 5.1: Calculating the effective magnetic moment from neutron powder diffraction data

$$\mu_{ord} = \sqrt{(\mu_{ref})^2 \left(\frac{PF_{ref}}{PF_{act}}\right)}$$

The ordered magnetic moment refined to a value of 4.5(1) μ_B, in agreement with previous report of 4.54(6) μ_B [142]. This corresponds to the S = 5/2 spin state of Mn^{2+}. The ordered magnetic moment decreases with increasing temperature until the magnetic transition at 13.7(3) K as shown in Figure 5.5. Above this temperature no magnetic Bragg peaks can be observed and no evidence of diffuse magnetic scattering is observed as shown in the inset of Figure 5.4 [172].

Table 5:4: Values obtained from Rietveld refinement carried out on neutron powder diffraction data collected on Sr_2MnWO_6 at 2 K. Sr_2MnWO_6 adopts the monoclinic space group *P2₁/n* where Mn sits on (1/2, 0, 0) and W on (1/2, 0, 1/2).

Refinement Parameter	**Value / error**
***a* / Å**	5.6654(1)
***b* / Å**	5.6685(1)
***c* / Å**	8.0035(1)
β / °	89.948(3)
V / Å^3	257.028(2)
Sr (x, y, z)	(0.9953(2), 0.0254(1), 0.2498(3))
Sr 100U_{iso} / Å^2	0.19(1)
Mn 100U_{iso} / Å^2	0.16(2)

W 100U_{iso} / Å^2	0.13(2)
O(1) (x, y, z)	(0.5602(3), 0.0111(2), -0.2642(2))
O(1) 100U_{iso} / Å^2	0.29(2)
O(2) (x, y, z)	(0.7346(4), 0.2944(3), 0.0307(3))
O(2) 100U_{iso} / Å^2	0.40(3)
O(3) (x, y, z)	(0.2013(3), 0.2311(4), -0.0331(3))
O(3) 100U_{iso} / Å^2	0.37(3)
R_{wp} global	3.34
X^2	5.97
Sr-O(1) / Å	3.156(2), 2.530(2), 3.065(1), 2.656(1)
Sr-O(2) / Å	2.754(3), 2.548(3), 3.266(3), 2.818(3)
Sr-O(3) / Å	2.801(3), 3.299(3), 2.523(3), 2.774(3)
Sr BVS	2.091(2)
Mn-O(1) / Å	2.143(2)*2
Mn-O(2) / Å	2.147(2)*2
Mn-O(3) / Å	2.157(2)*2
Mn BVS	2.274(1)
W-O(1) / Å	1.919(2)*2
W-O(2) / Å	1.918(2)*2
W-O(3) / Å	1.922(2)*2
W BVS	6.021(3)
Mn-O(1) –W / °	160.3(1)
Mn-O(2)–W / °	160.5(1)
Mn-O(3)–W / °	158.5(1)

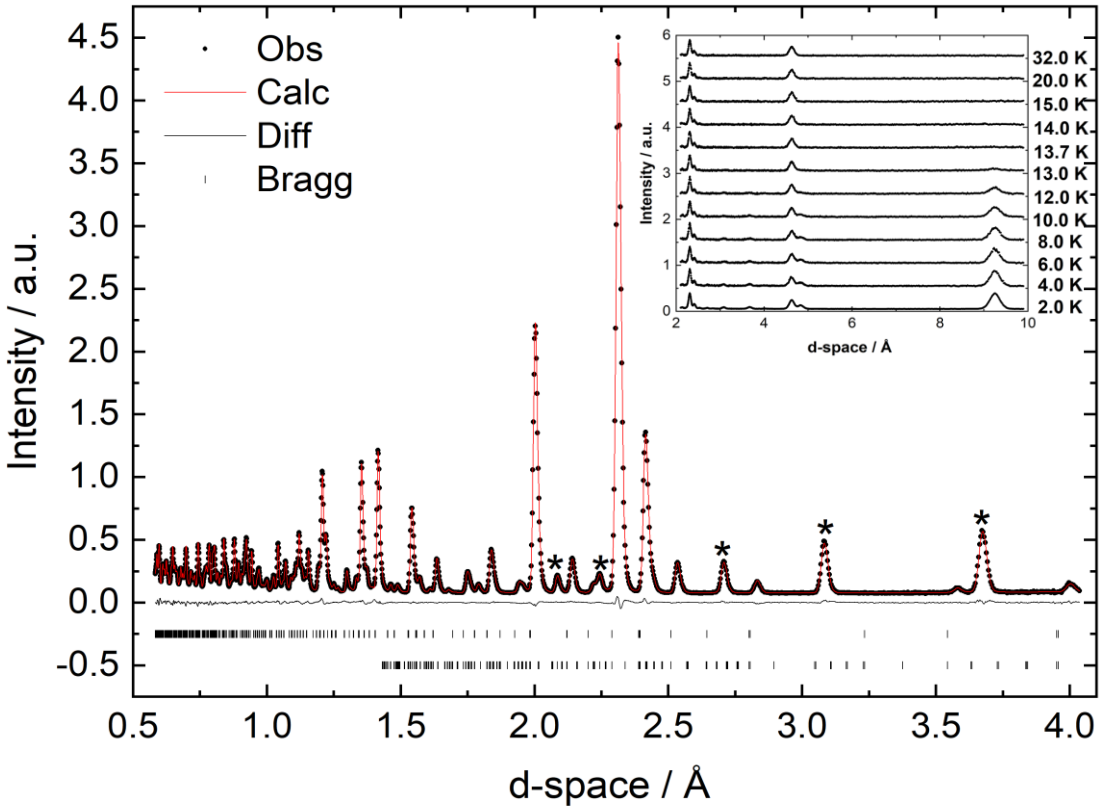

Figure 5.4: Rietveld refinement carried out against the neutron powder diffraction data set collected on Sr_2MnWO_6 at 2 K. The upper row of Bragg reflections corresponds to Sr_2MnWO_6 (*P2₁/n*) and the lower are attributed to the long-range antiferromagnetic structure, characterised using the P1 space group. Magnetic Bragg peaks are outlined by an asterisk (*). Inset image shows the diffraction pattern collected from detector bank 2 at a variety of temperatures. The feature around 9 Å corresponds to the first magnetic peak which cannot be observed above 13.7(2) K.

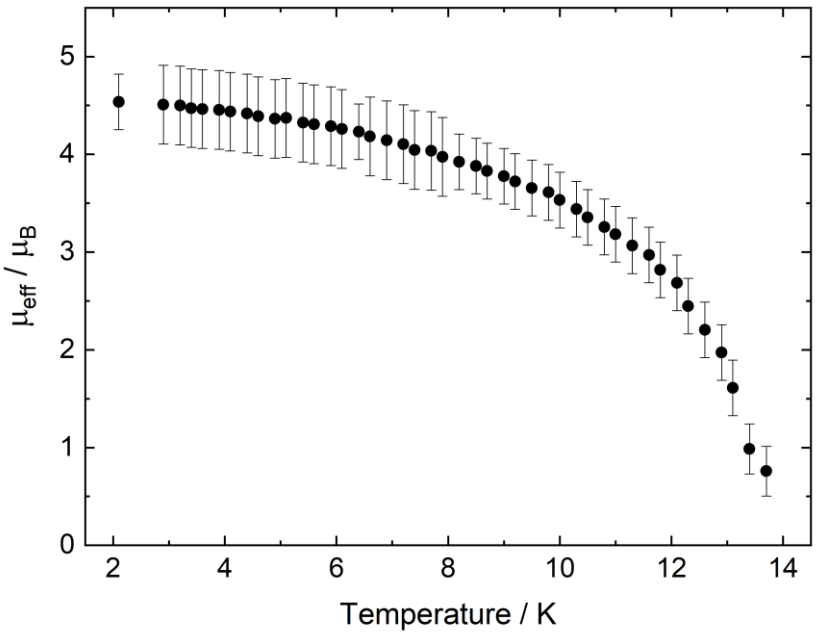

Figure 5.5: The temperature dependence of the effective magnetic moment of Sr_2MnWO6. This was calculated from the Rietveld refinement of the neutron powder diffraction data between 2.1 K and 13.7 K, which has been taken as the transition temperature. The maximum μ_{eff} arises at 2.1 K as expected.

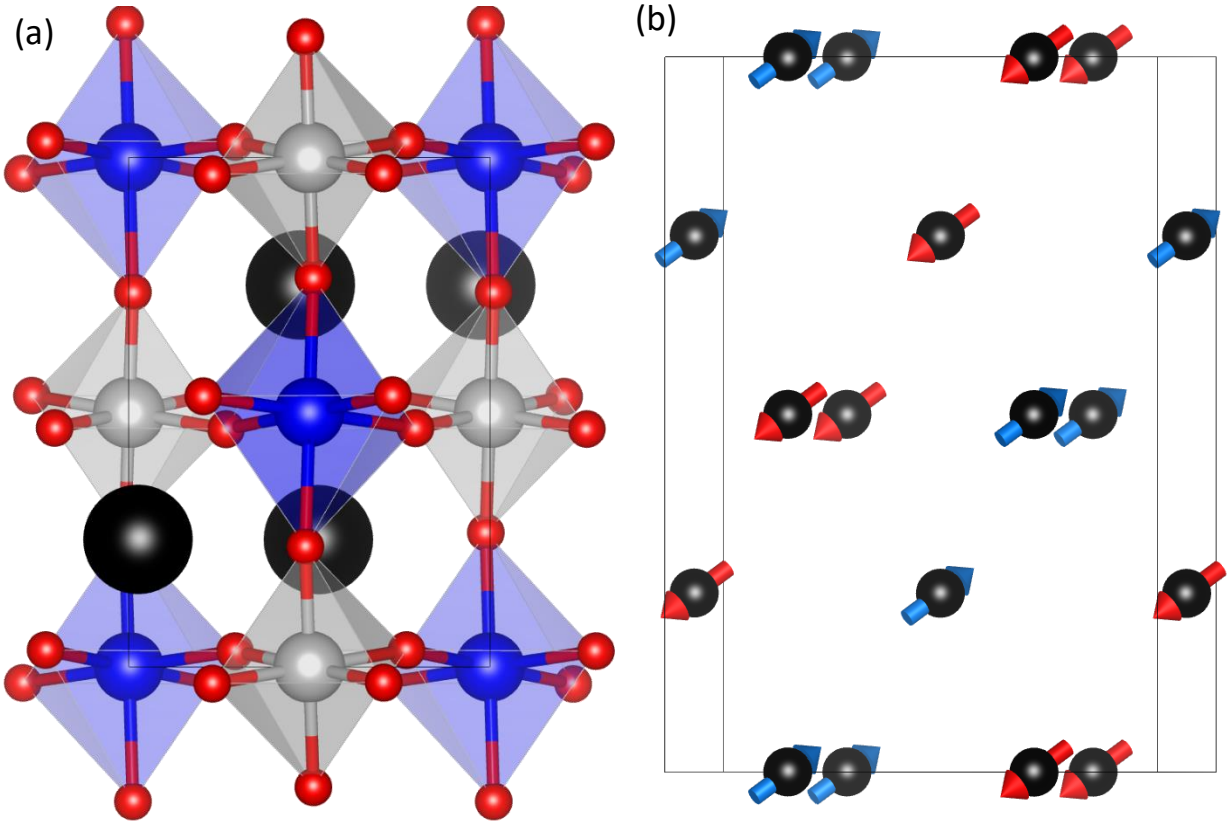

Figure 5.6: (a) A depiction of the nuclear structure of Sr_2MnWO_6. The black spheres represent the Sr^{2+} ions, the grey and blue spheres are Mn and W respectively and red spheres represent the oxide anions. (b) A depiction of the magnetic structure of Sr_2MnWO_6, only the Mn^{2+} cations are shown for simplicity, the vectors represent the direction of the magnetic moment.

DC-Susceptibility

Magnetometry measurements between 2 and 300 K indicated a Néel transition at 13.5(2) K with no ZFC/FC divergence as shown in Figure 5.7. Curie-Weiss analysis was carried out between 100 and 300 K which yielded C_{CW} = 4.82(1) cm^3 K mol^{-1}, θ_{CW} = -76(1) K and μ_{eff} = 6.2(3) μ_B. This agrees with the spin only μ_{eff} expected for high spin Mn^{2+}. The frustration index could then be calculated by dividing θ_{CW} by the transition temperature, resulting in f = 6(1), showing moderate frustration.

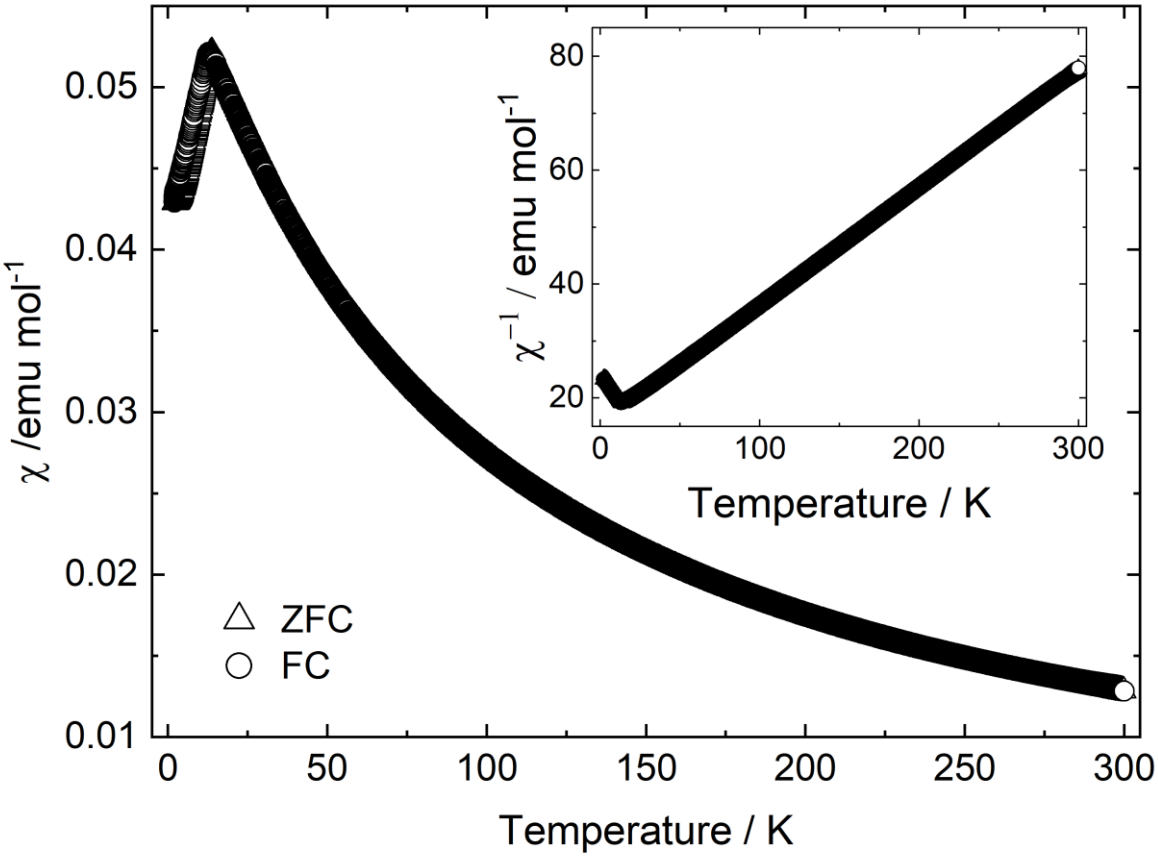

Figure 5.7: The magnetic susceptibility response of Sr_2MnWO_6 collected between 2 and 300 K. The main plot indicates the thermal dependence of the susceptibility and the inset graph contains the inverse susceptibility response. This indicates an antiferromagnetic transition at 13.5(2) K.

Muon Spin Relaxation

Transverse field muon spin relaxation measurements (TF-μSR) were performed between 1.5(1) and 70(2) K to accurately determine the transition temperature of Sr_2MnWO_6. Fits of the data at various temperatures are depicted in Figure 5.8. In general, the overall asymmetry is small at low temperatures and increases significantly at 12.8(2) K. This change in behaviour required different fitting functions to be applied over three specific temperature ranges. Throughout the temperature range 1.5(1) to 12.5(2) K, the data sets were fitted using the following function;

Equation 5.2: Asymmetry fitting function of TF-μSR of Sr_2MnWO_6 between 1.5(1) K and 12.5(2) K

$$A(t) = (A_{osc}\exp(-\lambda_{osc}t)\cos(2\pi fx+\varphi)) + (A_2\exp(-\lambda_2 t)) + A_3$$

Here, A_{osc}, A_2 and A_3 are the asymmetries attributed to the oscillating decay, the exponential decay and the constant signal respectively. The relaxation rate λ_{osc} corresponds to the oscillating component and λ_2 describes the exponential relaxing component. The frequency and phase of the oscillations are described by f and φ respectively. The A_3 constant signal represents ordered magnetism, whilst the oscillating decay and exponential relaxation describe paramagnetism.

At 1.5(1) K, A_3 has the largest magnitude, therefore, ordered magnetism comprises most of the system at this temperature. As the temperature increases, the magnitude of A_3 decreases and simultaneously A_2 increases in size. A_{osc} shows a significant increase at 12.5(2) K. Throughout the temperature range, λ_2 is approximately ten times faster than λ_{osc}. However, λ_{osc} is found to generally increase with temperature whilst λ_2 declines as the temperature increases. The thermal dependence of the asymmetry and the relaxation rates can be observed in Figure 5.9.

A change to the fitting function is necessary between 12.8(2) and 13.0(2) K as the constant contribution arising from the internal magnetic field is no longer detectable.

Equation 5.3: Asymmetry fitting function of TF-μSR of Sr_2MnWO_6 between 12.8(2) and 13.0(2) K

$$A(t) = (A_{osc}\exp(-\lambda_{osc}t)\cos(2\pi fx+\varphi)) + (A_2\exp(-\lambda_2 t))$$

Over this small temperature range, the oscillating component dominates. A_{osc} and λ_{osc} increase with temperature whilst A_2 and λ_2 decrease. As this is only two data points this will be excluded from any figures.

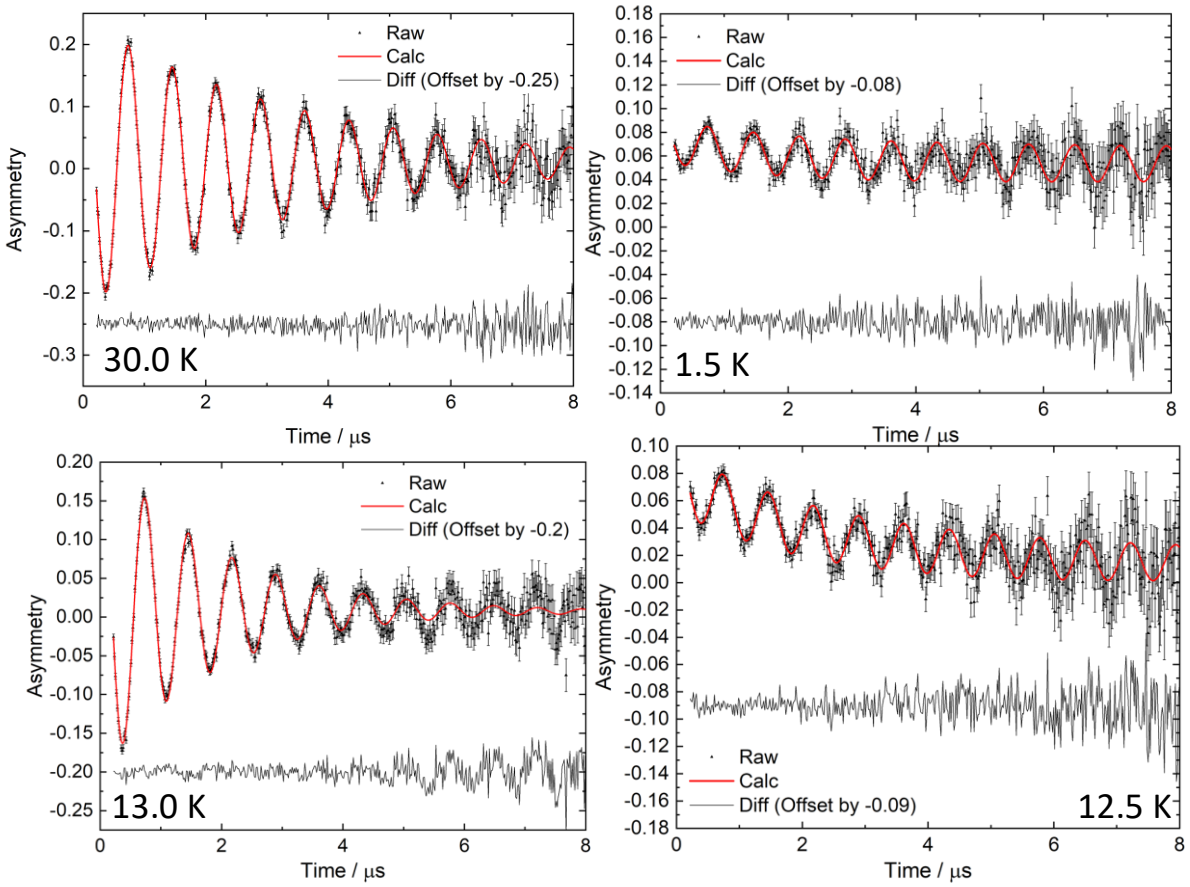

Figure 5.8: TF-μSR collected on Sr_2MnWO_6 at a variety of temperatures; 30(2) K, 1.5(1) K, 13.0(2) K and 12.5(2) K measured using a transverse field of 100 G. These were fitted using $A(t) = (A_{osc}\exp(-\lambda_{osc}t)\cos(2\pi fx+\varphi)) + (A_2\exp(-\lambda_2 t)) + A_3$. Each difference curve has been offset by a specific value, which is specified in the legend of each figure.

Above 13.0(2) K, the function changes again as the fluctuations of the exponential relaxation rate slow and are no longer observed by the muons. The fitting function then becomes;

Equation 5.4: Asymmetry fitting function of TF-μSR of Sr_2MnWO_6 between 14.0(5) K and 30(2) K.

$$A(t) = (A_{osc}\exp(-\lambda_{osc}t)\cos(2\pi fx+\phi)) + A_2$$

Over this temperature range, A_2 is present in a very small fraction, this experiences a minimal increase with temperature although within three standard deviations this parameter would be taken as constant. Conversely, A_{osc}, is present in a large proportion and the magnitude conclusively increases

with temperature. The relaxation rate of the oscillating component, λ_{osc}, decreases as the temperature is raised. Plots showing these effects can be observed in Figure 5.10.

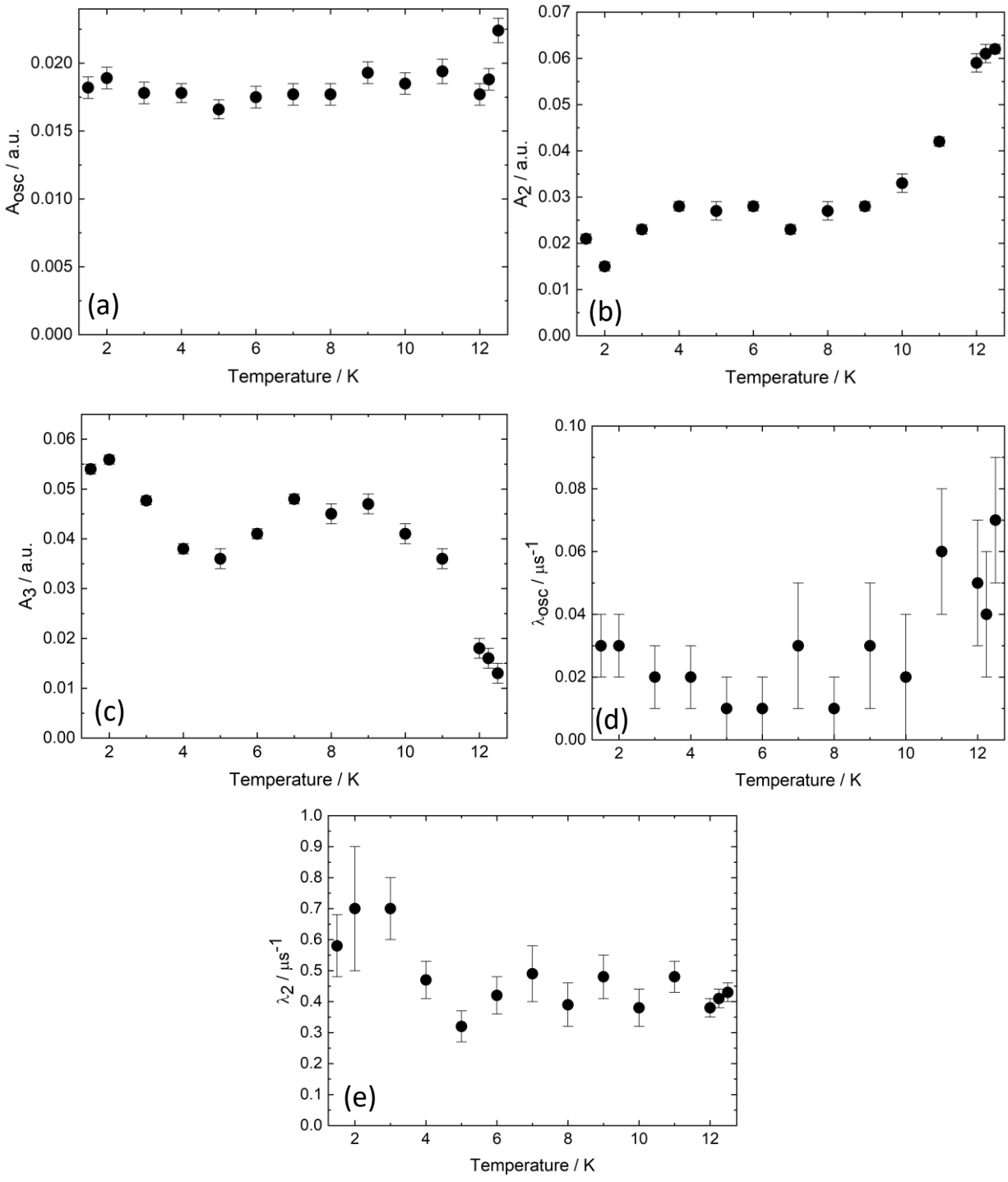

Figure 5.9: Results of fittings from TF-μSR collected on Sr_2MnWO_6 between 1.5(1) K and 12.5(2) K. The thermal dependence of (a) $A_{osc,}$ (b) A_2, (c) A_3, (d) λ_{osc} and (e) λ_2. A_{osc} remains fairly constant prior to increasing at 12.5(2) K, A_2 shows a general increase with temperature, A_3 shows a general decrease as temperature increases. The relaxation rate λ_{osc}, is fairly unchanged until an increase at 11.5(2) K and λ_2 shows a decrease but plateaus from 4.0(2) K onwards.

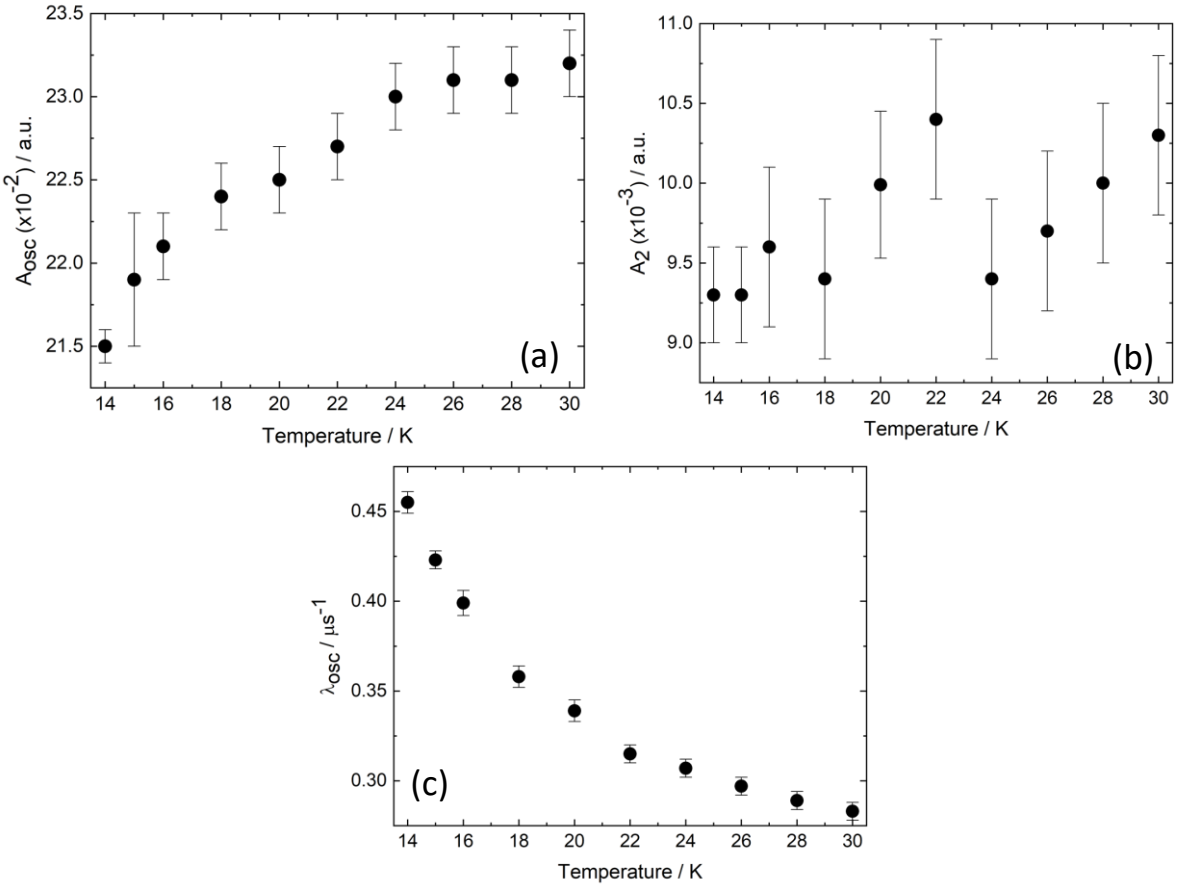

Figure 5.10: Results of fittings from TF-μSR collected on Sr_2MnWO_6 between 14.0(5) K and 30(2) K. The thermal dependence of (a) A_{osc}, (b) A_2 and (c) λ_2. A_{osc} experiences a steady increase from 14.0(5) K to 30(2) K, A_2 experiences a slight increase with temperature but this is within three standard deviations of remaining constant and λ_{osc} decreases progressively as the temperature increases.

Zero-field muon spin relaxation (ZF-μSR) measurements were carried out between 1.5 and 70 K. The fits carried out on the 1.5, 12, 13 and 30 K data sets are shown in Figure 5.11. Like the TF-μSR measurements, the overall asymmetry was small at low temperature but increased significantly at 12.8(2) K and different fitting functions were necessary over various temperature regions.

Between 1.5(5) and 12.5(2) K an exponential relaxation plus a constant signal term describes the muon behaviour, this is shown below;

Equation 5.5: Asymmetry fitting function of ZF-μSR for Sr_2MnWO_6 between 1.5(5) K and 12.5(2) K.

$$A(t) = (A_1 \exp(-\lambda_1 t)) + A_2$$

In this function, A_1 and λ_1 represent the asymmetry and the relaxation rate of the paramagnetic proportion of the system, and A_2 corresponds to any ordered magnetism within Sr_2MnWO_6. Over this

temperature range A_1 rises with temperature in conjunction with a general decrease in A_2. The relaxation rate, λ_1 is initially high before experiencing a significant decrease at 10.0(2) K followed by a gradual increase with the temperature. The error bars on λ_1 are significantly larger below 10.0(2) K, this is potentially due to issues stabilising the cryostat temperature which was at higher temperatures prior to these measurements being taken. The results of this are shown in Figure 5.12.

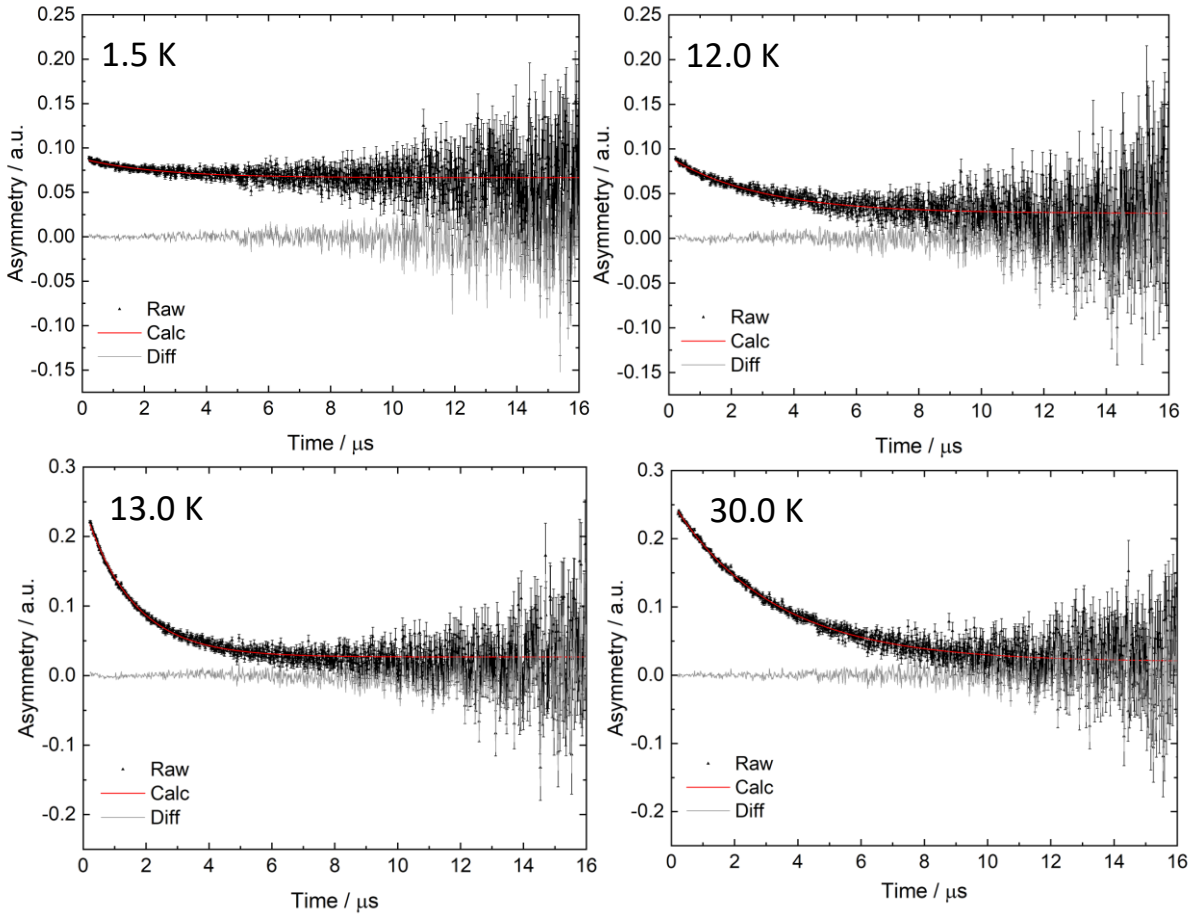

Figure 5.11: ZF-μSR measurements collected on Sr_2MnWO_6 at 1.5 K, 12 K, 13 K and 30 K. The calculated line is shown in red and lies directly in the centre of the relaxation curve indicating a satisfactory fit to the data set.

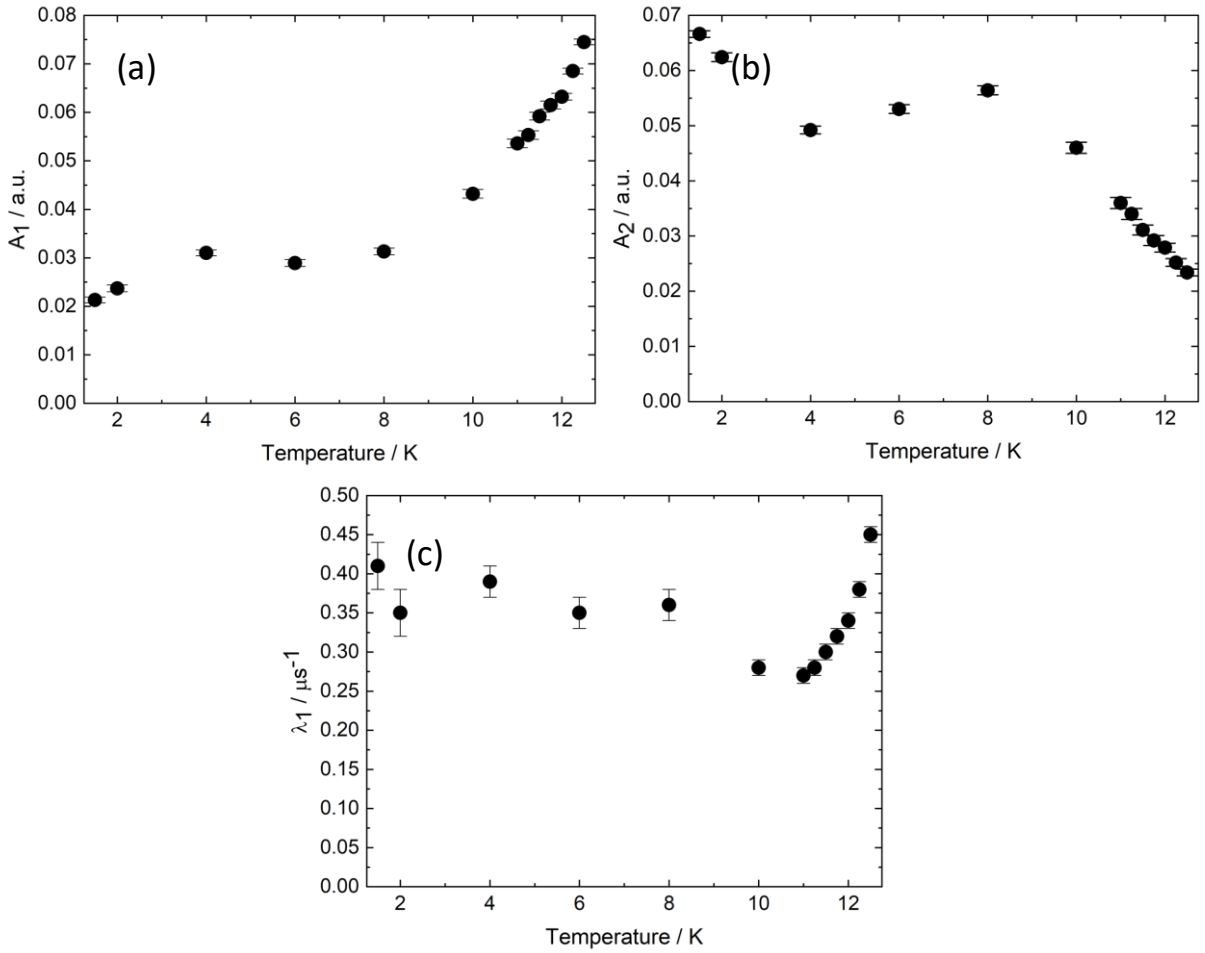

Figure 5.12: Results of fitting from ZF-μSR collected on Sr2MnWO6 between 1.5(5) and 12.5(2) K. This shows the thermal dependence of (a) A_1, (b) A_2 and (c) λ_2. The relaxing asymmetry is low and increases with temperature, conversely, the static asymmetry decreases as the temperature increase. The relaxation rate, λ_1 increases as the temperature increases.

Between 12.8(2) and 30(2) K, a distinct change is observed in the relaxation curve. This requires the stretching parameter, β, to be introduced to modify the fitting function to;

Equation 5.6: Asymmetry fitting function of ZF-μSR for Sr_2MnWO_6 between 12.8(2) K and 30.0(20) K.

$$A(t) = (A_1 \exp(-\lambda_1 t)^{\beta 1}) + A_2$$

The thermal dependence of the asymmetries, the relaxation rate and the stretching parameter are shown in Figure 5.13. The relaxing asymmetry is present in a significantly greater proportion than the ordered magnetism throughout the temperature range, resembling the results from TF-μSR. A_1 increases dramatically between 12.8(2) and 13.0(5) K, then experiences minimal change. A_2 remains constant within error, between 12.8(2) K and 30(2) K. The relaxation rate decreases as the

temperature increases, this is initially a sharp decrease, becoming more gradual at the higher temperatures within the range. The stretching parameter β_1 is initially much lower than 1, indicating that the material does not behave like a conventional paramagnet. As the temperature rises, β_1 tends to 1, which is expected for paramagnetic behaviour.

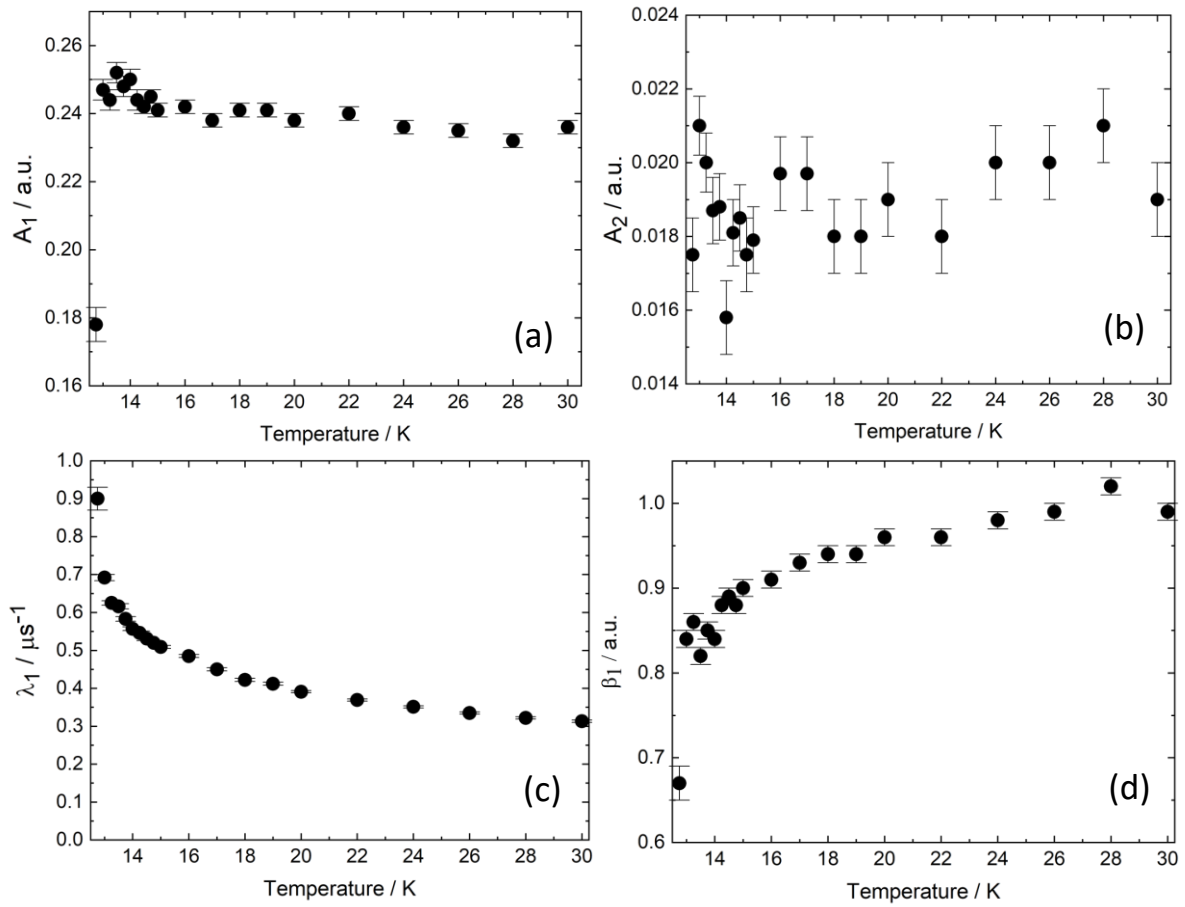

Figure 5.13: Results of the analysis and fitting from ZF-μSR collected on Sr_2MnWO_6 between 12.8(2) K and 30(2) K. The thermal dependence of (a) A_1, (b) A_2, (c) λ_1 and (d) β_1. A_1 increases dramatically above 12.8(2) K and then remains fairly constant over the temperature range. A_2 stays approximately equal throughout the temperature range. λ_1 decreases gradually as the temperature increases and β_1 increases to 1 over the temperature range.

LF-μSR was completed both above and below the expected transition temperature to observe the decoupling behaviour of the magnetic cations within Sr_2MnWO_6. The collected data at 1.5, 11, 15 and 30 K can be observed in Figure 5.14 (a), (b), (c) and (d) respectively. The relaxation curve follows a similar trend at each of the investigated temperatures where a full decoupling of the magnetic moment is not achieved even when significantly above the transition temperature. This could suggest potential short-range magnetic interactions within Sr_2MnWO_6.

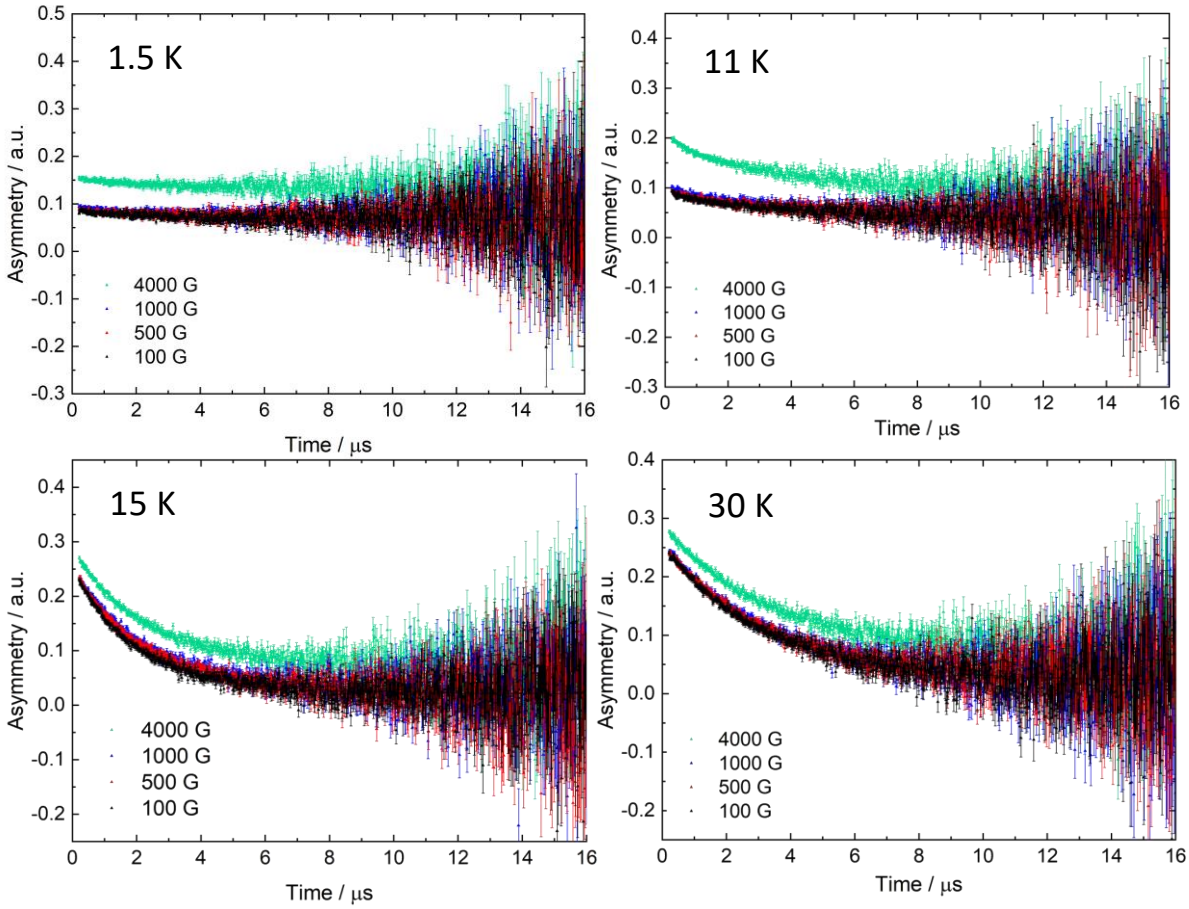

Figure 5.14: LF-μSR measurements collected on Sr_2MnWO_6 at 1.5, 11, 15 and 30 K between the magnetic field strengths 100 G and 4000 G. At all the indicated temperatures, the 4000 G magnetic field does not result in a completely flat signal. This suggests that a potential short-range correlated state may be present within the system as the internal magnetic fields are not decoupled even at 30 K, which is significantly above the transition temperature.

Above and below the transition temperature different fitting functions are required to describe the experimentally acquired data. This shows that the material is different above and below this temperature. However, in all cases the asymmetry and relaxation rates are unaffected by the strength of the magnetic field until the field strength is equal to 4000 G, where only the asymmetry increases. This suggests strong magnetic behaviour above the transition temperature.

Discussion

Sr_2MnWO_6 is a frustrated double perovskite which adopts the distorted monoclinic space group $P2_1/n$. This is deviated from $Fm\bar{3}m$ due to the small ionic radii of the Sr^{2+} cation, 1.44 Å compared to 1.61 Å for the Ba^{2+} cation [237]. This distortion can be predicted using the Goldschmidt tolerance factor, for Ba_2MnWO_6 this is equal to 1.01 whilst for Sr_2MnWO_6 the tolerance factor is equal to 0.96, which

suggests distortions will occur. The distortion occurs via octahedral tilting [48,238]. The tilting can be described by the Glazer tilt system, $a^-a^-c^+$. This allows the Sr^{2+} cation to receive the correct amount of bonding. This is established from bond valence sums which calculates a valence of 2.09, close to the ideal +2 oxidation state [10]. The tilting of the monoclinic structure also affects the magnetic superexchange angle which lies at 160.3(1) °, 160.5(1) ° and 158.5(1) °. These are significantly distorted from the ideal 180° which could allow competing ferromagnetic interactions to take place more easily than in the cubic structure. This could allow the onset of long-range order at a higher temperature.

The bulk magnetic behaviour observed in the neutron diffraction patterns of Ba_2MnWO_6 and Sr_2MnWO_6 are similar. Despite the distortion of Sr_2MnWO_6, both systems adopt a Type II antiferromagnetic structure [62]. DC-susceptibility measurements show that Sr_2MnWO_6 becomes antiferromagnetically ordered at 13.5(2) K, higher than the transition observed in Ba_2MnWO_6. Both materials exhibit Curie-Weiss behaviour between 100 and 300 K with similar values obtained for C_{CW} and θ_{CW} and no ZFC/FC divergence. This shows that substitution of the *A*-site cation has minimal effect on the magnetic interactions. However, a significant effect is observed in the frustration index, which could be attributed to the change in *A*-site cation and subsequent structure distortion. Ba_2MnWO_6 is more strongly frustrated, with f = 8(1) compared to f = 6 (1) for Sr_2MnWO_6. This is surmised to be linked to the structural change. Table 5:5 outlines the magnetic parameters of both systems.

Table 5:5: Comparison of the magnetic parameters extracted from the Curie-Weiss analysis of magnetic susceptibility measurements carried out on Ba_2MnWO_6 and Sr_2MnWO_6.

Parameter	**Ba_2MnWO_6**	**Sr_2MnWO_6**
T_N / K	8.4(2)	13.5(2)
C_{CW} / emu mol^{-1} K^{-1}	4.91(1)	4.82(1)
θ_{CW} / K	-63(1)	-76(1)
μ_{eff} / μ_B	6.3(3)	6.2(3)
f	8(1)	6(1)

Muon spin relaxation measurements agree with Sr_2MnWO_6 experiencing long-range antiferromagnetic order with Néel temperature equal to 12.8(2) K. TF-μSR allowed this to be observed clearly with the thermal dependence of the normalised oscillating asymmetry. This corresponds to paramagnetic behaviour within the structure, below T_N this is small as ordered magnetism dominates whilst above T_N paramagnetic behaviour takes place and therefore a large increase is observed. In a long range ordered system, oscillations in the relaxation curve are expected in the ZF-μSR below the transition temperature. These were not observed in these data sets due to the size of the pulse width at the muon source. Despite the lack of oscillations, the results from ZF-μSR also suggested that the material entered a long-range ordered phase with a quenched asymmetry below 12.8(2) K, with a large increase above this temperature. The trend observed in λ_1 prior to T_N has also been reported in Ba_2CaOsO_6, another frustrated double perovskite which experiences antiferromagnetic long-range order. The two materials have different fitting functions, as an oscillation is observed in these measurements, which suggest that the relaxation rate in Sr_2MnWO_6 could be comprised of more than one relaxation, however, this could not be confirmed from our measurements [189]. The function used to fit the ZF-μSR data sets above T_N could be indicative of short-range magnetic correlations taking place within the materials as the β_1 parameter suggests that the paramagnetic behaviour is unconventional. LF-μSR below 12.8(2) K suggest long range order is present within the material as a full decoupling of the relaxation curve is not observed when a 4000 G external field is applied. This implies that the internal magnetic fields are significantly stronger than this, and therefore, magnetic long-range order takes place. Above 12.8(2) K, this trend is still observed. This continues to take place at 30(2) K, which is significantly higher than the transition temperature, which suggests that potential short-range magnetic correlations take place within Sr_2MnWO_6.

Ba_2MnWO_6 and Sr_2MnWO_6 exhibit similar results from TF-μSR, although some distinct differences are present which can be clearly observed from the thermal dependence of the normalised oscillating asymmetry. A plot of these responses can be observed in Figure 5.16. In both systems, the oscillating component is small below their respective Néel temperatures before rising significantly. Above T_N, the

differences are apparent, Ba_2MnWO_6 only jumps to around 60% of its final asymmetry, whilst Sr_2MnWO_6 rises to approximately 90%. This suggests that Ba_2MnWO_6 experiences short-range magnetic correlations and that it is less likely that Sr_2MnWO_6 exhibits these. This could also suggest that any short-range correlations in Sr_2MnWO_6 may be weaker or take place over a smaller temperature range. However, the LF-μSR data contradicts this showing that it is entirely feasible that Sr_2MnWO_6 could show short-range magnetic correlations above T_N.

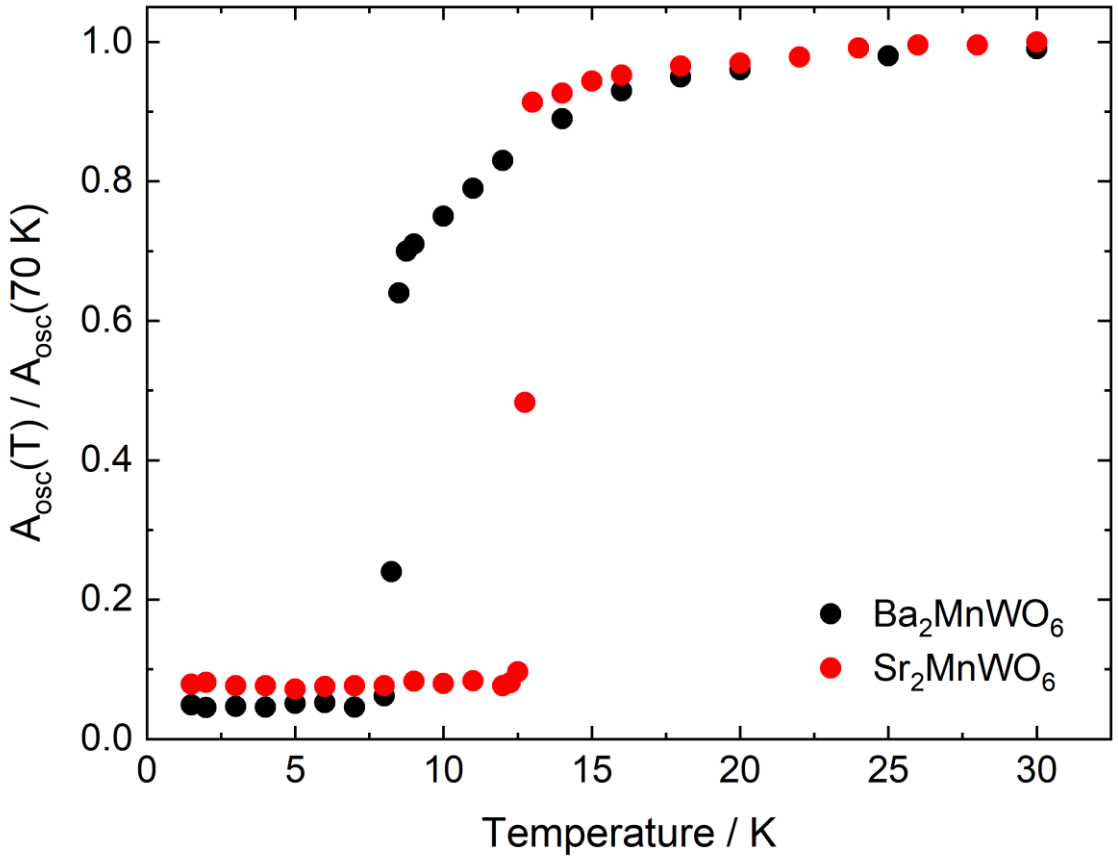

Figure 5.16: Comparison of the normalised oscillating asymmetry of Ba_2MnWO_6 and Sr_2MnWO_6. Below the respective transition temperatures, the magnitude of the normalised asymmetry is very low, which is attributed to long range magnetic order. Both materials experience large increases at T_N, this increase is larger in Sr_2MnWO_6. Above T_N, a subsequent increase is observed in the normalised asymmetry. Ba_2MnWO_6 shows a gradual increase surmised to be caused by potential short-range correlations. The normalised asymmetry of Sr_2MnWO_6, reaches 0.9 and then the increase to 1 occurs. This difference could suggest that Sr_2MnWO_6 does not experience any short-range magnetic correlations above the transition, or that these are much weaker compared to the cubic system. refe bars are displayed; however, these are smaller than the icons.

Comparing Sr_2MnWO_6 to Ba_2MnWO_6 has shown that the substitution of the *A*-site cation influences both the nuclear and magnetic behaviour. The smaller Sr^{2+} cation results in a monoclinic distortion but does not affect the Type II antiferromagnetic character. However, Sr_2MnWO_6 experiences a higher

transition temperature which is anticipated to be caused by this change in structure. This is rationalised by the change in the superexchange angles which deviate from linear. The local magnetic behaviour is slightly different although ultimately there is some suggestion that short range magnetic interactions do arise in both materials. The short-range correlated state is currently inconclusive for Sr_2MnWO_6 and further investigation is necessary to prove this.

Conclusion

Sr_2MnWO_6 was investigated using neutron powder diffraction, DC-susceptibility measurements and muon spin relaxation measurements. Sr_2MnWO_6 adopts the monoclinic space group $P2_1/n$ at ambient temperature and retains this structure to 2 K. This material is found to achieve long range antiferromagnetic order at 13.5(5) K with a propagation vector of **k** = (1/2, 0, 1/2) adopting a Type II antiferromagnetic arrangement. Longitudinal field muon spin relaxation measurements suggest the formation of a potentially short range magnetically correlated state above the magnetic ordering temperature, although at this stage this has not been confirmed.

Further work

The muon spin relaxation measurements tend to contradict themselves depending on the applied field. Transverse field measurements suggest that a short-range correlated state is unlikely to be present above the transition temperature. Simultaneously, longitudinal field measurements suggest that these short-range magnetic interactions may take place above the Néel temperature because the internal magnetic fields are not decoupled despite a 4000 G field being applied. Evidence of this potential short range correlated state should be investigated using inelastic neutron scattering or diffuse magnetic scattering. Until these measurements have been collected more conclusive statements cannot be made about the potential of short-range magnetic correlations above T_N in Sr_2MnWO_6.

6. Investigating Magnetic Percolation in S = 3/2 $Ba_2Co_{1-x}Zn_xMoO_6$

Moving from the S = 5/2 spin state to the S = 3/2 spin state allowed the solid solution $Ba_2Co_{1-x}Zn_xMoO_6$ to be investigated. This contains the Co^{2+} cation ($3d^7$) which can adopt either a high or low spin configuration in an octahedral field leading to S = 3/2 and S = 1/2 spin states respectively. Co^{2+} possesses an unequal occupancy of the 3d orbitals, which can result in a Jahn-Teller distortion of the CoO_6 octahedra and result in anisotropy. Anisotropy has been observed in CoO and is rationalised as arising from spin-spin interactions, permanent magnetic dipoles, orbital-orbital interactions, spin orbital coupling, and as a result of structural deformation [131]. Strong spin orbital effects cause crystal field splitting allowing thermal dependent magnetic behaviour. High temperature behaviour stems from electrons populating the J = 1/2 and J = 3/2 states, whilst at low temperature only the J = 1/2 spin state is populated [239]. Consequently, the Co^{2+} cation often deviates from Curie-Weiss behaviour.

In *fcc* lattices the percolation threshold is dependent on the magnetic interactions involved [3,4]. If only NN magnetic cations interact, the percolation threshold equals 0.198, therefore, long-range magnetism should persist when ≥19.8% of the cations are magnetic. The percolation threshold decreases as more interactions participate; if both NN, J_1 and NNN, J_2 contribute, the threshold falls to 0.136. When J_3 or J_4 interactions are significant, this falls to 0.061 and 0.050 respectively [33].

To investigate the magnetic behaviour of the Co^{2+} cation and the percolation effect on the *fcc* lattice, the solid solution $Ba_2Co_{1-x}Zn_xMoO_6$ ($0 \leq x \leq 1$) was synthesised. The parent Ba_2CoMoO_6, has been reported to become antiferromagnetically ordered below 20 K adopting a Type II antiferromagnetic structure, however, the magnetic behaviour deviates from Curie-Weiss behaviour [162].

The purpose of this chapter is to investigate the persistence of antiferromagnetic long-range order within the $Ba_2Co_{1-x}Zn_xMoO_6$ series upon magnetic dilution. The percolation threshold of 0.136 for NN plus NNN interactions is relevant as Ba_2CoMoO_6 has been reported to show Type II antiferromagnetism.

Experimental

Approximately 5 g samples of $Ba_2Co_{1-x}Zn_xMoO_6$ ($0 \leq x \leq 1$) were prepared using solid-state synthesis by stoichiometrically combining $BaCO_3$, Co_3O_4, MoO_3 and/or ZnO. A sacrificial powder of the same stoichiometry was utilised to minimise loss of Co^{2+} [240]. Each pellet was calcined for 24 hours at 800 °C and additional heating was carried out at 1100 °C in air. Diffraction data of Rietveld quality were collected using Cu Kα radiation and refined in GSAS [225]. The peak profile was modelled using the Pseudo-Voigt function and the background was fitted with a shifted Chebyshev function [241].

The GEM diffractometer at the ISIS Neutron and Muon Source [224] collected Time-of-flight powder neutron diffraction data from samples contained in 6 mm vanadium cans. Post measurement absorption corrections were applied to each data set. GSAS was used to perform simultaneous Rietveld refinement against banks 4-6. Peak shapes were characterised using a convolution of the Ikeda-Carpenter and Pseudo-Voigt functions, a shifted Chebyshev polynomial fitted the background [225] magnetic form factors were taken from literature [226]. All Rietveld refinements shown will be from detector bank 4, a high-resolution bank with the widest d-space range.

DC-magnetic susceptibility measurements were carried out using a Quantum Design magnetic property measurement system MPMS3. Thermal dependent susceptibility was measured between 2 and 300 K, using previously outlined techniques.

AC-susceptibility measurements were carried out on $Ba_2Co_{0.85}Zn_{0.15}MoO_6$, using a Quantum Design Physical Property Measurement System, PPMS, between 2 and 30 K at a range of frequencies; 100 Hz, 1 kHz, 3 kHz, 7.5 kHz and 10 kHz.

Results

X-ray Powder Diffraction

X-ray diffraction indicated that each composition of the $Ba_2Co_{1-x}Zn_xMoO_6$ series adopted the $Fm\bar{3}m$ space group. This was expected as both Ba_2CoMoO_6 and Ba_2ZnMoO_6 have been previously reported to adopt this structure [162,242]. Figure 6.1 indicates the results of the X-ray powder diffraction of Ba_2CoMoO_6 and the inset shows the compositional dependence of the lattice parameters. The ionic radii of Co^{2+} and Zn^{2+} is 0.745 Å and 0.740 Å respectively, this results in random distribution over their site and anomalously the lattice parameter experiences a slight increase as the concentration of Zn^{2+} increases [36,237]. Thermal parameters refined to slightly negative values and therefore were fixed at values of 0.001 $Å^2$ [243]. Each sample possessed small quantities of $BaMoO_4$. Ba_2ZnMoO_6 was also synthesised, however this contained significant impurities which could not be diminished after heating and therefore will not be covered in any detail.

Table 6:1: Structural parameters of the $Ba_2Co_{1-x}Zn_xMoO_6$ series obtained from Rietveld refinements against room temperature X-ray powder diffraction. Each material crystallises in $Fm\bar{3}m$ where; Ba^{2+} lies on the (1/4, 1/4, 1/4) position, Co^{2+} and Zn^{2+} reside on the origin (0, 0, 0) and Mo^{6+} sits on the (1/2, 0, 0) coordinate, whilst the oxide anion sits on (x, 0, 0).

x	**0**	**0.15**	**0.25**	**0.5**	**0.75**	**0.85**
a / Å	8.08206(7)	8.08648(5)	8.08864(7)	8.09534(5)	8.10463(6)	8.10508(6)
O x coordinate	0.2594(5)	0.2606(4)	0.2608(6)	0.2598(6)	0.2393(8)	0.2620(7)
Ba-O/ Å	2.8585(1)	2.8603(1)	2.8611(1)	2.6832(1)	2.8667(2)	2.8672(2)
Ba BVS	2.58	2.57	2.56	2.55	2.52	2.52
Co/Zn-O / Å	2.096(4)	2.107(4)	2.110(5)	2.103(5)	2.113(6)	2.123(5)
Co/Zn BVS	2.10	1.96	1.95	1.99	1.94	1.89
Mo-O / Å	1.945(4)	1.936(4)	1.935(5)	1.945(5)	1.939(6)	1.929(5)
Mo BVS	5.41	5.55	5.56	5.41	5.50	5.65

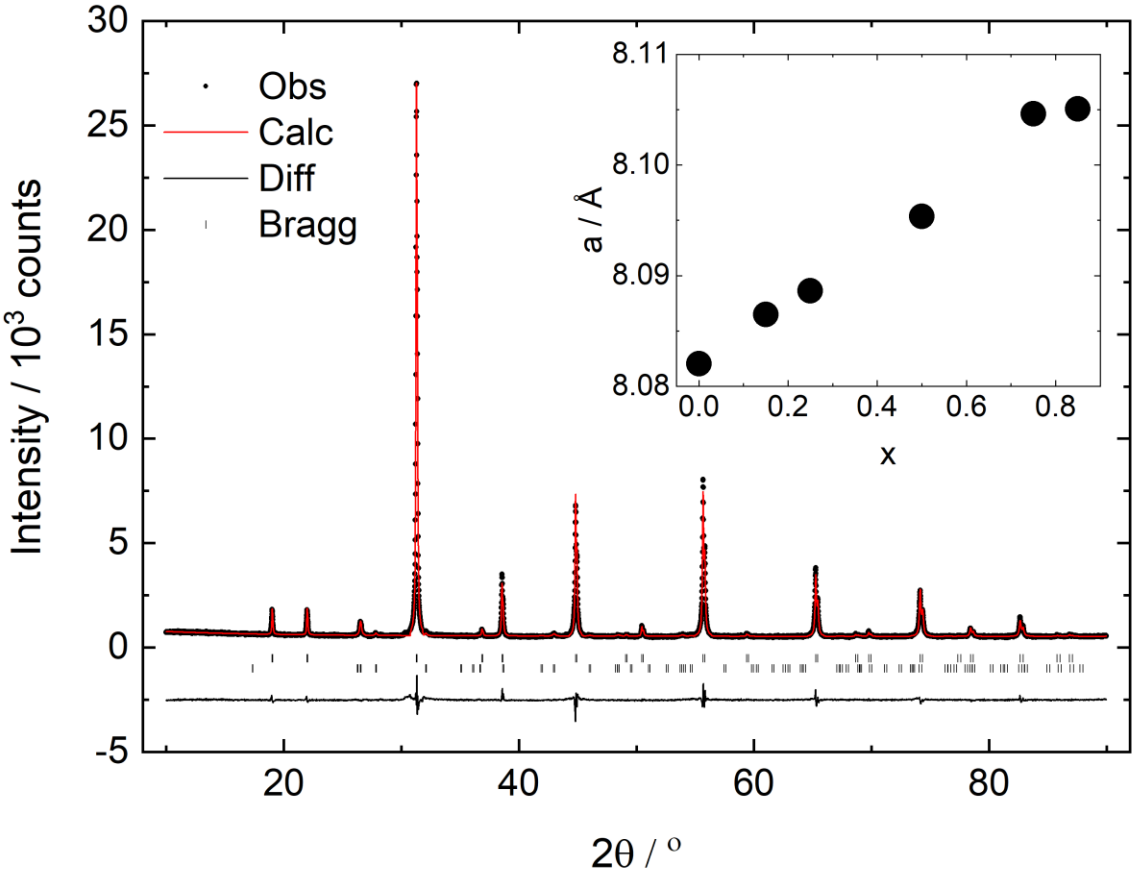

Figure 6.1: The results of Rietveld refinement against the X-ray powder diffraction pattern of Ba_2CoMoO_6 at ambient temperature. The upper row of the Bragg reflections corresponds to the double perovskite Ba_2CoMoO_6 which crystallises in the $Fm\bar{3}m$ space group. The bottom row corresponds to the impurity $BaMoO_4$ of 4.5 wt%. The Ba_2CoMoO_6 peaks are well fitted by the *fcc* space group resulting in the R_{wp} = 4.94. The inset image shows the compositional evolution of the lattice parameter at ambient temperature. The esd are shown but are smaller than the symbol size.

DC-Susceptibility

Analysis of the DC-susceptibility data indicated that the $Ba_2Co_{1-x}Zn_xMoO_6$ samples displayed unconventional behaviour shown in Figure 6.2, Figure 6.3, and Table 6:2. Ba_2CoMoO_6, displays ZFC/FC divergence, which is onset at approximately 250 K and extends to low temperatures, becoming more significant with decreasing temperature. The ZFC curve presents a distinct maximum at 23(1) K, decreasing until a slight upturn at 4(1) K. This upturn is attributed to a paramagnetic tail. The FC curve does not match this signature, instead the susceptibility increases as the temperature is dropped. The maximum in the ZFC curve has been assumed to be the Néel temperature, in agreement with previous literature [162]. The outlined divergence and curvature of ZFC/FC curves at high temperature result in a Curie-Weiss fit between 200 and 300 K. This analysis yielded C_{CW}, = 2.09(2) cm^3 K mol^{-1}, ϑ_{CW} = -65(2) K and μ_{eff} = 4.1(4) μ_B. $3d^7$ cations have μ_{SO} = 1.73 μ_B and μ_{SO} = 3.88 μ_B for low- and high-spin configurations, respectively. The calculated μ_{eff} corresponds to a slightly enhanced high spin moment, likely to arise from orbital contribution. The value observed is significantly lower than previous reports (*c.f.* 5.24 μ_B) [162]. The frustration index, $f = |\theta_{CW}|/T_N$ = 2.8(2), which indicates mild frustration.

$Ba_2Co_{0.85}Zn_{0.15}MoO_6$ and $Ba_2Co_{0.75}Zn_{0.25}MoO_6$ undergo antiferromagnetic transitions at 18(1) and 14(1) K respectively. Below the transition temperatures, slight ZFC/FC divergence is observed but both ZFC and FC curves experience a maximum, attributed to T_N. Curie-Weiss analyses between 200 and 300 K gave ϑ_{CW} = -57(2) K, μ_{eff} = 4.9(4) μ_B/Co^{2+} and f = 4.1(4) for $Ba_2Co_{0.85}Zn_{0.15}MoO_6$ whilst $Ba_2Co_{0.75}Zn_{0.25}MoO_6$ was calculated to have ϑ_{CW} = -54(1) K, μ_{eff} = 3.1(3) μ_B/Co^{2+} and f = 3.9(3).

The further substituted materials, x = 0.5, 0.75 and 0.85, show no evidence of antiferromagnetic transitions. The reciprocal susceptibilities are slightly curved and therefore Curie-Weiss analysis is applied with caution. This gave μ_{eff} equal to 4.3(3) μ_B/Co^{2+}, 5.1(3) μ_B/Co^{2+} and 5.2(3) μ_B/Co^{2+} for $Ba_2Co_{0.5}Zn_{0.5}MoO_6$, $Ba_2Co_{0.25}Zn_{0.75}MoO_6$ and $Ba_2Co_{0.15}Zn_{0.85}MoO_6$ and Weiss constants were calculated as -41(1) K, -19.9(4) K and -25.4(5) K respectively. These materials do not exhibit ZFC/FC divergence.

Table 6:2:Extracted data from the Curie-Weiss fittings of $Ba_2Co_{1-x}Zn_xMoO_6$ taken from DC-susceptibility measurements

x	**0**	**0.15**	**0.25**	**0.5**	**0.75**	**0.85**
C_{CW} / cm^3 K mol^{-1}	2.09(2)	2.149(2)	1.604(2)	1.214(3)	0.871(3)	0.529(3)
Θ_{CW} / K	-65(2)	-57(2)	-54(1)	-41(1)	-19.9(4)	-25.4(5)
μ_{eff} / μ_B per Co^{2+}	4.1(4)	4.9(4)	4.1(4)	4.3(3)	5.1(3)	5.2(3)
T_N / K	23(1)	18(1)	14(1)	-	-	-
f	2.8(2)	3.2(2)	3.9(3)	-	-	-

The magnitude of ϑ_{CW} increases whilst μ_{eff} decreases as the concentration of diamagnetic Zn^{2+} increases. Ba_2CoMoO_6 exhibits the largest ϑ_{CW}, potentially because it contains the highest number of magnetic cations and therefore is more inclined to behave antiferromagnetically. Ba_2CoMoO_6 is the least frustrated of the ordered systems, due to its higher transition temperature. The random distribution of Co^{2+} and Zn^{2+} results in magnetic order becoming more difficult as pathways are disrupted. When these pathways are disturbed, θ_{CW} declines as the cations no longer interact effectively but μ_{eff} increases as the cations are more isolated and tend to behave like free ions [244]. As the percentage of Zn^{2+} increases across the series, the ZFC/FC divergence is radically suppressed.

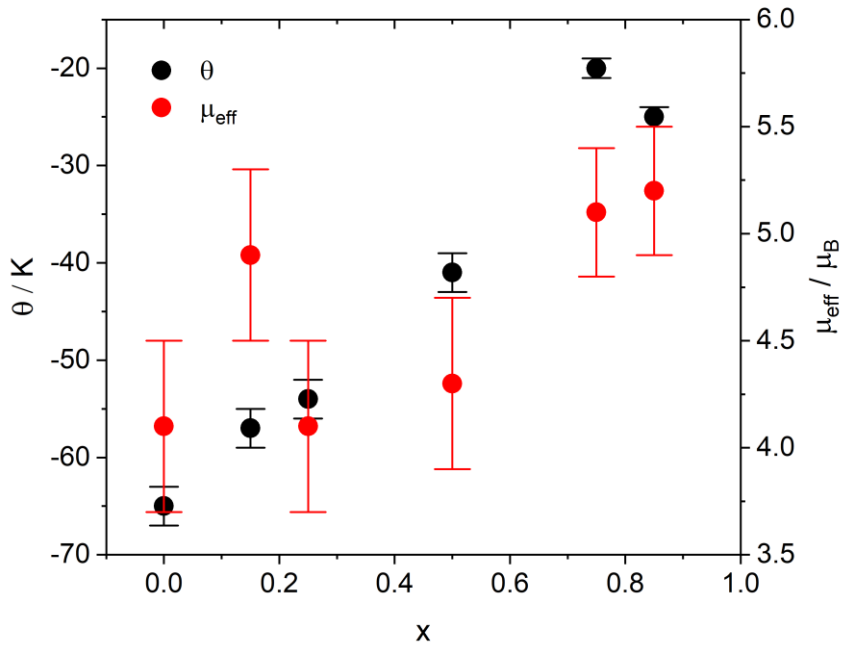

Figure 6.2: The compositional dependence of θ_{CW} and μ_{eff} across the $Ba_2Co_{1-x}Znx_xMoO_6$ series.

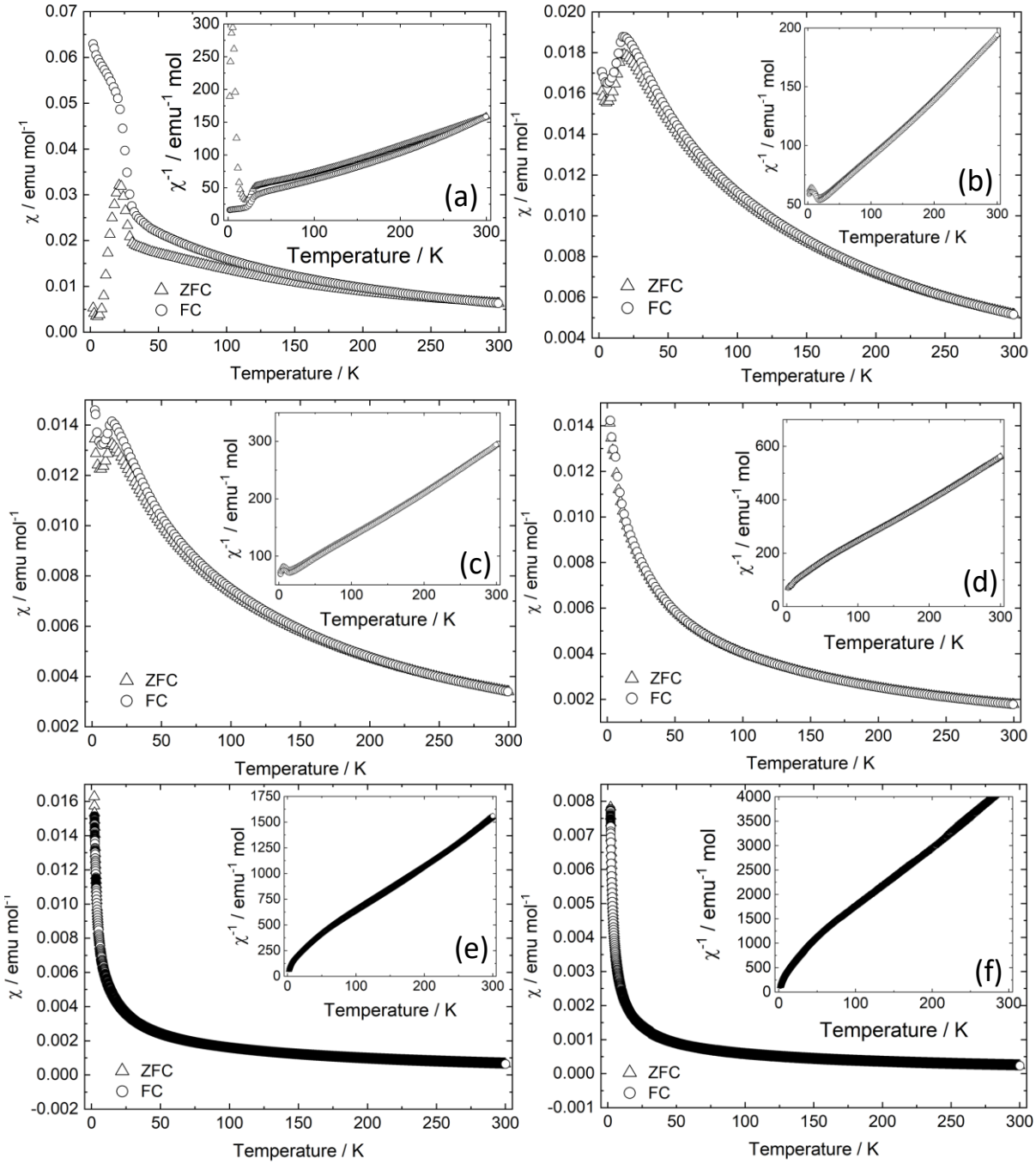

Figure 6.3: The temperature dependent DC-magnetometry of (a) Ba_2CoMoO_6, (b) $Ba_2Co_{0.85}Zn_{0.15}MoO_6$ (c) $Ba_2Co_{0.75}Zn_{0.25}MoO_6$,(d) $Ba_2Co_{0.50}Zn_{0.50}MoO_6$, (e) $Ba_2Co_{0.25}Zn_{0.75}MoO_6$ and (f) $Ba_2Co_{0.15}Zn_{0.85}MoO_6$. In all figures the main plot shows the magnetic susceptibility response whilst the inset shows the reciprocal susceptibility. These measurements were completed between 2 and 300 K in both zero field (ZFC) and in the presence of a magnetic field of 1000 G (FC).

AC-Susceptibility

AC-susceptibility carried out on $Ba_2Co_{0.85}Zn_{0.15}MoO_6$ showed that the real response of the AC-susceptibility closely resembled that obtained from DC-susceptibility with the transition temperature persisting around 18(1) K at all frequencies see Figure 6.4. This suggests that the ZFC/FC divergence is not the result of a spin glass transition, as the transition temperature is not frequency dependent. The imaginary response experienced a low signal to noise ratio, with large estimated standard deviation within range of zero and did not provide useful information.

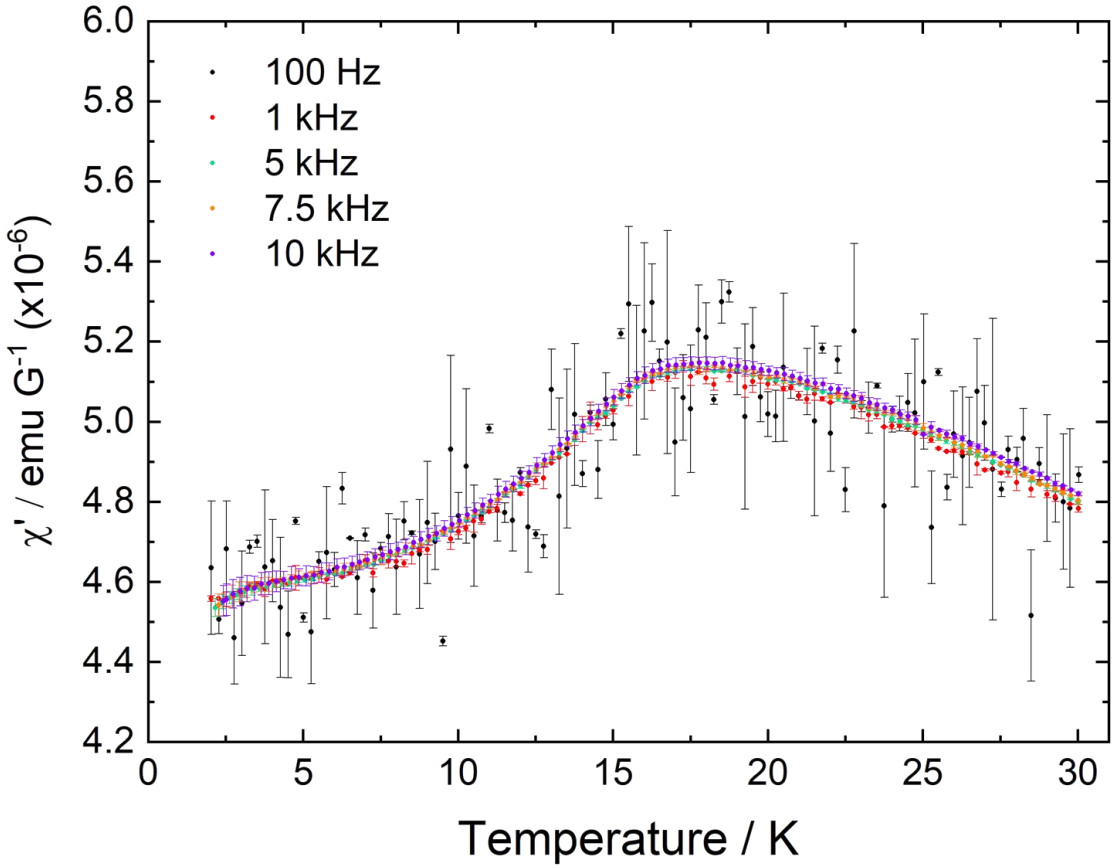

Figure 6.4: AC-susceptibility of $Ba_2Co_{0.85}Zn_{0.15}MoO_6$ between 2 and 30 K at a variety of frequencies ranging from 100 Hz to 10 kHz. This is reminiscent of the DC-susceptibility and indicates that the material does not enter into a spin glass state as there is no frequency dependence of the transition temperature observed.

Neutron Powder Diffraction

Ba_2CoMoO_6, $Ba_2Co_{0.85}Zn_{0.15}MoO_6$, $Ba_2Co_{0.75}Zn_{0.15}MoO_6$ and $Ba_2Co_{0.50}Zn_{0.50}MoO_6$ were each investigated by Time-of-flight neutron powder diffraction at a range of temperatures between 2 and 100 K. At 100 K, each composition retained the *fcc* structure from ambient temperature, Figure 6.5 displays the Rietveld refinement against neutron powder diffraction data Ba_2CoMoO_6 collected at 2 K. During Rietveld refinement, the thermal displacement of the Co^{2+} and Zn^{2+} cations were constrained to be equal as they occupy the same site. In these fits the cubic peaks corresponding to Ba_2CoMoO_6 are sharp with no peak broadening. The $BaMoO_4$ impurity (*I4₁/a*) was characterised also.

The lattice parameters generally increase as the concentration of the Zn^{2+} cation is increased. Anomalously, $Ba_2Co_{0.75}Zn_{0.25}MoO_6$ experiences a small increase compared to the other compositions, which is not observed in the X-ray diffraction patterns collected at ambient temperature. This composition resembles the other materials with similar fractional occupancy of the oxide anion, no evidence of antisite disorder of the Co^{2+} and Mo^{6+} cations and similar bond lengths and bond valence sums. Each material possesses a $BaMoO_4$ impurity which may affect the stoichiometry of each composition resulting in the trend observed in the lattice parameters. This impurity may be a result of Co^{2+} losses within each of the structure. If these Co^{2+} losses were significant enough then this could provide a solution to the unusual trend of the lattice parameter in $Ba_2Co_{0.75}Zn_{0.25}MoO_6$, however, it does not explain why this is not observed in the X-ray powder diffraction patterns.

Table 6:3:Results of the Rietveld refinements of neutron powder diffraction data sets collected on $Ba_2Co_{1-x}Zn_xMoO_6$ at 100 K. The $Ba_2Co_{1-x}Zn_xMoO_6$ series crystallise in $Fm\bar{3}m$ with each ion residing in the following positions; Ba^{2+} (1/4, 1/4, 1/4), Co^{2+}/Zn^{2+} (0, 0, 0), Mo^{6+} (1/2, 0, 0) and O^{2-} (*x*, 0, 0). * these were fixed as they went slightly negative.

x	**0**	**0.15**	**0.25**	**0.50**
a / Å	8.07656(3)	8.08120(2)	8.07712(3)	8.08490(2)
Ba $100U_{iso}$ / Å^3	0.176(9)	0.199(9)	0.160(9)	0.163(6)
Co/Zn $100U_{iso}$ / Å^3	0.41(5)	0.21(4)	0.56(4)	0.29(2)
Mo $100U_{iso}$ / Å^3	0.14(2)	0.16(2)	0.10(2)	0.12(1)
Antisite Disorder	2.5(3)	0*	0*	0*
O x coordinate	0.26130(6)	0.26163(5)	0.26177(5)	0.26210(3)
O $100U_{iso}$ / Å^3	0.467(7)	0.417(6)	0.437(7)	0.421(5)
O fractional occupancy	0.997(2)	0.996(1)	1.000(2)	1.000(1)
Ba-O bond length	2.857(1)	2.859(1)	2.857(1)	2.860(1)
Ba BVS	2.60	2.58	2.59	2.57
Co/Zn-O bond length	2.112(1)	2.115(1)	2.114(1)	2.120(1)
Co/Zn BVS	1.93	1.92	1.93	1.90
Mo bond length	1.927(1)	1.925(1)	1.924(1)	1.923(1)
Mo BVS	5.69	5.71	5.73	5.75
$BaMoO_4$ / wt%	10.0(2)	4.4(1)	5.2(2)	3.4(1)
R_{wp}	4.61	4.66	5.11	4.09

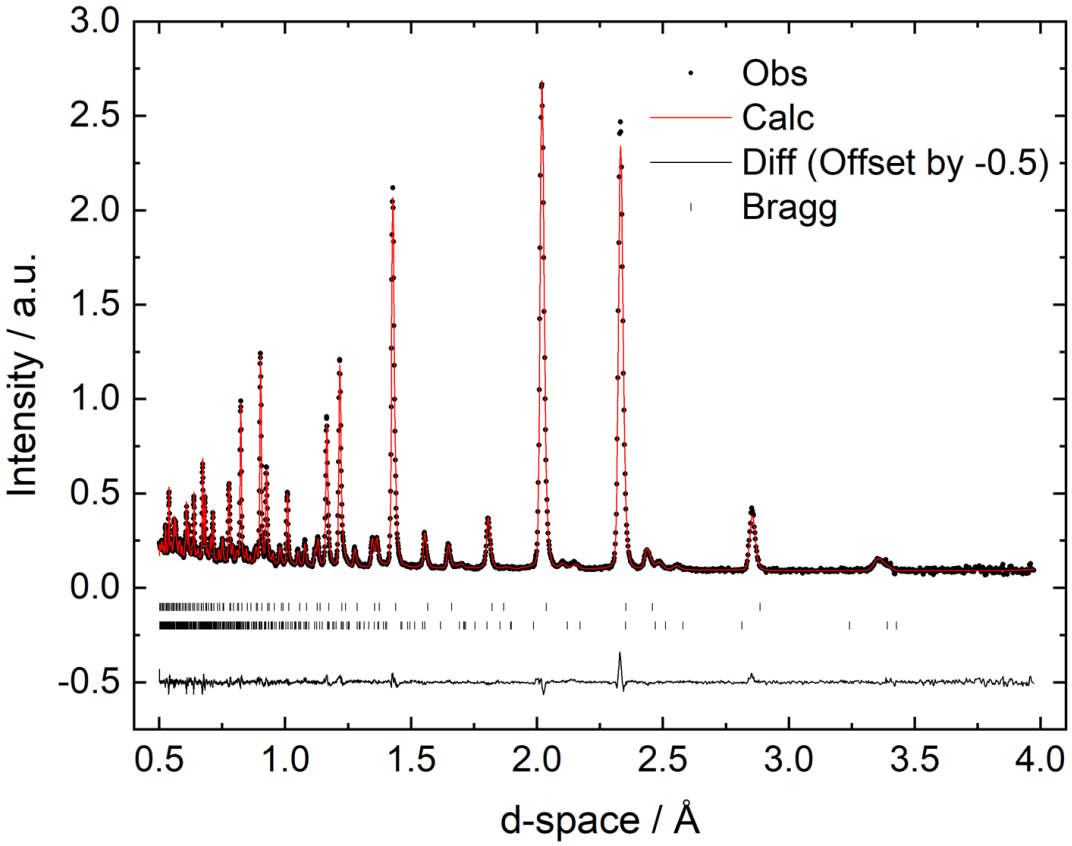

Figure 6.5: Rietveld refinement of neutron powder diffraction data collected on Ba_2CoMoO_6 at 100 K. The upper Bragg reflections correspond to the nuclear phase with cubic structure (space group $Fm\bar{3}m$) and the lower row of Bragg reflections correspond to the impurity phase $BaMoO_4$. The difference curve is offset by the quantity outlined in the legend.

The materials were cooled to 2 K to observe any long-range magnetic order. Ba_2CoMoO_6 retains the *fcc* structure at 2 K and is antiferromagnetically ordered. Indexing the magnetic Bragg peaks was carried out using FULLPROF, which calculated the propagation vector $\boldsymbol{k}$ = (1/2, 1/2, 1/2) [230]. The final Rietveld refinement of the 2 K data sets was carried out using GSAS, where the magnetic structure was added as a separate P1 phase to test the Ising and MnO models outlined previously. An alternative model involving moments aligned along the [111] directions calculated zero intensity for the magnetic Bragg peak observed at the lowest d-space value. Therefore, it did not describe the magnetic structure and as such will not be further mentioned. The Ising and MnO models vary only by the direction of the magnetic moments although both lie within the (111) plane. The results of these refinements are shown in Figure 6.6.

Both models generated Bragg peaks corresponding to the correct d-space positions, however, the intensity of the magnetic Bragg peaks at longest d-spacings are overestimated by the calculation, with significant error in the peak position. The higher resolution detector banks do not experience this intensity issue. Removal of the lower intensity banks results in the same structural parameters being extracted. An additional reason could be that the magnetic moments may be offset from the (111) plane. This has been suggested for Ba_2CoWO_6, with an orientation around 20° from the (111) plane [163]. Both models provide satisfactory fits to the data sets but as direction of the moments cannot be derived from powder diffraction, these models cannot be confirmed [144].

When comparing the two models, the extracted parameters yield results within estimated standard deviation of each other. In Ba_2CoMoO_6, the bond valence sums of the nuclear phase suggest that Ba^{2+} is significantly overbonded with a value of 2.60. The cobalt cations exhibit valences approximately equal to 2 and the molybdenum cations are slightly underbonded, with a bond valence sum of 5.69. The effective magnetic moment calculated for the Co^{2+} cations is found to be 1.9(3) μ_B when banks 2 and 3 are included and 1.3(3) μ_B when these are excluded. These are assumed to be lower when banks 2 and 3 are excluded as the magnetic Bragg peaks occur at lower d-space values and therefore have lower intensity. These values compare with low spin Co^{2+} cations, where the spin only value would be 1.73 μ_B.

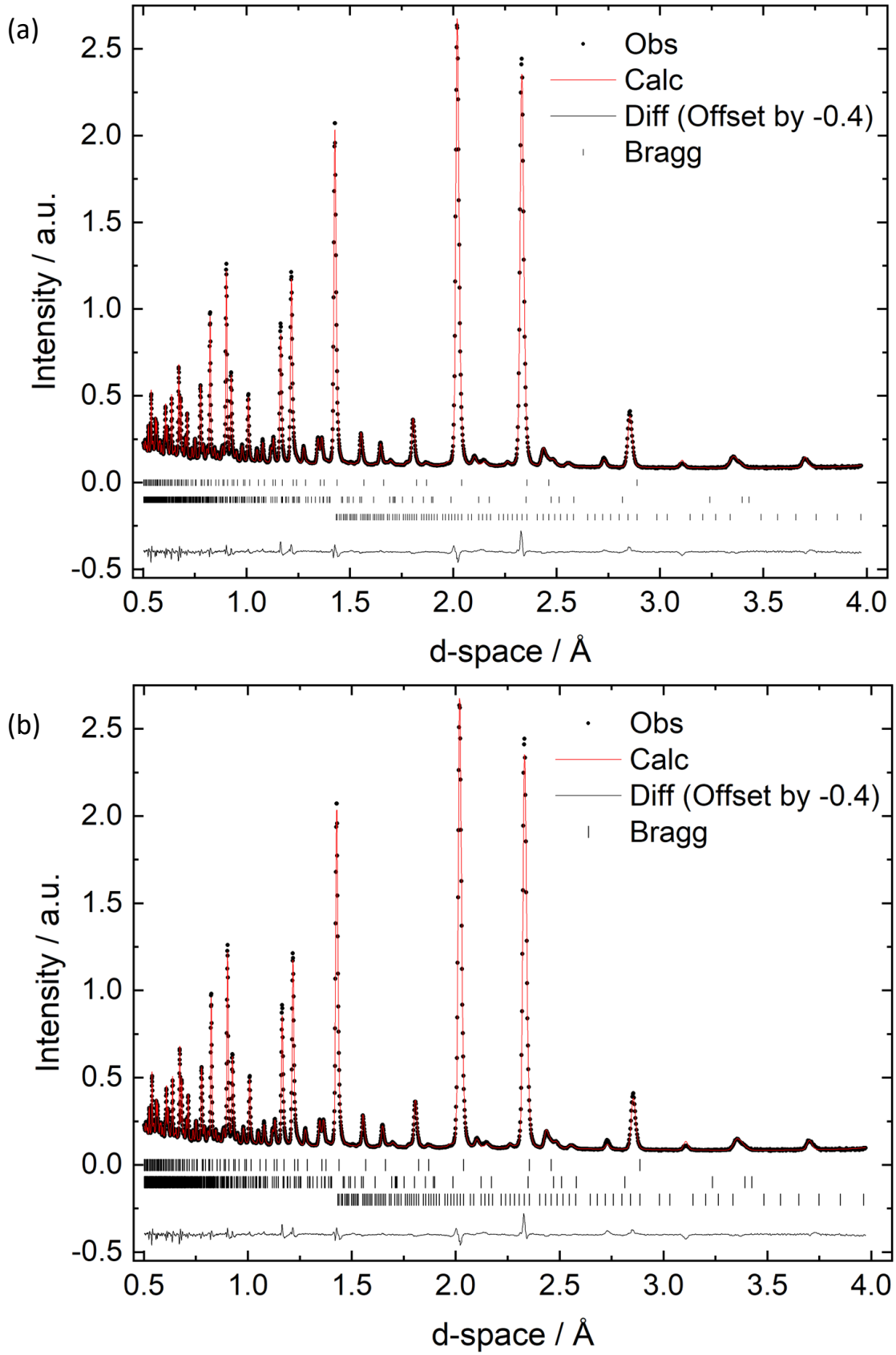

Figure 6.6: Rietveld refinement of neutron powder diffraction data sets collected on Ba_2CoMoO_6 at 2 K. The nuclear structure, $BaMoO_4$ and the antiferromagnetic structure are represented by the upper, middle and lower rows of Bragg reflections respectively. The difference curve has been offset by -0.4. Two different magnetic structures were attempted (a) the Ising spin model whilst (b) the MnO model, where the moments point in the $[11\bar{2}]$ direction.

The substituted compositions, $Ba_2Co_{0.85}Zn_{0.15}MoO_6$, $Ba_2Co_{0.75}Zn_{0.25}MoO_6$ and $Ba_2Co_{0.5}Zn_{0.5}MoO_6$ were also investigated down to 2 K. Each of these materials, retain the $Fm\bar{3}m$ symmetry down to 2 K, with conventional thermal expansion properties being observed as each of the lattices decrease in size from ambient temperature. $Ba_2Co_{0.85}Zn_{0.15}MoO_6$ and $Ba_2Co_{0.75}Zn_{0.25}MoO_6$ enter a long range antiferromagnetically ordered state, whilst $Ba_2Co_{0.5}Zn_{0.5}MoO_6$ shows no long-range magnetic order. The magnetic structure observed in $Ba_2Co_{0.85}Zn_{0.15}MoO_6$ and $Ba_2Co_{0.75}Zn_{0.25}MoO_6$ closely resembles that of Ba_2CoMoO_6 and therefore the magnetic models previously outlined were also applied to these materials, this led to the same trends described for Ba_2CoMoO_6.

Comparing the behaviour of each composition at 2 K shows a general increase in the lattice parameters which arises as the concentration of Zn^{2+} cations increases and $Ba_2Co_{0.75}Zn_{0.25}MoO_6$ shows the same anomalous behaviour as before, with only a small increase from the lattice parameter of Ba_2CoMoO_6 compared to the increase in $Ba_2Co_{0.85}Zn_{0.15}MoO_6$. There are minimal changes in atomic parameters across the solid solution. The Ba-O bond lengths experience very slight changes across the solid solution but display similar behaviours to the lattice parameters. As these increases are so slight the bond valence sum remains close to 2.60 across the series. This indicates that the anomalously high bond valence sum is observed universally across the series. As the concentration of Zn^{2+} increases, the Co/Zn-O bond lengths increase with a simultaneous decrease in the Mo-O bond length. This is unsurprising as the Zn^{2+} cation is larger than the Co^{2+} cation and therefore it was likely to increase the bond length, with the shortening of the Mo-O bond length occurring consequently [237]. Once again this shows minimal effect to the bond valence sums of the cations. Over the solid solution the effective magnetic moment per Co^{2+} remains roughly equal and is within error of the spin only value of the S = 1/2, low spin configuration of the Co^{2+} cation.

Table 6:4: Results of the Rietveld refinement using the Ising spin model for the neutron powder diffraction measurements carried out on $Ba_2Co_{1-x}Zn_xMoO_6$ at 2 K. Apart from x = 0.50 which displays no long range magnetic order. The MnO model is not shown as these changes are within error. Ba resides on (1/4, 1/4, 1/4), Co/Zn on (0, 0, 0), Mo on (1/2, 0, 0) and O on (x, 0, 0)

X	**0**	**0.15**	**0.25**	**0.50**
a / Å	8.07423(3)	8.07894(3)	8.07501(3)	8.08265(2)
Ba $100U_{iso}$ / $Å^2$	0.083(9)	0.033(9)	0.075(1)	0.078(8)
Co/Zn $100U_{iso}$ / $Å^2$	0.58(5)	0.58(5)	0.45(5)	0.38(3)
Mo $100U_{iso}$ / $Å^2$	0.07(2)	0.06(2)	0.05(2)	0.08(2)
O x coordinate	0.26137(5)	0.26174(5)	0.26173(5)	0.26215(4)
O $100U_{iso}$ / $Å^2$	0.428(6)	0.384(8)	0.391(6)	0.376(7)
O Fractional Occupancy / %	0.999(2)	1.009(2)	0.999(2)	1.000(2)
Magnetic phase fraction	0.109(3)	0.047(2)	0.053(2)	-
Co magnetic moment / μ_B per Co^{2+} cation	1.3(3)	1.0(3)	1.2(3)	-
Ba-O / Å	2.856(1)	2.858(1)	2.857(1)	2.859(1)
Ba BVS	2.60	2.59	2.60	2.58
Co/Zn-O / Å	2.112(1)	2.115(1)	2.113(1)	2.118(1)
Co BVS	1.93	1.93	1.94	1.91
Mo-O / Å	1.925(1)	1.925(1)	1.924(1)	1.923(1)
Mo BVS	5.71	5.70	5.73	5.75
R_{wp}	3.43	3.97	4.62	4.07

Discussion

Each member of the $Ba_2Co_{1-x}Zn_xMoO_6$ solid solution crystallises in the *Fm*$\bar{3}$*m* space group at ambient temperature. This is anticipated as the difference between the ionic radii of Zn^{2+} and high spin Co^{2+} is 0.005 Å, resulting in minimal changes in Goldschmidt tolerance factor [48,238]. According to the ionic radii the lattice parameter should decrease as the quantity of the Zn^{2+} cations increases. This is not observed within the $Ba_2Co_{1-x}Zn_xMoO_6$ solid solution and the lattice parameter experiences a slight increase as the composition of x increases. This is anomalous; however, this trend is also observed in the spinel solid solution of $Zn_{1-x}Co_xCr_2O_4$ and is reported to be the result of the increased covalency of the Zn^{2+} cation which permits longer bond lengths than the more ionic Co^{2+} cation [245]. Each system challenges the Jahn-Teller theorem when the $Co^{2+}O_6$ octahedra are undistorted. This is unexpected; however, this may be since the degeneracy occurs in the t_{2g} orbitals and not the e_g orbitals. This phenomenon has been observed in a number of cubic double perovskites including Ba_2LuMoO_6 [215]. Bond valence sums indicate the barium cation is significantly overbonded within all compositions, whilst the cobalt/zinc and molybdenum ions show expected +2 and +6 oxidation states [10]. This result corresponded fairly well with previous reports on Ba_2CoMoO_6 [162], however, the high BVS of Ba^{2+} is not reflected in many other double perovskites where the sum tends to lie around 2.3.

Upon cooling to 2 K, x = 0, 0.15, 0.25 and 0.50 remain cubic with normal thermal expansion behaviour. No structural phase transition or Jahn-Teller distortion is observed. This is also observed in other magnetically frustrated double perovskites such as Ba_2MnWO_6 Ba_2YMoO_6 and Ba_2NiWO_6 [163,210,211,221].

The magnetic behaviour of Ba_2CoMoO_6 deviates from Curie-Weiss law as evidenced by the substantial ZFC/FC divergence and curved susceptibility response. Further measurements carried out to 400 K remained non-linear. This exotic behaviour arises due to strong spin orbit coupling effects experienced by the Co^{2+} cations. As Russell-Saunders theory explains, the ground term of the Co^{2+} cation is described by $^{(2S+1)}L$. When the Co^{2+} cation is present in a high spin S = 3/2 state, the orbital angular

momentum L is equal to 3 (the number of electrons in each subshell, denoted by 0, ±1 or ±2, multiplied by the number of electrons in each subshell), giving the resultant ^4F ground term [246]. The ^4F term can then be split by a crystal field into different terms known as the A_{2g}, T_{1g} and T_{2g}. In an octahedral field, the T_{1g} becomes the lowest energy field after the crystal splitting. In Co^{2+}, the A_{2g} is a symmetrical non-degenerate orbital and the T_{1g} and T_{2g} orbitals are triply degenerate orbitals which vary dependent on their symmetry. In an octahedral field at room temperature, only the T_{1g} orbital will be populated, as the other energy levels are significantly higher in energy and therefore cannot be accessed. Spin orbit coupling of the Co^{2+} cation results in the splitting of the T_{1g} orbital into three individual levels denoted as the J = 5/2, J = 3/2 and J = 1/2, which are written in descending order of energy. [247] The splitting of these crystal fields explains the temperature dependent magnetic behaviour of the Co^{2+} cations. Previous reports outline the magnetic moment of Ba_2CoMoO_6 saturating around 1.8 μ_B, which is within three standard deviations of the value observed in this report. This could suggest that the magnetic moment which is observed is the result of covalence effects which result in reducing overlap between the Co and O ions and therefore a decreased magnetic moment [162].

The large ZFC/FC divergence observed in the magnetometry of Ba_2CoMoO_6 was further investigated using a magnetisation versus field measurement at the fixed temperatures of 2 and 100 K. This measurement was carried out to identify whether any magnetic impurities were present within the material. The inset of Figure 6.7, indicates the magnetic behaviour between -50 and 50 kG. This shows no clear hysteresis as there is no loops observed and also no saturation magnetisation, however, the curve is not entirely linear, which suggests that some remanent magnetisation could be present within Ba_2CoMoO_6. Placing emphasis around the zero field data, see Figure 6.7, indicates that the 100 K data set lies close to zero, but the 2 K data set does show a small remanent magnetisation. This could be due to an impurity such as Co_3O_4, CoO, $BaCoO_3$ or Co^0 which could have been brought about by the synthesis conditions. Co_3O_4 is not thought to be a likely candidate as the large ZFC/FC divergence in the thermal dependent susceptibility plot is not observed [248]. CoO is also thought to be unlikely as this has a reported transition temperature of 291 K, which is significantly above the point that ZFC/FC

divergence is observed in Ba_2CoMoO_6 [249]. $BaCoO_3$ has been reported to show similar ZFC/FC divergence to Ba_2CoMoO_6, however, it also has a transition temperature around 15 K which is not observed within the susceptibility data [250]. Finally metallic Co^0 was considered as a potential impurity due to its ferromagnetic behaviour, however, the hysteresis observed does not closely align with this and the transition does not occur at a temperature close to the point of ZFC/FC divergence

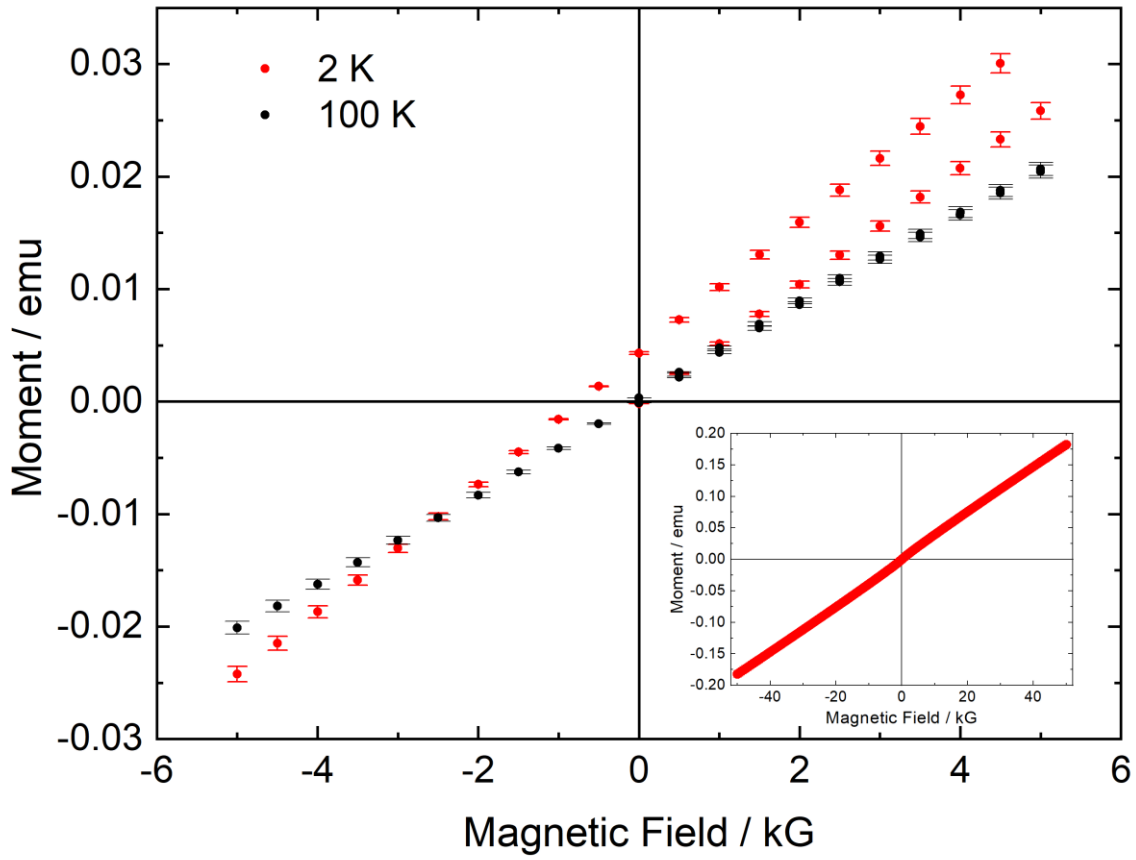

Figure 6.7: Magnetisation against Magnetic Field measurement carried out on Ba_2CoMoO_6 at 2 and 100 K. This measurement was carried out to identify whether any impurity was present within the material. This measurement shows that some hysteresis can be observed at 2 K, and a magnetic moment persists as the magnetic field returns to 0 G. The inset measurement shows the magnetic behaviour between fields of -50 to 50 kG at the fixed temperature of 2 K

Percolation considerations give insight into the complex behaviour of the $3d^7$ Co^{2+} cations in this series. When 15% of the Co^{2+} cations are removed a significant change is observed in the DC-susceptibility from the parent material. The ZFC/FC divergence is only observed below the transition temperature, and Curie-Weiss behaviour is observed between 200 and 300 K. In the absence of any other significant change in structure this must be due to the introduction of the Zn^{2+} cations. An antiferromagnetic

transition is no longer observed by x = 0.50 which suggests the separation between the Co^{2+} cations prevents magnetic interaction. The disorder of the Co^{2+} and Zn^{2+} cations may not be uniform and therefore areas rich in Zn^{2+} might be the result of this. This value of 0.50 is significantly higher than the theoretical value of the percolation threshold of a face centred cubic lattice which lies at 0.136 for nearest neighbour and next nearest neighbour interactions, as is expected in the $Ba_2Co_{1-x}Zn_xMoO_6$ solid solution [251]. This was not anticipated within the solid solution and is not observed in other cobalt containing systems such as $Co_pMg_{1-p}O$ which showed long range magnetic order persisting up to p = 0.136 [251]. A lower percolation threshold of x = 0.51 is observed in the ferromagnetic $Eu_xSr_{1-x}S$, below this threshold a spin glass phase is observed, which is rationalised through positional disorder within the material [252]. Spin glass behaviour has been reported in the related double perovskite Sr_2CoSbO_6, this is the result of large ZFC/FC divergence and positional disorder within this material. The cation ordering in Sr_2CoSbO_6 is taken to be approximately 77% [253]. The potential of antisite disorder of the *M*-site cations was investigated in the $Ba_2Co_{1-x}Zn_xMoO_6$ series using Rietveld refinement which showed that this was <3.3(8)%. This is significantly less than that observed in Sr_2CoSbO_6. The large ZFC/FC divergence of the DC-susceptibility measurements could have indicated a spin glass transition within these materials, however, there is no frequency dependence of the transition temperature in AC-susceptibility measurements.

As the concentration of the diamagnetic cations is increased a number of trends are established. The transition temperature decreases until it is no longer observed, this is anticipated to be the result of increased frustration between the Co^{2+} cations and a decrease in the concentration of magnetic cations within the system. The effective magnetic moment per Co^{2+} increases across the solid solution as the cations are more isolated from each other. The Weiss constants indicate weaker antiferromagnetic interactions as the concentration of Co^{2+} decreases. This results in the separation of the magnetic cations increasing resulting in an increase in the mean length of superexchange pathway decreasing the mean strength of antiferromagnetic interaction.

The neutron powder diffraction shows the same trend as was observed in the DC-susceptibility measurements, where no magnetic transition is observed in the material from x = 0.50. The three measured materials which do show magnetic behaviour appear to adopt the same magnetic structure. Each magnetic structure has been found to have the propagation vector $\boldsymbol{k}$ = (1/2, 1/2, 1/2) and appears to show Type II antiferromagnetic behaviour, however, the magnetic structure could not conclusively be determined. It is possible that the Co moments are slightly offset from the (111) plane, this has been reported in Ba_2CoWO_6 and is also observed in CoO, although this material is affected by a tetragonal distortion and therefore may not be a direct comparison [131,163].

Conclusion

The structural and magnetic properties of the solid solution $Ba_2Co_{1-x}Zn_xMoO_6$ ($0 \leq x \leq 1$) were investigated using magnetic percolation techniques. Ba_2CoMoO_6, the parent phase, was found to show an antiferromagnetic transition at 23(1) K from DC-susceptibility and the x = 0.15 and x = 0.25 phases were also found to attain an antiferromagnetically long range ordered states, albeit at lower temperatures as a consequence of the replacement of the magnetic Co^{2+} cations with diamagnetic Zn^{2+} cations. Magnetic ordering is disrupted at some dilution between x = 0.25 and x = 0.5, which is much higher than the typical percolation threshold of an *fcc* lattice which corresponds to x = 0.805 for NN and increases further when next nearest neighbours are also considered. Each of the antiferromagnetic structures possesses the propagation vector $\boldsymbol{k}$ = (1/2, 1/2, 1/2) and implements a Type II antiferromagnetic structure, however, the direction of the magnetic moments could not be determined from the powder diffraction patterns. The effective magnetic moments of the $Ba_2Co_{1-x}Zn_xMoO_6$ series appears to show high spin Co^{2+} behaviour at room temperature but is significantly smaller in neutron powder diffraction which is thought to be the result of covalency effects.

Future Work

It would be interesting to find ways to synthesise these materials and prevent any losses of Co^{2+} cations within the structure. This can currently be minimised by applying a sacrificial powder to the crucible, however, the Co^{2+} cations can still be lost to the alumina using this method which can mean that the structures are not ideally stoichiometric. Adding supplementary cobalt to the initial powder is not a viable solution as this can cause changes to the sample stoichiometry. One method of preventing cobalt loss could involve lowering the reaction temperature as the cobalt and alumina reaction occurs at high temperature. Ways to lower the reaction temperature include sol-gel reactions which require the formation of a gel by using organic based reagents, which are combined in water and heated. This heating continues until a gel forms and then any organic materials are decomposed and volatilised away. Another method could be using an alternative crucible made of a different material to alumina such as yttria stabilised zirconia or platinum which may not react with the cobalt.

The neutron powder diffraction results of the series cannot definitively determine the magnetic structure which each of the materials exhibit. This is because powder diffraction cannot extract the direction of the magnetic moments within the material. One way to assess this could be through single crystal neutron diffraction, this can allow the crystal to be orientated along the lattice planes and then allow the directions to be extracted. The magnetic Bragg peaks also appear smaller in the substituted materials which may mean that they are shrouded by the background in the more substituted materials.

The ZFC/FC divergence observed in the DC-susceptibility of each of the materials could indicate that there is canting of antiferromagnetic moments present in the material which can cause weak ferromagnetism within the structure. This could be investigated by carrying out some M/H measurements, where the field dependence of the magnetisation of the sample can be calculated and examined. This appears to not be a result of spin glass behaviour arising from the positional disorder of the Co^{2+} and Zn^{2+} cations.

7. Ba_2LuMoO_6: A Valence Bond Glass?

Double perovskites containing d^1 magnetic cations have been a source of increased interest since the discovery of ambient temperature magnetoresistance in the frustrated Sr_2FeMoO_6. Studies on this material have shown that synthetic conditions strongly affect structural ordering and system properties [154–156,158]. Debate about the oxidation state of molybdenum in related compounds motivated the synthesis of Ba_2LnMoO_6, Ln = rare earth cation. The presence of the trivalent rare earth cations forces the molybdenum cation to adopt the +5 oxidation state. This leads to the desirable $4d^1$ electronic configuration. Some notable heteromagnetic examples include; the ferroelastic Ba_2GdMoO_6 and Ba_2SmMoO_6 and Ba_2EuMoO_6 which experience high transition temperatures of 130 K and 112 K respectively [217,218]. No material in the Ba_2LnMoO_6 family shows the magnetoresistance behaviour, which was exhibited in Sr_2FeMoO_6, due to the more withdrawn nature of the lanthanide 4f orbitals compared to the 3d orbitals of Fe.

The large spin orbit coupling effect and strong electronic correlation experienced by the $4d^1$ Mo^{5+} cation leads to predictions of interesting properties including spin liquid behaviour [119,208,254]. Therefore, investigation of double perovskites containing Mo^{5+} as the sole magnetic cation may result in greater understanding of the relationship between these effects. Ba_2YMoO_6 is an example of this, having been reported as a valence bond glass [116,210].

The valence bond glass state has been hypothesised to arise due to the combination of strong quantum fluctuations with competing magnetic interactions. This minimises frustration by allowing an amorphous distribution of non-magnetic spin singlets to form. This is related to the valence bond crystal like that suggested in $MgTi_2O_4$, where singlets form periodically [255]. The valence bond glass phase is reported to have no electronic or spin gap, however, a pseudo-gap can be observed and does not exhibit any long-range magnetic ordering. The valence bond glass is difficult to experimentally identify, due to its closeness with the quantum spin liquid, spin ice and valence bond crystal phases, hence the application of a variety of techniques are necessary to distinguish it from these [213].

Ba_2YMoO_6 was extensively studied using neutron powder diffraction, bulk DC-and AC-magnetometry, muon spin relaxation measurements (μSR), heat capacity measurements, ^{89}Y magic angle spinning nuclear magnetic resonance (^{89}Y MAS NMR) and inelastic neutron scattering (INS) measurements. Ba_2YMoO_6 retains *fcc* symmetry until 2 K with no structural or magnetic phase transition observed. DC-magnetic susceptibility measurements reveal two Curie-Weiss regions, one at high temperature and the other at low temperature. At high temperature, Ba_2YMoO_6 experiences strong antiferromagnetic interactions, and a suppressed effective magnetic moment. At low temperature, the effective magnetic moment significantly drops, and strong magnetic interactions are no longer present. This behaviour was rationalised by the random distribution of the spin singlets [116,210]. Muon spin relaxation measurements suggest dynamic behaviour of the magnetic cations down to 50 mK [211]. AC-susceptibility measurements suggest that the material experiences a frequency dependent spin glass transition at approximately 1.3 K [211]. Inelastic neutron scattering illustrates a spin singlet to spin triplet excitation at approximately 28 meV which disappears above 125 K [212].

Initial reports theorise the valence bond glass phase to emerge due to spin singlets forming, leaving few residual magnetic moments [213]. Whilst further reports suggest that the thermal dependence of the magnetic moment is a result of the splitting of the t_{2g} orbital into J_{eff} = 3/2 and J_{eff} = 1/2, the latter being higher in energy. At higher temperature, population of the J_{eff} = 1/2 state can occur but at low temperature it cannot. The dangling spins are then proposed to be caused by thermal excitations [256]. This has also been proposed to be the result of a dynamic Jahn—Teller distortion which allows mixing of the two J_{eff} states [257].

Ba_2LuMoO_6 has also been reported to potentially behave as a valence bond glass [215]. This chapter provides further evidence of the potential valence bond glass state within Ba_2LuMoO_6 by utilising; μSR, heat capacity and INS.

Experimental

Ba_2LuMoO_6 was prepared using solid-state synthesis, combining $BaCO_3$, Lu_2O_3 and MoO_3 in a mortar and pestle. Thorough grinding was followed by pressing into a 13 mm pellet which was calcined for 24 hours at 800 °C. Subsequent heating at 1250 °C was completed under slightly reducing conditions using a flowing atmosphere of 5% H_2/N_2. Powder X-ray diffraction was measured using Cu Kα radiation and Rietveld refinement was carried out using the General Structure Analysis System (GSAS) software [225]. Peak shapes were fitted using the Pseudo-Voigt function and the background was described using a shifted Chebyshev 6^{th} order polynomial [82].

DC-susceptibility measurements were carried out between 2 and 300 K using a Quantum Design Magnetic Property Measurement System (MPMS3) based at the Materials Characterisation Laboratory at the Rutherford Appleton Laboratories based in Didcot, Oxfordshire, UK. The preparation technique has been previously outlined in the experimental theory chapter.

Muon Spin Relaxation (μSR) measurements were carried out on the MUSR instrument at the ISIS Neutron and Muon Source, Rutherford Appleton Laboratories, Oxfordshire. These measurements were completed between approximately 50 mK and 4 K, using a dilution fridge. Zero field measurements were carried out between 50 mK and 4 K, whilst longitudinal field measurements were completed at 50 mK utilising magnetic field strengths ranging between 20 and 3000 G. Approximately 3 g of the sample was mixed with a varnish, which would improve the thermal conduction of the insulating sample, and placed into a pocket of silver foil. The pocket plus its contents were then applied to a long stick which was placed into the dilution fridge.

Inelastic neutron scattering (INS) measurements were performed on the Time-of-flight direct geometry spectrometer MERLIN based at the ISIS Neutron and Muon Source [113]. The sample of Ba_2LuMoO_6 was placed into a 10 mm aluminium can with a sample depth of 30 mm. Each measurement was carried out for around three hours to ensure that the statistics of the measurements were fair. These were carried out between 7.5 and 200 K.

Heat capacity measurements were completed using a Quantum Design Physical Property Measurement System (PPMS) at the Department of Physics based at the University of Cambridge. To complete these measurements the Ba_2LuMoO_6 sample was mixed with powdered silver in a 1:1 mass ratio to aid thermal equilibration and this mixture was pressed into a pellet. This was also carried out on the diamagnetic analogue Ba_2LuNbO_6. The pellets were fractured and approximately 10 mg fragments were used to measure specific heat data which the silver contribution could be subtracted from.

Results

X-ray Powder Diffraction

X-ray diffraction patterns collected from Ba_2LuMoO_6 confirmed that the material crystallises in the *Fm*$\bar{3}$*m* space group with lattice parameter, 8.32102(3) Å as shown in Figure 7.1. The isotropic thermal displacement parameters were found to be 0.0026(5) $Å^2$ for Ba^{2+}, 0.0020(5) $Å^2$ for Lu^{3+} and Mo^{5+} which were constrained to be equal in this refinement and the oxide ions was significantly greater at 0.005(2) $Å^2$. The twelve Ba-O bond lengths equal 2.9442(3) Å, the Mo-O bond lengths were found to equal 1.965(6) Å and the Lu-O bond lengths were calculated as 2.196(6) Å. This leads to bond valence sums of 2.05, 3.27 and 5.13 for the barium, lutetium and molybdenum cations respectively, which indicates that they are present in the +2, +3 and +5 oxidation state as anticipated. Refinement suggests 7.6(4)% antisite disorder of the Lu^{3+} and Mo^{5+} cations.

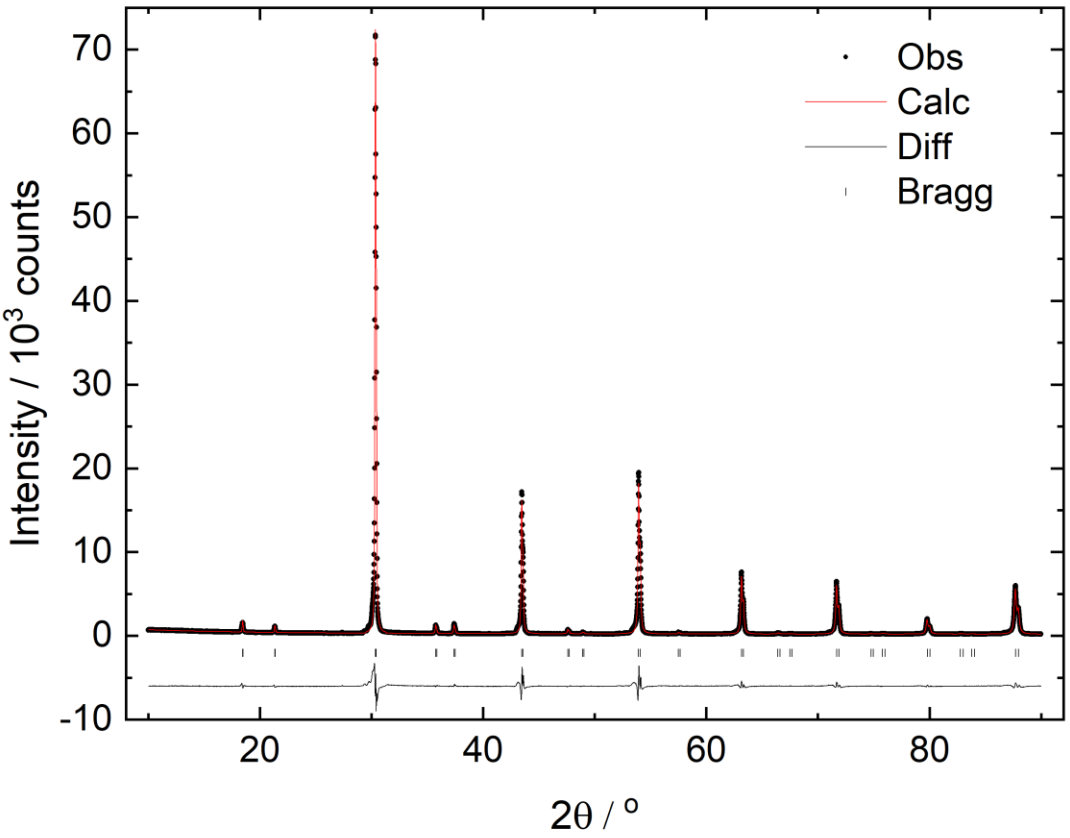

Figure 7.1: Results of the Rietveld refinement of the X-ray diffraction pattern collected on Ba_2LuMoO_6 at room temperature. The sample crystallises in *Fm*$\bar{3}$*m*. The Ba^{2+} cation resides on the (1/4, 1/4, 1/4) position, Lu^{3+} lies on (0, 0, 0) and Mo^{5+} sits at (1/2, 1/2, 1/2). The oxide position is (0.2639(8), 0, 0). The Bragg reflections indicated below are included in this. The difference curve is offset from zero by -6000. The intensities have been divided by 1000 throughout the diffraction pattern.

The lattice parameter of the sample is slightly smaller than that which is reported of 8.3265(1) Å. This difference may be a result of the different diffractometer used to measure the sample and the slight differences to the synthetic conditions. Despite the difference in lattice parameter, the reported bond lengths between the cations and the oxide anions are very similar. The first material also reports no antisite disorder between the Lu^{3+} and Mo^{5+} cations which once again could be caused by differences during preparation.

DC-Susceptibility

DC-susceptibility measurements, shown in Figure 7.2, do not give any clear indication of a magnetic transition. Inverse susceptibility measurements show two distinct regions of Curie-Weiss behaviour, at higher and lower temperatures. The high temperature region occurs between 200 and 300 K with C_{CW} = 0.230(1) emu mol^{-1} K^{-1}, θ_{CW} = -111(1) K and μ_{eff} = 1.36(9) μ_B. The effective magnetic moment is lower than expected for the S = ½ spin state and the Weiss constant indicates that Ba_2LuMoO_6 experience fairly strong antiferromagnetic interactions. Analysis of the low temperature region between 5 and 25 K show C_{CW} = 0.064(2) emu mol^{-1} K^{-1} θ_{CW} = -2.8(7) K and μ_{eff} = 0.7(1) μ_B.

Results obtained from this new sample and the previous report agree well. In the high temperature region, the effective magnetic moments are almost equal, and the Weiss- constants show minimal differences. A similar trend is observed in the previous report, however, in this sample the effective magnetic moment does not decrease as dramatically which may be a result of the antisite disorder. At low temperatures the Weiss constants are equal within error.

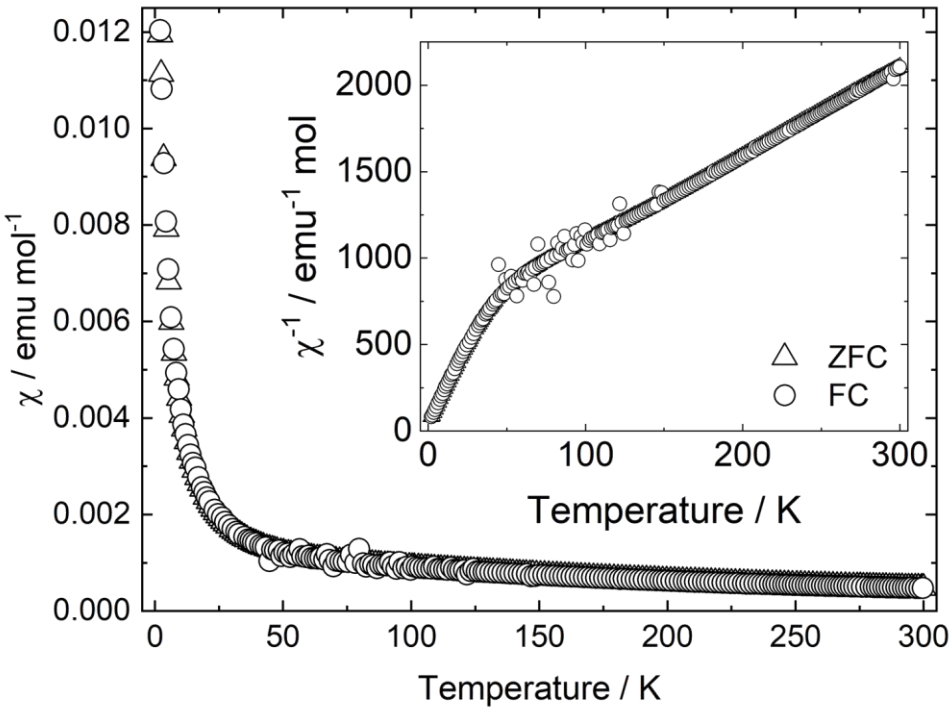

Figure 7.2: DC-magnetometry completed on Ba_2LuMoO_6 between 2 and 300 K. The main plot indicates the thermal dependence of the susceptibility, whilst the inset graph shows the temperature dependence of the reciprocal susceptibility. No ZFC/FC divergence is detected and no magnetic order is observed within the material. Two regions of Curie-Weiss behaviour are detected, a high temperature phase between 200 and 300 K and low temperature between 2 and 25 K.

Muon spin relaxation

Zero field muon spin relaxation (ZF-μSR) measurements were carried out between 0.05(5) and 4.0(1) K to determine the low temperature local behaviour of the magnetic moments. These measurements indicated that Ba_2LuMoO_6 experiences a relaxation down to 0.05(5) K. The experimentally collected responses are depicted in Figure 7.3. There are small differences in the relaxation behaviour between 0.05(5) and 1.0(1) K, but significantly larger changes are observed between 1.0(1) and 2.0(1) K.

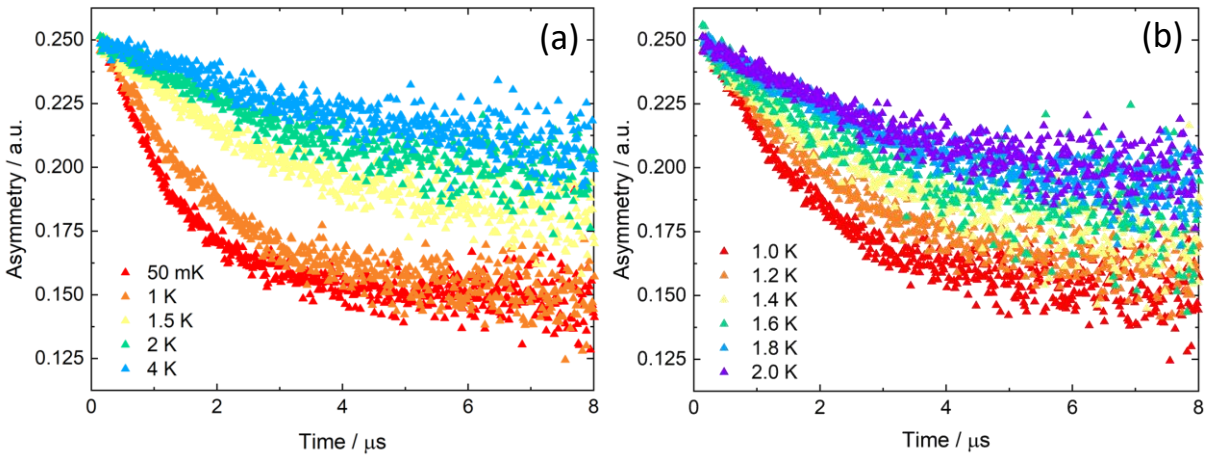

Figure 7.3: The measured data sets from ZF-μSR measurements carried out on Ba_2LuMoO_6. (a)The responses between 0.05(5) and 1.0(1) K the muons experience slight changes. A distinct change is observed between 1.0(1) and 1.5(1) K and therefore (b) displays measurements over the 1.0(1) and 2.0(1) K temperature range.

All results of ZF-μSR measured on Ba_2LuMoO_6 were fitted using the sum of an exponential relaxation and a constant. The relaxation corresponds to dynamic behaviour whilst the flat background is attributed to magnetism arising from a static magnetic field. The fitting function is shown below;

Equation 7.1: The asymmetry fitting function of the ZF-μSR for Ba_2LuMoO_6 used between 0.05(5) K and 4.0(1) K

$$A(t) = (A_1\exp(-\lambda_1 t)) + A_2$$

This fitting function can be used between 0.05(5) to 4.0(1) K. These fits were satisfactory across the temperature range, however, there was slight disparity observed at low time scales indicative of an incredibly fast relaxation that was not modelled by the fitting function. Attempts to fit these data using other fitting functions, such as the dynamic Kubo-Toyabe function, were all less successful. As this characteristic could not be described, it was rationalised that these fluctuations may have occurred at

a rate which was too fast to be accurately resolved by the instrument and therefore, Equation 7.1 was used to fit the data sets. The fittings at a variety of temperatures can be observed in Figure 7.4.

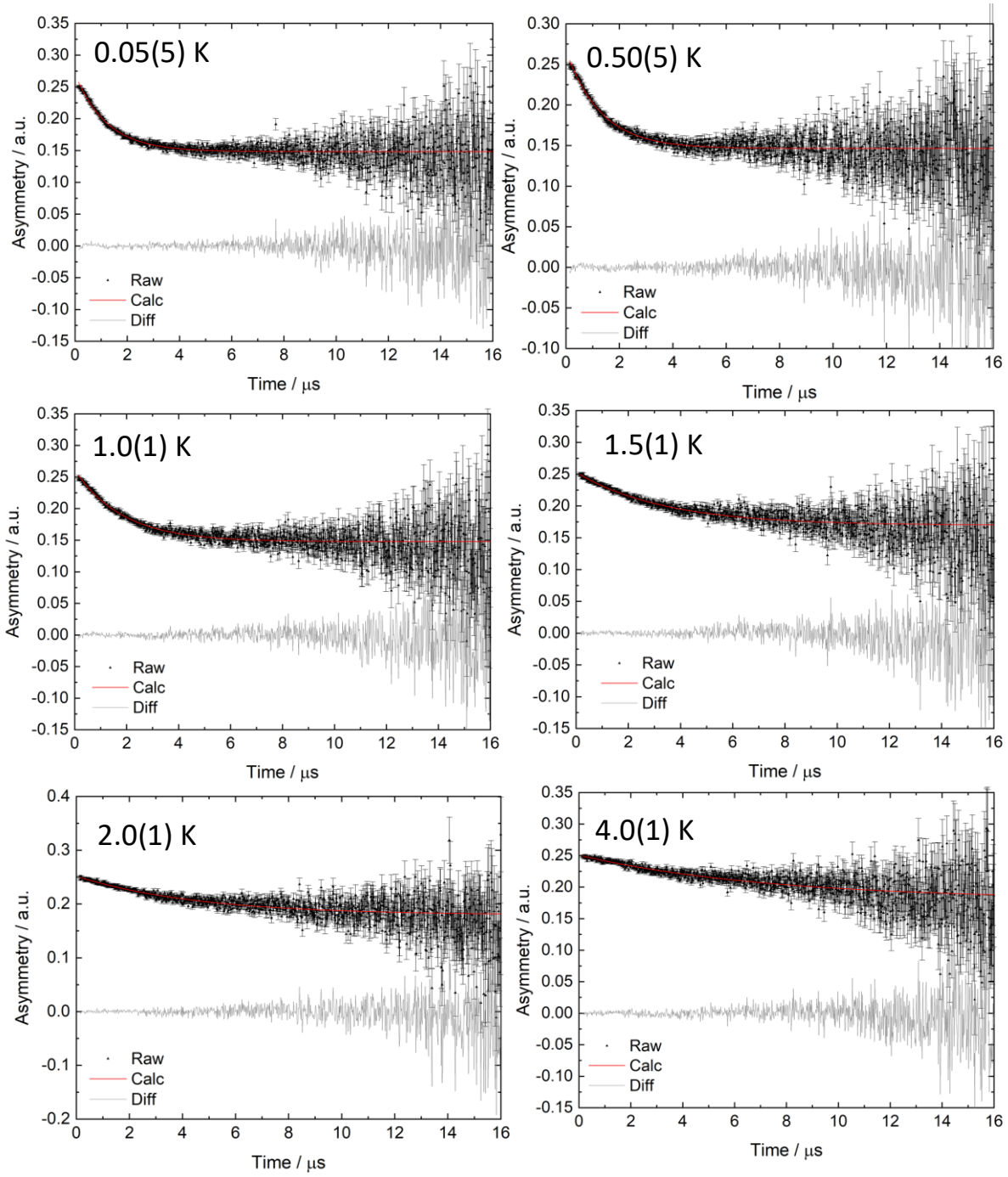

Figure 7.4: ZF-μSR carried out on Ba_2LuMoO_6 at 0.05, 0.5, 1, 1.5, 2 and 4 K. Each of these measurements were analysed using the fitting function $A(t) = (A_1\exp(-\lambda_1 t)) + A_2$. The calculated fit to the data is shown in a red line. A fairly large background is observed in the system and this is thought to be the result of the sample settling within the silver foil packet.

Completing these fittings allowed the thermal dependency of A_1, A_2 and λ_1 to be observed, see Figure 7.5 (a), (b) and (c) respectively. The magnitude of the asymmetries indicates the proportions of dynamic and static behaviour within Ba_2LuMoO_6. Throughout the temperature range A_2 is present in a greater proportion than the relaxing component. At 0.05(5) K, A_1 is at its highest value and remains close to this value until 1.0(1) K. Between 1.0(1) and 2.0(1) K, A_1 experiences a significant drop, before plateauing between 2.0(1) and 4.0(1) K. A_2 remains constant between 0.05(5) and 1.0(1) K, prior to a steady increase until 2.0(1) K. Above 2.0(1) K, the asymmetry varies slightly but is within error of being constant. The relaxation rate decreases with increasing temperature, with the sharpest decline observed between 1.0(1) and 2.0(1) K. Similarly, to the trends in the asymmetry, λ_1 experiences a plateau between 0.05(5) and 0.30(5) K. This provides evidence that Ba_2LuMoO_6 experiences dynamic behaviour down to 0.05(5) K and the plateau suggests that spin freezing does not take place in the measured temperature range.

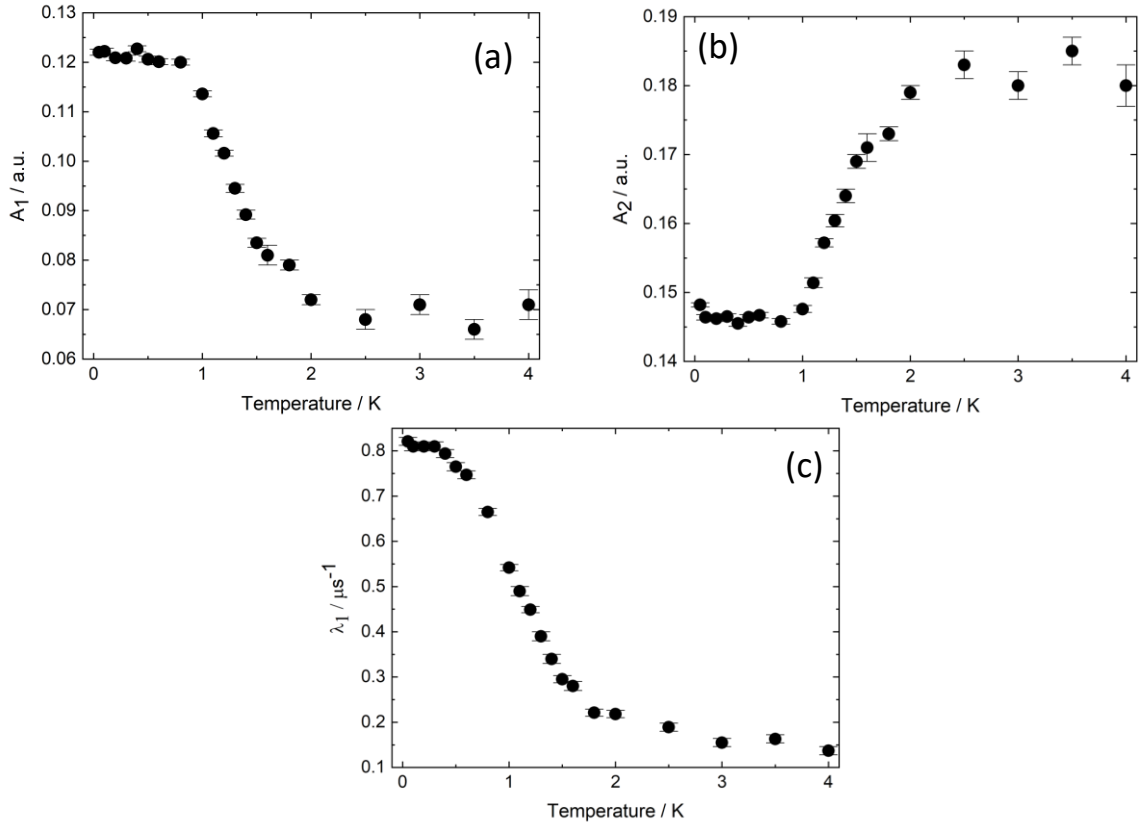

Figure 7.5: The fitting results on ZF- μSR measurements collected on Ba_2LuMoO_6 between 0.05(5) and 4.0(2) K. The thermal dependence of (a) A_1, (b) A_2 and (c) λ_1.

LF-μSR measurements were carried out on Ba_2LuMoO_6 at 0.10(5) K between 20 and 2000 G, see Figure 7.6 (a) . Some decoupling of the relaxation curve takes place in the 20 G data set, which indicates that weak nuclear moments are decoupled. As the field strength increases, further decoupling of the relaxation curve occurs but is most significant at 2000 G field strength. A minimal relaxation is still observed when a 2000 G field is applied to Ba_2LuMoO_6 which suggests that the dynamic behaviour at this temperature is the result of magnetic moments and not weak nuclear moments.

The LF-μSR measurements were fitted using Equation 7.1 which allowed a clear comparison to the ZF measurements. The trends of the field dependence of λ_1, A_1 and A_2 are illustrated in Figure 7.6. The relaxing asymmetry, A_1, decreases with increasing field strength whilst A_2 experiences a significant increase until 2000 G. The relaxation rate, λ_1, initially increases to a maximum at 20 G beyond this it decreases gradually until 1000 G, with a larger drop observed at 2000 G.

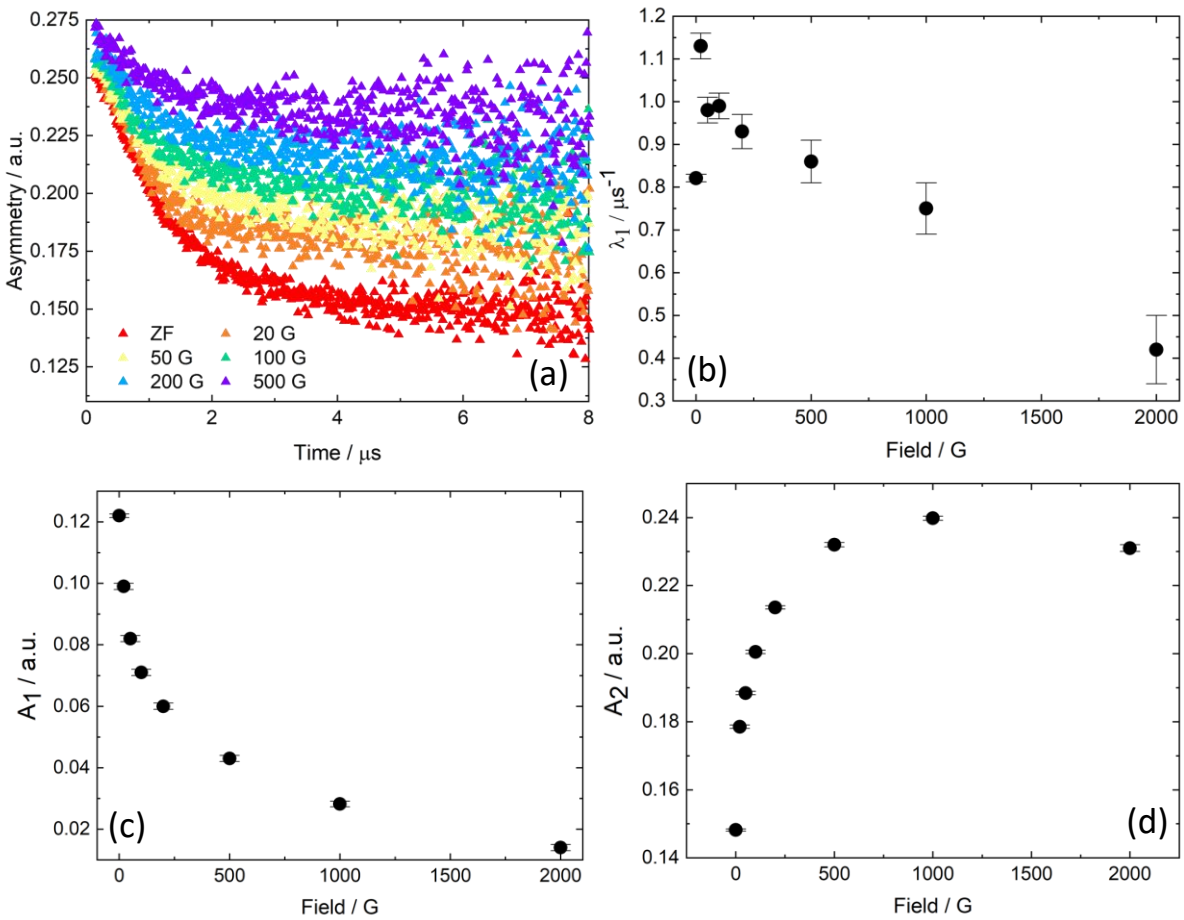

Figure 7.6: Observed data sets and results of fitting the longitudinal field muon spin relaxation measurements collected on Ba_2LuMoO_6 at 0.10(5) K in ZF and 2000 G. (a) Experimentally collected LF-μSR data measured on Ba_2LuMoO_6 at 0.10(5)K at ZF and LF between 20 and 2000 G. (b) field dependence of relaxation rate, λ_1. (c) field dependence of A_1, (d) the field dependence of A_2.

Inelastic Neutron Scattering

Inelastic neutron scattering was measured to gather insight into the structural and magnetic character of Ba_2LuMoO_6. Inelastic neutron scattering was measured at a range of temperatures between 7.5 and 200 K, which are shown in Figure 7.7. These measurements clearly showed that no long-range magnetic order took place within the system, agreeing with previous techniques.

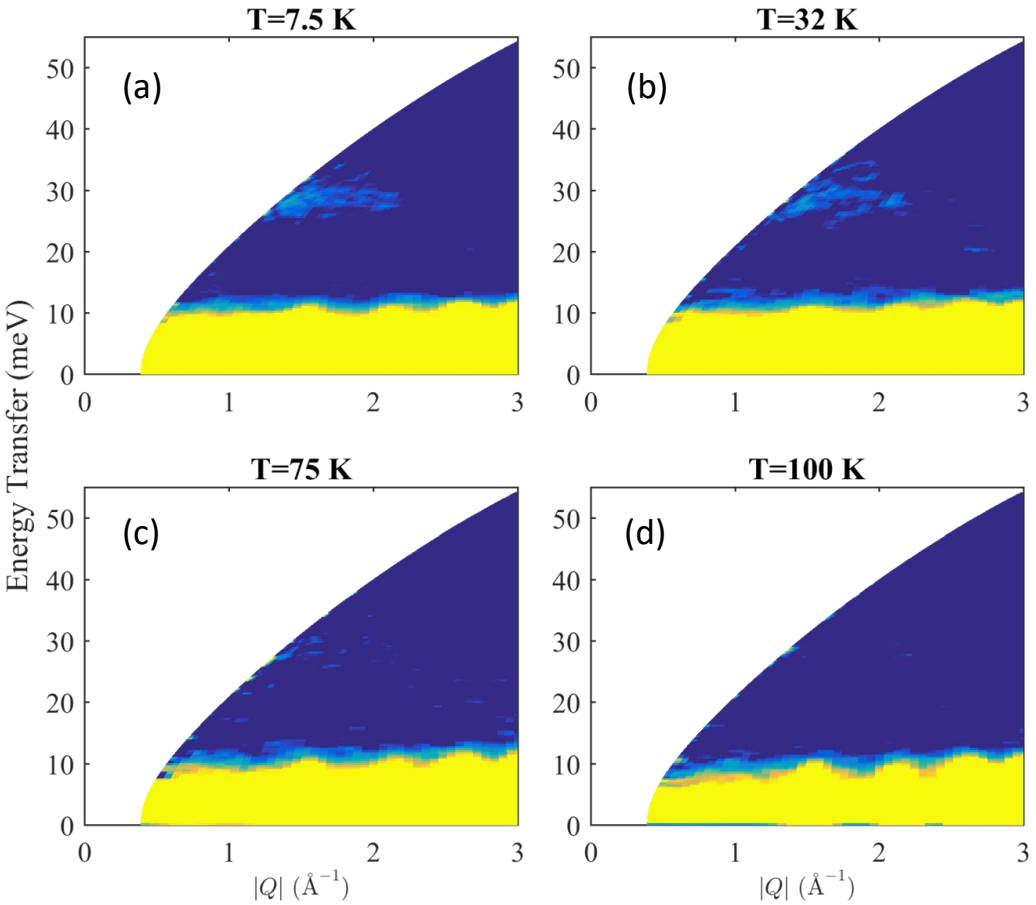

Figure 7.7: Inelastic neutron scattering measurements completed on Ba_2LuMoO_6 at (a) 7.5 K, (b) 32 K, (c) 75 K and (d) 100 K. These plots show the energy transfer in meV measured against momentum transferred *Q*. The brighter yellow and blue patches indicate high intensity whilst the dark blue regions are low intensity with little or no energy transfer. The white regions are outwith the detection area of the spectrometer. The yellow and light blue areas between 0 and 10 meV energy transferred is attributed to elastic processes. The excitations at 28 meV are observed at 7.5 and 32 K, however, are not observed at 75 and 100 K.

Each data set shows the measured energy transferred within Ba_2LuMoO_6 between 0 and 55 meV over the Q range 0 to 3 Å^{-1}. The elastic line, which corresponds to processes which conserve energy, extends from 0 to 10 meV and is observed in all data sets as a bright yellow proportion. A light blue band occurs just above the elastic line which is also attributed to elastic processes. The majority of each plot is

shaded dark blue which indicates no energy transferred over the Q range. At 7.5 K, a lighter blue section occurs which indicates excitations which take place at 28 meV between 1 and 2 $Å^{-1}$. This is most clearly observed in Figure 7.8, a cut of the data over the range $0 \leq Q \leq 2$ $Å^{-1}$.

The excitations at 28 meV persist at 32 K, with some remnants of these at 75 K, however, these are present in a substantially lower intensity than at the lower temperatures. By 100 K, these are no longer clearly observed, see Figure 7.8. The measurements show that these excitations are largest intensity at low temperatures. In conjunction, these excitations take place at low values of Q which confirms that these are magnetic in nature. The excitations do not extend from the elastic line and therefore are described as gapped which means that a defined energy jump is necessary. Excitations of this origin are characteristic of a weak transition from a spin singlet to spin triplet state and have also been observed in Ba_2YMoO_6 [171].

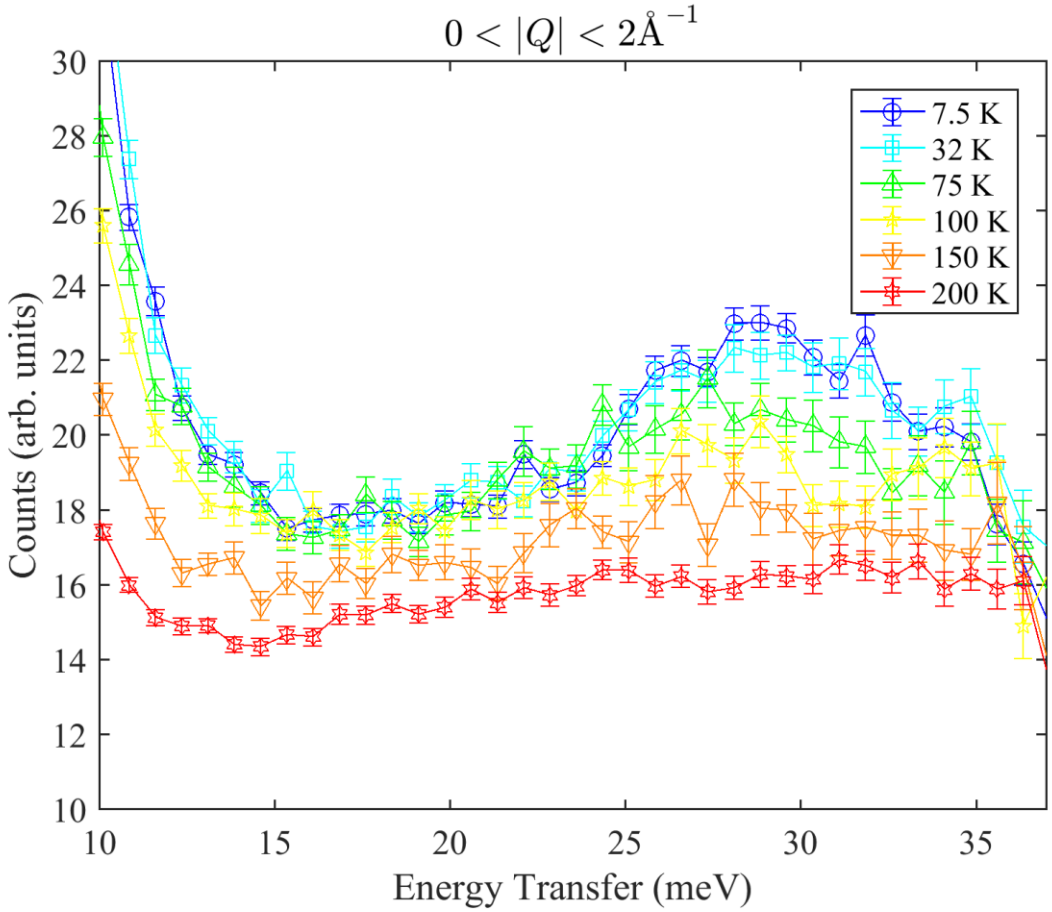

Figure 7.8: Inelastic neutron scattering measured on Ba_2LuMoO_6 between 7.5 and 200 K. This plot indicates a vertical cut taken through the system between $0 \leq |Q| \leq 2.0$ $Å^{-1}$. A broad bump is observed with a maximum at approximately 28 meV. This feature is clearly illustrated at 7.5 and 32 K but above this temperature it is not well defined.

Heat Capacity

Figure 7.9 depicts the results of heat capacity divided by temperature between Ba_2LuMoO_6 and its diamagnetic analogue Ba_2LuNbO_6. No lambda anomaly is observed in the heat capacity of either material which indicates that neither experience a structural or magnetic phase transition, which is in agreement with the related system Ba_2YMoO_6 [210]. The thermal dependence of the heat capacity divided by temperature is also depicted in Figure 7.9(b) to clearly highlight the differences between the magnetic and diamagnetic analogues. The C_P/T curve of Ba_2LuMoO_6 shows a slight increase at low temperature, which is intrinsically different to the experience of Ba_2LuNbO_6. The increase indicates that there is a magnetic contribution within Ba_2LuMoO_6 at these low temperatures. Unfortunately, due to the complicated nature of the heat capacity measurement the purely magnetic heat capacity could not be extracted from these data sets.

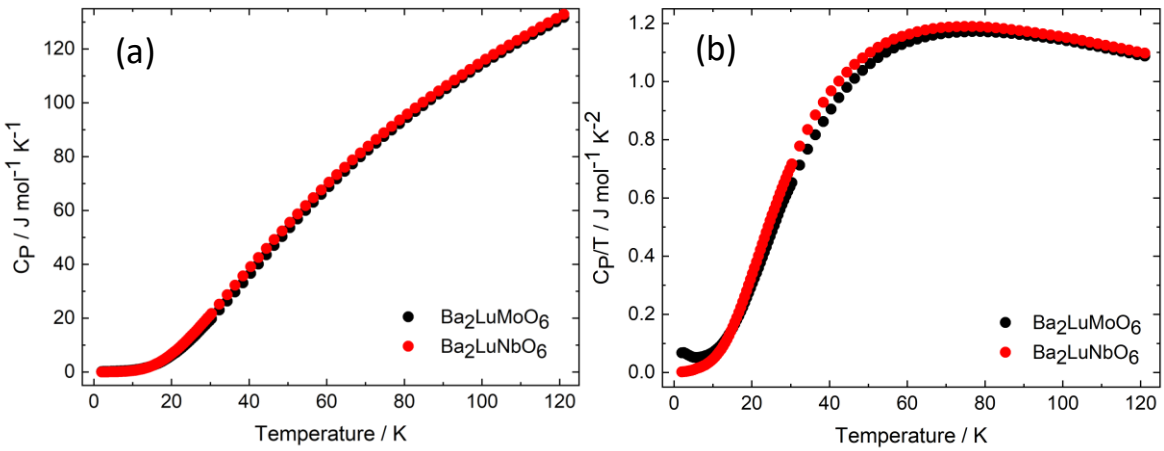

Figure 7.9: The results of heat capacity measurements carried out on Ba_2LuMoO_6 and its diamagnetic analogue Ba_2LuNbO_6. The thermal dependence of (a) the heat capacity (C_P) and (b) the heat capacity divided by temperature (C_P/T). (a) shows that no lambda anomaly takes place whilst (b) clearly illustrates differences at low temperature between the materials.

Discussion

Ba_2LuMoO_6 is a strongly frustrated double perovskite which contains the magnetic cation Mo^{5+} ($4d^1$, S = 1/2), and crystallises in the *fcc* space group $Fm\bar{3}m$. A previous report on this material suggests that Ba_2LuMoO_6 may enter a valence bond glass state at low temperature due to its similarities to Ba_2YMoO_6 which has been suggested to behave this way. Like Ba_2YMoO_6, Ba_2LuMoO_6 experiences no structural or magnetic phase transition on cooling. This lack of distortion from the cubic nuclear structure is controversial as the unequal occupancy of the d-orbitals suggests that a Jahn-Teller distortion should take place [116,210,215]. DC-susceptibility closely compares closely to that reported for Ba_2YMoO_6 and does suggest similar behaviour to what would be observed if this entered a valence bond glass state. When comparing the Curie-Weiss analysis of Ba_2LuMoO_6 and Ba_2YMoO_6 at high temperature, the effective magnetic moments show similar trends and are significantly smaller than what is anticipated for the S =1/2 spin state. The Weiss constants also indicate that the materials are strongly antiferromagnetic and Ba_2YMoO_6 appears to be more strongly frustrated than Ba_2LuMoO_6, which may be a result of a larger overlap between the Mo^{5+} cations. At lower temperature, the effective magnetic moments are found to decrease, and the Weiss constants are found to both be within error of zero indicating that the cations are no longer experiencing strong antiferromagnetic interactions. This is observed in both Ba_2YMoO_6 and Ba_2LuMoO_6 [116,215].

Muon spin relaxation measurements carried out down to 0.05(5) K indicate that Ba_2LuMoO_6 remains dynamic down to this temperature. The magnetism at this temperature originates from both dynamic and static fields at this temperature, with the dynamic behaviour present in a smaller proportion than the static behaviour. This corresponds with the hypothesis of the valence bond glass where a dilute proportion of residual paramagnetic moments distributed throughout a sea of spin singlets, however, the increasing proportion of dynamic magnetism may not agree with this [213]. The persistence of dynamic behaviour down to very low temperature is also a marker of quantum spin liquids and has been observed in a number of frustrated materials [60,117,195,258,259]. The LF-μSR measurements

confirm that the magnetic behaviour is electronic in origin due to the large external magnetic fields necessary for decoupling of the internal fields.

Comparing the μSR of Ba_2LuMoO_6 and Ba_2YMoO_6 indicate that the two materials experience slightly different behaviour. The relaxation curve of Ba_2LuMoO_6 is well-described by a single exponential plus a constant background, conversely Ba_2YMoO_6 requires two distinct relaxing proportions, one of which employs the stretch exponential, plus the flat signal [211]. Ba_2YMoO_6 also experiences a spin freezing temperature at 1.3 K which is not observed in the lutetium analogue. In both materials, the fraction of the relaxing component(s) is smaller than the static proportion, however, the trend of the relaxing proportions does not agree in the two systems. In Ba_2LuMoO_6, the magnitude of the relaxing phase increases with decreasing temperature until 1.0(1) K where it appears to stabilise. This is in direct contrast to what is observed in Ba_2YMoO_6 where the proportion of the paramagnetic behaviour only decreases with increasing temperature [211].

Inelastic neutron scattering measurements carried out on Ba_2LuMoO_6 show a magnetic gapped excitation, which persists until approximately 75 K. This excitation arises at approximately 28 meV which corresponds to that of a spin singlet to spin triplet transition. This conclusively provides evidence of Ba_2LuMoO_6 entering a spin singlet state, a prerequisite of the valence bond glass state. This was also observed in Ba_2YMoO_6 which is thought to be the first experimentally identified example of a valence bond glass in a face centered cubic frustrated material [212].

The combination of these results supports the valence bond glass state of Ba_2LuMoO_6. The strongest evidence for the emergence of this phase comes from the confirmation of spin singlets, provided by the inelastic neutron scattering results. The valence bond glass state requires the singlets, brought about by the coupling of the magnetic Mo^{5+} cations into non-magnetic pairs [213,256,257]. This investigation has not provided any evidence into which theory of the emergence of the valence bond glass theory is correct and further work is necessary to determine which is correct.

Conclusion

The supplementary measurements completed on Ba_2LuMoO_6, agree with the preliminary report of the emergence of a valence bond glass phase. This has been supported by μSR measurements which prove that electronic magnetic moments remain dynamic down to 0.05(5) mK and the proof of spin singlets from INS. The valence bond glass state is hypothesised as an amorphous distribution of spin singlets with residual spins which remain dynamic at low temperature.

8. Challenging the Valence Bond Glass State in $Ba_{2-x}Sr_xLuMoO_6$

This chapter comprises the research carried out on the $Ba_{2-x}Sr_xLuMoO_6$ (x = 0.5, 1.0, 1.5,2.0) series, which were synthesised to challenge the robustness of the valence bond glass state, suspected to occur in the parent material Ba_2LuMoO_6 [213,215]. Substitution of the *A*-site cation is regularly exercised within solid solutions of double perovskites and allows novel properties to be studied [134].The structure of a double perovskite is dependent on the Goldschmidt tolerance factor, which is defined by the ionic radii of the *A*-, *A'*-, *M*-, *M'*- and *X*-site ions [48,238]. If the tolerance factor deviates significantly below one the double perovskite deviates from ideal via octahedral tilting, and primarily affect the bond length between the *A*-site cations and anions [44,45]. This is of great interest in geometrically frustrated materials as these distortions influence the superexchange bond lengths and angles. Alterations to the superexchange pathways strongly affect the magnetic coupling constants and behaviour. The incorporation of this substitution with the low spin state of the $4d^1$ Mo^{5+} cation allows the valence bond glass state to be tested thoroughly.

Experimental

The $Ba_{2-x}Sr_xLuMoO_6$ solid solution was synthesised by combining stoichiometric quantities of $BaCO_3$, $SrCO_3$, Lu_2O_3 and MoO_3. The Lu_2O_3 was stored at 800 °C to prevent hydration. Calcination was completed at 800 °C for 24 hours prior to subsequent heating at 1250 °C utilising a closed atmosphere of 5% H_2/N_2. The sample was assessed using laboratory Cu X-ray diffraction of Rietveld standard.

Time-of-flight neutron powder diffraction was measured using the High Resolution Powder Diffractometer (HRPD) at the ISIS Neutron and Muon Source, Rutherford Appleton Laboratories in Didcot, Oxfordshire [260]. Approximately 6 g of each material was decanted into a vanadium can with internal diameter 6 mm. Post collection, absorption corrections were applied to each data set and Rietveld refinement was conducted using GSAS. The Time-of-flight peak shape was modelled using a convolution of the Ikeda-Carpenter and the Pseudo-Voigt functions and the background was refined with a shifted Chebyshev polynomial. [225]. HRPD has two data collection detector banks. Bank 1 is the highest resolution bank, whilst bank 2 is of lower resolution. Throughout this chapter, patterns from both shall be shown as bank 2 extends to further d-space which is necessary for observing magnetic Bragg peaks.

Magnetic susceptibility of Sr_2LuMoO_6 was measured using a Quantum Design magnetic property measurement system MPMS3. Measurements were collected between 2 and 300 K using the method previously described in the experimental theory section [98].

Muon spin relaxation measurements were completed on Sr_2LuMoO_6 at EMU based at the ISIS Neutron and Muon Source [227]. To carry out this measurement approximately 3 g of Sr_2LuMoO_6 was adhered to a silver sample holder. Calibration measurements were completed using a magnetic field of 100 G which was applied perpendicularly to the material, in a transverse geometry. Zero field measurements were carried out to investigate the local magnetic behaviour of Sr_2LuMoO_6 at a variety of temperatures between the range of 1.5 and 60 K. Longitudinal field measurements were carried out at 1 .5 and 60 K exclusively using fields between 5 to 4500 G at 1.5 K and 5 to 500 G at 60 K.

Results

X-ray Powder Diffraction

X-ray powder diffraction was carried out to monitor the phase purity of each sample and to observe any potential phase transitions across the series. These measurements provided evidence that $Ba_{1.5}Sr_{0.5}LuMoO_6$ crystallises in $Fm\bar{3}m$ and closely resembles Ba_2LuMoO_6. Conversely, the most substituted samples $Ba_{0.5}Sr_{1.5}LuMoO_6$ and Sr_2LuMoO_6 adopt the monoclinic space group $P2_1/n$, to accommodate the smaller Sr^{2+} cations [261]. The X-ray diffraction pattern of $BaSrLuMoO_6$ was more complex and therefore was fitted using both the cubic space group $Fm\bar{3}m$ and tetragonal space group $I4/m$. The fits yielded the following statistical parameters; R_{wp} = 14.20 and χ^2 = 10.81 for the cubic model and R_{wp} = 9.22 and χ^2 = 4.56 for the tetragonally distorted model. The difference suggested further investigation using neutron powder diffraction was necessary. Each of the materials contained small quantities of persistent impurities $SrLu_2O_4$ and Mo^0 which could not be removed through further heating steps [262,263]. Figure 8.1 shows the result of the Rietveld refinement carried out on the X-ray powder diffraction of $Ba_{1.5}Sr_{0.5}LuMoO_6$. This is shown to indicate the scale of the impurities within each of the $Ba_{2-x}Sr_xLuMoO_6$ materials. Each of the highest intensity impurity peaks are defined using a blue ($SrLu_2O_4$) or red (Mo^0) asterisk. Each of these peaks are very small in comparison to the highest intensity peak of $Ba_{1.5}Sr_{0.5}LuMoO_6$ which shows that the impurities are present in very small quantities.

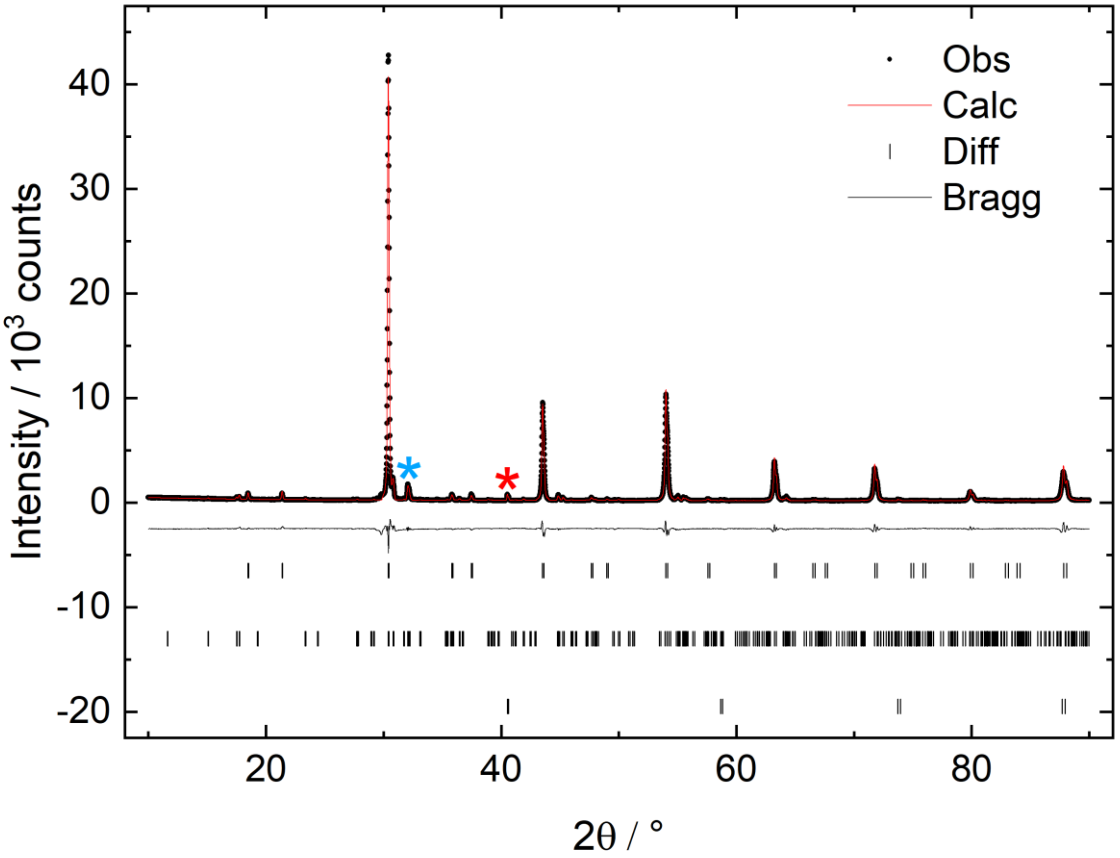

Figure 8.1: The result of Rietveld refinement carried out on the X-ray diffraction pattern collected on $Ba_{1.5}Sr_{0.5}LuMoO_6$ at ambient temperature. The top line of Bragg reflections corresponds to the perovskite phase, the second to $SrLu_2O_4$ impurity and the bottom line to Mo^0 impurity. The most prominent peak of $SrLu_2O_4$ and Mo^0 are indicated by the blue and red asterisks respectively to give an idea of the magnitude of the impurity.

Neutron Powder Diffraction

Rietveld refinement against neutron powder diffraction collected on $Ba_{1.5}Sr_{0.5}LuMoO_6$ at ambient temperature show it crystallises in the $Fm\bar{3}m$ space group with lattice parameter a = 8.3136(1) Å. Refinement of the fractional occupancy of the oxide anions indicates that this is within error of unity. No antisite disorder of the Lu^{3+} and Mo^{5+} cations was observed. The impurities $SrLu_2O_4$ and elemental molybdenum were characterised with quantities of 4.84(6) wt% and 0.61(2) wt% respectively [263]. An additional external impurity from the vanadium can was indexed. The fit yielded R_{wp} = 5.51.

Cooling to 2 K, $Ba_{1.5}Sr_{0.5}LuMoO_6$ retains the cubic symmetry with no structural or magnetic phase transition and conventional thermal expansion. Results of the refinement against data collected at 2 K are shown in Figure 8.2. The thermal parameters show little change between 2 and 60 K. The thermal displacement of the Mo^{5+} cation was fixed to a small positive value as it refined slightly negative, this fix made minimal change to the refinement as all refined parameters remained within the estimated standard deviations shown in Table 8:1. Over the temperature range, the Sr-O and Mo-O bond lengths increase with temperature, whilst the Lu-O bond lengths decrease slightly as temperature increases.

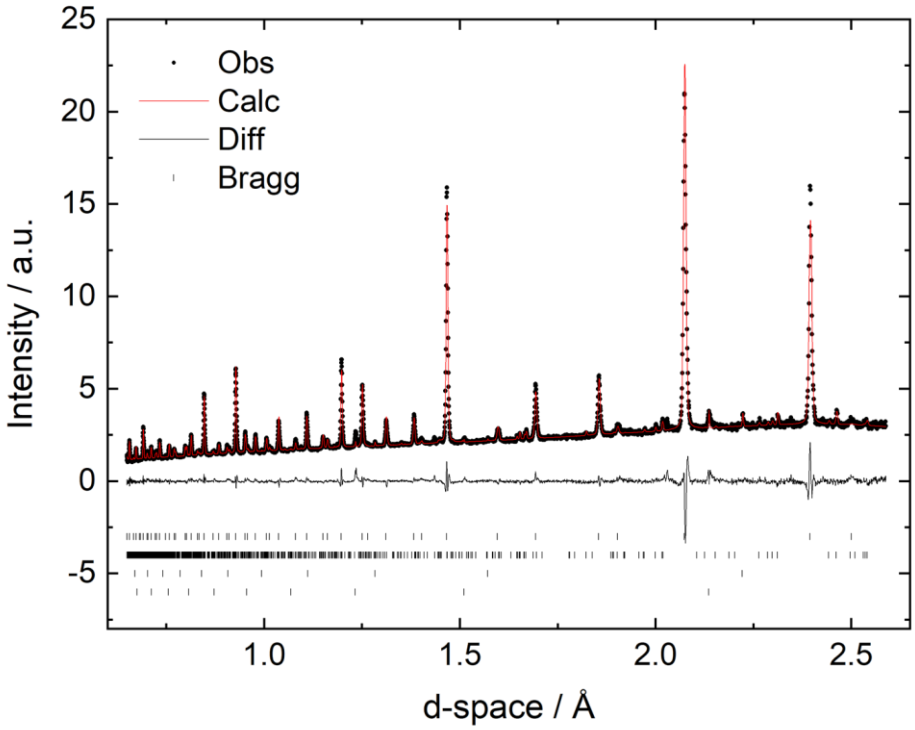

Figure 8.2: The results of Rietveld refinement performed against the neutron powder diffraction pattern of $Ba_{1.5}Sr_{0.5}LuMoO_6$ at 2 K. The rows of Bragg reflections correspond to the cubic $Ba_{1.5}Sr_{0.5}LuMoO_6$, $SrLu_2O_4$, Mo^0 and V^0 in descending order. $Ba_{1.5}Sr_{0.5}LuMoO_6$ retains cubic symmetry at 2 K, with no structural distortion.

Table 8:1: The results from the Rietveld refinement of the neutron powder diffraction data sets collected on $Ba_{1.5}Sr_{0.5}LuMoO_6$ at 295, 60, 15, 6 and 2 K. $Ba_{1.5}Sr_{0.5}LuMoO_6$ adopts the *fcc* space group $Fm\bar{3}m$, where Ba^{2+}/Sr^{2+}, Lu^{3+} and Mo^{5+} sit on the special positions (1/4, 1/4, 1/4), (0, 0, 0) and (1/2, 1/2, 1/2) respectively. The oxide anion lies on (x, 0, 0).

Temperature / K	**2**	**6**	**15**	**60**	**295**
a / Å	8.2985(2)	8.2986(2)	8.2987(2)	8.2993(2)	8.3136(1)
Ba/Sr 100U_{iso} / Å^2	0.64(3)	0.62(3)	0.63(3)	0.64(3)	1.10(3)
Lu 100U_{iso} / Å^2	1.39(6)	1.40(6)	1.39(6)	1.14(6)	0.72(4)
Mo 100U_{iso} / Å^2	0.10	0.10	0.10	0.10	0.35(4)
O x	0.2638(1)	0.2637(1)	0.2638(1)	0.2639(1)	0.26298(6)
O(1) 100U_{iso} / Å^2	1.61(3)	1.60(3)	1.60(3)	1.55(3)	1.70(2)
Ba(Sr)-O / Å	2.936(1)	2.936(1)	2.936(1)	2.937(1)	2.941(1)
Ba/Sr BVS	2.05	2.09	2.09	2.09	2.06
Lu-O / Å	2.189(1)	2.189(1)	2.189(1)	2.191(1)	2.187(1)
Lu BVS	3.27	3.33	3.33	3.32	3.35
Mo-O / Å	1.960(1)	1.961(1)	1.960(1)	1.959(1)	1.971(1)
Mo BVS	5.13	5.20	5.20	5.21	5.05
R_{wp}	3.37	3.37	3.46	3.49	5.51
X^2	7.616	7.565	8.051	4.312	4.541

The neutron powder diffraction pattern collected on $BaSrLuMoO_6$ at room temperature was fitted using the *fcc* space group $Fm\bar{3}m$ and the tetragonal distorted *I4/m,* to conclusively deduce the nuclear structure. The cubic model resulted in a poor fit with R_{wp} = 14.45 and χ^2 = 35.56. The tetragonal model showed a significant improvement with R_{wp} = 4.89 and χ^2 = 4.084. To ensure that this analysis was fair the two models were identical and only differed where necessary, i.e. space groups, lattice parameters and atomic positions. The results of the tetragonal Rietveld refinement of $BaSrLuMoO_6$ at room temperature are shown in Figure 8.3, an additional $SrLu_2O_4$ impurity was present.

The results of Rietveld refinement can be found in Table 8:2. The thermal displacement of the Mo^{5+} cation refined to a slightly negative value, however, this was within error of zero and therefore was fixed to a small positive displacement. The Mo-O bond lengths lie within error of each other indicating the octahedra are undistorted despite the tetragonal distortion of the overall structure, violating the Jahn-Teller effect. The LuO_6 octahedra also remain undistorted with minimal separation. Refinement indicates that oxide loss is negligible and no mixing of the Lu^{3+} and Mo^{5+} cations. A number of small intensity peaks are present within the diffraction pattern could not be indexed using a lower symmetry perovskite structure using the P1 space group and therefore this will not be covered in further detail.

Table 8:2: The results from the Rietveld refinement against the neutron powder diffraction data sets collected on $BaSrLuMoO_6$ at 295 K. This was completed using the tetragonal space group *I4/m*, where Ba^{2+}/Sr^{2+}, Lu^{3+} and Mo^{5+} sit on the special positions (0, 1/2, 1/4), (0, 0, 0) and (0, 0, 1/2) respectively.

Temperature / K	295
a / Å	5.8303(1)
c / Å	8.2867(2)
Ba/Sr 100U_{iso} / Å^2	0.0101(2)
Lu 100U_{iso} / Å^2	0.0073(4)
Mo 100U_{iso} / Å^2	0.010
O(1) coordinate	(0.2647(2), 0.2133(2), 0)
O(2) coordinate	(0, 0, 0.2384(3))
O(1) 100U_{iso} / Å^2	0.0170(2)
O(2) 100U_{iso} / Å^2	0.0191(5)
Ba(Sr)-O / Å	2.9167(3), 2.7787(5), 3.0768(5)
Lu-O / Å	1.976(3), 1.982(2)
Mo-O / Å	2.167(3), 2.163(3)

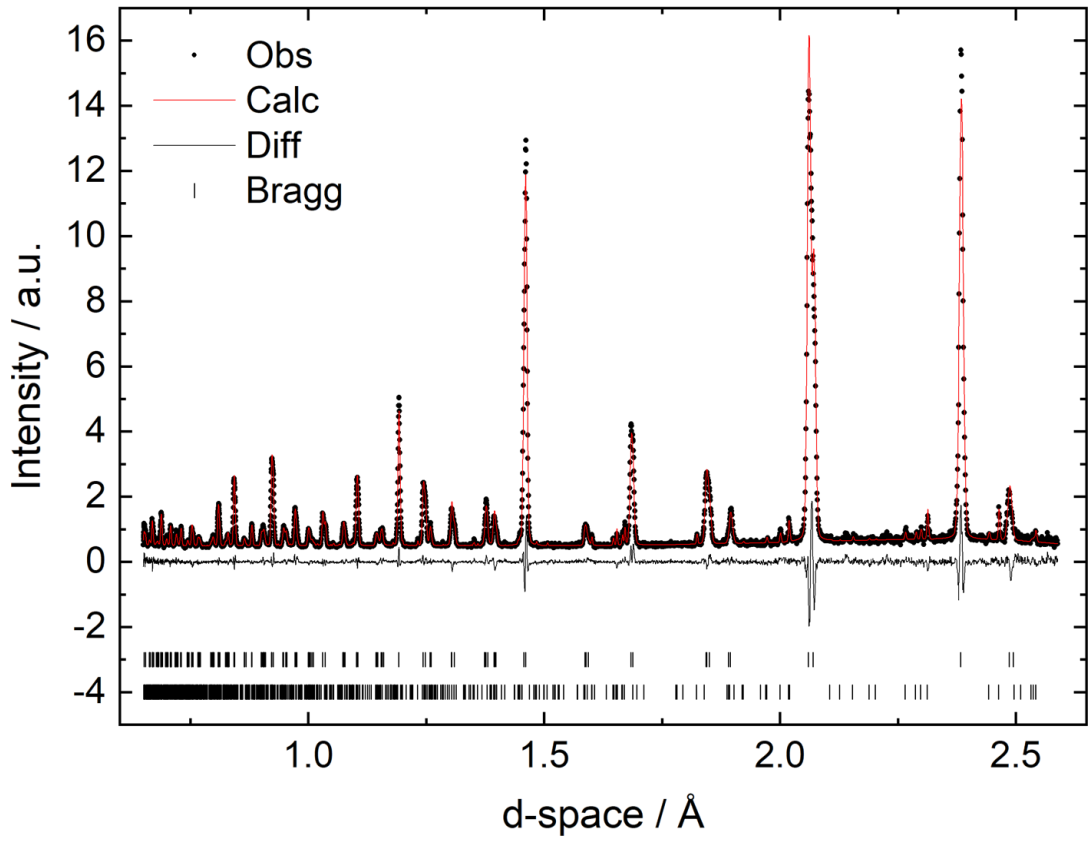

Figure 8.3: Rietveld refinement of the neutron powder diffraction pattern of $BaSrLuMoO_6$ measured at room temperature. The Bragg reflections correspond to *I4/m* $BaSrLuMoO_6$ (top) and $SrLu_2O_4$ (bottom).

$Ba_{0.5}Sr_{1.5}LuMoO_6$ was also investigated at room temperature and below. Rietveld refinement of these data sets indicate that it crystallises in the monoclinic space group $P2_1/n$. Two intrinsic impurities, $SrLu_2O_4$ and Mo^0 were included in the refinement with 3.32(5) wt% and 0.37(1) wt% respectively. A further V^0 impurity was introduced to the calculation. The refinement shows negligible antisite disorder and the oxide positions are within error of being fully occupied. At 2 K, $Ba_{0.5}Sr_{1.5}LuMoO_6$ retains it monoclinic symmetry as shown in the diffraction pattern in Figure 8.4.

Table 8:3: Results from Rietveld refinement of neutron powder diffraction measurements of $Ba_{0.5}Sr_{1.5}LuMoO_6$ at 2, 6, 15, 60 and 295 K. $Ba_{0.5}Sr_{1.5}LuMoO_6$ adopts the $P2_1/n$ space group. Lu^{3+} and Mo^{5+} lie on special positions (1/2, 0, 0) and (0, 1/2, 0), whilst the Ba^{2+}/Sr^{2+} cations and three separate oxide positions, O(1), O(2) or O(3), sit on those indicated.

Temperature / K	**2**	**6**	**15**	**60**	**295**
***a* / Å**	5.8062(2)	5.8061(1)	5.8061(2)	5.8068(2)	5.8172(1)
b / Å	5.7978(1)	5.7977(1)	5.7977(1)	5.7978(2)	5.8033(1)
c / Å	8.1755(1)	8.1754(1)	8.1754(1)	8.1761(2)	8.1920(1)
***β* / °**	90.112(2)	90.114(2)	90.112(2)	90.115(3)	90.071(3)
Ba(Sr) x	0.0040(4)	0.0038(4)	0.0039(4)	0.0037(5)	0.0051(3)
Ba(Sr) y	0.0194(2)	0.0193(2)	0.0192(2)	0.0191(3)	0.0125(3)
Ba(Sr) z	0.2489(7)	0.2491(7)	0.2491(7)	0.2492(7)	0.2445(5)
Ba(Sr) 100U_{iso} / Å^2	0.29(2)	0.26(2)	0.27(2)	0.29(2)	0.92(2)
Lu 100U_{iso} / Å^2	0.38(5)	0.26(2)	0.33(5)	0.35(5)	0.5(1)
Mo 100U_{iso} / Å^2	0.23(5)	0.31(5)	0.21(5)	0.15(6)	0.1(1)
O(1) x	0.9400(3)	0.9398(3)	0.9397(3)	0.9400(3)	0.9483(3)
O(1) y	0.4907(4)	0.4903(4)	0.4909(4)	0.4906(4)	0.4925(4)
O(1) z	0.2353(3)	0.2354(3)	0.2354(3)	0.2356(4)	0.2371(4)
O(1) 100U_{iso} / Å^2	0.61(5)	0.59(5)	0.62(5)	0.62(6)	1.32(5)
O(2) x	0.2626(6)	0.2637(6)	0.2625(6)	0.2637(7)	0.2530(4)
O(2) y	0.2824(8)	0.2839(7)	0.2826(8)	0.2841(8)	0.2646(7)
O(2) z	0.0293(6)	0.0296(6)	0.0287(6)	0.0297(6)	0.0289(4)
O(2) 100U_{iso} / Å^2	1.0(1)	0.8(1)	0.9(1)	0.8(1)	1.79(8)
O(3) x	0.2839(7)	0.2829(6)	0.2844(7)	0.2827(7)	0.2840(4)
O(3) y	0.2637(8)	0.2622(8)	0.2634(8)	0.2615(8)	0.2759(7)
O(3) z	0.4709(6)	0.4713(6)	0.4706(6)	0.4715(7)	0.4724(4)
O(3) 100U_{iso} / Å^2	1.4(1)	1.4(1)	1.3(1)	1.5(1)	1.46(7)
R_{wp}	2.37	2.35	2.38	2.63	4.24
X^2	3.941	3.867	3.974	2.576	3.077

$Ba_{0.5}Sr_{1.5}LuMoO_6$ exhibits conventional thermal expansion behaviour in all lattice parameters. In $Ba_{0.5}Sr_{1.5}LuMoO_6$, the β angle experiences a larger distortion from 90° at 2 K compared to room temperature. The atomic parameters remain constant between 2 and 60 K, with larger changes

observed at room temperature. The Ba/Sr – O bond lengths are split into three significantly greater than 3.0 Å and three significantly smaller than 2.7 Å, suggesting the coordination of the Sr^{2+} cation is 9. The MoO_6 octahedra are tetragonally elongated and consequently the LuO_6 octahedra distort.

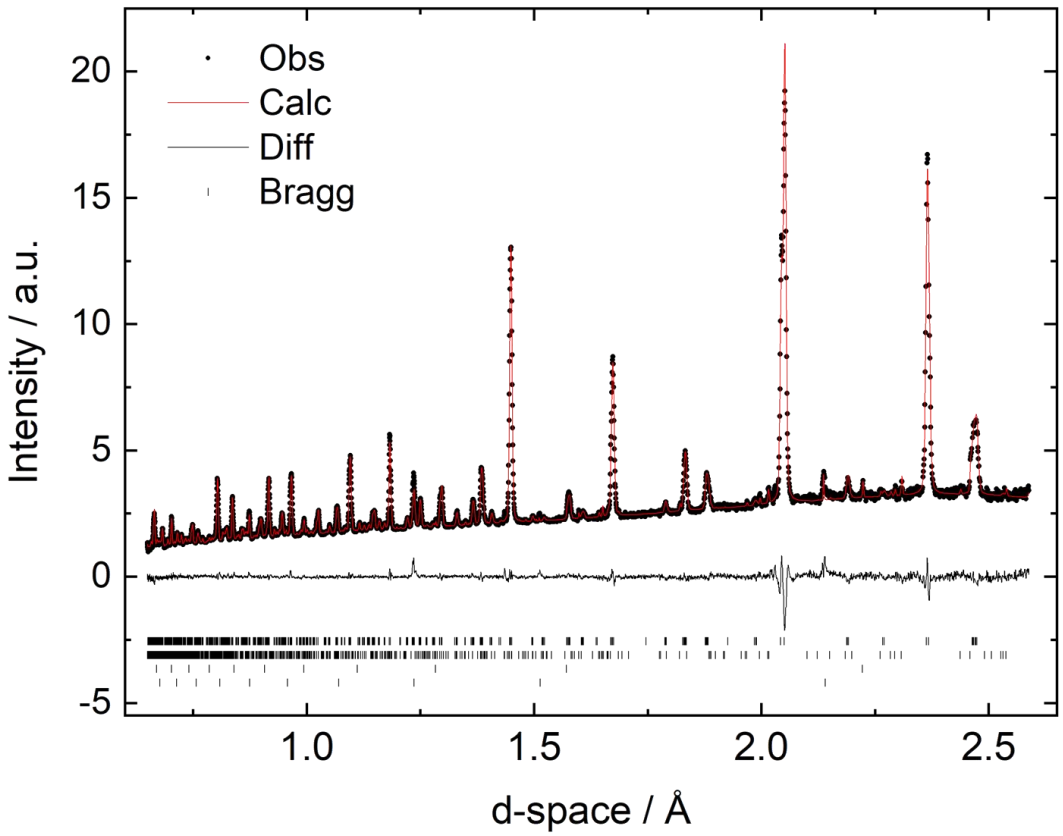

Figure 8.4: The results of Rietveld refinement of neutron powder diffraction measured on $Ba_{0.5}Sr_{1.5}LuMoO_6$ at room temperature. The Bragg reflections are attributed to $Ba_{0.5}Sr_{1.5}LuMoO_6$ (*P2₁/n*), $SrLu_2O_4$, Mo^0 and V^0.

Table 8:4: Results from Rietveld refinement of the neutron powder diffraction data sets collected on $Ba_{0.5}Sr_{1.5}LuMoO_6$ at 2, 6, 15, 60 and 295 K. This table shows the Ba/Sr-O, Lu-O and Mo-O bond lengths and the calculated bond valence sums. The three distinct superexchange angles are significantly distorted from the ideal antiferromagnetic superexchange angle of 180°.

Temperature / K	**2**	**6**	**15**	**60**	**295**
Ba(Sr)-O(1) / Å	3.090(2)	3.091(2)	3.088(2)	3.088(2)	3.036(2)
	2.760(2)	2.758(2)	2.762(2)	2.761(2)	2.806(2)
	2.586(3)	2.584(3)	2.584(3)	2.585(3)	2.645(3)
	3.235(3)	3.238(3)	3.237(3)	3.236(3)	3.185(3)
Ba(Sr)-O(2) / Å	2.796(7)	2.804(6)	2.800(6)	2.805(6)	2.711(6)
	2.646(5)	2.637(5)	2.648(5)	2.634(5)	2.736(5)
	3.258(6)	3.267(6)	3.256(6)	3.269(6)	3.139(6)
	2.924(7)	2.918(7)	2.920(7)	2.919(7)	2.850(7)
Ba(Sr)-O(3) / Å	2.816(6)	2.811(6)	2.815(6)	2.809(6)	2.906(6)
	2.637(6)	2.648(6)	2.636(6)	2.652(6)	2.560(6)
	3.279(6)	3.267(6)	3.279(6)	3.262(6)	3.319(6)
	2.893(6)	2.897(6)	2.895(6)	2.900(6)	2.850(6)
Ba(Sr) BVS	1.91	1.91	1.91	1.91	1.94
Lu-O / Å	2.192(3)	2.191(3)	2.192(3)	2.189(3)	2.175(3)
	2.154(3)	2.156(3)	2.155(3)	2.158(3)	2.117(3)
	2.157(3)	2.158(3)	2.161(3)	2.159(3)	2.115(3)
Lu BVS	3.53	3.52	3.51	3.52	3.86
Mo-O / Å	1.956(3)	1.958(3)	1.957(3)	1.959(3)	1.966(3)
	1.993(4)	1.993(3)	1.991(3)	1.993(3)	2.022(3)
	1.992(4)	1.988(4)	1.989(4)	1.986(4)	2.048(4)
Mo BVS	4.93	4.93	4.94	4.94	4.54
Mo-O-Lu / °	160.4(1)	160.3(1)	160.3(1)	160.4(1)	163.1(1)
	163.2(2)	162.8(2)	162.8(2)	162.7(2)	166.3(2)
	162.9(3)	163.4(3)	163.4(3)	163.6(3)	161.5(2)

At ambient temperature Sr_2LuMoO_6 crystallises in the monoclinic space group $P2_1/n$ with no antisite disorder and oxide content within error of full site occupancy. The additional impurity phases of $SrLu_2O_4$ and Mo^0 were present in small quantities of 3.73(7) wt% and 0.44(2) wt% respectively. Additional unindexed peaks were characterised as elemental vanadium. Once all four phases were added the diffraction pattern were found to be well characterised with no supplementary unindexed peaks present, giving R_{wp} = 4.40.

Upon cooling Sr_2LuMoO_6 retains its monoclinic symmetry with no structural phase shift or significant change of profile intensity. The lack of additional peaks shows no antiferromagnetic ordering occurs. The diffraction pattern collected at 2 K is shown in Figure 8.5. Across the series a contraction of the Sr_2LuMoO_6 lattice is observed as the temperature decreases conventionally as displayed in Figure 8.6. The *a* and *c* axes increase significantly with temperature, whilst the *b* axis exhibits a slight decrease. The decrease in *b* may be a result of the *β* angle becoming more distorted from the ideal value of 90° at the lower temperature. These changes can be observed in Table 8:5.

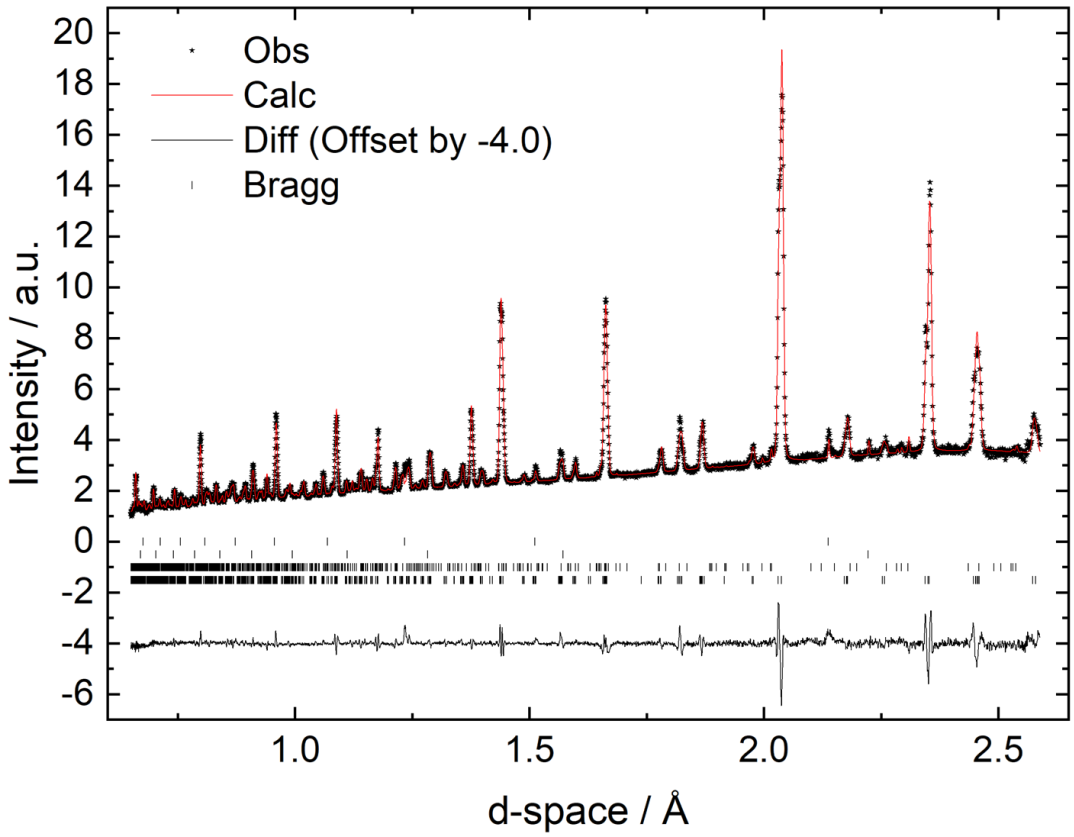

Figure 8.5: Rietveld refinement of neutron powder diffraction measurements collected on Sr_2LuMoO_6 at 2 K. From top to bottom the Bragg reflections correspond to Sr_2LuMoO_6, $SrLu_2O_4$, Mo^0 and the final row corresponds to the vanadium can.

Table 8:5: The results of Rietveld refinement of neutron powder diffraction data sets collected on Sr_2LuMoO_6 at 2.0(2), 6.0(2), 15.0(5), 60(1) and 295(2) K. Sr_2LuMoO_6 inhabits the *P2₁/n* space group. Here, the Lu^{3+} and Mo^{5+} cations are constrained to special positions (0.5, 0, 0) and (0, 0.5, 0) respectively. Sr^{2+} can reside on any point of the x, y and z axes. Three distinct oxide positions are available, these are denoted as O(1), O(2) or O(3).

Temperature / K	**2**	**6**	**15**	**60**	**295**
Sr x	0.0083(5)	0.0077(5)	0.0081(5)	0.0080(5)	0.0062(4)
Sr y	0.0302(2)	0.0301(2)	0.0302(2)	0.0303(2)	0.0257(2)
Sr z	0.2555(5)	0.2553(6)	0.2558(5)	0.2569(5)	0.2526(4)
Sr U_{iso} x100 / Å²	0.32(4)	0.34(4)	0.30(4)	0.27(4)	0.83(2)
Lu U_{iso} x100 / Å²	0.35(7)	0.32(7)	0.36(7)	0.29(7)	0.17(4)
Mo U_{iso} x100 / Å²	0.65(8)	0.71(8)	0.59(9)	0.71(9)	0.59(5)
O(1) x	0.9284(5)	0.9285(5)	0.9285(5)	0.9287(5)	0.9314(4)
O(1) y	0.4864(4)	0.4864(4)	0.4862(4)	0.4861(4)	0.4886(3)
O(1) z	0.2395(4)	0.2400(4)	0.2404(4)	0.2402(4)	0.2363(3)
O(1) U_{iso} x100 / Å²	1.01(5)	1.03(5)	1.00(5)	0.96(5)	1.01(4)
O(2) x	0.2812(6)	0.2809(6)	0.2810(6)	0.2823(6)	0.2811(4)
O(2) y	0.2997(6)	0.2998(6)	0.2998(6)	0.2979(7)	0.2974(4)
O(2) z	0.0331(4)	0.0330(4)	0.0328(4)	0.0328(4)	0.0322(3)
O(2) U_{iso} x100 / Å²	1.16(9)	1.10(9)	1.14(9)	1.20(9)	1.38(6)
O(3) x	0.2870(5)	0.2873(5)	0.2871(5)	0.2860(5)	0.2852(4)
O(3) y	0.2674(5)	0.2672(5)	0.2675(5)	0.2689(6)	0.2677(4)
O(3) z	0.4642(4)	0.4639(4)	0.4640(5)	0.4640(4)	0.4669(3)
O(3) U_{iso} x100 / Å²	0.87(9)	0.91(9)	0.95(9)	1.05(9)	0.93(6)
R_{wp}	2.87	2.91	2.91	2.97	4.40
X^2	5.943	6.106	6.069	3.824	3.962

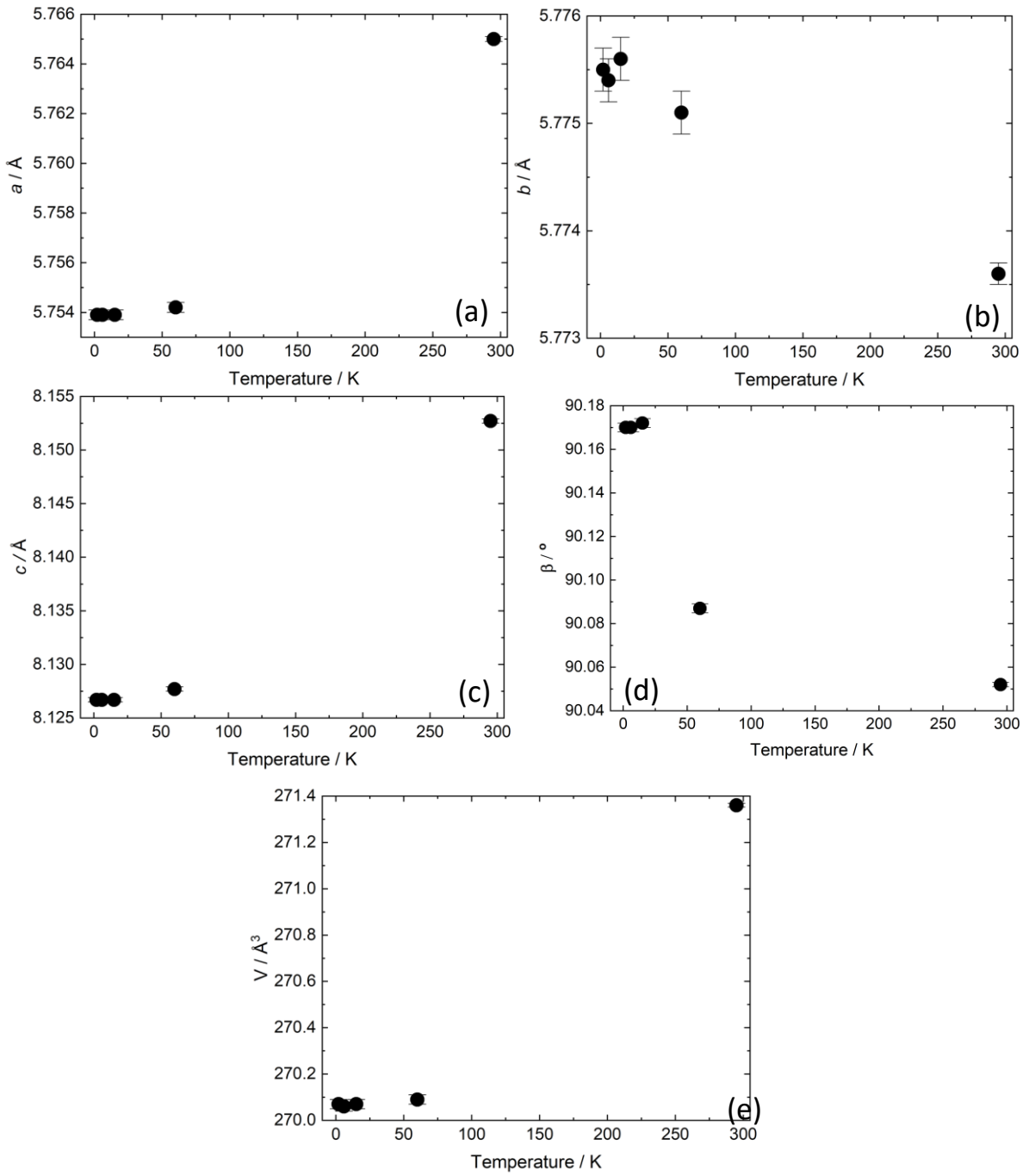

Figure 8.6: Results from neutron powder diffraction measurements collected on Sr_2LuMoO_6 between 2 and 295 K. These indicate the thermal dependence of (a), (b), (c) lattice parameter *a*, *b* and *c*, (d) lattice angle *β* and (e) cell volume, *V*.

Structural analysis of Sr_2LuMoO_6 indicates that at any temperature it possesses 11 or 12 distinct Sr-O bond lengths and three pairs of Lu-O and Mo-O bond lengths see, Table 8:6. At room temperature there are 12 calculated Sr-O bond lengths which reduces to 11 at 60(1) K. The coordination number of Sr^{2+} is anticipated to be 8 as all other bond lengths are considerably larger than 2.9 Å. At room temperature, both MoO_6 and LuO_6 octahedra are distorted. The MoO_6 octahedra experience a

tetragonal compression brought about by the Jahn-Teller effect of the Mo^{5+} ion, which affects the surrounding LuO_6 octahedra. Below room temperature the differences between the Lu-O and Mo-O bond lengths are far less pronounced and the LuO_6 and MoO_6 octahedra appear undistorted. The superexchange angles are distorted from 180° and experience minimal thermal dependence.

Table 8:6: The results from Rietveld refinement of the neutron powder diffraction pattern of Sr_2LuMoO_6 at all the measuring temperatures. This table indicates the bond lengths of the cation to oxygen bond lengths and the calculated bond valence sums. The three separate bond angles are also quoted.

Temperature / K	**2**	**6**	**15**	**60**	**295**
Sr-O(1) / Å	3.177(2) 2.678(2) 2.526(4) 3.252(4)	3.175(2) 2.677(2) 2.522(4) 3.255(4)	3.177(2) 2.677(2) 2.525(4) 3.252(4)	3.179(2), 2.675(2), 2.525(4), 3.252(4)	3.134(2), 2.711(2), 2.533(3), 3.251(3)
Sr-O(2) 1/ Å	2.853(4) 2.491(4) 2.783(5)	2.854(4) 2.494(5) 2.782(5)	2.856(4) 2.491(4) 2.779(5)	2.860(4) 2.488(4) 2.771(5)	2.861(3) 2.516(3) 3.411(3) 2.812(4)
Sr-O(3) / Å	2.709(4) 2.620(4) 3.318(4) 2.934(4)	2.712(4) 2.619(4) 3.318(4) 2.933(4)	2.708(4) 2.621(4) 3.317(4) 2.937(4)	2.704(4) 2.626(4) 3.311(4) 2.943(4)	2.619(3) 2.758(3) 3.301(3) 2.914(3)
Sr BVS [10]	1.93	1.93	1.93	1.94	1.89
Lu-O / Å	2.159(3) 2.156(4) 2.148(3)	2.155(3) 2.158(4) 2.150(3)	2.152(3) 2.157(4) 2.148(3)	2.154(3) 2.144(4) 2.138(3)	2.188(2)* 2.147(3) 2.138(2)
Lu BVS [10]	3.66	3.66	3.68	3.75	3.63
Mo-O / Å	1.990(3) 2.008(4) 1.994(3)	1.994(3) 2.006(4) 1.992(3)	1.997(3) 2.007(4) 1.994(3)	1.995(3) 2.019(4) 2.004(3)	1.967(2) 2.016(3) 1.999(2)
Mo BVS [10]	4.70	4.70	4.68	4.59	4.75
Mo-O-Lu / °	156.6(1) 156.4(2) 159.6(2)	156.7(1) 156.4(2) 159.5(2)	156.7(1) 156.5(2) 159.5(2)	156.7(2) 156.5(2) 159.5(2)	157.6(1), 157.0(1), 160.8(1)

DC-Susceptibility

Thermal dependent DC-susceptibility measurements were carried out between 2 and 300 K. Each composition experienced paramagnetic behaviour with no distinct magnetic transition or ZFC/FC divergence. Curie-Weiss fits between 200 and 300 K yield magnetic parameters tabulated in Table 8:7. The Weiss constants suggest that strong antiferromagnetic interactions take place in each material and the effective moments are all lower than the S=1/2 spin only value of 1.73μ_B. Between 5 and 25 K, low temperature Curie-Weiss behaviour is observed. Over this temperature range, the Curie constant decreases significantly from high temperature, corresponding to 28%, 32%, 42% and 49% of the higher temperature range in $Ba_{1.5}Sr_{0.5}LuMoO_6$, $BaSrLuMoO_6$, $Ba_{0.5}Sr_{1.5}LuMoO_6$ and Sr_2LuMoO_6 respectively. Each Weiss constant remains negative but experiences a significant decrease in magnitude lying within error of zero, indicating that no significant antiferromagnetic interactions are taking place within the materials at these low temperatures.

Table 8:7: The compositional dependence of the properties of the $Ba_{2-x}Sr_xLuMoO_6$ solid solution. This includes the results of the high temperature, HT (200 – 300 K) and low temperature, LT (5 -25 K) Curie-Weiss analysis are also shown.

X	**0**	**0.5**	**1**	**1.5**	**2**
C_{CW} (HT) / emu mol^{-1} K^{-1}	0.2441(6)	0.184(1)	0.233(1)	0.1773(6)	0.324(1)
θ_{CW} (HT) / K	-128.5(10)	-153(1)	-123(1)	-77(1)	-69(1)
μ_{eff} (HT) / μ_B	1.397(2)	1.21(7)	1.37(9)	1.19(7)	1.61(9)
C_{CW} (LT) / emu mol^{-1} K^{-1}	0.0452(7)	0.052(2)	0.075(3)	0.074(3)	0.16(1)
θ_{CW} (LT) / K	-2.8(2)	-2.4(7)	-2.1(7)	-1.6(7)	-2(1)
μ_{eff} (LT) / μ_B	0.6(1)	0.6(1)	0.8(2)	0.8(2)	1.1(3)
% mag moments C_{CW} (LT)/ C_{CW} (HT)	18	28	32	42	49

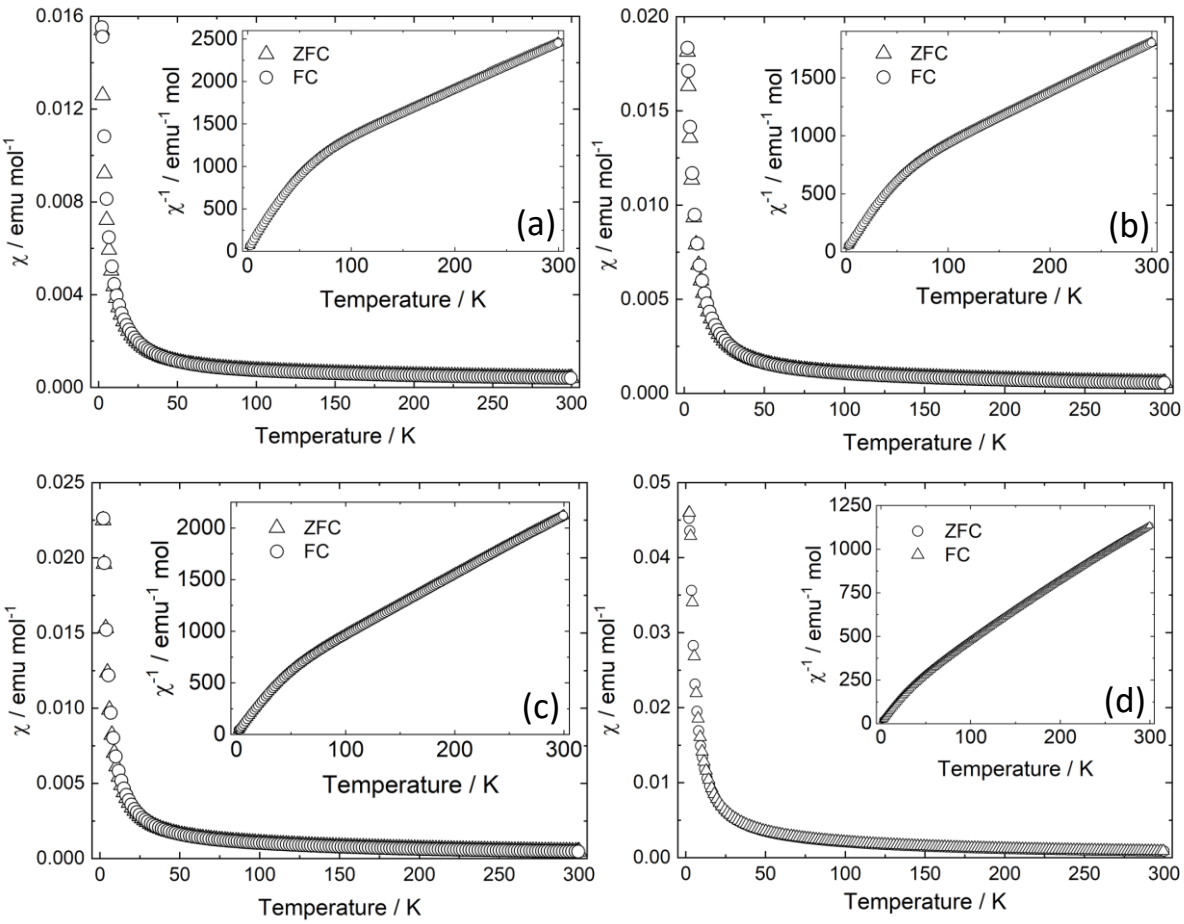

Figure 8.7: Thermal dependent DC-magnetometry measured between 2 and 300 K, of (a) $Ba_{1.5}Sr_{0.5}LuMoO_6$, (b) $BaSrLuMoO_6$, (c) $Ba_{0.5}Sr_{1.5}LuMoO_6$ and (d) Sr_2LuMoO_6. The inset depicts the thermal dependence of the reciprocal susceptibility.

Muon Spin Relaxation

By carrying out both zero field and longitudinal field muon spin relaxation measurements on Sr_2LuMoO_6 the local low temperature magnetic behaviour could be identified. Zero field muon spin relaxation measurements (ZF-μSR) were completed between 1.5(2) and 60(1) K. At 1.5(2) K the initial asymmetry was approximately 0.14, which is low compared to the expected value of 0.25 [102]. This can be observed in Figure 8.8 (a).

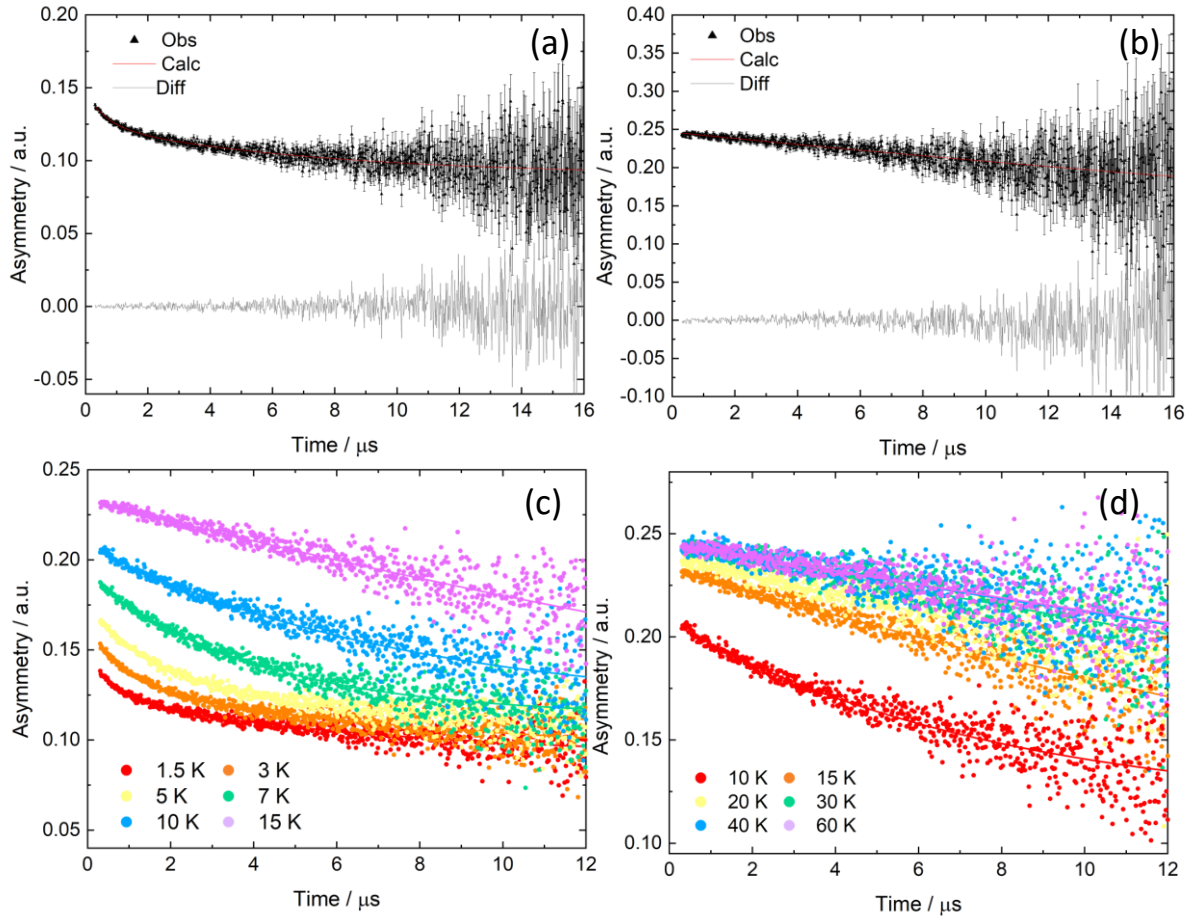

Figure 8.8: Results of ZF-μSR measurements completed on Sr_2LuMoO_6. (a) The experimental and calculated fit completed on the 1.5(2) K data set, which was analysed using $A(t) = (A_1\exp(-\lambda_1 t)) + (A_2\exp(-\lambda_2 t)) + A_3$. (b) The experimental and calculated fit applied to the 30(1) K data set, which was fitted using $A(t) = (A_1\exp(-\lambda_1 t))$. (c) Shows the raw data of the ZF-μSR measurements between 1.5(2) and 15.0(2) K, the solid lines are lines which lead the eye along the points. (d) Depicts the raw data of the ZF-μSR measurements of Sr_2LuMoO_6 between 10.0(2) and 60(1) K, once again the solid lines are aids to ensure that the data can be observed facilely.

The relaxation curve collected at 1.5(2) K requires three separate components to be accurately fitted: a fast relaxation, a comparatively slow relaxation and a constant signal. The relaxing components describe dynamic behaviour taking place within the Sr_2LuMoO_6, whilst the fixed component describes

magnetism originating from a static magnetic field. The fitting function which was used is shown below.

Equation 8.1: Zero field muon spin relaxation fitting function for Sr_2LuMoO_6 which is valid between 1.5(2) K and 3.9(2) K.

$$A(t) = (A_1\exp(-\lambda_1 t)) + (A_2\exp(-\lambda_2 t)) + A_3$$

In this function, A(*t*) corresponds to the asymmetry observed at a specific time, *t*, *A* describes the asymmetries and therefore the fractions of the relaxing and static components. The λ parameter represents the relaxation rate of the decaying proportions. The subscripts denote which component is being described within the function, subscript 1 corresponds to the fast relaxation, 2 to the relatively slower relaxation and 3 to the static fraction of the Mo^{5+} cations.

As previously stated, the initial asymmetry is low at 1.5 K which could indicate that Sr_2LuMoO_6 is present in a magnetically ordered long range state at this temperature, however, the oscillations in asymmetry which would prove this are absent. At 1.5(2) K, the proportion of the fast relaxation is significantly smaller than the asymmetry attributed to the slower relaxation i.e. $A_1<A_2$. Furthermore, both relaxing components are present in significantly smaller quantities that the static proportion, which corresponds to almost half of the response. Therefore, it is deduced that a large proportion of the system is comprised of magnetism from a static field, with two minor regions which are dynamic. The function given above applies between 1.5(2) and 3.9(2) K. Over this temperature range A_1 and A_2 increase in magnitude with temperature whilst A_3 simultaneously decreases. This suggests that a significant proportion of the relaxing components stop moving as the temperature drops and instead contribute to the stationary state. Both the fast and slow relaxation rates decrease significantly as the temperature increases from 1.5(2) K to 3.9(2) K. The results of these fittings can be observed in Figure 8.9.

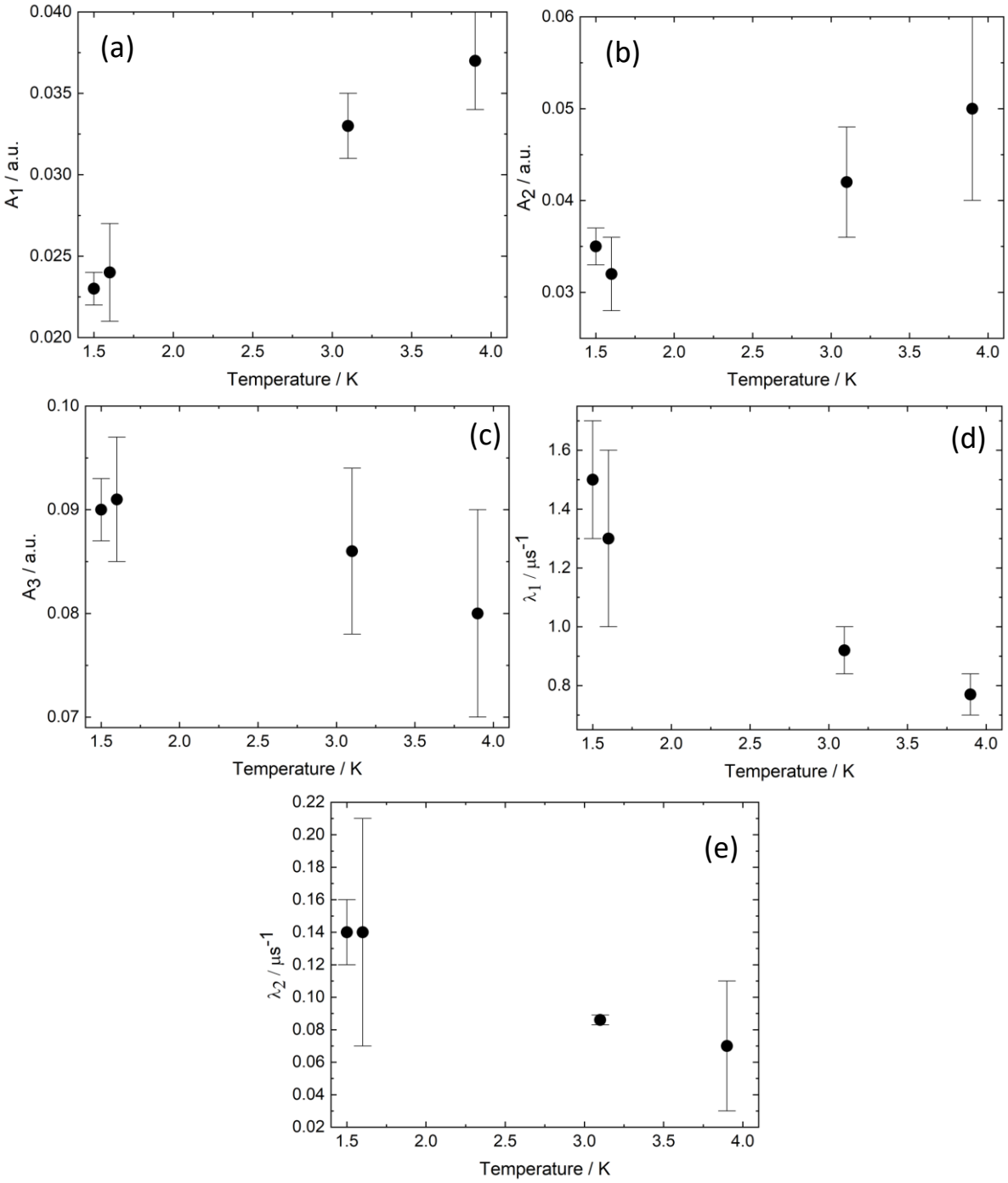

Figure 8.9: Results of ZF-μSR measurements collected on Sr_2LuMoO_6 between 1.5(2) and 3.9(2) K, fitted using $A(t) = (A_1\exp(-\lambda_1 t)) + (A_2\exp(-\lambda_2 t)) + A_3$. The thermal dependence of (a) A_1, (b) A_2, (c) A_3, (d) λ_1 and (e) λ_2. Both A_1 and A_2 increase with temperature whilst A_3 generally decreases. Both relaxation rates decrease as the temperature is raised.

Between 4.5(2) and 9.7(2) K, the fitting function simplifies to Equation 2;

Equation 8.2: Zero field muon spin relaxation fitting function for Sr_2LuMoO_6 which is valid between 4.5(2) K and 9.7(2) K.

$$A(t) = (A_1\exp(-\lambda_1 t)) + A_3$$

This suggests that the slow relaxation can no longer be detected by the implanted muons. This may be a result of the fluctuation rate decreasing out of the muon temporal detection range and so contributing to the static background. Support for this assignment is found in the low value of λ_1 = 0.07(4) μs^{-1}, at 3.9(2) K, within two standard deviations of zero, suggesting that this was already tending to zero at this temperature. As a result of this, it is suspected that these muons add to the background. For 4.5(2) ≥ T / K ≥ 9.7(2), both A_1 and A_3 experience a general increase with temperature, albeit with relatively large uncertainty for A_3 and anomalous decrease at 7.5 K, resulting in an increase to the overall asymmetry which tends towards the expected value of 0.25. The relaxation rate decreases as the temperature escalates.

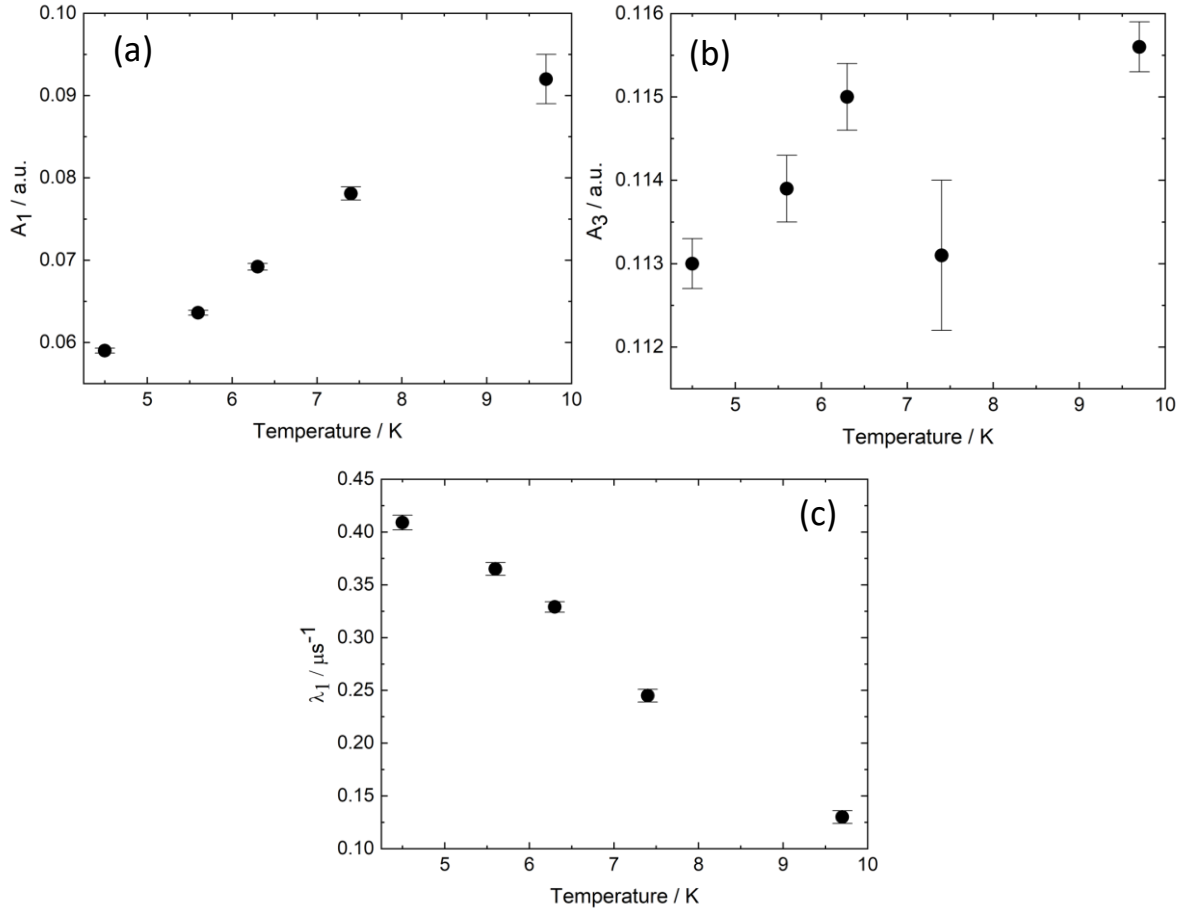

Figure 8.10: Results of ZF-μSR measurements collected on Sr_2LuMoO_6 between 4.5(2) and 9.7(2) K, fitted using A(t) = (A_1exp(-$\lambda_1 t$)) + A_3. The thermal dependence of (a) A_1 the proportion of fast relaxation, (b) A_2 the asymmetry of the slow decay, (c) A_3, the fraction of the static magnetism, (d) λ_1, the fast relaxation rate and (e) λ_2, the slower relaxation rate. Both A_1 and A_3 increase with temperature whilst λ_1 decreases.

Between 14.8(2) and 60(1) K, the fitting function must be modified further to a single exponential decay. The removal of the constant signal suggests that only dynamic magnetism is observed by the muons within Sr_2LuMoO_6. Figure 8.8(c) and (d) show the measured data sets at various temperatures which indicate a distinct change in the shape of the relaxation curve.

Equation 8.3: Zero field muon spin relaxation fitting function for Sr_2LuMoO_6 which is valid between 14.8(2) and 60(1) K.

$$A(t) = (A_1 \exp(-\lambda_1 t))$$

Between 14.8(2) and 60(1) K, the overall asymmetry continues to increase before reaching a value close to 0.25 at 30(1) K. The relaxation rate exhibits a significant decrease as the temperature increases which indicates that the moments are slowing down.

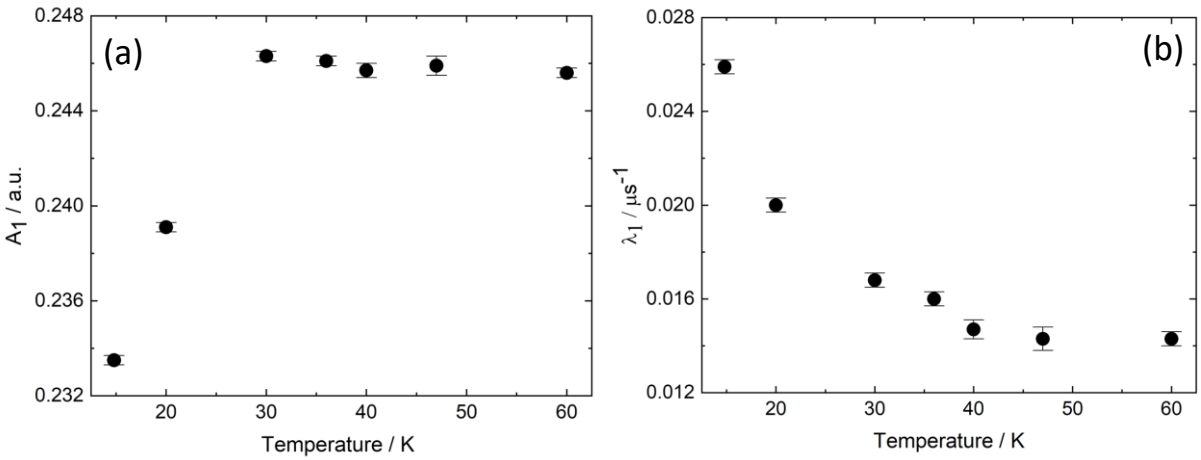

Figure 8.11: Results of ZF-μSR measurements collected on Sr_2LuMoO_6 between 14.8(2) and 60(1) K, fitted using $A(t) = A_1 \exp(-\lambda_1 t)$. The thermal dependence of (a) A_1 and (b) λ_1 the relaxation rate. A_1 increases with temperature whilst λ_1 experience a decrease.

LF-μSR measurements were carried out at 1.5(2) and 60(1) K. 1.5(2) K was chosen due to the lower than expected initial asymmetry at this temperature. 60(1) K was chosen as a suitable comparison as Sr_2LuMoO_6 is suspected to behave paramagnetically at this temperature. The experimentally collected results of the LF-μSR measurements at the temperatures can be observed in Figure 8.12 (a) and (b) respectively.

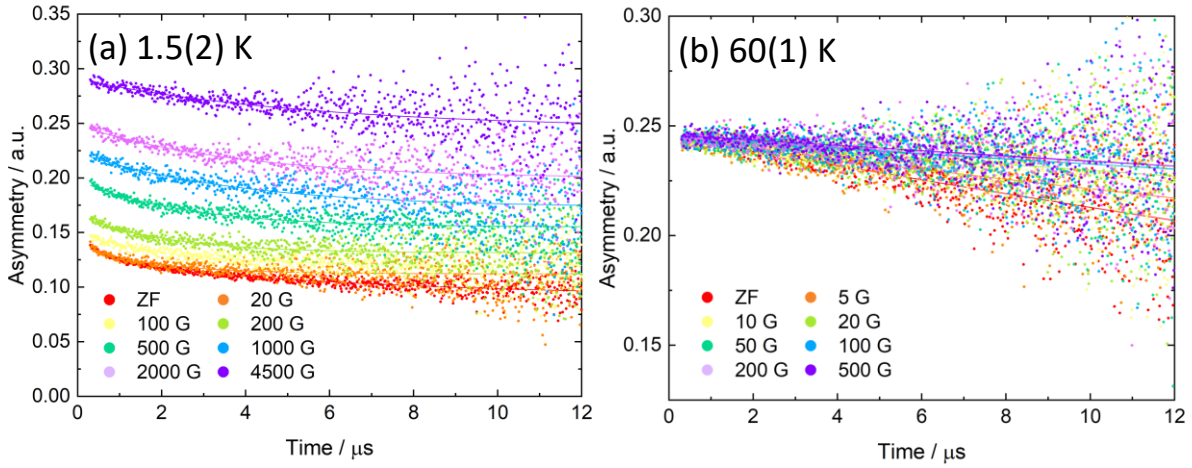

Figure 8.12: The results of LF-μSR measurements carried out on Sr_2LuMoO_6. The experimentally collected data at (a) 1.5(2) K and (b) 60(1) K. The ZF measurements are shown for comparisons sake. At 1.5(2) K, the relaxation curve is not fully decoupled, even when a 4500 G field is applied to the measurement.

At 1.5(2) K, the following function was used to describe the LF-μSR measurements;

Equation 8.4: Longitudinal field muon spin relaxation fitting function for Sr_2LuMoO_6 at 1.5(2) K for 5 G to 4500 G.

$$A(t) = (A_1\exp(-\lambda_1 t)) + A_3$$

This differed from the ZF measurement as the additional exponential decay was removed from the system and was applied to all LF experiments at this temperature. The difference between the two functions suggests that the additional relaxation necessary for ZF analysis was decoupled by the small magnetic field of 5 G. No further decoupling was observed on increasing field strength even when LF = 4500 G was applied. The field dependence of the function parameters was also analysed where both A_1 and A_3 grew significantly with increasing field strength. The relaxation rate initially increases, reaching a maximum at 10 G, after this it then drops of as the applied field strength increases from 10 to 4500 G. The results of these fittings can be observed in Figure 8.13.

At 60(1) K, the function used to characterise the LF data set is identical to that used for the ZF μSR data sets;

Equation 8.5: Longitudinal field muon spin relaxation fitting function for Sr_2LuMoO_6 at 60(1) K for 5 G to 500 G.

$$A(t) = (A_1\exp(-\lambda_1 t))$$

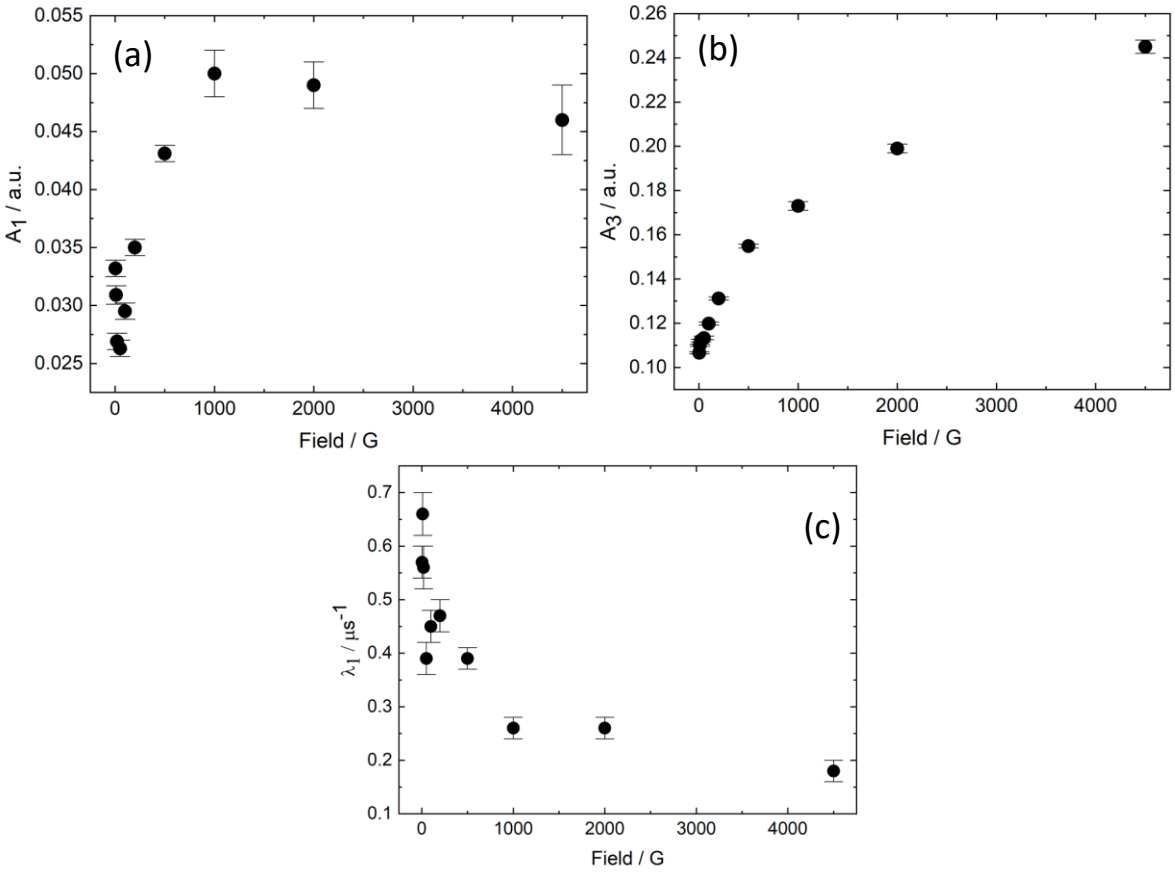

Figure 8.13: Results of LF-μSR measurements collected on Sr_2LuMoO_6 at 1.5(2) K, fitted using A(t) = A_1exp(-$\lambda_1 t$) + A_3. The field dependence of (a) A_1, (b) A_3 and (c) λ_1.

The analysis of these fits indicates that there is a minimal increase in the asymmetry. Throughout, the field range A_1 lies closely to the expected value of 0.25. The relaxation rate decreases towards zero as the magnetic LF strength increases, suggesting the magnetic cations cannot keep up with the field.

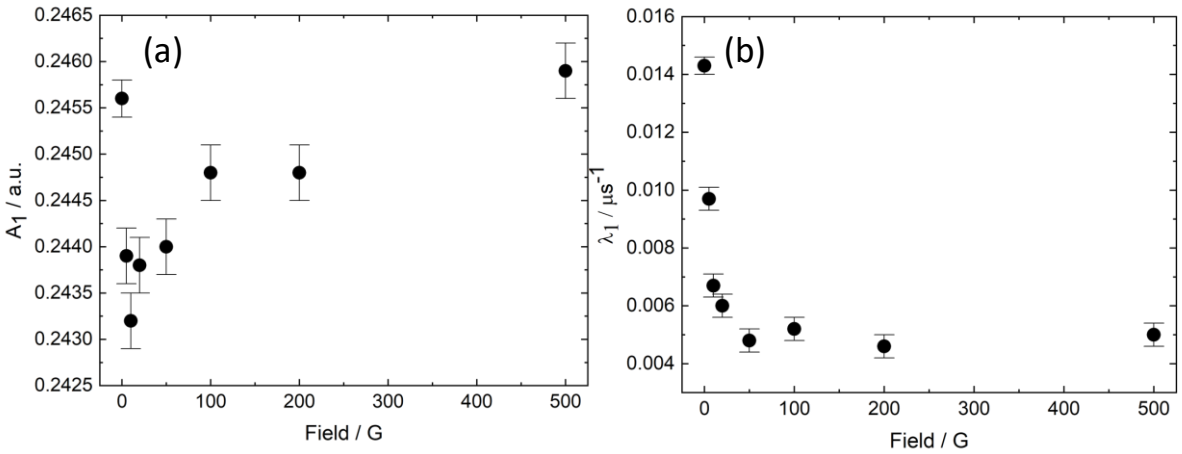

Figure 8.14: Results of LF-μSR measurements collected on Sr_2LuMoO_6 at 60(1) K, fitted using A(t) = A_1exp(-$\lambda_1 t$). The field dependence of (a) A_1 and (b) λ_1.

Discussion

The $Ba_{2-x}Sr_xLuMoO_6$ ($0 \leq x \leq 2$) series are frustrated double perovskites. Across the series, distortions from the ideal *fcc* double perovskite occur as the concentration of Sr^{2+} cations increases. Both Ba_2LuMoO_6 and $Ba_{1.5}Sr_{0.5}LuMoO_6$ crystallise in $Fm\bar{3}m$, this is expected as the Goldschmidt tolerance factors equal 1.00 and 0.99 respectively [48,215,238]. As the Sr^{2+} cation concentration is increased to 50% in $BaSrLuMoO_6$, the tolerance factor falls to 0.97, resulting in a tetragonal distortion brought about by octahedral rotation. Further increasing the concentration of the smaller Sr^{2+} cations results in a monoclinic distortion to $P2_1/n$ in $Ba_{0.5}Sr_{1.5}LuMoO_6$ and Sr_2LuMoO_6. These distortions take place through octahedral tilting, which accommodates the smaller Sr^{2+} cations. As x increases across the solid solution, the volume decreases significantly from 577.28(2) $Å^3$ in Ba_2LuMoO_6 to 271.357(8) $Å^3$ in Sr_2LuMoO_6 (542.714(8) $Å^3$ when altered for the differences in expansion), as anticipated from the smaller ionic radii of Sr^{2+}. Neutron powder diffraction shows no indication of structural or magnetic phase transition in any composition as the temperature is decreased to 2 K, mirroring the behaviour of Ba_2LuMoO_6, Ba_2YMoO_6 and Sr_2YMoO_6 [116,210,214,215]. Ba_2YMoO_6 has been suggested to be a valence bond glass which is the reasoning behind the lack of magnetic transition as the material is found to enter a singlet state [116,211].

Bond valence sums analysis on the structures derived from these neutron data indicate that the *A*-site cations have a valence of approximately 2 and the molybdenum cations lie in a +5 oxidation state, which is anticipated within these materials. Anomalously, the lutetium cations appear to be significantly overbonded in each material when using the parameters outlined by Brese and O'Keeffe [10]. This characteristic is also observed in the double perovskites Ba_2LuRuO_6 and Sr_2LuRuO_6 [169]. There are only a handful of double perovskites which contain Lu^{3+} as a *M*-site cation which could suggest that the tabulated values given for the bond valence sum could need updated. Values which are much closer to the expected +3 oxidation state are obtained when using a revised valence bond parameter $R_i = 1.947$ [264].

The DC-susceptibility of each material indicates that there is no transition to a long range magnetically ordered state and two distinct temperature ranges of Curie-Weiss behaviour. This is another characteristic observed in Ba_2LuMoO_6 and the $Ba_{2-x}Sr_xYMoO_6$ solid solution, which have all been suggested to behave as valence bond glasses [116,214]. The high temperature Curie-Weiss analysis indicates that μ_{eff} is slightly lower in Sr_2LuMoO_6 and significantly suppressed in the intermediate materials from the expected $\mu_{eff} = 1.971\ \mu_B$ for the S = 1/2 system. The suppressed μ_{eff} resembles the related materials, however, in Sr_2LuMoO_6 this is still significantly larger than the μ_{eff} observed in Ba_2LuMoO_6 at the same temperature [215]. In fact, this more closely agrees with the reports by Aharen *et al* on Ba_2YMoO_6 where μ_{eff} was in error of the expected μ_{SO} for S = 1/2 [210]. The differences observed in the effective magnetic moments of the related materials may indicate that the properties observed in DC-susceptibility results are highly dependent on the method of preparation. The large negative Weiss constant obtained at these high temperatures, indicate strong antiferromagnetic interactions within each material. The Weiss constants have a larger magnitude in the cubic materials which suggests that they are significantly more frustrated than those which experience a structural distortion.

The DC-susceptibility of Ba_2LuMoO_6 and Sr_2LuMoO_6 are compared in Figure 8.15, where a clear difference is observed in the responses. The magnetic susceptibility is approximately two times larger in Sr_2LuMoO_6 at base temperature than in Ba_2LuMoO_6. The high temperature Curie Weiss analyses indicate that Ba_2LuMoO_6 exhibits $\mu_{eff} = 1.397(2)\ \mu_B$ which is significantly lower than the $1.61(9)\ \mu_B$ observed in Sr_2LuMoO_6. Ba_2LuMoO_6 also experiences a very large negative Weiss constant of -128.5(10) K, which is almost double that of Sr_2LuMoO_6. In the cubic system the material is more likely to experience antiferromagnetic interactions as the superexchange pathways are at the optimal angle, 180°, superexchange. In the monoclinically distorted structure the pathways deviate from this and therefore the drive behind antiferromagnetic coupling is not as strong. These Weiss constants suggest that Ba_2LuMoO_6 is significantly more frustrated than the Sr_2LuMoO_6 system, which is expected due to the structural distortion of Sr_2LuMoO_6.

The low temperature Curie-Weiss analysis shows an increase in C_{CW} and μ_{eff} as the value of x increases and θ_{CW} all lie close to zero. The effective moment is significantly reduced at low temperature. Only 18% of the magnetic moments in Ba_2LuMoO_6 are available over this temperature range compared to high temperature, whilst 49% are accessible Sr_2LuMoO_6. This increase is potentially caused by the structural distortion where the distances between the Mo^{5+} cations may prevent coupling into singlets. As the number of singlets rises the effective magnetic moment drops due to their diamagnetic nature. When singlets form, the residual Mo^{5+} cations are isolated from each other which prevents them from interacting, which causes θ_{CW} to tend towards zero. These preliminary results suggest that each composition could experience valence bond glass like properties. If the first theorem behind valence bond glass behaviour is utilised, then the monoclinic distortion may allow for a larger number of orphan or dangling Mo^{5+} cations to remain within the system. As the monoclinic distortion takes place the Mo^{5+} cations may be close to each other and form singlets whilst those which are further away from each other cannot couple and therefore remain residual behaving paramagnetically and corresponding to the effective magnetic moment [213]. Over these temperature ranges the Weiss constants of both materials are within error of 0 and therefore strong antiferromagnetic interactions no longer take place. The singlet state disrupts the magnetic behaviour of the system and the residual cations can no longer interact.

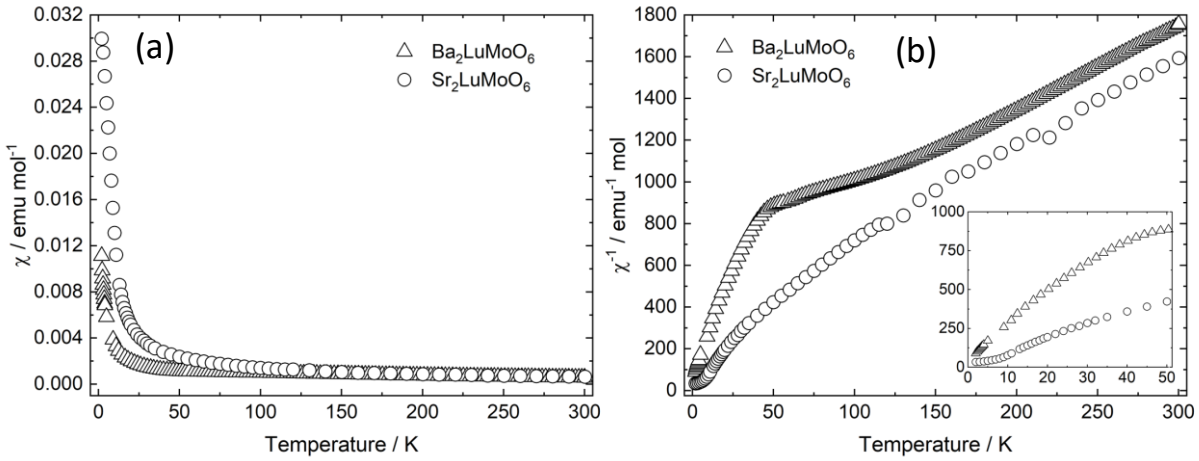

Figure 8.15: Comparison of DC-magnetometry collected on Ba_2LuMoO_6 and Sr_2LuMoO_6. (a) the thermal dependence of the DC-susceptibility. (b) the thermal dependence of the reciprocal susceptibility.

Muon spin relaxation measurements suggest that Sr_2LuMoO_6 may enter a long range magnetically ordered state. This is evidenced by the low initial asymmetry observed at 1.5(2) K, which is significantly smaller than that which is anticipated of approximately 0.25. No oscillations are observed in the data set which would help to prove this magnetic order, however, there is potential that these do take place and rather are not resolved. The fitting function used to describe the ZF-μSR data set at 1.5(2) K, is equivalent to that of Ba_2MnWO_6 which is known to experience antiferromagnetic order [236]. Therefore, there is potential that Sr_2LuMoO_6 experiences long range magnetic order. This claim is further bolstered by the behaviour observed in LF measurements carried out at this temperature, where the relaxation curve is not fully decoupled by a large LF of 4500 G. This suggests that strong internal fields may be present in the material. The change in the fitting function at 3.7(2) K may be a result of the material no longer experiencing 3D magnetic order. As the temperature rises, especially above 30(1) K, Sr_2LuMoO_6 behaves like a conventional paramagnet.

These μSR measurements can also be used to compare the intrinsically different behaviour of Ba_2LuMoO_6 and Sr_2LuMoO_6. The low initial asymmetry of Sr_2LuMoO_6 is not observed in Ba_2LuMoO_6, which persistently demonstrates an initial asymmetry close to 0.25 down to 50 mK and presents dynamic behaviour at this temperature. The fitting functions used for each material are not equivalent as Sr_2LuMoO_6 requires an additional exponential decay. This indicates that although the bulk magnetic behaviour of each system appears similar, the local magnetic behaviour is clearly different.

The behaviour outlined for the $Ba_{2-x}Sr_xLuMoO_6$ solid solution, closely resembles that reported in the $Ba_{2-x}Sr_xYMoO_6$ series. One slight difference is that Sr_2YMoO_6 exhibit weak ferromagnetic behaviour and enters into a ferromagnetically long range ordered state at approximately 8 K, which is not definitively observed in Sr_2LuMoO_6 [214].

The purpose of this chapter was to investigate whether the $Ba_{2-x}Sr_xLuMoO_6$ solid solution presents behaviours which are characteristic of the valence bond glass phase. The valence bond glass state has been rationalised using several theories which involve the structure transferring into a spin singlet

state. The first way of rationalising the valence bond glass behaviour is by considering that at high temperatures the cations are not present in this state and rather they behave as paramagnets with the μ_{eff} close to the spin only magnetic moment of the Mo^{5+} cations. The slight reduction in effective magnetic moment is explained to be caused by quantum fluctuations which arise due to the entanglement of the Mo^{5+} $4d^1$ electrons [116,213]. The other theories indicate that this behaviour occurs as a result of strong spin orbit coupling of the Mo^{5+} cations which causes the t_{2g} orbital to split into j = 3/2 and j = 1/2 states [256]. The large effective magnetic moment at high temperature has been theorised to result due to mixing of the j = 3/2 and j = 1/2 states and could occur in conjunction with a dynamic Jahn-Teller distortion [257]. So far, the correct theory has not been experimentally verified. These theories all suggest that a significant reduction in the effective magnetic moment should take place as the temperature decreases. This behaviour is observed in the DC-susceptibility data set of each of the materials within the $Ba_{2-x}Sr_xLuMoO_6$ series, however, this is not enough information to definitively state whether they are valence bond glasses.

Conclusion

The $Ba_{2-x}Sr_xLuMoO_6$ solid solution was synthesised and investigated using neutron powder diffraction and thermal dependent DC-magnetometry. The structures distort from *fcc* as the concentration of Sr^{2+} increases. $Ba_{1.5}Sr_{0.5}LuMoO_6$ adopts the $Fm\bar{3}m$ space group whilst $BaSrLuMoO_6$, $Ba_{0.5}Sr_{1.5}LuMoO_6$ and Sr_2LuMoO_6 are distorted crystallising in the lower symmetry space groups *I4/m* and $P2_1/n$ respectively. Decreasing the temperature does not incite any structural or magnetic phase transitions within any of the materials. The compositions experience two separate temperature ranges of Curie-Weiss behaviour. At high temperature each material experiences strong antiferromagnetic interactions and the effective magnetic moments appear to be quenched from the S = 1/2 spin state of the $4d^1$ Mo^{5+} cation. At low temperature, the Curie constants are significantly lower than those calculated at high temperature and the antiferromagnetic interactions lie around zero. Muon spin relaxation measurements carried out on Sr_2LuMoO_6 indicate some dynamic behaviour down to low temperature

within the material but also suggest that it may experience some long-range order. This is not observed in any other measurement technique which was completed on Sr_2LuMoO_6. Preliminary measurements suggest that all the materials within the solid solution appear to behave like valence bond glasses, however, further supporting evidence is necessary to ensure that this is the case.

Future Work

The valence bond glass state is difficult to experimentally confirm due to its closeness in nature to the spin glass behaviour and the absence of a single unique experimental signature for this state. One way to identify the spin singlet nature is to carry out inelastic neutron scattering, where a spin singlet to triplet transition can be observed. Another property which appears to indicate the presence of a valence bond glass is the slow release of entropy over a fairly wide temperature range. This can be measured using magnetic heat capacity measurements. This would require the magnetic samples to be measured and the heat capacity of the diamagnetic analogues $Ba_{2-x}Sr_xLuNbO_6$ to be measured. The magnetic contribution could then be observed by removing diamagnetic behaviour from the heat capacity data collected on the magnetic samples.

The potential long-range magnetic order which is suggested by the muon spin relaxation measurement of Sr_2LuMoO_6 should also be investigated. The fact that this is not observed in neutron powder diffraction is not surprising as this could be due to a very small effective magnetic moment which would not be observed within the data sets. If this is like Sr_2YMoO_6 then this may be the result of an incredibly weak ferromagnetic order arising at low temperatures, although our DC measurements show that the weak uncompensated magnetisation observed in Sr_2YMoO_6 is absent in Sr_2LuMoO_6. This may be evidenced by DC-susceptibility carried out at lower temperature. The potential for hysteresis could also be investigated by carrying out M/H measurements. Inelastic neutron scattering may also be useful for this as this could show long range antiferromagnetic order by displaying spin waves within the data sets. These measurements are necessary to gain further information about Sr_2LuMoO_6, without this nothing more definitive can be said about Sr_2LuMoO_6.

9. Conclusion

The research within this thesis has provided insight into frustrated magnetism arising from the face centered cubic lattice of the double perovskite. This has been completed by exploiting the versatility of the double perovskite structure and incorporating magnetic cations with varying spin states, S = 5/2, 3/2 and 1/2, and comparing the differences in the structural and magnetic properties exhibited by each of these materials.

The investigation into the S = 5/2 systems, Ba_2MnWO_6 and Sr_2MnWO_6 showed that these materials were more complex than initially reported. Ba_2MnWO_6 has been clearly shown to exhibit short-range magnetic excitations above the Néel temperature. Evidence of short-range magnetism in Sr_2MnWO_6 is tenuous although not entirely unsubstantiated. Shifting to the lower spin state of S = 3/2, in $Ba_2Co_{1-x}Zn_xMoO_6$ provided new challenges and considerations. High spin Co^{2+} experiences spin orbit coupling and a thermal dependent population of the d-orbitals. Examination of the percolation threshold showed that this was significantly off from the expected value of 0.195 as the systems showed no long-range antiferromagnetic order below x = 0.5. Moving to the S = 1/2 state in $Ba_{2-x}Sr_xLuMoO_6$, allowed significantly more complex behaviour to be observed. Each of the materials within this solid solution are presumed to be valence bond glasses, however, it can be challenging to state that these properties are observed due to valence bond glass nature exclusively. As this novel spin state has similar markers to other novel spin states and lacks a unique experimentally observable signature.

To summarise, identifying trends within the magnetically frustrated double perovskites is not a facile task. This is due to the sheer quantity of competing variables with each material; the cations and anions incorporated, the adopted structure, structural or magnetic phase transitions in conjunction with quantum fluctuations in the lower spin states are all factors in the configuration of the ground state(s). The notion that decreasing the spin state increases the complexity of the magnetic behaviour is highly subjective and should instead be based on the exhibited properties of the magnetic cations, the magnetic transition temperatures, the frustration index or the exchange coupling constants. The

magnetic cations which experience a lower spin state tend to be more susceptible to spin orbit coupling effects due to orbital angular momentum which can result in enhanced or quenched magnetic moments. Our findings also indicate that the spin state of the magnetic cation does not have a clear trend on the frustration index of the material as Ba_2CoMoO_6 has a lower frustration index that Ba_2MnWO_6 which is again lower than that which would be expected for Ba_2LuMoO_6. This is related to the transition temperatures of these materials where Ba_2MnWO_6 orders at a significantly lower temperature than Ba_2CoMoO_6. In conclusion, each of these double perovskites must be considered separately before being related to others. Furthermore, supplementary research into their magnetic behaviours, i.e. identifying their exchange constants, must be completed so that the trends which these systems experience can be determined.

10. Future Work

This research has provided a platform to study the intricacies of geometrical frustration and its effects within face centered cubic double perovskites. Simultaneously, this has highlighted limitations within the field and potential improvements which could benefit researchers studying these materials. Within this section, these potential developments will be covered alongside any interesting experiments and gaps in the literature.

The underlying mechanisms of the solid-state synthesis technique are still not well understood by researchers within solid-state chemistry, this lies in the differences between this and molecular chemistry. Retrosynthetic techniques are not applied to solid-state chemistry and more often than not trial and error is necessary to form new materials [265]. This is not desirable or economical and therefore, it would be preferable to understand the process using reaction rate as a basis. This is complicated to do for solid-state reactions as the scale of the materials means that information is lost on a molecular level and that the solid diffusion properties must be understood to gain information about the kinetics. Progress is further hindered by a lack of complete understanding of the nucleation and crystallisation properties. This combined with a diverse range of variables brought about during material processing all affect the rate and outcome of the reaction. These variables include; the purity of the reagents used, the time spent grinding and how thoroughly this has been achieved, the load applied to create a pellet, the reaction temperature (which may not be consistent from furnace to furnace) and the type and flowrate of the atmosphere utilised. This is by no means an extensive list and contains numerous others and makes it very difficult to predict the reaction time and temperature. In order to evaluate reaction lengths and outcomes, in-situ measurements should be utilised more frequently to analyse intermediate states. This would be particularly useful in areas of solid-state science where the materials would be manufactured on a large scale such as in lithium ion batteries. The proposal of retrosynthetic solid state synthesis is by no means a novel idea with articles published on the necessity of this within the field of solid state chemistry approximately 50 years

ago [266]. These articles have catalysed people to carry out in-situ diffraction studies using a range of radiation sources to extract kinetic information from the intensity of the Bragg peaks [267]. Furthermore, other in-situ analytical approaches have been used to identify any intermediate states, these include; infrared spectroscopy, and mass spectroscopy [265]. Since this original study, monumental technological advances have taken place in both instrumentation and analysis techniques. This advancement means that the field is better positioned to ascertain these reaction pathways and hopefully leave behind the trial and error approach which is predominately used.

The versatility of the double perovskite structure means that new materials are continuously being synthesised, yielding an abundance of new compounds and properties. The sheer quantity of these means that the community could wholly benefit from a database comprised of these materials and their reported structural, physical, chemical and electronic properties. The database would provide a set place where it would be easy to find literature and make comparisons. It could also make it easier to remove "junk" science papers which would benefit early researchers who may not be able to distinguish between this and "good" science. Other databases such as the Inorganic Crystal Structure Database (ICSD) are useful tools within solid-state chemistry, providing models for Rietveld refinement. The introduction of a perovskite only database could provide a platform for more geometrically frustrated materials being formed. The synthesis of these new materials could be achieved through using software such as SPuDS and PIEFACE to evaluate the structure and determine the properties [268,269]. The formation of new geometrically frustrated double perovskites and a hub where they are all based would result in significantly greater understanding of the subject and may also allow gaps in the literature to be identified quickly. This may also promote further collaboration between research groups who synthesise similar materials and could result in more comprehensive studies being completed. The creation of this database could have several difficulties; the breadth of the literature means this would take significant time to compile and verification of properties is also a lengthy process. However, the outlined benefits strongly outweigh any negatives, and the review of literature could be tasked to Masters students or early PhD students.

More specifically within the field of geometrically frustrated double perovskites, the previously reported S = 5/2 materials deserve further analysis. Many of these systems were formed in the 1960s and 1970s and have had only preliminary measurements of neutron powder diffraction and magnetometry carried out on them. Ba_2MnWO_6 is a prime example for reinvestigation of these systems, as further study has shown that it is more complex than it initially seemed with the discovery of a short-range correlated magnetic state above the transition temperature [236]. It would be interesting to gather information about the ordered antiferromagnetic states and exchange coupling constants of these S = 5/2 double perovskites and be able to compare them to examples from the literature. For my own personal interest I would like to see the properties of Ba_2TcMoO_6 or Ba_2TcWO_6, however, this is highly unlikely to be synthesised due to the radioactivity and subsequent instability of this cation in conjunction with the fact that it is a 4d cation and therefore would rather lie in a higher oxidation state. Interest in technetium stems from its positioning in the periodic table as it lies in the same triad as manganese and rhenium and between molybdenum and ruthenium. Each of the elements surrounding this have resulted in interesting properties throughout the double perovskite and therefore technetium may give rise to further interesting behaviour.

The cobalt ion Co^{2+} is more complex than the Mn^{2+} cation due to the strong spin orbit coupling effects which it exhibits, and therefore further investigation should be carried out on these systems. This could be achieved through preparation of other perovskites containing the cobalt ion in various oxidation states. Co^{3+} ($3d^6$) has been reported to have an intermediate spin state and therefore the formation of a double perovskite which ensures that cobalt remains in the +3 oxidation state could help to prove or disprove this claim. An ideal candidate for this could have been Ba_2CoNbO_6, as this contains Co^{3+} as the only magnetic cation, however, this has been previously synthesised and is reported to be positionally disordered. The effective magnetic moment is proposed to be a result of a mixture between the high and intermediate spin states [270]. Magnetic percolation of this using zinc to create a solid solution could be a reasonable comparison point for $Ba_2Co_{1-x}Zn_xMoO_6$. Personally, evidence for the intermediate spin state is not wholly convincing and it could result from a mixture of

high and low spin states, a claim which could be strengthened by the temperature dependent behaviour of Co^{2+}. Further work could also identify why the percolation threshold does not agree with what is anticipated from percolation theory.

The S = 1/2 spin state continues to produce exotic spin phases. The highly interactive nature of the unpaired electrons appears to be the way to understand the quantum state to a much greater degree. S = 1/2 materials, using Cu^{2+}, Ru^{6+}, Mo^{5+} or Os^{7+} as the magnetic cation have all proven to provide exotic spin states. This may involve generating new phases with external high pressure or creating analogues of reduced dimensionality such as Ruddlesden-Popper phases. The quantum fluctuations that cause these novel behaviours require further investigation as numerous theoretical accounts require experimental validation. The theoretical novel spin states which have been described recently are often hard to measure experimentally and due to experimentally observable behaviour overlapping with closely related magnetic phenomena. Further work is necessary into understanding how these can be shown conclusively experimentally, alternatively, further technological advancements are necessary to conclusively establish the behaviour by accessing new experimental conditions. A more readily accessible test of the valence bond glass state itself could be achieved by magnetic dilution in a series such as $Ba_2LuMo_{1-x}M'O_6$ where *M'* = Ta, Sb or Nb. This dilution would disrupt the valence bond glass state but single ion effects of the Mo^{5+} cations would be largely unaffected and so these two phenomena could be examined independently. The analogous series $Ba_2YMo_{1-x}M'O_6$ could also be tested and the structural and magnetic properties could be compared.

References

[1] B. D. Fahlman, in *Mater. Chem.*, 2nd ed. (Springer Netherlands, 2011), pp. 13–156.

[2] A. R. West, in *Basic Solid State Chem.* (John Wiley & Sons, Ltd, 1984), pp. 1–64.

[3] C. N. R. Rao and J. Gopalakrishnan, in *New Dir. Solid State Chem.* (Cambridge University Press, Cambridge, 1997), pp. 1–72.

[4] A. Kelly and K. M. Knowles, in *Crystallogr. Cryst. Defects* (Wiley, 2012), pp. 3–41.

[5] G. Burns and A. M. Glazer, in *Sp. Groups Solid State Sci.*, edited by G. BURNS and A. M. B. T.-S. G. for S. S. S. (Second E. GLAZER (Academic Press, San Diego, 1990), pp. 34–54.

[6] A. R. West, in *Basic Solid State Chem.* (John Wiley & Sons, Ltd, 1984), pp. 206–280.

[7] P. Cox, in *Electron. Struct. Chem. Solids* (Oxford University Press, 1987), pp. 195–242.

[8] D. P. Almond, G. K. Duncan, and A. R. West, Solid State Ionics **8**, 159 (1983).

[9] P. Cox, in *Electron. Struct. Chem. Solids* (Oxford University Press, 1987), pp. 1–24.

[10] N. E. Brese and M. O'Keeffe, Acta. Cryst. **B47**, 192 (1991).

[11] J. Conradie, Inorganica Chim. Acta **486**, 193 (2019).

[12] M. Getzlaff, in *Fundam. Magn.* (Springer, 2007), pp. 1–6.

[13] A. H. Morrish, in *Phys. Princ. Magn.* (IEEE Press, 1965), pp. 31–75.

[14] C.-G. Stefanita, in *Magn. Basics Appl.* (Springer, 2012), pp. 1–37.

[15] M. D. Simon and A. K. Geim, J. Appl. Phys. **87**, 6200 (2000).

[16] A. H. Morrish, in *Phys. Princ. Magn.* (IEEE Press, 1965).

[17] B. D. Cullity and C. D. Graham, in *Introd. to Magn. Mater.* (Wiley-IEEE Press, 2009), pp. 87–114.

[18] M. Blume and R. E. Watson, Proc. R. Soc. London A **270**, 127 (1969).

[19] M. Blume and R. E. Watson, Proc. R. Soc. London A **271**, 565 (1963).

[20] A. H. Morrish, in *Phys. Princ. Magn.* (IEEE Press, 1965), pp. 432–486.

[21] L. M. Corliss, J. M. Hastings, and R. J. Weiss, Phys. Rev. Lett. **3**, 211 (1959).

[22] P. W. Anderson, Phys. Rev. **79**, 350 (1950).

[23] P. W. Anderson, Phys. Rev. **115**, 2 (1959).

[24] J. B. Goodenough, Phys. Rev. **117**, 1442 (1960).

[25] J. Kanamori, J. Phys. Chem. Solids **10**, 87 (1959).

[26] P. W. Anderson, Solid State Phys. **14**, 99 (1963).

[27] I. Dzyaloshinsky, J. Phys. Chem. Solids **4**, 241 (1958).

[28] T. Moriya, Phys. Rev. **120**, 91 (1960).

[29] J. W. Essam, Rep. Prog. Phys. **43**, 833 (1980).

[30] R. A. Cowley, Philos. Trans. R. Soc. London **B 290**, 583 (1980).

[31] R. J. Birgeneau, R. A. Cowley, G. Shirane, and H. Yoshizawa, J. Stat. Phys. **34**, 817 (1984).

[32] J. L. Mattei, O. Minot, and M. Le Floc'h, J. Magn. Magn. Mater. **140**–**144**, 2189 (1995).

[33] T. R. Gawron and M. Cieplak, Acta Phys. Pol. A **80**, 461 (1991).

[34] S. Vasala and M. Karppinen, Prog. Solid State Chem. 1 (2015).

[35] N. W. Thomas, Acta Crystallogr. **B52**, 16 (1996).

[36] M. T. Anderson, K. B. Greenwood, G. A. Taylor, and K. R. Poeppelmeier, Prog. Solid State Chem. **22**, 197 (1993).

[37] G. King and P. M. Woodward, J. Mater. Chem. **20**, 5785 (2010).

[38] M. T. Anderson and K. R. Poeppelmeier, Chem. Mater. **3**, 476 (1991).

[39] M. C. Knapp and P. M. Woodward, J. Solid State Chem. **179**, 1076 (2006).

[40] M. W. Lufaso and P. M. Woodward, Acta Crystallogr. **B60**, 10 (2004).

[41] P. Garcia-Fernandez, J. A. Aramburu, M. T. Barriuso, and M. Moreno, J. Phys. Chem. Lett. **1**, 647 (2010).

[42] K. M. Ok, E. O. Chi, and P. S. Halasyamani, Chem. Soc. Rev. **35**, 710 (2006).

[43] P. M. Woodward, Acta Crystallogr. **B53**, 32 (1997).

[44] A. M. Glazer, Acta Crystallogr. **A31**, 756 (1975).

[45] A. M. Glazer, Acta Crystallogr. **B28**, 3384 (1972).

[46] C. J. Howard and H. T. Stokes, Acta Crystallogr. **B58**, 565 (2002).

[47] P. M. Woodward, Acta Crystallogr. **B53**, 44 (1997).

[48] H. D. Megaw, Proc. Phys. Soc. **58**, 133 (1946).

[49] E. Reynolds, G. J. Thorogood, M. Avdeev, H. E. A. Brand, Q. Gu, and B. J. Kennedy, Dalt. Trans. **44**, 16036 (2015).

[50] F. C. Coomer, J. Campbell, N. Giordano, O. M. Collins, and E. J. Cussen, J. Solid State Chem. **221**, 411 (2015).

[51] J. E. Greedan, J. Mater. Chem. **11**, 37 (2001).

[52] A. P. Ramirez, Annu. Rev. Mater. Sci. **24**, 453 (1994).

[53] J. A. Mydosh, J. Magn. Magn. Mater. **157**–**158**, 606 (1996).

[54] J. A. Mydosh, Reports Prog. Phys. **78**, 52501 (2015).

[55] Y. J. Uemura, T. Yamazaki, D. R. Harshman, M. Senba, and E. J. Ansaldo, Phys. Rev. B **31**, 546 (1985).

[56] T. Fennell, P. P. Deen, A. R. Wildes, K. Schmalzl, D. Prabhakaran, A. T. Boothroyd, R. J. Aldus, D. F. McMorrow, and S. T. Bramwell, Science (80-.). **326**, 415 (2009).

[57] C. R. Wiebe, J. S. Gardner, S.-J. Kim, G. M. Luke, A. S. Wills, B. D. Gaulin, J. E. Greedan, I. Swainson, Y. Qiu, and C. Y. Jones, Phys. Rev. Lett. **93**, 076403 (2004).

[58] S. T. Bramwell, S. R. Giblin, S. Calder, R. Aldus, D. Prabhakaran, and T. Fennell, Nature **461**, 956 (2009).

[59] P. W. Anderson, Mater. Res. Bull. **8**, 153 (1973).

[60] L. Savary and L. Balents, Reports Prog. Phys. **80**, 16502 (2016).

[61] L. Balents, Nature **464**, 199 (2010).

[62] N. N. Sun and H. Y. Wang, J. Magn. Magn. Mater. **454**, 176 (2018).

[63] R. Merkle and J. Maier, Angew. Chemie Int. Ed. **47**, 3874 (2008).

[64] A. Stein, S. W. Keller, and T. E. Mallouk, Science (80-.). **259**, 1558 (1993).

[65] V. K. Pecharsky and P. Y. Zavalij, in *Fundam. Powder Diffr. Struct. Charact. Mater.* (Springer, 2009), pp. 107–131.

[66] R. A. Dalla Betta, M. Boudart, K. Foger, D. G. Löffler, and J. Sánchez-Arrieta, Rev. Sci. Instrum. **55**, 1910 (1984).

[67] S. Kneip, C. McGuffey, J. L. Martins, S. F. Martins, C. Bellei, V. Chvykov, F. Dollar, R. Fonseca, C. Huntington, G. Kalintchenko, A. Maksimchuk, S. P. D. Mangles, T. Matsuoka, S. R. Nagel, C. A. J. Palmer, J. Schreiber, K. T. Phuoc, A. G. R. Thomas, V. Yanovsky, L. O. Silva, K. Krushelnick, and Z. Najmudin, Nat. Phys. **6**, 980 (2010).

[68] K. J. S. Sawhney, I. P. Dolbnya, M. K. Tiwari, L. Alianelli, S. M. Scott, G. M. Preece, U. K. Pedersen, and R. D. Walton, AIP Conf. Proc. **1234**, 387 (2010).

[69] G. C. Smith, Synchrotron Radiat. News **4**, 24 (1991).

[70] M. Nikl, Meas. Sci. Technol. **17**, (2006).

[71] D. Renker and E. Lorenz, J. Instrum. **4**, P04004 (2009).

[72] R. Jenkins and S. R. L., in *Introd. to X-Ray Powder Diffractometry* (John Wiley & Sons, Ltd, 1996), pp. 121–150.

[73] A. Gabriel, Rev. Sci. Instrum. **48**, 1303 (1977).

[74] G. Da Costa, F. Vurpillot, A. Bostel, M. Bouet, and B. Deconihout, Rev. Sci. Instrum. **76**, 13304 (2004).

[75] G. Schriever, R. Lebert, A. Naweed, S. Mager, W. Neff, S. Kraft, F. Scholze, and G. Ulm, Rev. Sci. Instrum. **68**, 3301 (1997).

[76] S. G. Gales and C. D. Bentley, Rev. Sci. Instrum. **75**, 4001 (2004).

[77] R. Jenkins and R. L. Snyder, in *Introd. to X-Ray Powder Diffractometry* (John Wiley & Sons, Ltd, 1996), pp. 47–95.

[78] A. H. Compton, Phys. Rev. **21**, 483 (1923).

[79] V. K. Pecharsky and P. Y. Zavalij, in *Fundam. Powder Diffr. Struct. Charact. Mater.* (Springer, 2009), p. 133.

[80] D. T. Cromer and J. B. Mann, Acta Crystallogr. Sect. A **24**, 321 (1968).

[81] K. D. M. Harris, in *Powder Diffr. Crystallogr. Mol. Solids* (Springer, 2011), pp. 134–136.

[82] R. A. Young and D. B. Wiles, J. Appl. Crystallogr. **15**, 430 (1982).

[83] H. M. Rietveld, J. Appl. Crystallogr. **2**, 65 (1969).

[84] B. E. Warren, J. Appl. Phys. **12**, 375 (1941).

[85] R. Yogamalar, R. Srinivasan, A. Vinu, K. Ariga, and A. C. Bose, Solid State Commun. **149**, 1919 (2009).

[86] L. W. Finger, D. E. Cox, and A. P. Jephcoat, J. Appl. Crystallogr. **27**, 892 (1994).

[87] M. Ahtee, M. Nurmela, P. Suortti, and M. Järvinen, J. Appl. Crystallogr. **22**, 261 (1989).

[88] W. A. Dollase, J. Appl. Crystallogr. **19**, 267 (1986).

[89] V. K. Pecharsky and P. Y. Zavalij, in *Fundam. Powder Diffr. Struct. Charact. Mater.* (Springer, 2009), pp. 151–203.

[90] W. I. F. David and R. M. Ibberson, in *Struct. Determ. from Powder Diffr. Data* (Oxford University Press, 2010).

[91] E. H. Kisi and C. J. Howard, in *Appl. Neutron Powder Diffr.* (Oxford University Press, 2008).

[92] A. K. Cheetham, W. I. F. David, M. M. Eddy, R. J. B. Jakeman, M. W. Johnson, and C. C. Torardi, Nature **320**, 46 (1986).

[93] J. M. A. Reichelt and A. L. Rodgers, Nucl. Instruments Methods **45**, 245 (1966).

[94] L. B. McCusker, R. B. Von Dreele, D. E. Cox, D. Louër, and P. Scardi, J. Appl. Crystallogr. **32**, 36 (1999).

[95] R. A. Young, H. M. Rietveld, E. Prince, T. M. Sabine, R. J. Hill, J. W. Richardson Jr, R. L. Snyder, R. Delhez, T. H. de Keijser, J. I. Langford, D. Louer, E. J. Mittemeijer, E. J. Sonneveld, P. Suortti, C. Barlocher, W. I. F. David, J. D. Jorgensen, R. B. Von Dreele, F. Izumi, H. Toraya, and A. K. Cheetham, *The Rietveld Method* (Oxford University Press, 1995).

[96] W. I. F. David, J. Reasearch Natl. Inst. Stand. Technol. **109**, 107 (2004).

[97] B. H. Toby, Powder Diffr. **21**, 67 (2006).

[98] Q. Design, Measurement 56 (1999).

[99] M. Buchner, K. Höfler, B. Henne, V. Ney, and A. Ney, J. Appl. Phys. **124**, (2018).

[100] W. G. Jenks, S. S. H. Sadeghi, and J. P. Wikswo, J. Phys. D. Appl. Phys. **30**, 293 (1997).

[101] C. D. Tesche and J. Clarke, J. Low Temp. Phys. **29**, 301 (1977).

[102] S. J. Blundell, Contemp. Phys. **40**, 175 (1999).

[103] T. A. Claxton, Chem. Soc. Rev. **24**, 437 (1995).

[104] P. Dalmas De Réotier and A. Yaouanc, J. Phys. Condens. Matter **9**, 9113 (1997).

[105] F. Riggi, P. La Rocca, and S. Riggi, Eur. J. Phys. **37**, (2016).

[106] P. Dalmas De Réotier, P. C. M. Gubbens, and A. Yaouanc, J. Phys. Condens. Matter **16**, (2004).

[107] S. F. J. Cox, J. Phys. C Solid State Phys. **20**, 3187 (1987).

[108] O. Arnold, J. C. Bilheux, J. M. Borreguero, A. Buts, S. I. Campbell, L. Chapon, M. Doucet, N. Draper, R. Ferraz Leal, M. A. Gigg, V. E. Lynch, A. Markvardsen, D. J. Mikkelson, R. L. Mikkelson, R. Miller, K. Palmen, P. Parker, G. Passos, T. G. Perring, P. F. Peterson, S. Ren, M. A. Reuter, A. T. Savici, J. W. Taylor, R. J. Taylor, R. Tolchenov, W. Zhou, and J. Zikovsky, Nucl. Instruments Methods Phys. Res. Sect. A Accel. Spectrometers, Detect. Assoc. Equip. **764**, 156 (2014).

[109] C. G. Windsor, *Pulsed Neutron Scattering* (Taylor & Francis ; Halsted Press, London; New York, 1981).

[110] B. S. Hudson, J. Phys. Chem. A **105**, 3949 (2001).

[111] S. Raymond, Collect. SFN **13**, 02003 (2014).

[112] R. I. Bewley, J. W. Taylor, and S. M. Bennington., Nucl. Instruments Methods Phys. Res. Sect. A Accel. Spectrometers, Detect. Assoc. Equip. **637**, 128 (2011).

[113] R. I. Bewley, R. S. Eccleston, K. A. McEwen, S. M. Hayden, M. T. Dove, S. M. Bennington, J. R. Treadgold, and R. L. S. Coleman, Phys. B Condens. Matter **385**–**386**, 1029 (2006).

[114] D. Colognesi, M. Celli, F. Cilloco, R. J. Newport, S. F. Parker, V. Rossi-Albertini, F. Sacchetti, J. Tomkinson, and M. Zoppi, Appl. Phys. A Mater. Sci. Process. **74**, 64 (2002).

[115] S. . Campbell, M. T. . Telling, and C. . Carlile, Phys. B Condens. Matter **276**–**278**, 206 (2000).

[116] M. A. De Vries, A. C. McLaughlin, and J. W. G. Bos, Phys. Rev. Lett. **104**, 177202 (2010).

[117] O. Mustonen, S. Vasala, E. Sadrollahi, K. P. Schmidt, C. Baines, H. C. Walker, I. Terasaki, F. J. Litterst, E. Baggio-Saitovitch, and M. Karppinen, Nat. Commun. **9**, 1085 (2018).

[118] A. V. Mikheenkov, V. E. Valiulin, A. V. Shvartsberg, and A. F. Barabanov, J. Exp. Theor. Phys. **126**, 404 (2018).

[119] W. M. H. Natori, M. Daghofer, and R. G. Pereira, Phys. Rev. B **96**, (2017).

[120] J. S. Hwang, K. J. Lin, and C. Tien, Rev. Sci. Instrum. **68**, 94 (1997).

[121] Quantum Design, Test 43 (1999).

[122] G. T. Furukawa, M. L. Reilly, and J. S. Gallagher, J. Phys. Chem. Ref. Data **3**, 163 (1974).

[123] R. Moessner and A. P. Ramirez, Phys. Today **59**, 24 (2006).

[124] M. J. Harris, S. T. Bramwell, D. F. McMorrow, T. Zeiske, and K. W. Godfrey, Phys. Rev. Lett. **79**, 2554 (1997).

[125] J. S. Gardner, S. R. Dunsiger, B. D. Gaulin, M. J. P. Gingras, J. E. Greedan, R. F. Kiefl, M. D. Lumsden, W. A. Mac Farlane, N. P. Raju, J. E. Sonier, I. Swainson, and Z. Tun, Phys. Rev. Lett. **82**, 1012 (1999).

[126] C. G. Shull and J. S. Smart, Phys. Rev. **76**, 1256 (1949).

[127] M. E. Lines and E. D. Jones, Phys. Rev. **139**, 1313 (1965).

[128] C. G. Shull, W. A. Strauser, and E. O. Wollan, Phys. Rev. **83**, 333 (1951).

[129] F. Keffer and W. O'Sullivan, Phys. Rev. **108**, 637 (1957).

[130] J. I. Kaplan, J. Chem. Phys. **22**, 1709 (1954).

[131] W. L. Roth, Phys. Rev. **110**, 1333 (1958).

[132] A. L. Goodwin, M. G. Tucker, M. T. Dove, and D. A. Keen, Phys. Rev. Lett. **96**, 047209 (2006).

[133] J. A. M. Paddison, M. J. Gutmann, J. R. Stewart, M. G. Tucker, M. T. Dove, D. A. Keen, and A. L. Goodwin, Phys. Rev. B **97**, 014429 (2018).

[134] S. Vasala and M. Karppinen, Prog. Solid State Chem. **43**, 1 (2015).

[135] C. P. Khattak, D. E. Cox, and F. F. Y. Wang, J. Solid State Chem. **17**, 323 (1976).

[136] A. K. Azad, S. G. Eriksson, A. Mellergård, S. A. Ivanov, J. Eriksen, and H. Rundlöf, Mater. Res. Bull. **37**, 1797 (2002).

[137] B. Boucher, R. Buhl, and M. Perrin, J. Appl. Phys. **42**, 1615 (1971).

[138] G. B. Jensen and O. V. Nielsen, J. Phys. C Solid State Phys. **7**, 409 (1974).

[139] J. Cheng and Z. Q. Yang, Phys. Status Solidi Basic Res. **243**, 1151 (2006).

[140] Y. Fujioka, J. Frantti, and R. M. Nieminen, J. Phys. Chem. B **112**, 6742 (2008).

[141] A. K. Azad, S. Ivanov, S. G. Eriksson, H. Rundlöf, J. Eriksen, R. Mathieu, and P. Svedlindh, J. Magn. Magn. Mater. **237**, 124 (2001).

[142] A. Muñoz, J. A. Alonso, M. T. Casais, M. J. Martínez-Lope, and M. T. Fernández-Díaz, J. Phys. Condens. Matter **14**, 8817 (2002).

[143] Q. Lin, M. Greenblatt, and M. Croft, J. Solid State Chem. **178**, 1356 (2005).

[144] J. A. Alonso, M. T. Casais, and M. J. Martinez-Lope, Z. Naturforsch **58b**, 571 (2003).

[145] R. Cardona, D. A. Landínez Téllez, J. Arbey Rodríguez M., F. Fajardo, and J. Roa-Rojas, J. Magn. Magn. Mater. **320**, e85 (2008).

[146] S. Lv, X. Liu, H. Li, Z. Wu, and J. Meng, Comput. Mater. Sci. **49**, 266 (2010).

[147] A. K. Azad, S. G. Eriksson, S. A. Ivanov, R. Mathieu, P. Svedlindh, J. Eriksen, and H. Rundlöf, J. Alloys Compd. **364**, 77 (2004).

[148] H. Wu, Phys. Rev. B **64**, 1251261 (2001).

[149] R. Rodriguez, A. Fernandez, A. Isalgue, J. Rodriguez, A. Labarta, J. Tejada, and X. Obradorst, J. Phys. C Solid State Phys. **18**, 401 (1985).

[150] S. Tao, J. Canales-Vázquez, and J. T. S. Irvine, Chem. Mater. **16**, 2309 (2004).

[151] K. Tezuka, K. Henmi, Y. Hinatsu, and N. M. Masaki, J. Solid State Chem. **154**, 591 (2000).

[152] J. E. Greedan, S. Derakhshan, F. Ramezanipour, J. Siewenie, and T. H. Proffen, J. Phys. Condens. Matter **23**, (2011).

[153] R. Morrow, M. A. McGuire, J. Yan, and P. M. Woodward, Inorg. Chem. **57**, 2989 (2018).

[154] K. I. Kobayashi, T. Kimura, H. Sawada, K. Terakura, and Y. Tokura, Nature **395**, 677 (1998).

[155] B. García-Landa, C. Ritter, M. . Ibarra, J. Blasco, P. . Algarabel, R. Mahendiran, and J. García, Solid State Commun. **110**, 435 (1999).

[156] O. Chmaissem, R. Kruk, B. Dabrowski, D. E. Brown, X. Xiong, S. Kolesnik, J. D. Jorgensen, and C. W. Kimball, Phys. Rev. B **62**, 14197 (2000).

[157] M. K. Chung, P. J. Huang, W. H. Li, C. C. Yang, T. S. Chan, R. S. Liu, S. Y. Wu, and J. W. Lynn, Phys. B Condens. Matter **385**-**386 I**, 418 (2006).

[158] J. Navarro, L. Balcells, F. Sandiumenge, M. Bibes, A. Roig, B. Martínez, and J. Fontcuberta, J. Phys. Condens. Matter **13**, 8481 (2001).

[159] F. L. Zabotto, A. J. Gualdi, and J. A. Eiras, Mater. Res. **15**, 428 (2012).

[160] P. C. R. Varma, R. S. Manna, D. Banerjee, M. R. Varma, K. G. Suresh, and A. K. Nigam, J. Alloys Compd. **453**, 298 (2008).

[161] K. El Maalam, L. Fkhar, Z. Mahhouti, O. Mounkachi, M. Aitali, M. Hamedoun, and A. Benyoussef, J. Phys. Conf. Ser. **758**, (2016).

[162] M. J. Martinez-Lope, J. A. Alonso, M. T. Casais, and T. Fernandez-Diaz, M, Eur. J. Inorg. Chem. **6**, 2463 (2002).

[163] D. E. Cox, G. Shirane, and B. C. Frazer, J. Appl. Phys. **38**, 1459 (1967).

[164] T. Hirama, N. Tsujii, H. Kitazawa, and G. Kido, Phys. B Condens. Matter **359**–**361**, 1336 (2005).

[165] M. C. Viola, M. J. Martínez-Lope, J. A. Alonso, J. L. Martínez, J. M. De Paoli, S. Pagola, J. C. Pedregosa, M. T. Fernández-Díaz, and R. E. Carbonio, Chem. Mater. **15**, 1655 (2003).

[166] M. Gateshki, J. M. Igartua, and E. Hernández-Bocanegra, J. Phys. Condens. Matter **15**, 6199 (2003).

[167] S. A. Ivanov, S. G. Eriksson, R. Tellgren, H. Rundlöf, and M. Tseggai, Mater. Res. Bull. **40**, 840 (2005).

[168] S. A. Ivanov, S. G. Eriksson, R. Tellgren, H. Rundlöf, and M. Tssegai, Zeitschrift Fur Krist. Suppl. **2**, 537 (2006).

[169] P. D. Battle and C. W. Jones, J. Solid State Chem. **78**, 108 (1989).

[170] T. Aharen, J. E. Greedan, F. Ning, T. Imai, V. Michaelis, S. Kroeker, H. Zhou, C. R. Wiebe, and L. M. D. Cranswick, Phys. Rev. B - Condens. Matter Mater. Phys. **80**, 4 (2009).

[171] J. P. Carlo, J. P. Clancy, K. Fritsch, C. A. Marjerrison, G. E. Granroth, J. E. Greedan, H. A. Dabkowska, and B. D. Gaulin, Phys. Rev. B - Condens. Matter Mater. Phys. **88**, 2 (2013).

[172] G. J. Nilsen, C. M. Thompson, G. Ehlers, C. A. Marjerrison, and J. E. Greedan, Phys. Rev. B - Condens. Matter Mater. Phys. **91**, 1 (2015).

[173] P. D. Battle and W. J. Macklin, J. Solid State Chem. **52**, 138 (1984).

[174] R. P. Singh and C. V. Tomy, Phys. Rev. B - Condens. Matter Mater. Phys. **78**, (2008).

[175] P. Kayser, B. Ranjbar, B. J. Kennedy, and M. Avdeev, J. Solid State Chem. **249**, 154 (2017).

[176] E. Granado, J. W. Lynn, R. F. Jardim, and M. S. Torikachvili, Phys. Rev. Lett. **110**, 1 (2013).

[177] R. P. Singh, C. V. Tomy, and A. K. Grover, J. Phys. Conf. Ser. **200**, (2010).

[178] Y. Doi and Y. Hinatsu, J. Phys. Condens. Matter **11**, 4813 (1999).

[179] W. R. Gemmill, M. D. Smith, and H.-C. zur Loye, J. Solid State Chem. **177**, 3560 (2004).

[180] A. A. Aczel, D. E. Bugaris, L. Li, J. Q. Yan, C. De La Cruz, H. C. Zur Loye, and S. E. Nagler, Phys. Rev. B - Condens. Matter Mater. Phys. **87**, 1 (2013).

[181] S. J. Makowski, J. A. Rodgers, P. F. Henry, J. P. Attfield, and J. W. G. Bos, Chem. Mater. **21**, 264 (2009).

[182] A. A. Aczel, P. J. Baker, D. E. Bugaris, J. Yeon, H. C. Zur Loye, T. Guidi, and D. T. Adroja, Phys. Rev. Lett. **112**, (2014).

[183] Y. Todate, J. Phys. Chem. Solids **60**, 1173 (1999).

[184] D. Iwanaga, Y. Inaguma, and M. Itoh, Mater. Res. Bull. **35**, 449 (2000).

[185] C. G. F. Blum, A. Holcombe, M. Gellesch, M. I. Sturza, S. Rodan, R. Morrow, A. Maljuk, P. Woodward, P. Morris, A. U. B. Wolter, B. Büchner, and S. Wurmehl, J. Cryst. Growth **421**, 39 (2015).

[186] N. Rezaei, T. Hashemifar, M. Alaei, F. Shahbazi, S. J. Hashemifar, and H. Akbarzadeh, Phys. Rev. B **99**, 104411 (2019).

[187] M. J. Martínez-Lope, J. A. Alonso, and M. T. Casais, Eur. J. Inorg. Chem. **6**, 2839 (2003).

[188] K. Yamamura, M. Wakeshima, and Y. Hinatsu, J. Solid State Chem. **179**, 605 (2006).

[189] C. M. Thompson, J. P. Carlo, R. Flacau, T. Aharen, I. A. Leahy, J. R. Pollichemi, T. J. S. Munsie, T. Medina, G. M. Luke, J. Munevar, S. Cheung, T. Goko, Y. J. Uemura, and J. E. Greedan, J. Phys. Condens. Matter **26**, (2014).

[190] Y. Sasaki, Y. Doi, and Y. Hinatsu, J. Mater. Chem. **12**, 2361 (2002).

[191] T. Aharen, J. E. Greedan, C. A. Bridges, A. A. Aczel, J. Rodriguez, G. MacDougall, G. M. Luke, V. K. Michaelis, S. Kroeker, C. R. Wiebe, H. Zhou, and L. M. D. Cranswick, Phys. Rev. B - Condens. Matter Mater. Phys. **81**, 1 (2010).

[192] G. Chen and L. Balents, Phys. Rev. B - Condens. Matter Mater. Phys. **84**, 1 (2011).

[193] A. Nishiyama, Y. Doi, and Y. Hinatsu, J. Solid State Chem. **248**, 134 (2017).

[194] Y. Todate, W. Higemoto, K. Nishiyama, and K. Hirota, J. Phys. Chem. Solids **68**, 2107 (2007).

[195] O. Mustonen, S. Vasala, H. Mutch, C. I. Thomas, G. B. G. Stenning, E. Baggio-Saitovitch, E. J. Cussen, and M. Karppinen, Chem. Commun. **55**, 1132 (2019).

[196] S. Vasala, M. Avdeev, S. Danilkin, O. Chmaissem, and M. Karppinen, J. Phys. Condens. Matter **26**, (2014).

[197] D. Iwanaga, Y. Inaguma, and M. Itoh, **295**, 291 (1999).

[198] T. Koga, N. Kurita, M. Avdeev, S. Danilkin, T. J. Sato, and H. Tanaka, Phys. Rev. B **93**, 1 (2016).

[199] S. Vasala, H. Saadaoui, E. Morenzoni, O. Chmaissem, T. S. Chan, J. M. Chen, Y. Y. Hsu, H. Yamauchi, and M. Karppinen, Phys. Rev. B **89**, 134419 (2014).

[200] H. C. Walker, O. Mustonen, S. Vasala, D. J. Voneshen, M. D. Le, D. T. Adroja, and M. Karppinen, Phys. Rev. B **94**, 064411 (2016).

[201] Y. Xu, S. Liu, N. Qu, Y. Cui, Q. Gao, R. Chen, J. Wang, F. Gao, and X. Hao, J. Phys. Condens. Matter **29**, (2017).

[202] A. Glamazda, Y. S. Choi, S. H. Do, S. Lee, P. Lemmens, A. N. Ponomaryov, S. A. Zvyagin, J. Wosnitza, D. P. Sari, I. Watanabe, and K. Y. Choi, Phys. Rev. B **95**, 1 (2017).

[203] G. N. Rao, R. Sankar, A. Singh, I. P. Muthuselvam, W. T. Chen, V. N. Singh, G. Y. Guo, and F. C. Chou, Phys. Rev. B **93**, 1 (2016).

[204] D. Macdougal, A. S. Gibbs, T. Ying, S. Wessel, H. C. Walker, D. Voneshen, F. Mila, H. Takagi, and R. Coldea, Phys. Rev. B **98**, 1 (2018).

[205] A. S. Gibbs, A. Yamamoto, A. N. Yaresko, K. S. Knight, H. Yasuoka, M. Majumder, M. Baenitz, P. J. Saines, J. R. Hester, D. Hashizume, A. Kondo, K. Kindo, and H. Takagi, Phys. Rev. B **95**, 2 (2017).

[206] O. J. Burrows, G. J. Nilsen, E. Suard, M. Telling, J. R. Stewart, and M. A. de Vries, 1 (2016).

[207] S. Vasala, J. G. Cheng, H. Yamauchi, J. B. Goodenough, and M. Karppinen, Chem. Mater. **24**, 2764 (2012).

[208] W. Witczak-Krempa, G. Chen, Y. B. Kim, and L. Balents, Annu. Rev. Condens. Matter Phys. **5**, 57 (2014).

[209] E. J. Cussen, D. R. Lynham, and J. Rogers, Chem. Mater. **18**, 2855 (2006).

[210] T. Aharen, J. E. Greedan, C. A. Bridges, A. A. Aczel, J. Rodriguez, G. MacDougall, G. M. Luke, T. Imai, V. K. Michaelis, S. Kroeker, H. Zhou, C. R. Wiebe, and L. M. D. Cranswick, Phys. Rev. B - Condens. Matter Mater. Phys. **81**, 224409 (2010).

[211] M. A. De Vries, J. O. Piatek, M. Misek, J. S. Lord, H. M. Rønnow, and J. W. G. Bos, New J. Phys. **15**, 0 (2013).

[212] J. P. Carlo, J. P. Clancy, T. Aharen, Z. Yamani, J. P. C. Ruff, J. J. Wagman, G. J. Van Gastel, H. M.

L. Noad, G. E. Granroth, J. E. Greedan, H. A. Dabkowska, and B. D. Gaulin, Phys. Rev. B - Condens. Matter Mater. Phys. **84**, 29 (2011).

[213] M. Tarzia and G. Biroli, Epl **82**, (2008).

[214] A. C. McLaughlin, M. A. De Vries, and J. W. G. Bos, Phys. Rev. B **82**, 1 (2010).

[215] F. C. Coomer and E. J. Cussen, J. Phys. Condens. Matter **25**, (2013).

[216] E. J. Cussen, J. Solid State Chem. **180**, 474 (2007).

[217] A. C. McLaughlin, Solid State Commun. **137**, 354 (2006).

[218] T. K. Wallace, R. H. Colman, and A. C. McLaughlin, Phys. Chem. Chem. Phys. **15**, 8672 (2013).

[219] C. R. Wiebe, J. E. Greedan, G. M. Luke, and J. S. Gardner, Phys. Rev. B **65**, 144413 (2002).

[220] R. Wiebe, E. Greedan, P. Kyriakou, M. Luke, S. Gardner, A. Fukaya, M. Gat-Malureanu, L. Russo, T. Savici, and J. Uemura, Phys. Rev. B - Condens. Matter Mater. Phys. **68**, 1 (2003).

[221] A. K. Azad, S. A. Ivanov, S.-G. Eriksson, J. Eriksen, H. Rundlöf, and P. Mathieu, R.Svedlindh, Mater. Res. Bull. **36**, 2215 (2002).

[222] J. N. Reimers, J. E. Greedan, C. V. Stager, and M. Bjorgvinnsen, Phys. Rev. B **43**, 5692 (1991).

[223] M. A. McGuire and V. O. Garlea, Phys. Rev. B **93**, 054404 (2016).

[224] W. G. Williams, R. M. Ibberson, P. Day, and J. E. Enderby, Phys. B **241**–**243**, 234 (1998).

[225] A. C. Larson and R. B. Von Dreele, *General Structure Analysis System (GSAS)* (2004).

[226] A. Rauch, W. Waschkowski, D. Dubbers, R. P. May, R. Cubitt, C. C. Wilson, E. Lelievre-Berna, J. R. Stewart, F. Tasset, J. Brown, R. S. Eccleston, R. Currat, J. Kulda, B. Farago, A. W. Hewat, G. J. McIntyre, C. J. Carlile, I. Anderson, A. Oed, M. Johnson, S. A. Mason, R. B. Von Dreele, H. Borner, and J. Tribolet, *Neutron Data Booklet*, 2nd ed. (Old City Publishing Group, Philadelphia, 2003).

[227] S. R. Giblin, S. P. Cottrell, P. J. C. King, S. Tomlinson, S. J. S. Jago, L. J. Randall, M. J. Roberts, J. Norris, S. Howarth, Q. B. Mutamba, N. J. Rhodes, and F. A. Akeroyd, Nucl. Instruments Methods Phys. Res. Sect. A Accel. Spectrometers, Detect. Assoc. Equip. **751**, 70 (2014).

[228] S. Toth and B. Lake, J. Phys. Condens. Matter **27**, 166002 (2015).

[229] F. C. Coomer and E. J. Cussen, Inorg. Chem. **53**, 746 (2014).

[230] J. Rodríguez-Carvajal, Phys. B Condens. Matter **192**, 55 (1993).

[231] J. Cui, Q. Huang, and B. H. Toby, Powder Diffr. **21**, 71 (2006).

[232] B. C. Tofield and B. E. F. Fender, J. Phys. Chem. Solids **31**, 2741 (1970).

[233] J. Hubbard and W. Marshall, Proc. Phys. Soc. **86**, 561 (1965).

[234] M. F. Collins, in *Magn. Critcal Scatt.* (Oxford University Press, 1989), pp. 12–15.

[235] C. J. Howard, B. J. Kennedy, and P. M. Woodward, Acta Crystallogr. Sect. B Struct. Sci. **59**, 463 (2003).

[236] H. Mutch, O. Mustonen, H. C. Walker, P. J. Baker, G. B. G. Stenning, F. C. Coomer, and E. J. Cussen, Phys. Rev. Mater. **4**, 1 (2020).

[237] R. D. Shannon, Acta. Cryst. **A 32**, 751 (1976).

[238] V. M. Goldschmidt, Berichte Der Dtsch. Chem. Gesellschaft (A B Ser. **60**, 1263 (1927).

[239] M. Murrie, Chem. Soc. Rev. **39**, 1986 (2010).

[240] E. A. El-Sharkawy, S. S. Al-Shihry, and A. M. Youssef, Adsorpt. Sci. Technol. **24**, 657 (2006).

[241] R. A. Young and D. B. Wiles, J. Appl. Crystallogr. **15**, 430 (1982).

[242] Y. Li and X. Liu, Mater. Res. Bull. **64**, 88 (2015).

[243] P. G. Jones, Chem. Soc. Rev. **13**, 157 (1984).

[244] E. J. Cussen and P. D. Battle, J. Mater. Chem. **13**, 1210 (2003).

[245] B. C. Melot, J. E. Drewes, R. Seshadri, E. M. Stoudenmire, and A. P. Ramirez, J. Phys. Condens. Matter **21**, 1 (2009).

[246] E. J. Cussen and W. J. Cameron, J. Mater. Chem. **20**, 1340 (2010).

[247] F. Lloret, M. Julve, J. Cano, R. Ruiz-García, and E. Pardo, Inorganica Chim. Acta (2008).

[248] P. Dutta, M. S. Seehra, S. Thota, and J. Kumar, J. Phys. Condens. Matter **20**, (2008).

[249] I. Panagiotopoulos, V. Alexandrakis, G. Basina, S. Pal, H. Srikanth, D. Niarchos, G. Hadjipanayis, and V. Tzitzios, Cryst. Growth Des. **9**, 3353 (2009).

[250] H. Wang, J. Yang, C. Dong, Q. Mao, J. Du, and M. Fang, J. Cryst. Growth **430**, 52 (2015).

[251] R. Kannan and M. S. Seehra, Phys. Rev. B **35**, 6847 (1987).

[252] H. Maletta, J. Appl. Phys. **53**, 2185 (1982).

[253] V. Primo-Martín and M. Jansen, J. Solid State Chem. (2001).

[254] W. M. H. Natori, E. C. Andrade, E. Miranda, and R. G. Pereira, Phys. Rev. Lett. **117**, 017204 (2016).

[255] S. Di Matteo, G. Jackeli, C. Lacroix, and N. B. Perkins, Phys. Rev. Lett. **93**, 1 (2004).

[256] J. Romhányi, L. Balents, and G. Jackeli, Phys. Rev. Lett. **118**, 1 (2017).

[257] N. Iwahara, V. Vieru, and L. F. Chibotaru, Phys. Rev. B **98**, 075138 (2018).

[258] Y. Li, D. Adroja, P. K. Biswas, P. J. Baker, Q. Zhang, J. Liu, A. A. Tsirlin, P. Gegenwart, and Q. Zhang, Phys. Rev. Lett. **117**, 1 (2016).

[259] J. C. Orain, L. Clark, F. Bert, P. Mendels, P. Attfield, F. H. Aidoudi, R. E. Morris, P. Lightfoot, A. Amato, and C. Baines, J. Phys. Conf. Ser. **551**, (2014).

[260] M. W. Johnson and W. I. F. David, *HRPD: The High Resolution Powder Diffractometer at the SNS* (1985).

[261] P. M. Woodward, Acta Crystallogr. Sect. B Struct. Sci. **53**, 32 (1997).

[262] K. H. Kim, E. H. Kang, B. K. Kang, K. P. Kim, and S. H. Hong, J. Lumin. **183**, 13 (2017).

[263] S. Zhang, Z. Hao, L. Zhang, G. H. Pan, H. Wu, X. Zhang, Y. Luo, L. Zhang, H. Zhao, and J. Zhang, Sci. Rep. **8**, 2 (2018).

[264] A. Trzesowska, R. Kruszynski, and T. J. Bartczak, Acta Crystallogr. Sect. B Struct. Sci. **60**, 174 (2004).

[265] H. Kohlmann, Eur. J. Inorg. Chem. **2019**, 4174 (2019).

[266] H. Schafer, Angew. Chemie Int. Ed. **10**, 43 (1971).

[267] R. I. Walton and D. O'Hare, Chem. Commun. 2283 (2000).

[268] M. W. Lufaso and P. M. Woodward, Acta. Cryst. **B57**, 725 (2001).

[269] J. Cumby and J. P. Attfield, Nat. Commun. **8**, 14325 (2017).

[270] K. Yoshii, J. Solid State Chem. **151**, 294 (2000).